A Measurement of the Low Mass Drell-Yan Di fferential Cross Section in the Di-Muon Channel with º s = 7 TeV Proton-Proton Collisions at the ATLAS Experiment

Goddard, Jack Robert

A Measurement of the Low Mass Drell-Yan Differential Cross Section in the Di-Muon Channel with $\sqrt{s}$ = 7 TeV Proton-Proton Collisions at the ATLAS Experiment

Author:
Jack Robert Goddard

Supervisor:
Dr. Eram Rizvi

Submitted in partial fulfilment of the requrements for the degree of
Doctor of Philosophy
in the School of Physics and Astronomy.

February 2014

Statement of Orginality

I, Jack Robert Goddard, confirm that the research included within this thesis is my own work or that where it has been carried out in collaboration with, or supported by others, that this is duly acknowledged below and my contribution indicated. Previously published material is also acknowledged below.

I attest that I have exercised reasonable care to ensure that the work is original, and does not to the best of my knowledge break any UK law, infringe any third party's copyright or other Intellectual Property Right, or contain any confidential material.

I accept that the College has the right to use plagiarism detection software to check the electronic version of the thesis.

I confirm that this thesis has not been previously submitted for the award of a degree by this or any other university.

Signature:

Date: 21st February 2014

Details of collaboration and publications:

The analysis presented in this thesis forms part of an ATLAS Collaboration paper [1] which, at the time of writing, is currently undergoing internal approval. Any aspects of the analysis not produced by myself are fully referenced. In particular chapter 9 puts the analysis presented in this thesis in the context of the paper. Much of this chapter demonstrates the impact of this measurement once it has been combined with another. This is made clear and is fully referenced. A discussion of my sole contributions to the analysis is made in chapter 1.

Abstract

A measurement of the Drell-Yan differential cross section at low invariant mass is presented in the di-muon channel. A 1.64 pb^{-1} dataset of $\sqrt{s} = 7$ TeV proton-proton collision data collected by the ATLAS experiment at the LHC is used. The measurement is made in an invariant mass range of $26 < M_{\mu\mu} < 66$ GeV where $M_{\mu\mu}$ is the invariant mass of the muon pair. A review of the relevant theoretical physics and the ATLAS detector is made. The analysis is described with particular attention paid to the determination of the isolation efficiency corrections for the Monte Carlo and the estimate of the multijet background. The fiducial differential cross section is calculated with a statistical uncertainty that varies between 0.8% and 1.2%. The systematic uncertainty is seen to vary between 2.4% and 4.1%. A cross section extrapolated to the full phase space is also presented. This is dominated by theoretical uncertainties from the variation of the factorisation and renormalisation scales. The obtained fiducial differential mass cross section is compared to theoretical predictions at NLO and NNLO in perturbative QCD. It is shown that a move beyond NLO is needed to describe the distribution well due to the restrictions of using a fixed order theoretical prediction. A combination with the electron channel measurement is also briefly discussed as well as comparisons to a di-muon measurement in an extended invariant mass range. This allows similar, but stronger conclusions to be drawn. A discussion is made of a PDF fit that uses the measurement presented here. The fit demonstrates the impact of the measurement on the PDFs and further supports the conclusion that a move to NNLO in pQCD is needed to describe the data.

Acknowledgements

I would firstly like to thank my supervisor Eram Rizvi for suggesting what I found to be a very interesting thesis topic. His advice and guidance have been invaluable and his calm attitude to the many bugs I created and squashed in my code over the last four years was most welcome. I also need to thank Elisa Piccaro and Joesph Lilley who worked on other aspects of the Drell-Yan measurement for their many helpful conversations. I would also like to thank many of the students I was on LTA with at CERN for many informative conversations over lunch, coffee and beer. I would especially like to thank those students I lived with on Rue de l'Athénée from whom the useful conversations have continued well after the time we all left Geneva. Although the work is not presented in this thesis I would like to thank Marcella Bona for her help and supervision on my service task of measuring the Lorentz angle in the ATLAS SCT. I would also like to thank the STFC for funding my PhD and giving me the exciting opportunity of being based at CERN for so many months. Finally, but by no means least I would like to thank my parents, brother and family for their continued support and encouragement.

Contents

List of Figures

List of Tables

Chapter 1

Introduction

The Large Hadron Collider (LHC) is currently the highest energy particle accelerator in existence. In Run I it collided protons at a centre of mass energy of 7 TeV in 2010 and 2011 data taking and 8 TeV in 2012. This opens up phase space in which the Standard Model of particle physics has not been directly tested before. The parton distribution functions (PDFs) that describe the structure of the proton have been constrained by lower energy experiments and evolved to LHC energies. New measurements are needed to compare the evolved predictions with data at this new energy. These PDFs are described in chapter 2. Also, discussed is the Drell-Yan processes and how a measurement of the cross section, complementary to measurements made at the Z resonance help to distinguish between different PDFs within the proton. Chapter 3 gives an overview of the ATLAS detector, concentrating on the sub detectors that are most important for a measurement of the Drell-Yan process in the muon channel at low mass. Chapters 4 to 7 describe the analysis performed, selections made and the corrections that were applied to the Monte Carlo. Particular attention is paid to determination of the efficiency corrections (chapter 5) and the estimation of the background from multijet events (chapter 6). In chapter 8 the differential cross section is calculated and the uncertainties from a number of different sources are determined. Comparisons are made to theoretical predictions and the low mass Drell-Yan results from other LHC experiments. A short discussion is then made (chapter 9), positioning the measurement presented in this thesis in the context of the soon to be published ATLAS measurement of the differential low mass Drell-Yan cross section. Also discussed is a PDF fit using the measurement in this thesis. In chapter 10 the results are summarised in a conclusion.

The work presented in this thesis was carried out within the ATLAS collaboration. The nature of modern particle physics means that not all aspects of an analysis can be done by a single analyser. The Monte Carlo and many of the corrections applied to it are produced centrally to be used by analysis teams. Within the analysis teams themselves, work is divided up among the members. All of the plots in this thesis unless referenced otherwise were created by the author. In addition all work in this thesis by the author is listed below:

- **Chapter 4, Analysis and Selection:** Determination of the muon isolation selection, both of the muon isolation variable used and the cut upon it. Plots showing

the impact of the provided Monte Carlo corrections on the analysis were produced by the author, along with the control distributions. The calculation of the event yield was also the author's own work.

- **Chapter 5, Muon Isolation Efficiency:** The muon isolation efficiency Monte Carlo corrections and the associated uncertainties have been determined for `muid` combined muons by the author. The method in this chapter is based on the referenced Z resonance analysis.

- **Chapter 6, Multijet Background Studies:** All the work in this chapter is the author's own. Three methods for the estimation of the multijet background have been examined.

- **Chapter 7, Comparison of Data and Monte Carlo:** All plots showing the agreement between data and Monte Carlo and the cut flow tables were produced by the author.

- **Chapter 8, Low Mass Drell-Yan Differential Cross Sections:** The bin-by-bin unfolding and cross section measurement are the author's work. Propagation of the uncertainties from various sources was also carried out by the author. Correction factors to scale the measured cross section to the dressed and extrapolated cross section were provided, but applied by the author. Plots showing a comparison between the measured cross section and theoretical predictions were made using modified macros from the working group, which the author had a hand in creating.

As well as the analysis presented here, a number of studies of the Lorentz angle in the semiconductor tracker were also made during the course of my PhD. These are not included in this thesis as they are not related to the physics analysis presented in the thesis. The Lorentz angle is extracted from a fit to the distribution of the average cluster size vs. the angle of incidence of the track to the SCT sensor. Studies covered Monte Carlo and data comparisons, improvements to the track selection, an examination of an asymmetric fitting function. A series of null tests were examined that looked to measure the Lorentz angle in scenarios where no Lorentz angle is expected as a first step towards estimating a systematic uncertainty to assign to the fit result.

Chapter 2

Theory

This chapter covers the theory needed to understand the measurement made in this thesis and to put it into the context of its potential theoretical impact. The first section of this chapter describes the particles and forces and structure of the Standard Model, while the second section discusses some of the physics of proton-proton collisions. The Drell-Yan process and the potential impact of a low mass measurement is discussed in the final section.

2.1 The Standard Model

The Standard Model of particle physics is an incredibly successful model that can explain nearly all experimental measurements from high energy experiments. It was formulated in the 1970s and describes how matter is built from fundamental spin $\frac{1}{2}$ fermions and the interaction between these fermions which are mediated by bosons with integer spin. All the particles in the Standard Model are listed in table 2.1 with their masses and electrical charges. Each of the fermions in the table also has an antiparticle, which has the same mass, but opposite electric charge.

The Standard Model is based on three relativistic quantum field theories. These are Quantum Chromodynamics (QCD), Quantum Electrodynamics (QED) and the Weak Theory. These theories describe the strong, electromagnetic and weak forces respectively. Gravity is not represented in the Standard Model. Currently a relativistic quantum field theory has not been found for gravity, but as it is negligibly weak at the scales considered in particle physics this does not limit the usefulness of the Standard Model.

2.1.1 Fermions

The fermions in the model are divided into quarks and leptons. The quarks carry one of three colour charges, red, green or blue and are only found in bound colour singlet states. These states are in the form of hadrons which are either mesons, such as pions and kaons, or baryons, such as protons and neutrons. Mesons, which have integer spin, consist of two quarks, whereas the baryons have $\frac{1}{2}$ spin and consist of three bound quarks. The quarks themselves have fractional units of electric charge, e, and are grouped into pairs with $1e$

difference in charge. The pairs form three generations of increasing mass,

$$\begin{pmatrix} u \\ d \end{pmatrix}, \quad \begin{pmatrix} c \\ s \end{pmatrix}, \quad \begin{pmatrix} t \\ b \end{pmatrix}. \tag{2.1}$$

The leptons are also grouped as three sets of generational pairs, with each of the three charged leptons having an associated neutrino. Unlike the quarks, the leptons are not confined into bound states,

$$\begin{pmatrix} \nu_e \\ e^- \end{pmatrix}, \quad \begin{pmatrix} \nu_\mu \\ \mu^- \end{pmatrix}, \quad \begin{pmatrix} \nu_\tau \\ \tau^- \end{pmatrix}. \tag{2.2}$$

2.1.2 Bosons

The Standard Model also describes the interactions between the fermions which are mediated by the gauge bosons. The electromagnetic force which is responsible for the majority of interactions that occur outside of the nucleus is propagated via the spin 1 photon, which couples to electric charge. The strong force which is responsible for hadronic confinement is propagated via the massless gluons, which couple to colour charge. The gluons themselves also carry colour charge, allowing for self interactions. The final force described by the Standard Model, which couples to all fermions, is the weak force which has three associated massive gauge bosons, the neutral Z and the W^+ and W^- bosons which between them allow both neutral and charged current weak interactions to occur.

	Particle	Symbol	Mass	Charge $[Q_{\lvert e\rvert}]$
Quarks	Up	u	$2.3^{+0.7}_{-0.5}$ MeV	$+2/3$
	Down	d	$4.8^{+0.5}_{-0.3}$ MeV	$-1/3$
	Strange	s	95.0 ± 5.0 MeV	$+2/3$
	Charm	c	1.275 ± 0.025 GeV	$-1/3$
	Bottom	b	4.18 ± 0.03 GeV	$+2/3$
	Top	t	173.07 ± 0.89 GeV	$-1/3$
Leptons	Electron	e	0.51 ± 0.00 MeV	-1
	Muon	μ	105.66 ± 0.00 MeV	-1
	Tau	τ	1776.82 ± 0.16 MeV	-1
	Electron Neutrino	ν_e	< 460 eV†	0
	Muon Neutrino	ν_μ	< 0.19 MeV†	0
	Tau Neutrino	ν_τ	< 18.2 MeV†	0
Bosons	Photon	$\gamma^\star$	0	0
	Z	Z	91.188 ± 0.002 GeV	0
	$W^\pm$	$W^\pm$	80.385 ± 0.015 GeV	± 1
	Gluon	g	0	0
	Higgs	H	125.9 ± 0.4 GeV	0

Table 2.1: Particles of the Standard Model. Particle Data Group [2] values are used, with the charge of the particles expressed in units of the electron charge, $Q_{\lvert e\rvert}$.
†: The neutrino masses are predicted to be zero in the Standard Model but an extension to it allows them to be included.

2.1.3 Gauge Invariance

The Standard Model is a gauge theory, with the requirement that the Standard Model Lagrangian[1] is invariant under a set of space-time dependant transformations. This is known as local gauge invariance (as opposed to global gauge invariance where the transformations have no space-time dependence). The transformations are described by the gauge symmetry group $SU(3)_C \times SU(2)_L \times U(1)_Y$. The $SU(3)_C$ group describes the strong interaction, mediated by the gluons. The $SU(2)_L \times U(1)_Y$ group describes the electromagnetic and weak interactions, which are combined into Electroweak Theory, and mediated by the photon and the massive Z, W^- and W^+ bosons. These bosons arise in the theory from the act of imposing local gauge invariance, whereby new additional gauge fields need to be added to the Lagrangian to compensate for the local gauge transformation [3].

2.1.4 Electroweak Theory

In electroweak theory the transformations from the $SU(2)_L \times U(1)_Y$ group require four gauge fields to be added to ensure gauge invariance. These are the B_μ field arising from the $U(1)_Y$ group and the W^1_μ, W^2_μ, W^3_μ arising from $SU(2)_L$ [4].

One feature of weak theory is that it does not conserve parity. This means that different interactions occur for left handed and right-handed chiral states of a fermion. As such these chiral states are treated separately in the Standard Model. A fermion can be represented by a Dirac field as the sum of left-handed part ψ_L and right-handed part, ψ_R,

$$\psi = \psi_L + \psi_R \tag{2.3}$$

where

$$\psi_L = P_L\psi \quad \text{with} \quad P_L = \frac{(1-\gamma_5)}{2}, \tag{2.4}$$

$$\psi_R = P_R\psi \quad \text{with} \quad P_R = \frac{(1+\gamma_5)}{2}. \tag{2.5}$$

P_L and P_R are projection operators that project the left-handed and right-handed chirality states of the fermion respectively. The γ_5 matrix is a 4×4 matrix constructed from the product of the Dirac matrices, $\gamma^5 \equiv i\gamma^0\gamma^1\gamma^2\gamma^3$. The projection operators are related via,

$$P_L P_L = P_L, \quad P_R P_R = P_R, \quad \text{and} \quad P_L P_R = P_R P_L = 0. \tag{2.6}$$

Chirality is not a physical observable, but in the limit of massless fermions, the chirality is equal to the helicity of the particle. With helicity being the sign of the component of spin of the fermion in the direction of motion. The weak interaction is seen to break parity conservation experimentally as the W^- only couples to left-handed chiral states. This means that only left-handed neutrinos have been observed in experiment. This leads to right-handed neutrinos not being included in the Standard Model. This is addressed

[1] The Lagrangian is defined as $L = T - V$ where T is the kinetic energy of the system and V is the potential energy. As the Standard Model deals with fields, which are functions of space-time, and hence continuous, the Lagrangian density, $\mathcal{L}$, is used. This is defined as $L = \int \mathcal{L} d^3x$.

in electroweak theory by grouping the fermions together into left-handed $SU(2)$ doublets and right-handed $SU(2)$ singlets. As shown for the first generation of fermions,

$$\ell_L = \begin{pmatrix} \nu_L \\ e_L \end{pmatrix}, \quad e_R, \quad q_L = \begin{pmatrix} u_L \\ d_L \end{pmatrix}, \quad u_R, \quad d_R. \tag{2.7}$$

To allow the states in the doublets and singlets to be differentiated, a new quantum number is constructed. This is called weak hypercharge and is defined as,

$$Y = 2Q - 2I_3, \tag{2.8}$$

where, Q is the electric charge of the fermion, and I_3 the third component of isospin. The values for the first generation of particles is given in table 2.2. It can be seen that members of the doublets have the same value of Y, which differs to the corresponding singlet.

	I_W	I_3	Q	Y
ν_e	$1/2$	$1/2$	0	-1
e_L^-	$1/2$	$-1/2$	-1	-1
e_R^-	0	0	-1	-2
u_L	$1/2$	$1/2$	$2/3$	$1/3$
d_L	$1/2$	$-1/2$	$-1/3$	$1/3$
u_R	0	0	$2/3$	$4/3$
d_R	0	0	$-1/3$	$-2/3$

Table 2.2: Quantum numbers related to weak hypercharge (Y) for the first generation of fermions. Weak isospin is given by I_W, the third component of isospin by I_3 and electric charge by Q.

The $SU(2)$ singlets are invariant under $SU(2)$ transformations,

$$\ell_R \to \ell'_R = \ell_R. \tag{2.9}$$

This means that they do no couple to the W_μ^1, W_μ^2, W_μ^3 gauge fields. The doublets however transform as,

$$\ell_L \to \ell'_L = e^{-i\omega^a \mathbf{T}^a} \ell_L, \tag{2.10}$$

where $\mathbf{T}^a$ are the generators of the $SU(2)$ group and ω^a are real parameters, with $a = 1, 2, 3$. The generators of the group can be expressed in terms of the Pauli matrices, $\frac{1}{2}\sigma^a$, where

$$\sigma^1 = \begin{pmatrix} 0 & 1 \\ 1 & 0 \end{pmatrix}, \quad \sigma^2 = \begin{pmatrix} 0 & -i \\ i & 0 \end{pmatrix}, \quad \sigma^3 = \begin{pmatrix} 1 & 0 \\ 0 & 1 \end{pmatrix}. \tag{2.11}$$

In the $U(1)_Y$ symmetry group, the generator of the group is the weak hypercharge, Y, of the particle. Under $U(1)_Y$ transformations both the singlet and doublets transform in the same way, as,

$$\psi \to \psi' = e^{-i\omega' Y(\psi)} \psi. \tag{2.12}$$

The Lagrangian density describing a massless free fermion field ψ, is given by

$$\mathcal{L} = \bar{\psi}(i\gamma^\mu \partial_\mu)\psi \tag{2.13}$$

To make $\mathcal{L}$ invariant under the local gauge transformations of $SU(2)_L \times U(1)_Y$ the B_μ, W_μ^1, W_μ^2 and W_μ^3 fields are introduced. This is done by replacing ∂_μ by the covariant derivative D_μ, which is defined in such a way that it transforms in the same way as ψ. This is given by,

$$D_\mu = \partial_\mu + i2gI_W(f)\mathbf{T}^a W_\mu^a + ig'Y(f)B_\mu \tag{2.14}$$

where $I_W(f)$ and $Y(f)$ are the isospin and hypercharge of the fermion, f, as given in table 2.2. The couplings of the fermions to the $SU(2)$ and $U(1)$ gauge fields is given by g and g' respectively. Substituting $\partial_\mu \to D_\mu$ and including all of the considered fermion fields gives the electroweak Lagrangian density,

$$\begin{aligned}\mathcal{L}_{ew} = &-\frac{1}{4}B_{\mu\nu}B^{\mu\nu} - \frac{1}{4}F_{\mu\nu}F^{\mu\nu} \\ &+ i\bar{\ell}_L^T\gamma^\mu D_\mu \ell_L + i\bar{e}_R^T\gamma^\mu D_\mu e_R + i\bar{q}_L^T\gamma^\mu D_\mu q_L + i\bar{u}_R^T\gamma^\mu D_\mu u_R + i\bar{d}_R^T\gamma^\mu D_\mu d_R.\end{aligned} \tag{2.15}$$

Here, the hypercharge field strength is given by $B_{\mu\nu} = \partial_\mu B_\nu - \partial_\nu B_\mu$ and the weak $SU(2)$ field strength is given by $F_{\mu\nu}^a = \partial_\mu W_\nu^a - \partial_\nu W_\mu^a - gf^{abc}W_\mu^b W_\nu^c$. The difference in the form of the two field strengths arises from the fact that the $U(1)_Y$ group is an abelian group meaning that the transformations commute. The $SU(2)$ gauge group is a non-abelian group, leading to the addition of the $gf^{abc}W_\mu^b W_\nu^c$ term. Physically this term accounts for the triplet and quartic couplings of the W^a bosons. Together these first two terms of equation 2.15 represent the kinematic terms of the gauge fields. The remainder of equation 2.15 describes the kinematics of the fermions in the theory. Substituting equation 2.14 into equation 2.15, together with the appropriate group generators allows the interaction terms between all of the fermions considered and the gauge bosons to be calculated.

The interaction between the leptons and gauge bosons is given by,

$$-\frac{g}{2}\begin{pmatrix}\bar{\nu}_L \\ \bar{e}_L\end{pmatrix}^T \gamma^\mu \left(\begin{pmatrix} W_\mu^3 & \sqrt{2}W_\mu^+ \\ \sqrt{2}W_\mu^- & -W_\mu^3\end{pmatrix} - \tan\theta_W B_\mu\right)\begin{pmatrix}\nu_L \\ e_L\end{pmatrix} - ig\tan\theta_W \bar{e}_R\gamma^\mu B_\mu e_R, \tag{2.16}$$

where the charged $\mathrm{W}^\pm$ bosons are given by

$$W_\mu^\pm = \frac{W_\mu^1 \mp iW_\mu^2}{\sqrt{2}}. \tag{2.17}$$

The fields B_μ and W_μ^3 cannot be interpreted as the remaining electroweak bosons as both are seen to couple to the neutrino which the photon does not. This problem is solved by making a linear combination between B_μ and W_μ^3. The massless photon is identified as,

$$A_\mu \equiv B_\mu \cos\theta_W + W_\mu^3 \sin\theta_W, \tag{2.18}$$

and the neutral Z boson is given by

$$Z_\mu \equiv B_\mu \cos\theta_W - W_\mu^3 \sin\theta_W, \tag{2.19}$$

where θ_W is the weak mixing angle that needs to be determined from experiment. This is related to the electroweak couplings by

$$\tan\theta_W = \frac{g'}{g}. \tag{2.20}$$

By applying the parity operators the interactions between the left and right-handed fermions and each of the bosons can be written explicitly. The interactions involving the photon and the Z are discussed below.

The coupling of the photon with the charged fermions is given by,

$$g\sin\theta_W \bar{e}\gamma^\mu e A_\mu - \frac{2}{3} g\sin\theta_W \bar{u}\gamma^\mu u A_\mu + \frac{2}{3} g\sin\theta_W \bar{d}\gamma^\mu d A_\mu. \tag{2.21}$$

Here the photon has the same coupling to left and right-handed fermions. It can be seen from equation 2.21 that the quantity $g\sin\theta_W$ appears in each term and that the photon couples to the fermions with couplings proportional to their electric charge. This allows the relation,

$$g\sin\theta_W = e, \tag{2.22}$$

to be made where e is the electromagnetic charge.

The coupling of the Z to the fermions, f, is given by,

$$-\frac{g}{2\cos\theta_W} \bar{f}_i \left(I_i^3 \gamma^\mu \left(1 - \gamma^5\right) - 2Q_i \sin^2\theta_W \gamma^\mu \right) f_i Z_\mu, \tag{2.23}$$

which, can be seen to have both a vector (γ^μ) term, and an axial-vector ($\gamma^\mu\gamma^5$) term. This can be made more explicit as,

$$-\frac{g}{2\cos\theta_W} \bar{f}_i \gamma^\mu \left(v_f - a_f \gamma^5 \right) f_i Z_\mu, \tag{2.24}$$

where v_f and a_f are the vector and axial-vector couplings respectively. These constants are defined by

$$v_f = I_f^3 - 2\sin^2\theta_W Q_f, \tag{2.25}$$

$$a_f = I_f^3, \tag{2.26}$$

and are determined by the Standard Model given θ_W. The Z boson can clearly be seen to couple to the quarks with a coupling strength proportional to the weak isospin and charge of the quarks, with different coupling strengths for the different chiral states.

2.1.4.1 Electroweak Symmetry Breaking

The Lagrangian density shown in equation 2.15 is for massless bosons. Simply introducing the mass such that $\mathcal{L} = \bar{\psi}(i\gamma^\mu\partial_\mu - m)\psi$ is not invariant under $SU(2)_L U(1)_Y$ local transformations for $m \neq 0$. This is because the mass term causes a mixing of the left and right-handed components of the fermions.

In order to give the weak bosons masses, spontaneous symmetry breaking is imposed via the Brout-Englert-Higgs mechanism [5–9]. This introduces an $SU(2)$ doublet of complex scalar fields, known as the Higgs field. This has a potential of

$$V(\Phi) = \mu^2\Phi^\dagger\Phi + \lambda(\Phi^\dagger\Phi)^2. \tag{2.27}$$

If $\mu^2 < 0$ then the field has a minimum at $\Phi^\dagger\Phi = -\frac{1}{2}\mu^2/\lambda$, giving it a non-zero expectation value. This ensures gauge invariance of the Lagrangian, but the vacuum state is not invariant under gauge transformations. The gauge bosons acquire mass via interactions with the Higgs field. The masses of the $W^\pm$ and Z are given by

$$M_W = \frac{1}{2}gv, \qquad M_Z = \frac{1}{2}\frac{gv}{\cos\theta_W}. \tag{2.28}$$

where $v = \mu/\sqrt{\lambda}$ is the vacuum expectation value. The mass of the Higgs particle that is a consequence of the Higgs field is given by

$$M_H = \sqrt{2}|\mu|. \tag{2.29}$$

This is a free parameter in the Standard Model that needs to be measured from experiment. The Higgs boson was first observed by the ATLAS [10] and CMS [11] collaborations at the LHC in 2012. Higgs boson decays to two photons have been observed, which constrains the spin of the Higgs boson to be either zero or two. The Standard Model predicts that the spin should be zero, and initial measurements [12, 13] are favourable to that being the case.

2.1.5 Quantum Chromodynamics

Quantum Chromodynamics is a non-abelian gauge theory that is invariant under local gauge transformations described by the $SU(3)_C$ group. This means that the quarks are described by a field ψ_i where $i = 1, 2, 3$ where i is associated with the quantum number of colour (red, blue and green). In order to compensate for the local gauge transformations eight additional fields must be included into the Lagrangian. These are associated with the eight gluons. These fields are included via the covariant derivative $\mathbf{D}_\mu$ as was done in Electroweak Theory. This leads to the Lagrangian density of QCD being written as,

$$\mathcal{L}_{QCD} = -\frac{1}{4}G^a_{\mu\nu}G^{\mu\nu}_a + \bar{q}_a\left(i\gamma^\mu\mathbf{D}_\mu\right)_{ab}q_b \tag{2.30}$$

with

$$\mathbf{D}_\mu = \partial_\mu + ig_s\mathbf{T}^a G^a_\mu \tag{2.31}$$

where, $\mathbf{T}^a$ are the generators of $SU(3)_C$ and $G^a_{\mu\nu}$ is the field strength tensor, given by,

$$G^a_{\mu\nu} = \partial_\mu G^a_\nu - \partial_\nu G^a_\mu - g_s f^{abc} G^b_\mu G^c_\nu. \tag{2.32}$$

The indices $a, b, c = 1...8$. The gauge coupling is taken to be the strong coupling g_s, which is discussed further in section 2.2.1. As was seen for the $SU(2)$ group in the electroweak theory, the term $g_s f^{abc} G^b_\mu G^c_\nu$ arises due to the non-abelian nature of $SU(n)$ the gauge groups. This term gives rise to the self interactions of the gluons, which makes strong interaction processes so complex.

2.1.6 Limitations of the Standard Model

While the Standard Model has been very successful, with all of the predicted particles having been discovered, the masses of those particles are free parameters in the model that have to determined by experiment. The Standard Model can't explain certain observed symmetries such as why there are three generations of both quarks and leptons or why the charge on the electron is the same as the charge on the proton. At a larger scale it cannot explain the source of the matter-antimatter asymmetry in the universe or predict a particle that explains dark matter [14].

2.2 Proton-Proton Collisions

At the LHC, protons accelerated in opposite directions are brought together to collide in the centre of the detectors. These protons, rather than the simple valance uud quark model often used are in fact very complicated systems containing gluons, photons, and $u,\ d,\ s,\ c,\ b$ sea quarks as well as the u_v and d_v valance quarks. The valance quarks describe some of the macroscopic properties of the proton, whereas the sea quarks reflect much richer structure and dynamics. Hadrons, such as the proton, are bound together by the strong force as described by Quantum Chromodynamics (QCD).

2.2.1 Running Couplings in QED and QCD

The fine structure constant, α, determines the strength of the interaction between charged particles and is defined as

$$\alpha = \frac{e^2}{4\pi} = \frac{1}{137}, \tag{2.33}$$

where e is the electron charge. However, it is seen by experiment to have a scale dependence, increasing with the energy scale, Q, leading to α being known as a running coupling. This dependence on Q arises due to the screening effects of QED quantum fluctuations where e^+e^- pairs emitted by a photon propagator act to decrease the measured value of α. At larger scales (smaller distances) this screening is overcome and the measured value for α increases. The momenta in the loops that cause the screening can have any value, and problems arise in the theory when this tends to infinity (known as ultra violet divergence). In order to avoid these divergences the perturbation series describing α requires

renormalisation. This introduces an additional arbitrary mass scale, μ, to the definition of α, which is the point at which the subtractions to remove the ultra violet divergences are performed. The renormalisation group equation [15],

$$\frac{1}{\alpha(\mu^2)} = \frac{1}{\alpha(Q^2)} + \beta_0 \ln\left(\frac{Q^2}{\mu^2}\right) + ... \tag{2.34}$$

here truncated to just the first two terms. This gives the general dependence of the coupling on Q^2 expanded in powers of $\ln(Q^2/\mu^2)$. The quantity β_0 depends on the number of degrees of freedom within the loops, and is given by $\beta_0 = \frac{1}{12\pi}(4n_f)$ where $n_f = 3$ is the number of fermion generations. This gives

$$\alpha(Q^2) = \frac{\alpha(\mu^2)}{1 - \frac{\alpha(\mu^2)}{\pi}\ln\left(\frac{Q^2}{\mu^2}\right)}. \tag{2.35}$$

The arbitrary renormalisation scale has to be chosen such that, $\mu^2 << Q^2$ and acts as a cut off to prevent α becoming divergent, with the value of $\alpha(\mu^2)$ being determined from experiment.

The strong coupling constant, α_s, is defined as

$$\alpha_s = \frac{g_s^2}{4\pi}, \tag{2.36}$$

where g_s is the QCD gauge coupling. This definition is analogous to that of the QED fine structure constant. Again, from experiment, it is seen that α_s is dependent on the energy scale, Q^2, but this time α_s is large at low Q^2 and small as high Q^2. Again this behaviour is caused by virtual loops, and the fermions produced inside them. Here however, due to the self interaction of the gluons, further gluons can also be produced. The produced quark pairs cause a screening of the coupling, as was seen for α, but the gluons have the opposite effect, causing an augmentation of the coupling strength at low Q^2. As was seen for the QED example, ultra violet divergences are caused by these loops and a renormalisation scale, μ has to be introduced. The renormalisation group equation is used to do this, but here in QCD, due to the self-interactions of the gluons an additional term in β_0 is included to account for these extra degrees of freedom. This gives $\beta_0 = \frac{1}{12\pi}(4n_f - 11n_c)$ where again n_f is the number of available fermions (which itself is scale dependent) and n_c is the number of colour charges. This gives an expression for $\alpha_s(Q^2)$ of,

$$\alpha_s(Q^2) = \frac{\alpha_s(\mu^2)}{1 - \frac{\alpha_s(\mu^2)}{12\pi}(2n_f - 33)\ln\left(\frac{Q^2}{\mu^2}\right)}, \tag{2.37}$$

which is commonly rearranged to give,

$$\alpha_s(Q^2) = \frac{12\pi}{(33 - 2n_f)\ln\left(\frac{Q^2}{\Lambda^2_{QCD}}\right)}, \tag{2.38}$$

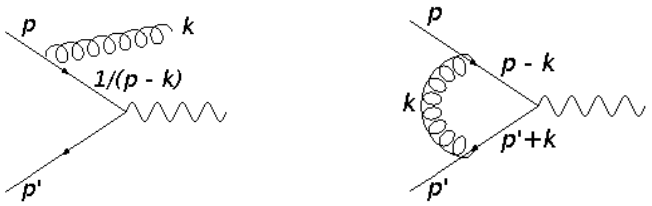

(a) Real (b) Virtual

Figure 2.1: Real and virtual gluon emission.

where Λ_{QCD} is the value of μ^2 for $\alpha_s(\mu^2) \to \infty$. This is interpreted as the scale that divides the perturbative and non-perturbative physics and is found from experiment to be ~ 0.3 GeV. It can be seen from equation 2.38 that the additional gluon term causes $\alpha_s(Q^2)$ to decrease with Q^2. This behaviour explains why at low Q^2 the quarks are fully bound together in a colour singlet state, yet when probed at high enough Q^2 it is possible to examine the structure of hadrons, such as the proton, taking advantage of this weakening of the coupling strength.

2.2.2 Cross Sections

The cross section of a process is a measure of the likelihood of it occurring and is expressed as an effective area, σ. For sufficiently large scales, $\alpha_s(Q^2)$ is small enough that the partonic cross section can be expressed as the perturbative expansion in α_s. This means each term is progressively smaller than the last, leading to a convergent power series. Each term in α_s introduces new sub-processes into the calculation. These corrections to the leading order cross section can take the form of real corrections, where partons are emitted, contributing to the final state (figure 2.1(a)), or virtual corrections which arise from quarks and gluons being produced in loops (figure 2.1(b)). Both of these scenarios can cause problems to the theoretical calculation of the cross section as they can produce divergences in the calculation. The ultra violet divergences from the virtual corrections are treated by the inclusion of the renormalisation factor μ_R as discussed in section 2.2.1. The real corrections from the emitted gluons introduce a $1/(p-k)^2$ propagator term to the calculation, where p is the four-momentum of the incoming quark, and k is the four momentum of the gluon. When the gluon is emitted collinearly to the quark, this term becomes divergent. To avoid this an additional scale is introduced, called the factorisation scale, μ_F. This is the scale at which the perturbative and non-perturbative physics is separated, allowing the soft gluon emission to be absorbed into the PDF rather than described by the perturbative expansion. A value of $\mu_F = Q$ is usually chosen. Once divergences have been avoided the real and virtual corrections should cancel at any given order of the perturbative expansion. If the cross section could be calculated to all orders, there would be no scale dependence on the cross section, however in practice this can be done with very few processes and the perturbative expansion is truncated. Many processes are now calculated to LO and NLO in α_s with an increasing number having the NNLO term calculated. The dependence on the calculated cross section on μ_R and μ_F is treated

as an uncertainty to the theoretical calculation. It is common to assess this uncertainty by varying each of the scales by a factor of two, and examining the change in the predicted cross section.

2.2.3 The Factorisation Theorem

As it is difficult to perform analytical calculations of proton-proton interactions from first principles the factorisation theorem [16] is used. This allows the non-perturbative parton distribution functions, $f_{a/A}$ and $f_{b/B}$, which are calculated from fits to data, to be separated from the partonic cross section, $\hat{\sigma}_{ab\to X}$. These can then be calculated perturbatively as a power series in $\alpha_s(Q^2)$. These components of a proton-proton collision are shown in figure 2.2. The hadronic cross section, σ_{AB}, for a process is expressed via the factorisation theorem as,

$$\sigma_{AB} = \sum_{a.b} C_{ab} \int \mathrm{d}x_a \mathrm{d}x_b \left[f_{a/A}\left(x_a, Q^2\right) f_{b/B}\left(x_b, Q^2\right) + (A \leftrightarrow B) \right] \hat{\sigma}_{ab\to X}, \tag{2.39}$$

where x_a is the fraction of the momentum of proton A carried by the colliding parton a, (similarly for x_b). The PDFs also depend on Q^2, the large momentum scale that

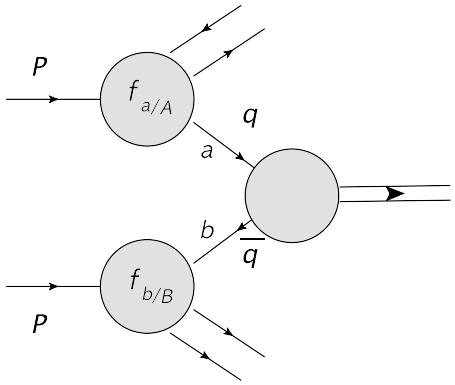

Figure 2.2: Schematic of a proton-proton collision. The labels are described in the text.

characterises the hard scatter. The equation sums over the initial and final colour states with the initial colour averaging factor, C_{ab}, given by

$$C_{q\bar{q}} = \frac{1}{9}, \qquad C_{qg} = \frac{1}{24}, \qquad C_{gg} = \frac{1}{64}, \tag{2.40}$$

where the denominator of C_{ab} is given by the square of the number of available colours (three for quarks and eight for gluons). Neglecting the masses of the particles, the invariant mass of the ab system, $\sqrt{\hat{s}}$, is related to the invariant mass of the AB system, $\sqrt{s}$, by

$$\hat{s} = (p_a + p_b)^2 = x_a x_b s = \tau s, \tag{2.41}$$

introducing the new variable $\tau = x_a x_b$. The factorisation theorem can be rewritten in terms of τ, giving

$$\sigma_{AB} = \sum_{a,b} C_{ab} \int_0^1 \mathrm{d}\tau \int_\tau^1 \frac{\mathrm{d}x_a}{x_a} \left[f_{a/A}\left(x_a, Q^2\right) f_{b/B}\left(\frac{\tau}{x_a}, Q^2\right) + (A \leftrightarrow B) \right] \hat{\sigma}_{ab\to X}, \tag{2.42}$$

which when considered differentially in terms of τ, gives,

$$\frac{\mathrm{d}\sigma_{AB}}{\mathrm{d}\tau} = \sum_{a,b} \frac{\mathrm{d}\mathcal{L}_{ab}}{\mathrm{d}\tau} \hat{\sigma}_{ab\to X}, \tag{2.43}$$

where

$$\frac{\mathrm{d}\mathcal{L}_{ab}}{\mathrm{d}\tau} = C_{ab} \int_\tau^1 \frac{\mathrm{d}x_a}{x_a} \left[f_{a/A}\left(x_a, Q^2\right) f_{b/B}\left(\frac{\tau}{x_a}, Q^2\right) + (A \leftrightarrow B) \right], \tag{2.44}$$

is called the parton luminosity [17] .

2.2.4 Parton Distribution Functions

The PDFs define the probability, $k(x)$, to find a parton of type k with a 4-momentum fraction between x and $x + dx$. The PDFs are determined from fits to data largely from deep inelastic scattering (DIS), Drell-Yan and jet production measurements. A number of different groups carry out these fits using different assumptions, parameterisations and choices of dataset for their fits. The MSTW [18] (previously MSRT) and CTEQ [19] groups carry out global fits using a large selection of datasets using many types of measurement. The NNPDF [20] group also include a wide range of datasets, but fit the PDFs using a multivariate technique not explained here. A final group worth mentioning is HERAPDF who produce PDF sets fitted exclusively to the H1 [21] and Zeus DIS data from HERA. The discussion given here attempts to discuss PDFs in a generalised sense rather than concentrating on the approach of any one collaboration.

The general approach to determining the PDFs, is to define a set of functions describing the PDFs at some initial scale, Q_0^2. In principle these can take any arbitrary form but need to have enough flexibility to allow them to be fitted to the data. The data, which is collected at various x and Q^2 is then used to fit the PDFs, which have been evolved up to the scale of the data using the DGLAP equations. The DGLAP (Dokshitzer-Gribov-Lipatov-Atarelli-Parisi) [22] [23] [24] [25] equations describe the evolution from one scale to another. They consist of a perturbative expansion of splitting functions. These splitting functions, which are calculated to NLO and NNLO, describe the probability of a parton producing a daughter parton with a given momentum fraction. It is through the DGLAP equations that the factorisation scale is introduced to the PDFs as they describe the PDFs integrated over the transverse momentum up to μ_F. The fits are carried out using a χ^2 minimisation technique that adjusts the values of the free parameters at the initial scale to give a good χ^2 at the scale of the data. While the Q^2 dependence of the PDFs is described by the DGLAP equations, the x dependence is determined from the data.

In general the QCD fits are obtained by parameterising the parton distribution functions at Q_0^2 using an analytical form. A common choice [26] is to parameterise the gluon

density as

$$xg(x), \tag{2.45}$$

the valence quark densities as,

$$xu_v(x) = x\left(u(x) - \bar{u}(x)\right), \tag{2.46}$$
$$xd_v(x) = x\left(d(x) - \bar{d}(x)\right), \tag{2.47}$$

and the light sea distributions as,

$$xS(x) = x\left[2\left(\bar{u}(x) + \bar{d}(x)\right) + s(x) + \bar{s}(x)\right], \tag{2.48}$$
$$x\Delta(x) \equiv x\left(\bar{d}(x) - \bar{u}(x)\right). \tag{2.49}$$

With most groups using a functional form similar to

$$xf_i(x, Q_0^2) = A_i x^{\alpha_i}(1-x)^{\beta_i} P_i(x), \tag{2.50}$$

where α_i and β_i are free parameters in the fit and $P_i(x)$ can be a polynomial function in x or $\sqrt{x}$. Additional constraints are also included such as the counting sum rules,

$$\int_0^1 \left[u(x) - \bar{u}(x)\right] dx = 2, \qquad \int_0^1 \left[d(x) - \bar{d}(x)\right] dx = 1, \qquad \int_0^1 \left[q(x) - \bar{q}(x)\right] dx = 0, \tag{2.51}$$

for $q = s, c, b$. These ensure the proton valence structure corresponds to uud and are used to set the value of the normalisation term A_i. Momentum conservation is also ensured by requiring,

$$\int_0^1 \sum_i^{n_f} x\left[q_i(x) + \bar{q}_i(x)\right] + xg(x)dx = 1, \tag{2.52}$$

where the sum runs over all active parton flavours, allows the value of A_g to be determined.

Once the densities are parameterised at Q_0^2, the DGLAP evolution equations, are used to obtain $xf(x, Q^2)$ at any Q^2. Figure 2.3 shows the parton densities for the gluons and valence and sea quarks at NLO as described by the MSTW PDF group at $Q^2 = 10$ GeV^2 and evolved to $Q^2 = 10^4$ GeV^2. It is evident that the gluon and sea quark densities vary quickly with Q^2, playing a larger role in the high Q^2 collisions at the LHC. As the change in the sea quark and gluon densities is so dramatic understanding the evolution from the energy regime in which the input measurements were made to the new energy regime of the LHC is important. DGLAP evolution to any Q^2 allows the theoretical cross sections of any process of interest to be computed.

The parameters α_i and β_i in equation 2.50 that describe the PDF at the initial scale are obtained by fitting the theoretical predictions to the experimental measurements. This

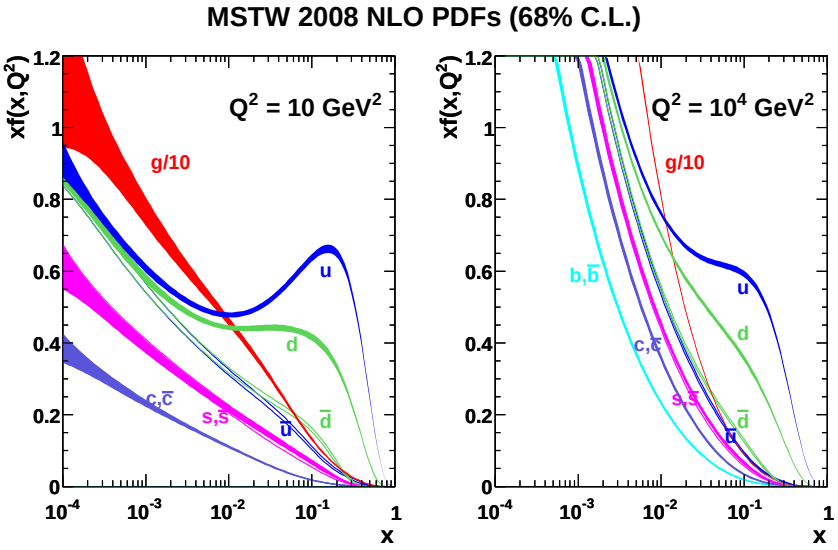

Figure 2.3: Parton densities obtained from NLO MSTW2008 $Q^2 = 10\ GeV^2$ on the left and $Q^2 = 10^4\ GeV^2$ on the right. [18]

is done by minimising a χ^2 function, often defined as,

$$\chi^2 = \sum_{\text{exp}} \chi^2_{\text{exp}}, \tag{2.53}$$

where, χ^2_{exp} is the individual contribution from each independent dataset [27–29], given by

$$\chi^2_{\text{exp}} = \sum_i \frac{\left(d_i - \sum_k \beta_{k,i} t_i s_k - t_i\right)^2}{\alpha_i^2} + \sum_k s_k^2, \tag{2.54}$$

where d_i and t_i are the measurement values and the corresponding theoretical predictions respectively. The total uncorrelated uncertainty for the measurement i, is given by α_i, which is the sum in quadrature of the statistical and uncorrelated systematic uncertainties. The sources of correlated uncertainty are labelled as k. When a source k is shifted by one standard deviation ($s_k = 1$), the amount of change in d_i is given by $\beta_{k,i}$. The values in $\beta_{k,i}$ are the experimental correlated systematic uncertainties published by the experiments. The second term in equation 2.54 introduces a penalty of s_k^2 when the data points are moved by $\beta_{i,k} s_k$, this restricts large deviations from $s_k = 0$. Although most of the PDF groups use a χ^2 minimisation technique with functions similar to equations 2.53 and 2.54, two approaches can be taken with respect to the treatment of s_k in the fit. The parameter s_k can either be a free parameter in the fit which is determined by the χ^2 minimisation. This means that the fit is not performed to the raw data but to the data once it has been shifted to its optimal settings for the systematic uncertainties as determined by the fit. The second choice is to fit the data with $s_k = 0$, ignoring the correlated systematic uncertainties. As discussed in section 2.2.4.1 these two approaches lead to different methods of determining the uncertainties associated with the fit.

Theoretical comparisons to LHC measurements, such as those described in [30], demon-

strate the over all good evolution of the PDFs. They provide an example of the universality of the PDFs allowing measurements from DIS data to be used when considering proton-proton collisions.

2.2.4.1 Error Sets

Until recently the uncertainty associated with a PDF prediction was estimated by comparing the predictions from the different PDF groups who, as mentioned previously, use different assumptions and datasets in their fits. However many of the same datasets enter into multiple groups' fits, meaning that the different PDFs obtained are not fully independent. More recently, effort has been made to estimate and make available the uncertainties associated with the different fits [31]. There are three main approaches to estimating the uncertainties associated with the fit, the *offset method*, the *Hessian method*, and the *Monte Carlo method*, these are discussed below. In all three methods a set of PDFs are produced, the central PDF, S_0, which is obtained from the χ^2 minimisation, along with a series of PDF error sets, S_i.

The Offset Method uses $s_k = 0$ for the central fit, S_0, meaning that the experimental correlated systematic errors are not considered, due to the fact they cannot be considered to be Gaussian distributed. To obtain an uncertainty for this central fit, s_k is set to ± 1 for each source of systematic uncertainty and the fit is repeated. The total uncertainty associated with the fit is obtained by adding in quadrature all the differences from the central fit. This method produces theoretical predictions that are as close as possible to the data. However, as it does not use the full statistical power of the fit it produces more conservative uncertainties than the other methods and can result in an over estimate of the uncertainty. Another disadvantage of this method is that the goodness of fit cannot be determined from the χ^2 calculated with only the statistical uncertainties. This means that to obtain a measure of the goodness of fit the χ^2 needs to be recalculated with the experimental statistical and systematic uncertainties added in quadrature [31].

The Hessian Method uses s_k as a free parameter in the fit meaning that the theoretical predictions are based on the data points once they have been shifted within their respective correlated uncertainty to the optimal position as determined by the fit. The uncertainties on the fitted PDF parameters are obtained from examining the parameters around the χ^2 minimum, $\chi^2_0 = \chi^2(S_0)$, which is obtained by considering the leading quadratic terms from the Taylor expansion of the χ^2 function. Uncertainties for the central PDF set are calculated using a Hessian matrix evaluated at the χ^2 minimum. The Hessian matrix is a matrix of second derivatives of the χ^2 function with dimensions equal to the number of free parameters in the fit. The eigenvectors of the Hessian matrix are used to produce an Eigenvector Basis set of PDFs $\{S^{\pm}_l; 1, ..., d\}$, where $S^{\pm}$ are defined by displacements of a standard magnitude up or down along each of the d eigenvector directions. The Hessian matrix can be diagonalised and rescaled using an iterative method [27–29] so that the eigenvectors are orthogonal to each other. Moving the parameters away from the minimum causes the χ^2 to increase by $\Delta\chi^2$. The neighbourhood around the minimum

in which the parameters are varied is defined via the tolerance parameter, T, such that $\Delta\chi^2 \leq T^2$ [27]. If the PDF fit was using consistent datasets with Gaussian uncertainties compared to a well defined theory then the error bands corresponding to $\Delta\chi^2 = 1$ or $\Delta\chi^2 = 2.71$ for the 68% (one standard deviation) and 90% (two standard deviations) confidence levels respectively would be used. The consistent H1 and Zeus datasets allow the HERAPDF group to do this. For the large global fits used by the CTEQ and MRST groups these criteria are not met and so the tolerance parameter is used. This allows inconsistencies between datasets to be reflected in the uncertainties of the fit. A value of T is determined for each eigenvector by considering candidate fits along the eigenvector direction in the neighbourhood of the minimum [29]. These are obtained individually for each of the experimental datasets. The final value of T for the 90% CL fit as a whole can be obtained from an averaging of the values obtained from each of the eigenvectors. This is the approach CTEQ. Another option is to use a dynamic tolerance, where the value of T is different for different eigenvectors, as is the case with MSTW fits [18]. The uncertainties of the PDF's are all linearly proportional to T, so the 68% confidence limit can be obtained by scaling the values of T appropriately. The diagonalisation of the matrix means that each of the eigenvectors are an admixture of the free PDF parameters meaning that each eigenvector does not correspond to a single uncertainty source. However, as the eigenvectors are orthogonal it allows the uncertainty, σ_F, from the PDFs on any physical quantity that has a PDF dependence, $F(S)$, to be easily calculated from [32]

$$\sigma_F^2 = \frac{1}{2}\sum_{l=1}^{d}\left(F(S_l^+) - F(S_l^-)\right)^2, \tag{2.55}$$

or if asymmetric uncertainties are required, the following can be used,

$$\sigma_{F,max}^{+} = \sqrt{\sum_{l=1}^{d}\left[\max\left(F(S_l^+) - F(S_0),\ F(S_l^-) - F(S_0),\ 0\right)\right]^2}, \tag{2.56}$$

$$\sigma_{F,max}^{-} = \sqrt{\sum_{l=1}^{d}\left[\max\left(F(S_0) - F(S_l^+),\ F(S_0) - F(S_l^-),\ 0\right)\right]^2}. \tag{2.57}$$

Large asymmetries in the PDF uncertainties are indicative of a problem with the fit.

The Monte Carlo Method is the third common method used for calculating PDF uncertainties and is used by the NNPDF group and the more recent HERAPDF sets. Here, for each of the n experimental measurements d Monte Carlo replicas are created such that any sufficiently large sample of them has the same mean, variance and covariance as the experimental measurement [33]. A PDF can then be fitted for each of the Monte Carlo replicas with the best fit being the average of the obtained fits and the uncertainty taken as the variance between the fits. This method has the advantage that it can be used with any parameterisation of the parton densities and becomes most useful for more complex parameterisations with a larger number of free parameters [26].

2.2.4.2 Uncertainty from the Strong Coupling

The PDFs are currently fitted at LO, NLO and NNLO in pQCD. But the value of $\alpha_s(M_Z^2)$ itself has an uncertainty that should be represented in PDF uncertainties. A value of α_s can be extracted from the PDF fits themselves by including α_s as a free parameter in the fit. However the most precise measurements of α_s entering the world average published by the Particle Data Group are from processes that are free of PDF uncertainties for example from τ and onia decays and the e^+e^- event shapes at the Z resonance. The shape of the gluon PDF varies considerably with different values of α_s so the most accurate one is desirable. Another issue with leaving the value of α_s completely free is that the value of α_s used in partonic cross sections matched to the PDF needs to be consistent with the version used in the PDFs.

There are two main approaches to including an uncertainty from α_s into the PDF uncertainties. The CTEQ, HERAPDF and NNPDF groups use the PDG value of $\alpha_s(M_z)$ as an input in their fits, whereas the MSTW group obtain a value from the fit, but without allowing $\alpha_s(M_z)$ to be a free parameter. The two approaches are discussed below concentrating on the CTEQ and MSTW groups.

CTEQ includes the PDG α_s value into the fit much like any of the other experimental measurement, allowing it to vary within the 90% CL PDG uncertainty. They then diagonalise the parameter space [34, 35]such that changes in α_s only effect one eigenvector. The uncertainty calculated from this eigenvector can be added in quadrature with the others. This approach has the advantage that the uncertainties are directly related to those determined by the world average.

The MSTW group use 20 different values for $\alpha_s(M_Z^2)$, and carries out a PDF fit using each of them on all of the datasets that go into their global fit. For each fit, the difference in χ^2 obtained and the χ^2 from the global fit is taken. For each dataset these 20 χ^2 differences are plotted as a function of α_s. A quadratic curve can then be fitted to these points, for each of these curves the 68% and 90% CL are taken. The curves for each of the datasets are combined such that all of them are described by their 68% and 90% confidence level limits. Figure 2.4 shows the combined quadratic function for an NNLO fit (an NLO fit is also done). A best fit value of $\alpha_s(M_Z^2)$ ($\alpha_s^0(M_Z^2)$) is obtained from the minima of the fit, the 68% and 90% confidence limits are also shown.

The full global fit is done (with the $2d$ error sets) using α_s^0 and the value of α_s at the 68% and 90% limits (as well as at half of these limits). To obtain the uncertainty on a physical quantity, F, that depends on the PDFs, the asymmetric PDF uncertainties are calculated. This is done using equations 2.56 (giving $(\Delta F_{PDF}^{\alpha_s})_+$) and 2.57 (giving $(\Delta F_{PDF}^{\alpha_s})_-$) for each of the PDFs produced with the different fixed values of α_s. For α_s^0 the quantity $F^{\alpha_s^0}(S_0)$ is obtained. If the 68% CL on F is required, only the PDFs fitted using α_s^0, and the α_S values at the 68% limits (and at half of them) need to be used. Similarly if the 90% CL on F is required. To get the total uncertainty on the PDF from both the usual error sources and from α_s, the spread of predictions for each α_s value, including the PDF uncertainties is considered. Asymmetric uncertainties are then

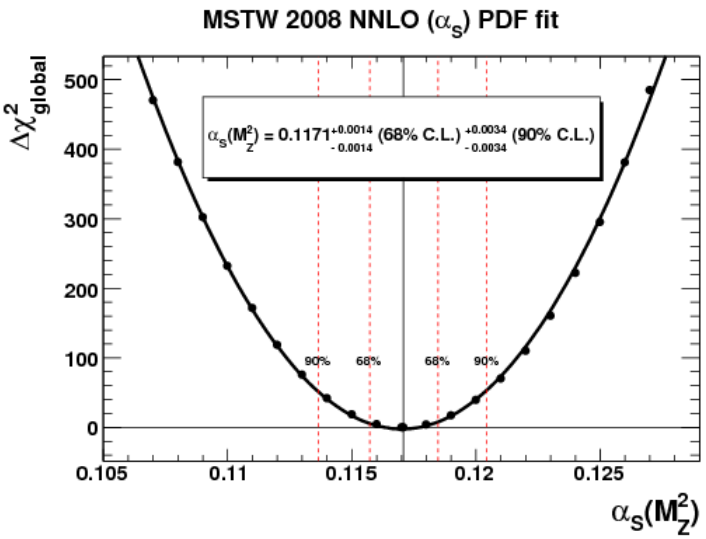

Figure 2.4: Best fit value of α_s obtained for an NNLO fit. The 68% and 90% confidence limits are also indicated [36].

calculated as,

$$(\Delta F_{PDF+\alpha_s})_+ = \max_{\alpha_s}\left(\{F^{\alpha_s}(S_0) + \left(\Delta F^{\alpha_s}_{PDF}\right)_+\}\right) - F^{\alpha_s^0}(S_0), \tag{2.58}$$

$$(\Delta F_{PDF+\alpha_s})_- = F^{\alpha_s^0}(S_0) - \min_{\alpha_s}(\{F^{\alpha_s}(S_0) - \left(\Delta F^{\alpha_s}_{PDF}\right)_-\}), \tag{2.59}$$

where the minimum and maximum are determined from the five values of α_s considered.

The values of α_s at the mid-points of the uncertainty band need to be considered. The PDF uncertainty decreases as α_s gets further from its best fit value, while correlations between PDFs and α_s can enhance α_s dependence and anti-correlations decrease it. This means that the extrema could occur for any value of α_s in the CL band. Ideally α_s would be varied continuously to calculate these uncertainties, but only the two values either side of $F^{\alpha_s^0}(S_0)$ are used for ease of use. In practice, for the majority of processes considered by the MSTW authors the extrema are found at the limits of the range considered. Reference [36] shows that while the addition of the α_s uncertainty doesn't have a large effect on the uncertainty bands for the quark distributions, the effect on the gluon distribution is much more marked.

2.2.4.3 Photon Parton Distribution

As well as the quark and gluon components of the proton there is also a component from photons, which are produced from QED radiation from the quarks. Currently only two PDF sets are available which include the photon PDF, $\gamma(x, Q^2)$, in the PDF fits. Both the MRST2004qed [36] and the recently released NNPDF2.3 QED [37, 38] PDF sets are NLO $\mathcal{O}(\alpha_s^2)$ in pQCD with LO $\mathcal{O}(\alpha)$ QED corrections made to the DGLAP evolution equations [39]. This choice is motivated by the expectation that the LO QED and NLO QCD corrections should be of similar size due to $\alpha_s^2(M_z^2)$ and $\alpha(M_Z^2)$ being of similar magnitude. Figure 2.5 shows the parton densities for the different constituents evaluated at $Q^2 = 20$ GeV from the MRST2004qed PDF set. Here the quark and gluon distributions

are very similar to those obtained from previous MRST analyses. It is clear that while the photon density is small at this scale, it is larger than the b quark distribution, due to the scale being only slightly higher than $Q^2 = m_b^2$ where the b quark contribution turns on from zero. It can also be seen to be larger than the sea quark distribution at large x. This is due to the fact that the photons are emitted from the high x valance quarks directly, whereas the sea quarks have to be produced via gluon emission. A recent measurement of the high mass ($116 < M_{ee} < 1500$ GeV) Drell-Yan differential cross section from ATLAS [40] has demonstrated that the corrections from the photon PDF can have a sizeable effect on the size of the predicted cross sections.

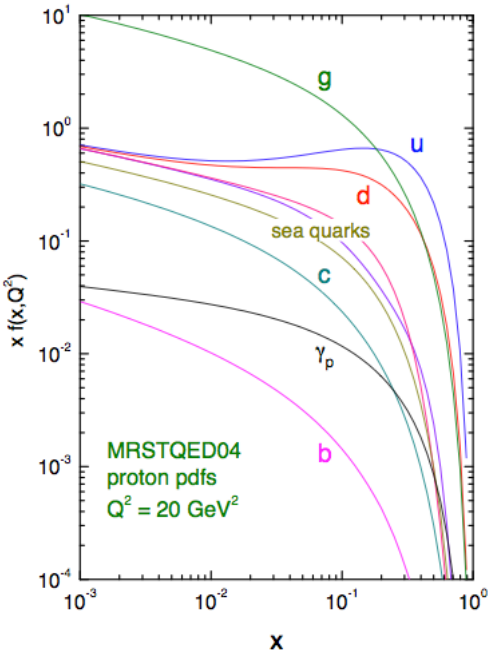

Figure 2.5: Proton PDF from the MRST2004QED set at $Q^2 = 20$ GeV obtained from the NLO pQCD + LO QED global fit [36].

2.3 The Drell-Yan Process

A quark and antiquark in the colliding protons annihilating to produce a lepton pair is referred to as the Drell-Yan process. It was first described in 1970 [41] by Sidney Drell and Tung-Mow Yan as a way of explaining the appearance of lepton pairs in hadronic collisions in the context of Feynman's parton model [42]. Figure 2.6 illustrates the leading order process as a Feynman diagram. The phase space available at the LHC to the ATLAS, CMS and LHCb experiments at $\sqrt{s} = 7$ TeV is shown in figure 2.7 in comparison to the phase space available to the experiments at HERA. The phase space is expressed in terms of the parton variables x and Q^2, with the relation to final state variables of mass, M, and rapidity, y, indicated. More formally, they are related via,

$$x_{a,b} = \frac{\sqrt{Q^2}}{\sqrt{s}} e^{\pm y}, \tag{2.60}$$

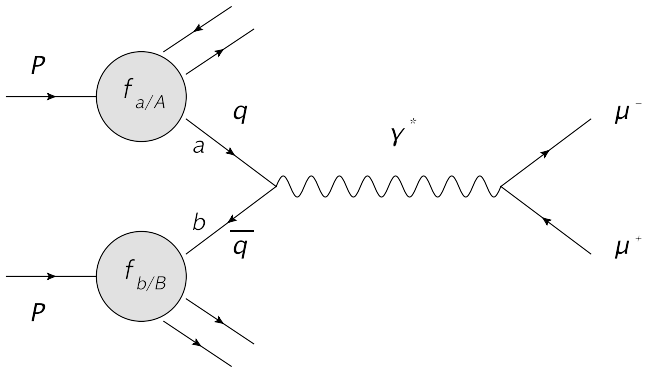

Figure 2.6: The Drell-Yan process.

with $M = Q$. The rapidity y is defined as,

$$y = \frac{1}{2} \ln \frac{E + p_z}{E - p_z} = \frac{1}{2} \ln \frac{x_a}{x_b}, \tag{2.61}$$

where E is the energy of the particle and p_z its momentum in the longitudinal direction, z, (as defined in chapter 3 for ATLAS). The region of phase space studied in the measurement

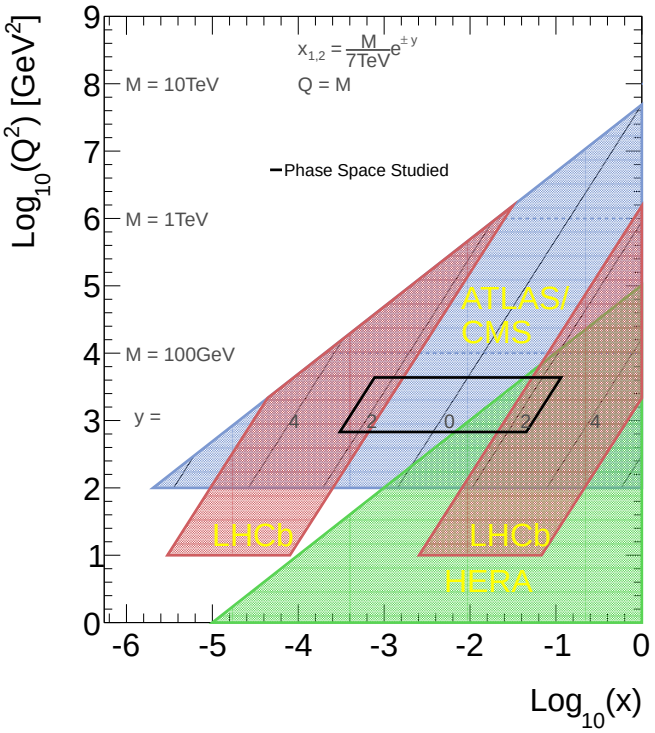

Figure 2.7: Phase space available at the LHC in comparison to HERA. The region of phase space studied in the measurement presented in this thesis is indicated.

presented in this thesis is indicated on the diagram. The phase space is constrained within the $26 < \sqrt{Q^2} < 66$ GeV mass range considered. The constraint on the rapidity of the virtual photon is due to the physical acceptance of the ATLAS inner detector. The overlap of the ATLAS phase space with LHCb at larger rapidities. This allows complimentary measurements to be made in different x regions.

2.3.1 Leading Order Cross Section

At leading order in α_s ($\mathcal{O}(\alpha_s^0)$) the Drell-Yan electromagnetic partonic cross section is given by [43],

$$\hat{\sigma}\left(q\bar{q} \to l^+l^-\right) = \frac{4\pi\alpha^2}{3\hat{s}}\frac{1}{N_c}Q_q^2, \tag{2.62}$$

where $\hat{s} = M_{ll}^2$, the invariant mass of the lepton pair produced in the process which can be physically measured. The quark electric charge is given by Q_q and listed in table 2.1. The fine structure constant, α, is also seen. A colour factor of $\frac{1}{N_c}$ which has a value of $\frac{1}{3}$ as the quark and antiquark need to be of the same colour type, is included to allow annihilation into a colour singlet final state. As the lepton pairs are produced with a range of invariant masses, the differential cross section as a function of invariant mass is an interesting quantity to study, this is given by,

$$\frac{\mathrm{d}\hat{\sigma}}{\mathrm{d}M^2} = \frac{\hat{\sigma}_0}{N_c}Q_q^2\delta(\hat{s} - M_{ll}^2), \qquad \hat{\sigma}_0 = \frac{4\pi\alpha^2}{3M_{ll}^2}, \tag{2.63}$$

where the delta function ensures that $\hat{s} = M_{ll}^2$. To get the total hadronic cross section the factorisation theorem, defined in equation 2.39, is used to obtain

$$\frac{\mathrm{d}\sigma}{\mathrm{d}M_{ll}^2} = \int_0^1 \sum_q \left[f_{q/A}(x_1, M_{ll}^2)f_{\bar{q}/B}(x_2, M_{ll}^2) + (q \leftrightarrow \bar{q})\right] \times \frac{\mathrm{d}\hat{\sigma}}{\mathrm{d}M_{ll}^2}(q\bar{q} \to l^+l^-) \tag{2.64}$$

$$= \frac{\hat{\sigma}_0}{N_c}C_{q\bar{q}}\int_0^1 \mathrm{d}x_1\mathrm{d}x_2\delta(\hat{s} - M_{ll}^2) \times \sum_q Q_q^2\left[f_{q/A}(x_1, M_{ll}^2)f_{\bar{q}/B}(x_2, M_{ll}^2) + (q \leftrightarrow \bar{q})\right] \tag{2.65}$$

$$= \frac{2\hat{\sigma}_0}{N_c}\sum_q Q_q^2\tau\frac{\mathrm{d}\mathcal{L}(\tau)}{\mathrm{d}\tau}, \tag{2.66}$$

where $\frac{\mathrm{d}\mathcal{L}(\tau)}{\mathrm{d}\tau}$ is the parton luminosity, as defined in equation 2.44.

To include the production of the Z boson, Q_q is modified to include terms for the weak interaction,

$$Q_q^2 \to Q_q^2 + 2Q_q v_l v_q \chi_1(\hat{s}) + (a_l^2 + v_l^2)(a_q^2 + v_q^2)\chi_2(\hat{s}), \tag{2.67}$$

which introduces two additional terms [44], one to include the weak contribution (third term) and one taking into account interference between the electromagnetic and weak components (second term). The weak axial and vector couplings a_f and v_f, introduced in section 2.1.4 now enter into the equation. These are related via $v_f = a_f - 2Q_f\sin^2\theta_W$, where $a_f = +\frac{1}{2}$ for $\nu, u, ...$ and $a_f = -\frac{1}{2}$ for $\mu, d, ...$ and θ_W is the weak mixing angle. The $\hat{s}$ dependent χ variables are defined as,

$$\chi_1(\hat{s}) = \kappa\frac{\hat{s}(\hat{s} - M_Z^2)}{(\hat{s} - M_Z^2)^2 + \Gamma_Z^2 M_Z^2}, \tag{2.68}$$

$$\chi_2(\hat{s}) = \kappa^2\frac{\hat{s}^2}{(\hat{s} - M_Z^2)^2 + \Gamma_Z^2 M_Z^2}, \tag{2.69}$$

where M_Z and Γ_Z are the mass and width of the Z boson respectively, both of which are

determined from experiment. The constant term κ is given by,

$$\kappa = \frac{\sqrt{2} G_F M_Z^2}{4\pi\alpha}, \tag{2.70}$$

where G_F is the Fermi constant. For partonic centre of mass energies, $\sqrt{\hat{s}}$, well below the Z resonance, the ratio $\hat{s}/M_Z$ is small, leading to $1 \gg |\chi_1| \gg \chi_2$, such that the weak effects are small enough to be neglected leaving equation 2.62 as a suitable approximation. For the case of $\sqrt{\hat{s}} = M_Z$ the χ_2 term dominates. Figure 2.8 shows graphically the contributions from the three components to the total Drell-Yan differential mass cross section when calculated at NNLO which demonstrates the same behaviour as at LO.

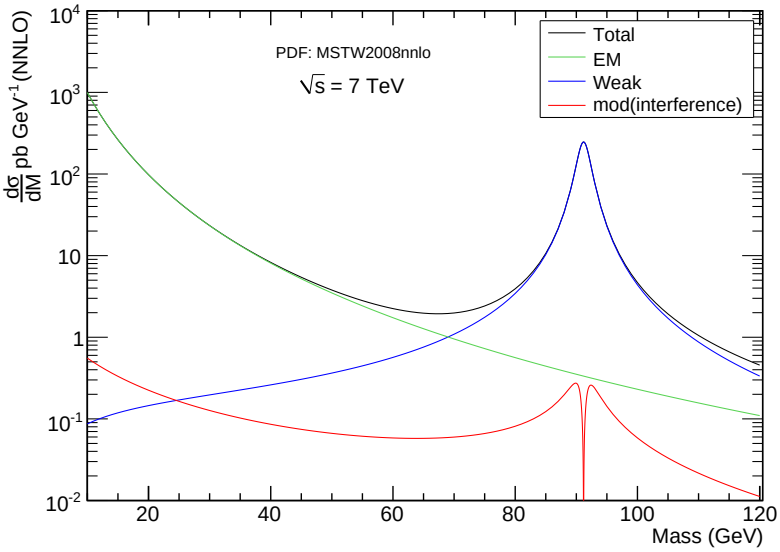

Figure 2.8: The contributions to the total Drell-Yan differential mass cross section calculated at NNLO using `VRAP` *[45]*

2.3.2 Higher Order Corrections

Higher order terms in the perturbative expansion come from additional Feynman diagrams with additional α_s vertices. These additional terms are represented by a range of Feynman diagrams and constitute either real or virtual corrections. Real terms come from external gluon lines, whereas virtual corrections come from internal gluon loops. The corrections at NLO ($\mathcal{O}(\alpha_s)$) for the Drell-Yan process are shown in figure 2.9, where figures 2.9(a) and 2.9(b) show the virtual corrections and figure 2.9(c) shows the real corrections. Figure 2.9(d) shows a gluon induced process where a gluon in the proton produces one of the initial state quarks. NNLO ($\mathcal{O}(\alpha_s^2)$) corrections include diagrams with loops that produce quark-antiquark pairs, but are too numerous to list here.

Theoretical calculations of the Drell-Yan process can be performed at NLO accuracy matched to leading-long (LL) or next-to-leading log (NNL) calculations to account for soft collinear partonic emission in the initial state [46–48]. Calculations at NNLO precision can also be performed reliably [49–51].

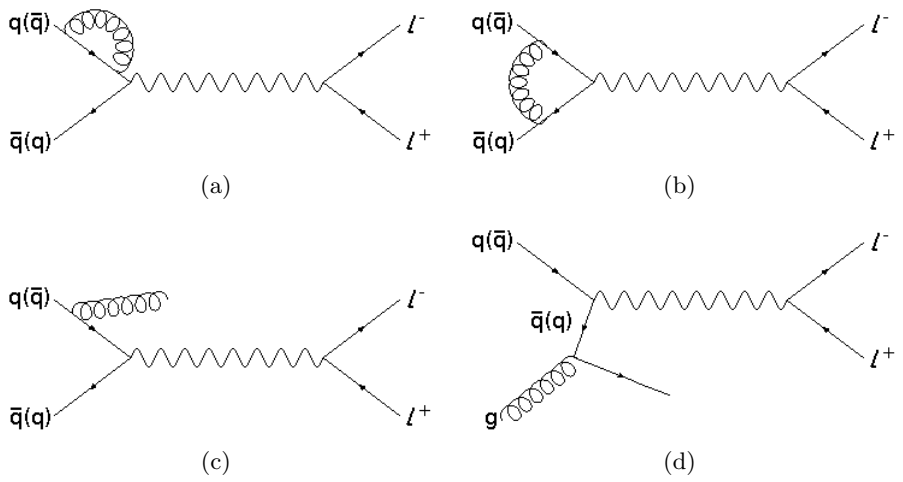

Figure 2.9: Drell-Yan NLO diagrams.

2.3.3 Backgrounds to the Low Mass Drell-Yan Process

As can be seen from figures 2.9 the NLO diagrams lead to a final state of $pp \to \mu^-\mu^+ + X$ where X is any particles produced from the QCD initial state radiation. The main background to this process are other processes that produce two or more oppositely charged muons. These backgrounds are discussed in chapter 4.

2.3.4 Potential to Constrain the PDFs with a Low Mass Drell-Yan Measurement

Figure 2.10 shows the quark-antiquark parton luminosity as a function of $\sqrt{\hat{s}/s}$ ($\sqrt{\tau}$) for a number of NLO PDF sets as a ratio to the MSTW2008NLO PDF set. The invariant

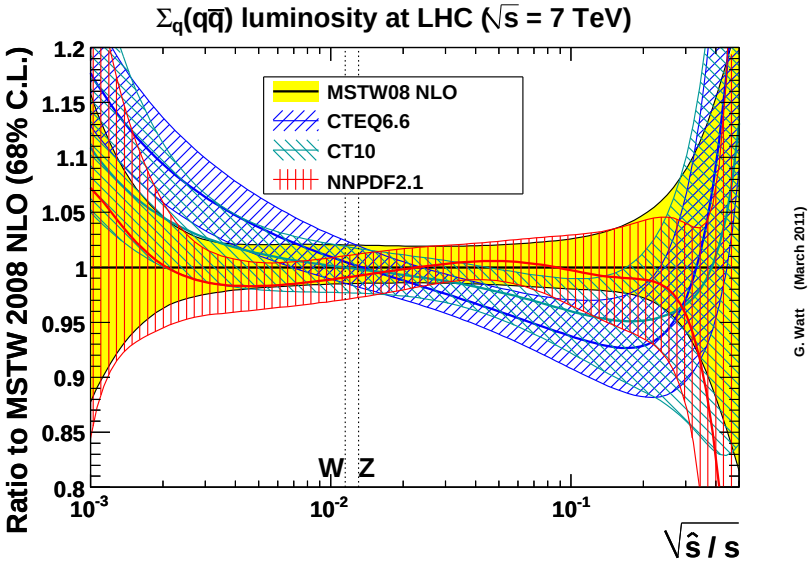

Figure 2.10: Parton luminosities for various PDF sets as a ratio to MSTW2008nlo [52].

masses of the W and Z bosons are given on the $\sqrt{\hat{s}/s}$ axis for reference. It can be seen that in the region of these boson resonances the different PDF groups are in relative good

agreement with small uncertainties, but the agreement decreases rapidity at lower and higher values of $\sqrt{\hat{s}/s}$. Further measurements in these regions will help to constrain the PDFs. It is the region below the Z resonance that the Drell-Yan measurement made in this thesis studies. As discussed in chapter 4 the measurement is made in the invariant mass region of $26 < M_{\mu\mu} < 66$ GeV which corresponds to $7.2 \times 10^{-3} \lesssim \sqrt{\hat{s}/s} \lesssim 1.1 \times 10^{-2}$, where it is evident from figure 2.10 improvements can be made.

Drell-Yan production in proton-proton collisions at the LHC is predominantly from $u\bar{u} \to \gamma^*/Z \to l^+l^-$ and $d\bar{d} \to \gamma^*/Z \to l^+l^-$ processes, but there is an invariant mass dependence to which of these two processes is dominant. As was seen in section 2.3.1 at low invariant masses the electromagnetic terms in the cross section dominate, however at the Z resonance the weak term is dominant. Examining these two regimes separately using the factorisation theorem, it is possible to make the approximation that

$$\sigma_Z \approx (a_u^2 + v_u^2) \times u(x_1)\bar{u}(x_2) + (a_d^2 + v_d^2) \times d(x_1)\bar{d}(x_2) + [1 \leftrightarrow 2], \tag{2.71}$$

$$\sigma_{\gamma^*} \approx \frac{4}{9} \times u(x_1)\bar{u}(x_2) + \frac{1}{9} \times d(x_1)\bar{d}(x_2) + [1 \leftrightarrow 2], \tag{2.72}$$

where $(a_u^2 + v_u^2) \simeq 0.29$ and $(a_d^2 + v_d^2) \simeq 0.37$. As such, a low mass Drell-Yan measurement is more sensitive to the $u\bar{u}$ processes and is complementary to measurements made at the Z resonance where the $d\bar{d}$ process is more dominantly probed. Measuring both provides a QCD fit more information to disentangle the u and d contributions.

Figure 2.7 shows the phase space of the measurement. This allows x to be between $x \sim 5 \times 10^{-4}$ and $x \sim 1.1 \times 10^{-1}$ at a value of Q^2 almost an order of magnitude larger than was available at HERA for the same x.

In the lower x region of this measurement the valance quark distributions are less well constrained by HERA data. This is particularly true for the d_v distribution, the main constraint for which comes from low statistics neutral current DIS measurements at high x. In this same lower x region the HERA data strongly constrains the $\bar{u}$ and $\bar{d}$ densities [26]. As such, although a low mass Drell-Yan measurement will have the largest impact on PDFs when included together with Z resonance measurements. When included on its own, it may help to constrain the valance quark densities at lower x.

The cross section measured in this thesis is combined with an electron channel measurement and included in a preliminary QCD fit with HERA-I data. This is discussed in chapter 9 where the impact on both the u_v and d_v PDFs is shown in relation to a fit on the HERA-I data alone.

Chapter 3

The Large Hadron Collider and the ATLAS Experiment

The Large Hadron Collider [53] (LHC) is a superconducting particle accelerator situated at the European Organisation for Nuclear Research (CERN) on the French-Swiss border near Geneva. The LHC is designed for proton-proton, lead ion-ion, and proton-lead ion collisions. It is currently the highest energy particle accelerator ever constructed, designed to have a centre of mass energy of 14 TeV. It was built to find the Higgs Boson and allow searches for new physics and studies of QCD. There are four interaction points around the LHC ring at which four detectors are positioned. Two of these, ATLAS [54] and CMS [55], are general purpose detectors designed to measure a large selection of physics. They are similar in design, although use different detector technologies. The ALICE [56] and LHCb [57] experiments are positioned at the remaining two interaction points, these have more specialised designs. The LHCb experiment is a single-arm forward spectrometer designed to study hadrons containing b and c quarks. The ALICE experiment is designed to study the particles produced in the heavy ion collisions, the large particle fluxes produced in these collisions leads to different design decisions compared those to study proton-proton collisions.

This chapter briefly describes the LHC and the CERN accelerator complex, before a description of the ATLAS detector is given, concentrating on the sub-detectors most important for the measurement of muons.

3.1 The Large Hadron Collider

The LHC is housed within the 26.7 km underground tunnel constructed for the LEP machine in the 1980s. The tunnel is inclined by 1.4% towards Lac Léman, varying in depth between 45 m and 170 m below the surface. As the majority of the collision schedule was proton-proton collisions and these were used to produce the physics explored in this thesis the description of the LHC in this section concentrates on proton-proton running.

In order to reach the high energies in the LHC the protons need to go though a series of smaller accelerators, mostly made up of previous CERN colliders. Each one increases the energy of the proton beams or collects the protons together into bunches, these are

shown in figure 3.1. Protons destined for the LHC are produced by ionising hydrogen, they are then accelerated up to 50 MeV with the Linac 2 linear accelerator, before being injected into the Proton Synchrotron Booster (PSB) where they are further accelerated up to 1.4 GeV. The protons are then injected into the Proton Synchrotron (PS) where a bunch structure with 2 ns spacing is applied to the beam. The PS also further accelerates the protons to 26 GeV. Next they are injected into the Super Proton Synchrotron (SPS) which accelerates them up to 450 GeV before finally injecting them into the LHC to create beams travelling in opposite directions around the ring. In the LHC the final acceleration up to collision energy is achieved before the beams are brought to collide in the experimental halls positioned at four points around the LHC circumference where the ATLAS, ALICE, CMS and LHCb experiments are housed.

Due to construction imperfections in the LHC magnets, the first phase of LHC running in 2010-2012 has been at a centre of mass energy of 7-8 TeV, rather than the design centre of mass energy of 14 TeV. A planned downtime during 2013 will see the upgrades needed to the machine to reach design collision energy.

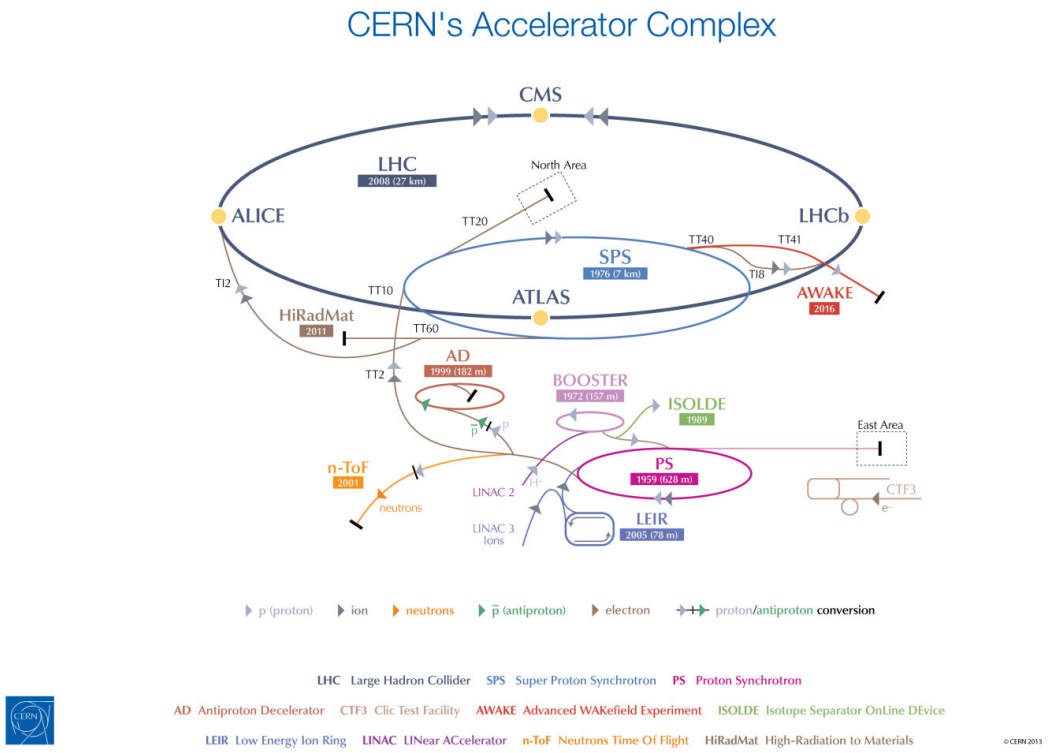

Figure 3.1: The CERN accelerator complex [58]

Instantaneous luminosity, $\mathcal{L}$, is a measure of the intensity of particle colliders. The rate at which a process occurs is given by $R = \mathcal{L}\sigma$, where σ is the cross section for the process. It is therefore beneficial to have high intensity beams to get a higher rate of production. The LHC was designed to achieve a instantaneous luminosity of 10^{34} cm^{-2}s^{-1} when running at 14 TeV centre of mass energy using a 25 ns bunch spacing [53]. To date the LHC has achieved a maximum instantaneous luminosity of about 3.65×10^{33} cm^{-2}s^{-1} in 2011 increasing to about 7.73×10^{33} cm^{-2}s^{-1} in 2012 with 50 ns bunch spacing [59].

Luminosity is increased by increasing the number of bunches, increasing the density of protons in the bunch or by increasing the beam focusing. The total luminosity is the time integral of the instantaneous luminosity and is used as a measure of the number of events produced or collected. When comparing Monte Carlo to data, the total luminosity of the sample is normalised to that of the data to give an appropriate comparison, as discussed in section 4.3.1.2.

3.2 The ATLAS Experiment

ATLAS (A Toroidal Lhc ApparatuS) is one of the two multi-purpose detectors at the LHC. It has a wide physics programme and as such has been designed to observe many physics processes. Particle physics detectors such as ATLAS are built to identify the particles that pass through them by exploiting differences in how they interact with matter. As described in section 2.1 there are twelve fermions (plus the anti-fermions) and six bosons in the Standard Model, but of these only the photon, the electron and the muon will be seen directly by ATLAS. Due to confinement, individual quarks cannot exist, but of the hadrons they form, only pions, kaons, protons and neutrons produced at the interaction point (IP) are long lived enough to reach the detector where they can be directly detected. The hadrons are produced in a cone in the detector called a jet. The direction and energy of the jet can be interpreted as that of the originating quark or gluon. A number of jet reconstruction algorithms are available to collect the detected particles into the jet. ATLAS utilises a range of different sub-detectors and technologies in order to measure this relatively small number of particles available to it as well as possible. Particles that are not detected by ATLAS directly can be inferred by looking at the topology of the event and the kinematics and species of particles that were detected.

Particles that pass through the detector without being detected such as neutrinos, are inferred by the missing energy in an event, taking advantage of the momentum imbalance between the initial and final states. An ideal particle physics detector would completely surround the IP so that the full energy and momentum of the event can be measured allowing a more accurate measurement of the missing energy. In practice this is not possible as the beam pipes supplying the colliding protons to the interaction point at the centre of the experiment require gaps in the detector. The detector itself also requires that there be gaps in the active material to allow space for support structures, magnets, cooling, and cabling.

ATLAS is a cylindrical detector encasing the LHC beamline, and centred on the interaction point. It consists of a barrel, with two end-caps either side of it. The inner detector sits at the centre of ATLAS and consists of the a pixel detector, a silicon strip detector and straw tracking detector. The inner detector is encased within the solenoid magnet, upstream of which lie the electromagnetic and hadronic calorimeters. Finally, the muon spectrometer surrounds the calorimeters, this consists of a toroidal magnet system and tracking chambers for the detection of muons.

Not all particles will interact with each section of the detector as illustrated for ATLAS in figure 3.2. Due to their charge electrons leave a track in the tracking detector as well

as a deposit in the electromagnetic calorimeter (ECal). Photons which also get absorbed in the ECal, producing electromagnetic showers similar to an electron can be identified by the fact that they are neutral and leave no tracks in the tracking detector. Charged hadrons such as protons will leave tracks in the tracking detector and in the ECal, but will not be fully absorbed until showering in the hadronic calorimeter (HCal). Neutral hadrons however will not be seen in the detector at all until they shower in the HCal. Using these differences in how the particles interact with the detector, the species of the particle can be determined. figure 3.3 shows the ATLAS detector with the different sub-

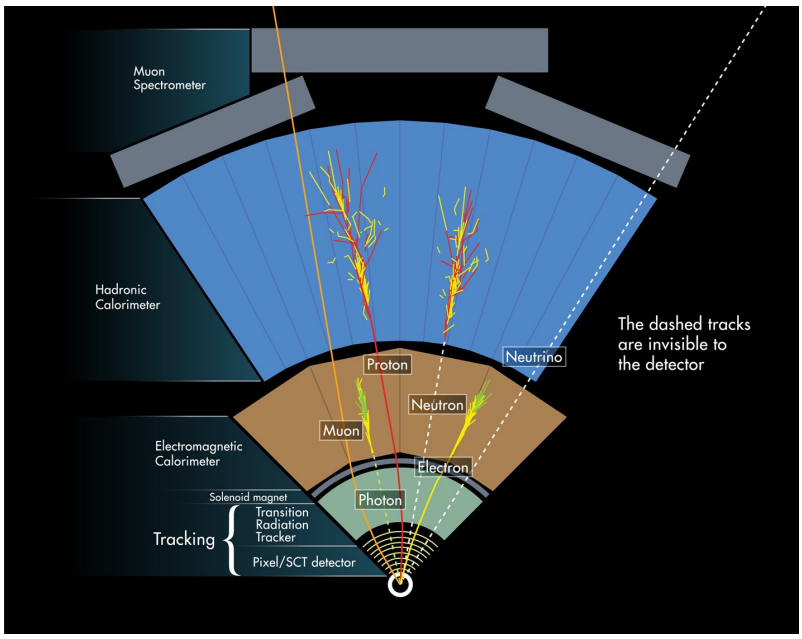

Figure 3.2: Detection of particles in ATLAS [60].

detectors labelled. A more detailed description is given in the following sections, where the reasoning behind the choice of technology for each sub-detector is described.

3.2.1 Nomenclature

ATLAS uses a right-handed coordinate system. The z axis is defined by the beam pipe with positive z being in the clockwise direction around the LHC ring. The z axis is intersected at zero by the perpendicular $x-y$ plane, which has positive x pointing towards the centre of the LHC ring and positive y pointing upwards. Due to the tilt of the LHC, the ATLAS coordinate system, also has a tilt, as can be seen in figure 3.4. The azimuthal angle, ϕ, is measured around the beam pipe, where $\phi = 0$ corresponds to the x-axis. The value of ϕ increases clockwise looking into the positive z direction, it is measured in the range $[-\pi, +\pi]$. The polar angle, θ, is the angle from the beam axis. This is more often expressed in terms of the pseudorapidity $\eta = -\ln\tan(\theta/2)$. This is an approximation of rapidity, making the assumption that the mass of the particle is zero. Pseudorapidity is a popular choice of coordinate because the particle flux from the interaction point is roughly constant as a function of η. Transverse variables are defined in the $x-y$ plane, where p_T, E_T and $\not{E}_T$ are the transverse momentum, transverse energy and missing transverse energy respectively. The transverse energy is the energy of the particle projected onto the

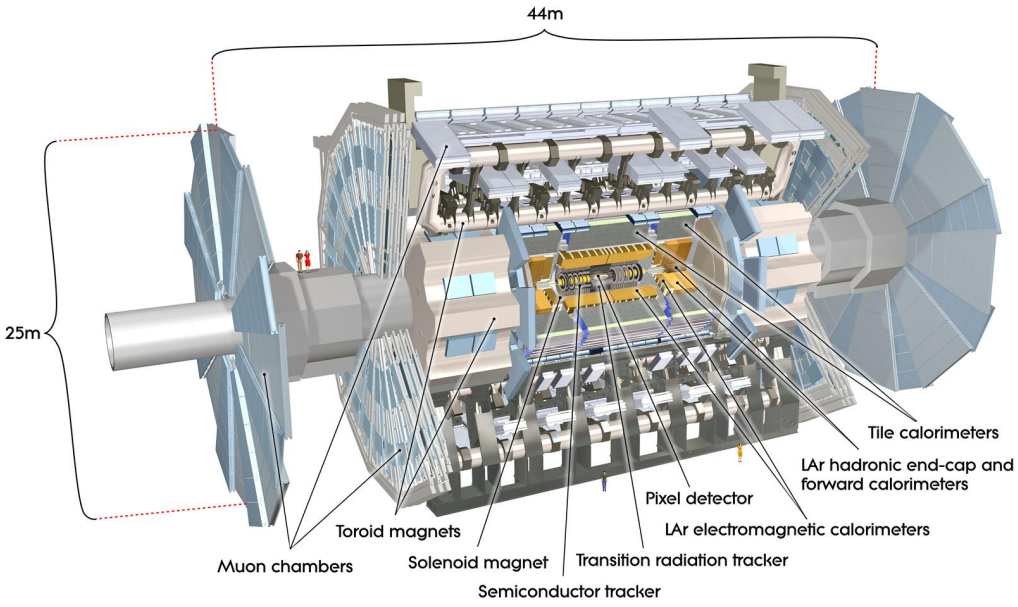

Figure 3.3: The ATLAS detector [61].

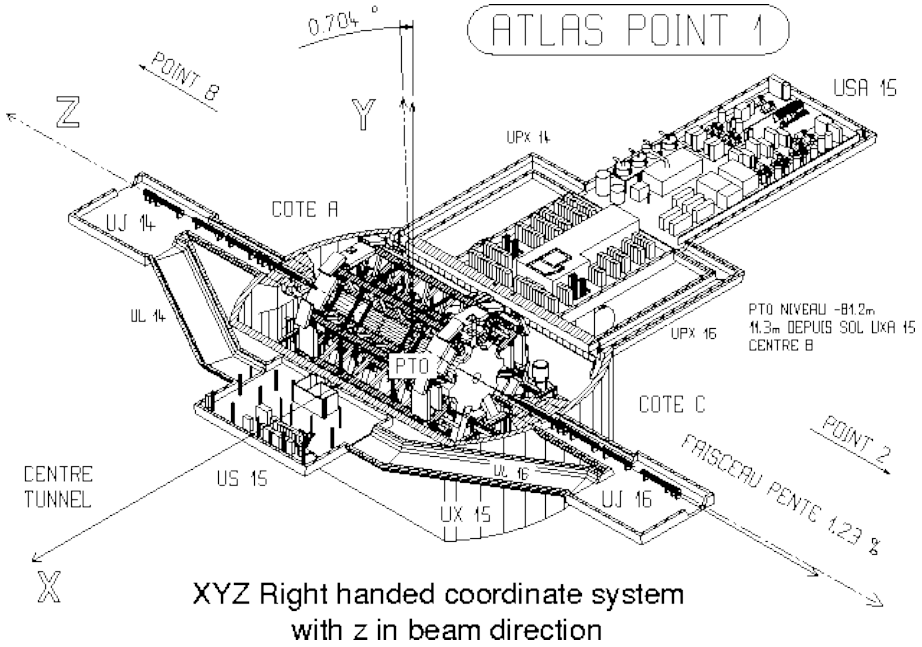

Figure 3.4: The ATLAS coordinate system [62].

$x-y$ plane, such that $E_T^2 = m^2 + p_T^2$, where m is the invariant mass of the particle. The missing energy is defined as $\not{E}_T = -\sum_i E_T^i$, where the sum is over all final state particles in the event. The distance ΔR in pseudorapidity-azimuthal angle space is defined as $\Delta R = \sqrt{\Delta^2\eta + \Delta^2\phi}$. The two ends of the detector are referred to as Side A and Side C with A being the side with positive z and C the side with negative z. [63]

3.2.2 Tracking

The ATLAS inner detector (ID) consists of three sub-detectors of decreasing granularity moving away from the interaction point. The layout of the ID can be seen in figure 3.5

where closest to the interaction point is the silicon Pixel Detector, followed by the Semiconductor Tracker (SCT), and the Transition Radiation Tracker (TRT). The entire inner detector is immersed in a 2 T magnetic field.

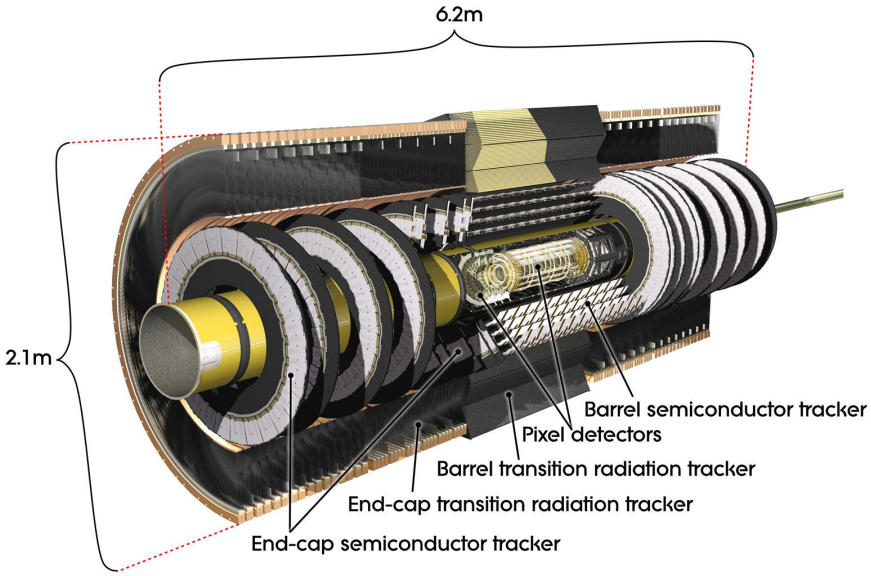

Figure 3.5: The ATLAS inner detector [64].

The trajectories of charged particles are reconstructed as they pass through the ID from ionisation deposits left behind after interacting with the detector material.

The ATLAS inner detector is designed to have a p_T resolution of $\frac{\sigma_{p_T}}{p_T} = 0.05\%\ p_T \oplus 1\%$ [54].

3.2.2.1 The Pixel Detector

The pixel detector is the sub-detector closest to the IP, and is thus the sub-detector most important for determining the impact parameter resolution and for the ability of the ID to find short lived particles. It has high granularity consisting of identical silicon pixel sensors each with a minimum $R\phi \times z$ pixel size with a coverage of 50×400 µm^2.

As a charged particle passes through the silicon, ionisation causes mobile charge carriers in the form of electron-hole pairs to be created in the semiconductor. By applying an electric field across the sensor the charge carriers are attracted to the electrodes inducing an electric current. By integrating the signal current, the signal charge is obtained, which is proportional to the ionisation energy deposited [65].

The two dimensional segmentation of the sensors allows space points to be measured without the ambiguities associated with strip detectors. The system consists of three barrel layers between 50.5 mm and 122.5 mm in R and three end-cap disks either side of the IP arranged between 495 mm and 650 mm in $|z|$. The pixel elements are bump-bonded onto readout chips to achieve the required density of pixels. The chips have a large area, with circuits for each individual pixel element including buffering to store data while waiting for the Level 1 trigger decision (see section 3.2.7). Sixteen chips are combined together to form modules, which are identical in the barrel and end-caps. They are arranged on the

support structures so that they overlap providing a hermetic coverage. The modules have a spatial resolution in $R\phi$ of 10 µm and 155 µm in z (or R in the case of the end-caps). [54]

3.2.2.2 The Semi-Conductor Tracker

The semi-conductor tracker (SCT) is a silicon micro-strip detector consisting of four barrel layers between 255 mm and 549 mm from the IP in R, and nine end-cap disks either side of the IP positioned between 810 mm and 2797 mm from the IP in $|z|$. The design of the SCT modules is different in the barrel and the end-caps.

Barrel modules consist of four singled sided silicon detectors which are 6.36 × 6.40 cm in size with 786 readout strips of 80 µm pitch (inter-strip spacing). The detectors are mounted either side of a heat transport plate in pairs, so that each pair form 12.8 cm long strips in which ionisation occurs as in the pixels. Electronics are mounted above the detectors on a hybrid, this includes a buffer to store hits above threshold while waiting for the Level 1 trigger decision [54]. The two sides of the module are arranged at a small stereo angle of 40 mrad. The modules are mounted on the barrel support structure with the strips of one of the layers running parallel to the beam pipe. $R\phi$ space points on the module are determined from knowledge of the position of the strip on the module, with the z coordinate determined by the examining the coincidence of hits by two crossing strips on either side of the module. A single module with one $R\phi$ and one stereo measurement achieves a spatial resolution of 16 µm in $R\phi$ and 580 µm in z. The barrel modules are mounted on carbon-fibre cylinders which also carry the cooling system. The modules are arranged to give a hermetic coverage, a requirement that leads to there being a slight overlap between the modules.

The end-cap modules in the SCT follow a similar design to the barrel modules except that they have a trapezoidal shape with an average strip pitch of 80 µm. This allows them to be arranged so that one set of strips is radial to the beam pipe. As with the barrel modules, two planes of sensors are mounted back-to-back at a relative angle of 40 mrad. This gives a position resolution of 16 µm in $R\phi$ and 500 µm in R. The modules are mounted onto the end-cap disks in up to three concentric rings. The number of rings depends on the z position of the disk, in such a way to limit the coverage to $|\eta| \leq 2.5$. To achieve this coverage in η, four types of end-cap module are used, each of similar design but of different dimensions dependant on their position in z and R. [54]

3.2.2.3 The Transition Radiation Tracker

The transition radiation tracker (TRT) is a straw tube detector. It consists of modules of 4 mm diameter gas filled polyimide tubes containing 31 µm diameter gold plated tungsten wires. The barrel contains 96 modules, covering a radial range of 55.4 cm to 108.2 cm, with two end-caps, each made up of 20 modules, extending from 82.7 cm to 274.4 cm in $|z|$.

The straw tubes are 144 cm in length in the barrel, but divided in the centre and read out at each end to reduce occupancy. The end-cap tubes are 37 cm in length and read out only at one end. In both the barrel and end-caps, the tube acts as the cathode with the central anode wire directly connected to the front end electronics and kept at

ground potential. A gas mixture of 70% Xe, 27% CO_2 and 3% O_2, is used in the tubes. As a charged particle passes through the gas volume it ionises the gas, freeing electrons which then drift to the anode wire. The $R\phi$ position of the particle in the detector can be determined to a much better resolution than 4 mm straw diameter by making a drift time measurement. The collection time is determined from drift velocity as a function of the electric field in the straw and of the direction and magnitude of the magnetic field [66]. This gives an improved spatial resolution of 130 µm per straw.

The barrel is divided into three rings of 32 modules, with each module containing a carbon-fibre laminate shell with a internal array of axially aligned straws embedded in a matrix of polypropylene fibres which act as the radiator to produce transition radiation.

Transition radiation is emitted when a relativistic particle crosses the interface of two materials with different dielectric constants [67], and can be used to give good separation of electrons and hadrons. The Xe gas in the straws serves as the ionisation medium for standard particle tracking but also has the added benefit of allowing the transition radiation to be detected when a relativistic electron passes through the polypropylene radiator. The TRT has two independent thresholds allowing the distinction between tracking hits which pass the lower threshold and transition radiation hits which pass the higher one, with the decision being made on the front end electronics. For a selection criteria that gives a 90% electron efficiency, the TRT achieves a pion misidentification probability of 5% for the majority of the detector. The misidentification probability can be as low as 1-2% in the best performing parts of the TRT [68]. The end-caps work on the same principle, with the modules installed with the straws running radially, with the readout at the outer radius. The end-cap modules are constructed with foils of polypropylene interleaved between the planes of straws. The end-caps consist of two sets of wheels, with the 12 wheels closest to the IP constructed with 8 successive layers of straws spaced 8 mm apart. The outer set of 8 wheels is also constructed with 8 layers but with a 15 mm spacing between them providing a reduced granularity. [54]

3.2.3 Calorimetry

ATLAS uses sampling calorimeters covering a pseudorapidity range of $|\eta| < 4.9$. Sampling calorimeters use alternating layers of an active detector material and a passive absorber. They sample the ionisation energy at each point in the shower and allow large or awkward detector volumes to be filled at reasonable cost. Different technologies are used for the different physics and radiation environments over this large η range, as is seen in figure 3.6. Matching the range of the ID tracking, a fine granularity electromagnetic calorimeter is used to give precision measurements of electrons and photons. The courser granularity used over the rest of the calorimetry is sufficient for the requirements of jet reconstruction and $\not{E}_T$ measurements. One of the considerations when designing a calorimeter system is that both electromagnetic and hadronic showers need to be contained, and that punch-through (where a shower deposits energy beyond the hadronic calorimeters) into the muon system minimised, this leads to the total depth of the calorimetry being important. Electromagnetic shower depth is measured in terms of radiation lengths, X_0, which is the mean distance over which an electron's energy is reduced to a fraction of $1/e$ of the initial

value. Hadronic showers are measured in interaction lengths, λ, which is the mean free path over which a relativistic charged particle transverses a medium without an elastic or quasi-elastic (diffractive) interaction [69]. The ATLAS electromagnetic calorimeter has a total depth of $> 22X_0$ in the barrel and $> 24X_0$ in the end-caps. The total depth of the calorimeters including the outer support is about 11λ at $\eta = 0$. [54]

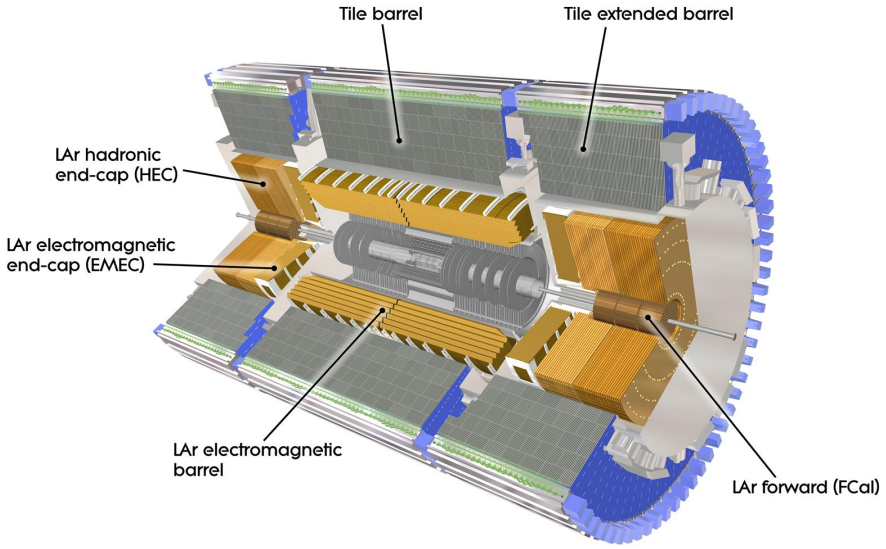

Figure 3.6: The ATLAS calorimeters [70].

3.2.3.1 Electromagnetic Calorimeter

The electromagnetic calorimeter (ECal) is a lead liquid-argon (LAr) sampling calorimeter which is positioned downstream of the central solenoid magnet. The barrel has a coverage of $|\eta| < 1.475$ which is separated into two identical half barrels parted by a 4 mm gap at $z = 0$. The end-caps are each divided into two coaxial wheels which together cover a range of $1.375 < |\eta| < 3.2$.

The ECal has accordion shaped kapton electrodes interleaved with lead absorber plates. The lead absorber is held at ground potential, with the electrodes consisting of three copper layers separated by the insulating polyimide sheets. The outer two layers of copper are held at a high-voltage potential with the central layer used for reading out the signal. The volume between the lead and the electrode is filled with liquid argon which acts as the ionisation medium. The accordion geometry allows a complete ϕ symmetry without any azimuthal cracks.

The primary source of energy loss for electrons is bremsstrahlung caused by deflection in the electric field of the lead nuclei. Photons, above a few MeV, primarily lose energy due to pair production. The photon interacts with the nucleus or atomic electrons in the lead to produce electron-positron pairs [71]. Due to these two processes an electron or photon transversing the lead produces a cascade of lower energy electrons and photons. Through these cascades in the multiple layers of absorber material an electromagnetic shower develops. The shower is sampled in the layers of liquid argon between the lead

plates. The secondary particles produced in the shower cause ionisation of the liquid argon. The ionisation electrons are then read out from kapton electrodes.

The thickness of the lead plates varies as a function of η to optimise the energy resolution of the calorimeter. The region of $|\eta| < 2.5$, which matches up with the η range of the tracking, is devoted to precision physics and is segmented into three sections in depth, each decreasing in granularity. The end-cap inner wheel is segmented into two sections with courser lateral granularity than the rest of the acceptance.

For $|\eta| < 1.8$ a presampler consisting of a single active layer of LAr is used to correct for energy loss of electrons and photons upstream of the calorimeter. [54]

The electromagnetic calorimeter is designed to have an energy resolution of $\frac{\sigma_E}{E} = \frac{10\%}{\sqrt{E}} \oplus 0.7\%$ [54]. Where the energy dependant term is due to stochastic effects from fluctuations related to the physical development of the shower. The constant term is due to instrumental effects that result in non-uniformity of the detector response [72].

3.2.3.2 Hadronic Calorimeter

The Hadronic Calorimeter (HCal) consists of three sub-detectors; the Tile Calorimeter, the Hadronic End-Cap Calorimeter (HEC), and the Forward Calorimeter (FCal). All three are sampling calorimeters and are described below; their positions within ATLAS can be seen in figure 3.6. The hadronic calorimeter is designed to have a jet energy resolution in the barrel and endcap of $\frac{\sigma_E}{E} = \frac{50\%}{\sqrt{E}} \oplus 3\%$ and in the forward calorimeter of $\frac{\sigma_E}{E} = \frac{100\%}{\sqrt{E}} \oplus 10\%$ [54].

The hadronic calorimeters work on a similar basis to the electromagnetic calorimeter. Particles interact in the absorber material, producing a cascade of particles that ionise the active material. Differences lie in how the particles interact with the absorber material, with hadrons interacting with the nuclei of the absorber material via the strong force. This produces cascades of lighter hadrons forming the hadronic showers. Hadronic showers are much larger than electromagnetic showers leading to the hadronic calorimeter being deeper than the electromagnetic calorimeter in order to contain the shower.

The Tile Calorimeter is positioned directly behind the electromagnetic calorimeter, it uses steel is the absorber material, with scintillator tiles at the active medium. It covers $|\eta| < 1.7$ and is sub-divided into a 2.6 m long central barrel and two 2.6 m long extended barrels. Each section has an inner and outer radius of 2.28 m and 4.25 m respectively, with radial depth of about 7.4λ. The tiles are arranged radially and so that they are normal to the beamline. They are read out at the edges by wavelength shifting fibres. This arrangement gives almost continuous azimuthal coverage. [54]

The LAr Hadronic End-Cap Calorimeter (HEC) is a copper-liquid argon sampling calorimeter consisting of two independent wheels per end-cap (referred to as the front and rear wheels) each positioned directly behind the end-caps of the electromagnetic calorimeter. The HEC covers the region $1.5 < |\eta| < 3.2$ overlapping with the forward calorimeter reducing the drop in material density in the transition between the two. Each of the wheels in divided into two segments in depth producing four layers per end-cap. Each of the wheels is constructed of 32 identical wedge-shaped modules. The modules in

the front wheels use twenty-four 25 mm copper plates for the absorber material, with the rear wheels, which have a courser sampling fraction, using sixteen 50 mm copper plates. For all four wheels the first plate of the wheel is made at half the thickness. The gaps between the plates are further segmented by three electrodes into separate LAr drift zones, providing the read out and potential difference to attract the ionisation electrons. [54]

The LAr Forward Calorimeter (FCal) is integrated into the end-cap cryostats, this acts to reduce the radiation levels in the muon spectrometer and provides improved uniformity of the calorimeter coverage. The front face of the FCal is recessed by about 1.2 m with respect to the electromagnetic calorimeter front face, this is to reduce the amount of neutron back scattering in the ID volume. This limitation in depth requires a high density design. The calorimeter is about 10λ deep and consists of three modules per end-cap. The first module, made of copper is optimised for electromagnetic measurements. The following two modules are made from tungsten and mainly measure hadronic interactions. All three modules are made of a metal matrix with regularly spaced channels running longitudinally throughout the metal. Electrodes consisting of concentric rods and tubes are inserted into these channels running parallel to the beamline. The gap between the rod and tube is filled with liquid argon which acts as the sensitive material [54].

3.2.4 Muon Spectrometer

The muon system is based on the magnetic deflection of muons in the large superconducting air-core toroid magnets. The system contains separate chambers for triggering and for high-precision tracking. In the $|\eta| < 1.4$ region the muon bending is achieved by the use of the large barrel toroid. In the $1.6 < |\eta| < 2.7$ region the bending is due to two smaller end-cap magnets positioned inside the ends of the barrel magnet. In the transition region of $1.4 < |\eta| < 1.6$ deflection is due to a combination of the barrel and end-cap magnetic fields. This configuration gives a field that is mostly perpendicular to the muon trajectories, and defines the η plane of ATLAS as the bending plane and the ϕ plane as the non-bending plane. In the muon spectrometer the transverse momentum and charge of the muon track is calculated using the sagitta of the track. The sagitta is a measure of the curvature of the track and is defined as

$$s = \frac{1}{8}\frac{qBL^2}{p_T}, \tag{3.1}$$

where q is the charge of the track, B the strength of the magnetic field (2 T), p_T the transverse momentum, and L the length of the track as shown in figure 3.7. The charge of the track is determined from observing which direction the muon curves in the magnetic field. The p_T of the track is obtained from the re-arrangement of equation 3.1. Mismeasurements of the sagitta can therefore directly lead to the uncertainty of the track p_T with $\frac{\sigma_{p_T}}{p_T} = \frac{\sigma_s}{s}$. The aim of the muon system is to achieve a 10% p_T resolution for standalone (see section 3.2.5) 1 TeV muon tracks, which corresponds to measuring a sagitta along the z axis of about 500 µm to be measured with a resolution of $\leq$ 50 µm. For most of the η-range precision tracking is achieved using Monitored Drift Tube Chambers, with

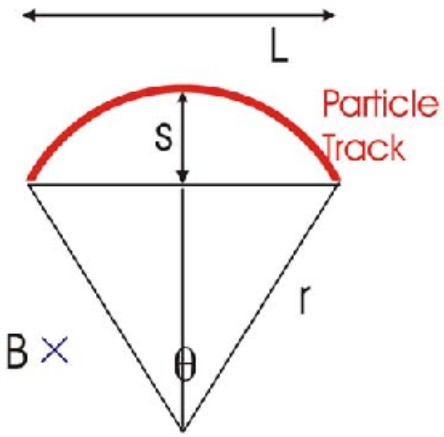

Figure 3.7: Sagitta of a track.

Cathode Strip Chambers used at larger η. The muon trigger system covers an η-range of $|\eta| < 2.4$ and uses Resistive Plate Chambers in the barrel and Thin Gap Chambers in the end-cap region. [54]

3.2.4.1 Precision Tracking Chambers

Monitored Drift Tube Chambers (MDTs) consist of 29.87 mm diameter aluminium pressurised drift tubes, with a 50 µm diameter tungsten-rhenium wire at the centre of the tube. An Ar/CO_2 gas mixture is used, which is shown to have excellent ageing properties. The anode wire is kept at 3080 V with the high voltage supply being attached to the wire at one end and the readout at the other. The MDTs are designed to measure the spatial coordinate in the bending plane, with the non-bending plane coordinate coming from an associated hit in the trigger chambers, as such the tubes in the barrel and end-caps are arranged to run along ϕ. The MDTs achieve an average resolution per chamber of about 35 µm in z. The chambers themselves are constructed of an aluminium frame containing two multi-layers separated by a mechanical spacer. Each multi-layer consists of three or four layers of drift tubes. The chambers are rectangular in the barrel and trapezoidal in the end-caps. The shapes and dimensions of the chambers were chosen to optimise the solid angle coverage while being constrained by the shape of the magnetic coils and support structures. [54]

Cathode Strip Chambers (CSCs) are used for precision tracking in the first layer of the end-caps for $|\eta| > 2$, where counting rates exceed the maximum MDT counting rate of 150 $Hzcm^{-2}$. The CSC system consists of two end-cap disks each with four small chambers and four large chambers, all segmented in ϕ. Each of the chambers has four CSC planes which give four independent measurements in η and ϕ.

The CSCs are multi-wire proportional chambers which have wires orientated in the radial direction, in such a way that the central wire extends away from the beamline radially with the remaining wires running parallel to it. Either side of the plane of anode wires are cathode strips with one set running parallel to the wires and one running orthogonal to them in order to get the two coordinates. Position of the track is determined by

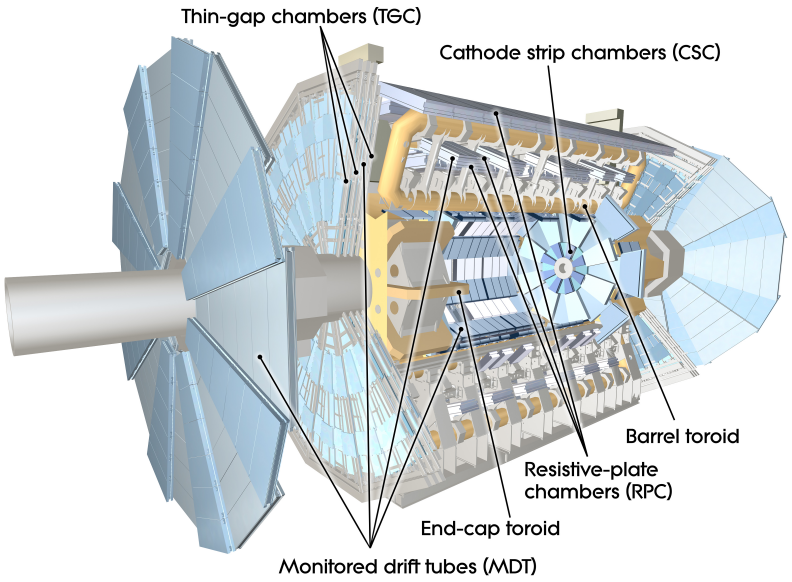

(a)

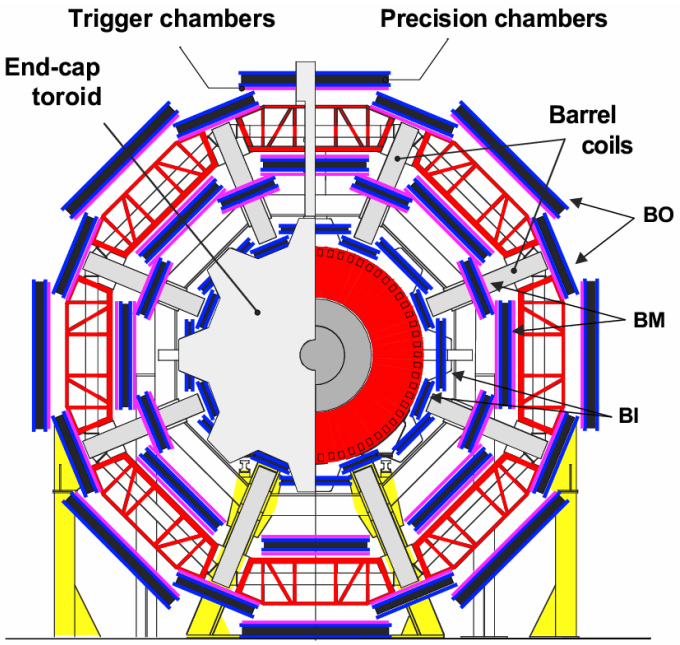

(b)

Figure 3.8: The position of the ATLAS muon chambers are shown in (a) [73], while the arrangement in the $x-y$ plane is shown in (b) [74].

interpolation between charges induced on neighbouring cathode strips rather than from reading out the anode wires directly. The gas between the cathodes in which ionisation occurs is a mixture of Ar (80%) and CO_2 (20%). The CSC obtains a spatial resolution of 50 µm per plane in the bending direction with a 5 mm resolution in the non-bending plane due to the courser cathode segmentation. [54]

3.2.4.2 Trigger Chambers

The requirements of the trigger chambers are different to those of the precision tracking chambers. They are required to quickly provide information on muons traversing the detector, allowing the Level 1 trigger logic (see section 3.2.7) to recognise their approximate momentum range and multiplicity. Much coarser tracking information than the precision chambers is sufficient for this. The trigger chambers need to provide an acceptance over the full ϕ-range and in the range of $|\eta| \leq 2.4$. As the end-caps require higher granularity and suffer from up to ten times as much radiation as the barrel region, different technologies are used for the barrel ($|\eta| \leq 1.05$) and end-cap ($1.05 \leq |\eta| \leq 2.4$) trigger chambers. In the barrel Resistive Plate Chambers (RPCs) are used due to their good spatial resolution and adequate rate capability. In the end-caps Thin Gap Chambers (TGCs) are used as they provide good time resolution and high rate capabilities. A schematic of the placement of the muon trigger chambers within ATLAS is shown in figure 3.9. To enable fast decisions on the p_T of the muon an algorithm that considers the coincidences between the layers is used. This looks at hits in a "pivot" layer (RPC2 for the RPCs and TGC3 for the TGCs), and compares the deviation from straightness of the hit in pivot layer and a hit in another layer to a straight line between the pivot layer hit and the IP. For example the low p_T trigger in the barrel examines the deviation of the slope between the RPC2 and RPC1 layers to the straight line between the RPC2 and the IP. This is also illustrated in figure 3.9. [54]

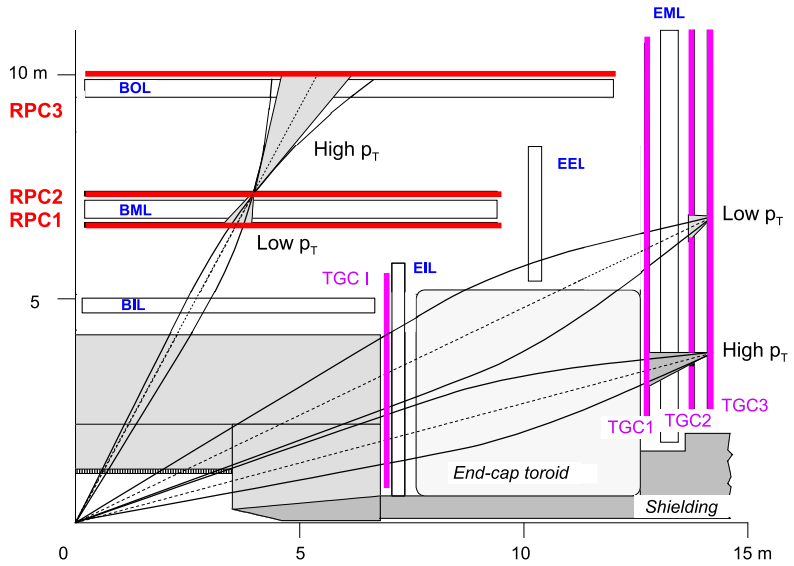

Figure 3.9: The ATLAS muon trigger chambers [54]

Resistive Plate Chambers (RPCs) are arranged in three concentric cylindrical layers around the beam axis and are referred to as trigger stations. Each of the trigger stations consist of three independent layers of detector, each with the ability to measure η and ϕ. The RPCs achieve a 10 mm resolution in both z and ϕ

The RPCs are gaseous parallel electrode-plate detectors using a gas mix of $C_2H_2F_4$/Iso-C_4H_{10}/SF_6 (94.7%/5%/0.3%). Two resistive plates are kept parallel to each other by 2 mm

insulating spacers. The electric field between the plates allows avalanches towards the anode to form along the ionising tracks. The signal is read out via capacitive coupling to metallic strips mounted on the outer sides of the resistive plates. The readout strips on either side of the gas gap are arranged orthogonally to each other allowing both a η and ϕ coordinate to be obtained. A requirement of a coincidence in the η and ϕ readouts helps to reject noise. Each RPC unit consists of two gas gaps and four panels of readout strips. Three lightweight paper honeycomb structures are interleaved between the detectors to support them. [54]

Thin Gap Chambers (TGCs) are multi-wire proportional chambers that provide triggering for the muons in the end-cap region as well as determining the azimuthal coordinate of muon tracks to compliment the η measurement of the MDTs. The TGCs achieve a 2-6 mm resolution in R and a 3-7 mm resolution to ϕ. The arrangement of the chambers can be seen in figure 3.9, with one wheel of chambers positioned before the end-cap toroid (TGCI) and three after it (TGC1-3).

The chambers themselves consist of two cathodes held at ground between which is a 2.8 mm gas gap containing a mixture of CO_2 and n-C_5H_{12}. At the centre of the gas gap are anode wires spaced 1.8 mm apart. Pick-up strips on the outer side of the cathode run orthogonal to the wires. The signal is read out from both the pick-up strips and the anode wires to obtain the required two coordinates. The high electric field around the wires and the small spacing between them leads to very good time resolution for the majority of track, meaning that signals arrive with 99% probability of being within a 25 ns time window. [54]

3.2.5 Muon Identification Algorithms

There are three different strategies towards muon identification in ATLAS. Standalone reconstruction only uses the muon spectrometer to reconstruct the muon track. Whereas, combined reconstruction uses information from both the muon spectrometer and the inner detector. The third approach is to use the information in the inner detector with partially reconstructed MS tracks or information from the calorimeters, these are referred to as tagged tracks. There are two families of muon reconstruction algorithms in ATLAS[1] `staco` (sometimes referred to as chain 1) and `muid` (chain 2), each have a range of algorithms covering the three strategies outlined above [75]. As described in section 4.4, the analysis presented in this thesis uses combined `muid` muons.

Standalone Reconstruction only uses tracks in the muon spectrometer. Hits in the same chamber are fitted with a straight line to form a segment. Segments from all three chamber stations are then used to fit a track using hits from all four sub-detector technologies. The reconstructed track is then extrapolated back to the interaction point taking into account energy loss and multiple scattering in the calorimeters. The `muid` family does this is two phases, first it creates the tracks in the MS using it's `moore` algorithm.

[1] There is now a third family of algorithms called "third chain", which combines many of the approaches used by `muid` and `staco` and will replace them to become the only set of ATLAS muon reconstruction algorithms. It is not mentioned here in detail as it is a new development.

The fitted track is then extrapolated back to the IP using `muid standalone` which uses a parameterisation of energy loss in the calorimeter. The `staco` standalone algorithm is called `Muonboy`. This reconstructs a track by taking a segment in the outer station and obtaining a full track by iteratively adding segments from the middle and inner MS layers, which is then extrapolated back to the IP.

Combined Reconstruction uses standalone tracks and matches them to inner detector tracks creating a single track within the $|\eta| < 2.5$ coverage of the ID. The benefit of the combined muons is that they take advantage of both the good low p_T sensitivity of the ID and the good high p_T sensitivity of the MS. The `muid standalone` tracks are matched to the ID tracks by doing a full track refit using the original hits. `Muid` also has an algorithm called `MuGirl` which extrapolates ID tracks into the MS and creates new segments using the MS hits near to the extrapolated tracks. This produces a combined muon if the refit is successful, or creates a tagged muon if not. The `staco` approach is to take the reconstructed ID and MS track vectors and combines them using a statistical combination. Both the `muid` and `staco` approaches achieve similar p_T resolutions.

Tagged Inner Detector Tracks are used to obtain additional muon candidates by associating ID tracks with MS measurements to create a tagged track. This approach can recover low energy muons due to being less sensitive to coulomb scattering and energy loss. It is also useful at recovering muons that pass through areas of the MS with limited coverage. The `staco` algorithm uses `muTag` which associates the extrapolated ID track to the first available `muonboy` segment in the inner or middles MS layer, creating a tagged muon. Only ID tracks and MS segments not already used in previous staco combinations are used. The `muid` family uses a tagger called `MuTagIMO` which uses associates the ID track to existing `moore` segments.

3.2.6 Muon Performance in ATLAS

In this section the performance of ATLAS with regards to muons is discussed. Below, the muon momentum resolution, the muon reconstruction efficiency and the mass resolution are discussed. The muon trigger efficiency, for the trigger used in this analysis is discussed in section 4.3.2.2 in relation to the corrections applied to the Monte Carlo. The muon isolation efficiency is calculated as part of this thesis and can be seen in chapter 5.

As discussed in section 4.4 the muons used in this analysis are required to have $p_T >$ 12 GeV, with very few of the selected muons having a $p_T > 60$ GeV (as seen in chapter 7). An attempt has been made to find performance plots for combined `muid` muons in the p_T range of the measurement presented in this thesis. Where this has not been completely possible, the performance plots are chosen to be as relevant as possible.

3.2.6.1 Momentum Resolution

As discussed in section 3.2.5, combined muons are measured both in the muon spectrometer and in the inner detector. The momentum resolution of the muons in these two regions

of the detector is measured separately [76, 77]. The momentum resolution is measured using a sample of $Z \to \mu^+\mu^-$ events, where the resolution is determined from a template fit to the Z line-shape. The relative momentum resolution, $\sigma(p)/p$, in the inner detector takes into account multiple scattering and the intrinsic momentum resolution of the detector. The relative momentum in the muon spectrometer also accounts for energy loss in the calorimeters. Figure 3.10(a) shows the measured resolution on the curvature, $\sigma(1/p_T)$, in the barrel for the inner detector as a function of muon p_T. Figure 3.10(b) shows the relative momentum for muons in the muon spectrometer as a function of muon p_T. The different representations of the resolution means that the values cannot be directly compared. The resolutions shown were calculated with 2.54 fb^{-1} of data in 2011. The resolutions are measured in the first pass of reconstruction which uses preliminary calibration and alignment. The resolution in simulation is also shown, before it is corrected to the data. At low and high p_T the resolution in data is obtained from an extrapolation to a p_T range not available in the analysis. Up to about 20 GeV the resolution in the ID and about 10 GeV in the MS is seen to fall sharply with increasing p_T. This is due to the contributions from the multiple scattering becoming smaller (lower p_T leads to more multiple scattering). After this sharp fall, $\sigma(1/p_T)$ in the inner detector is seen to continue to fall, whereas the $\sigma(p_T)/p_T$ muon spectrometer it begins to rise again. Both effects are due to the fact the sagitta discussed at the start of section 3.2.4, is harder to measure as muon p_T increases. The combined muons used in this thesis will have a momentum resolution that is a combination of the resolution in both the ID and the MS.

3.2.6.2 Reconstruction Efficiency

The reconstruction efficiency for a combined muon can be expressed as $\varepsilon_{reco} = \varepsilon_{ID} \cdot \varepsilon_{comb} \cdot \varepsilon_{MS}$ where ε_{ID} is the reconstruction efficiency in the ID, ε_{MS} the reconstruction efficiency in the MS and ε_{comb} the efficiency of the matching the ID and MS tracks. As the different parts of the reconstruction efficiency can be measured separately it can be calculated uses a tag and probe method. This is done using $Z \to \mu^+\mu^-$ resonance events [79]. This allows one muon to be reconstructed in both the ID and MS (the tag muon). The other muon is then identified using only one of the systems, allowing the efficiency of the other to be measured. This means that for ε_{ID} standalone muons are are used as the probe, with ε_{ID} being the fraction of probes that as be associated with an ID track. Using an ID track as the probe the $\varepsilon_{comb} \cdot \varepsilon_{MS}$ can be measured. This is given by the fraction of ID probes that can be associated with a combined muon.

Figure 3.11 shows the 2011 combined `muid` muon reconstruction efficiency with respect to the inner detector efficiency for muons with $p_T > 20$ GeV as a function of muon η. The efficiency can be seen to be high and relatively constant as a function of the muon η. The obvious exception is at central pseudorapidity where the efficiency is lower due to a gap in the muon spectrometer acceptance to allow for cabling.

A more informative plot would be to show the reconstruction efficiency as a function of the muon p_T, as it might be expected to worsen with at lower p_T. This could not be found for 2011 data, but figure 3.12 shows this measured in 2010 data, using the same tag and probe approach. Although this is not the same reconstruction efficiencies that the muons

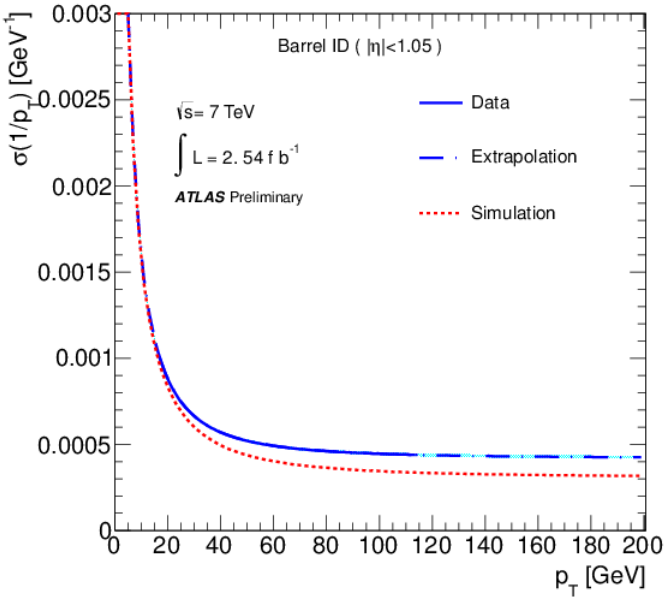

(a) Resolution of Curvature in the Inner Detector Barrel

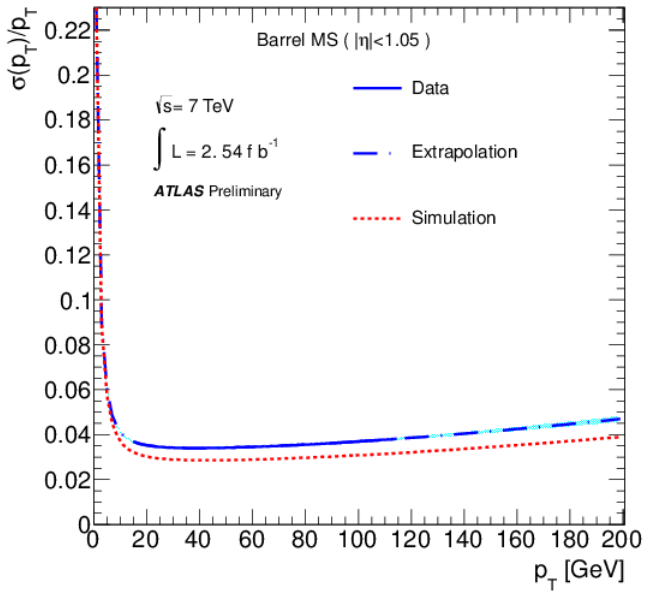

(b) Relative Momentum Resolution in the Muon Spectrometer Barrel

Figure 3.10: `Muid` *muon momentum resolution efficiency as measured with* $Z \to \mu^+\mu^-$ *decays as a function of the muon* p_T*. These plots were produced using 2.54* fb^{-1} *of 2011 data. Figure (a) shows the resolution on the curvature,* $\sigma(1/p_T)$ *as a function of muons* p_T *in the ID. Figure (b) shows the relative momentum resolution,* $\sigma(p_T)/p_T$ *as a function of muons* p_T *in the MS. In both plots a comparison is made to Monte Carlo before corrections to the modelled momentum resolution are made [78].*

in this thesis have, the 2011 reconstruction efficiency would be expected to be the same or marginally better. This is due to the understanding of the detector improving from one year to the next and any effects due to misalignment of the detector becoming better

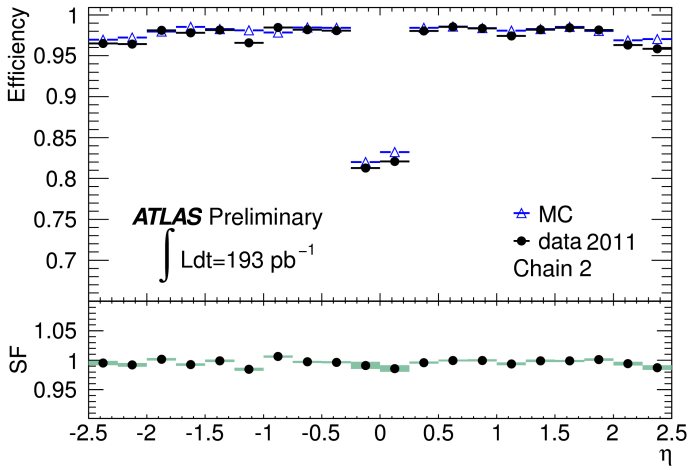

Figure 3.11: `Muid` *muon (chain 2) reconstruction efficiency as measured with Z boson decays as a function of the muon η. This plots is for $p_T^{\mu} > 20$ GeV muons using 2011 data [80].*

addressed. It can be seen in figure 3.12 that in 2010 the efficiency is high and relatively constant as a function of the muon p_T.

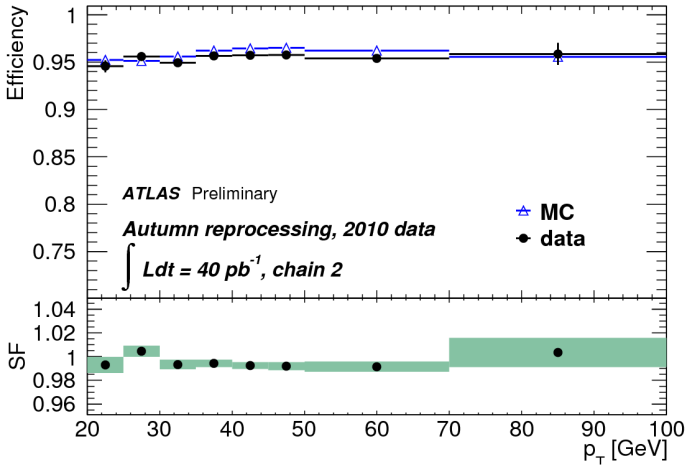

Figure 3.12: `Muid` *muon (chain 2) reconstruction efficiency as measured with Z boson decays as a function of the muon p_T for 2010 data [79].*

Although no plots are available, the 2011 muon reconstruction efficiency is calculated with this tag and probe method for muons down to p_T = 7 GeV.

3.2.6.3 Mass Resolution

The di-muon mass resolution is a measure of the performance of the detector as the measurement of the invariant mass of two particles depends on the measurements of their momenta and of their direction. The mass resolution is calculated using a sample of $Z \to \mu^+\mu^-$ resonance events [77]. The resolution is determined from a fit to the resonance peak using a fit function that consists of the di-muon invariant mass resonance at the generator level in Monte Carlo convoluted with a Gaussian representing the resolution. The resolution at $M_{\mu\mu}$ = 90 GeV is plotted as a function of η for muons with $p_T > 20$ GeV in figure 3.13. The resolution is shown in data at two points in 2011 with different pileup

conditions ($\langle\mu\rangle$ is the average number of interactions per bunch crossing). The variation with pileup is seen to be small. The mass resolution is seen to be ~ 2.2 GeV everywhere accept at central pseudorapidity, where it drops to ~ 1.8 GeV. Also shown is the mass resolution measured in Monte Carlo. The difference between the data and simulation is due to residual internal misalignments of the ID and the MS.

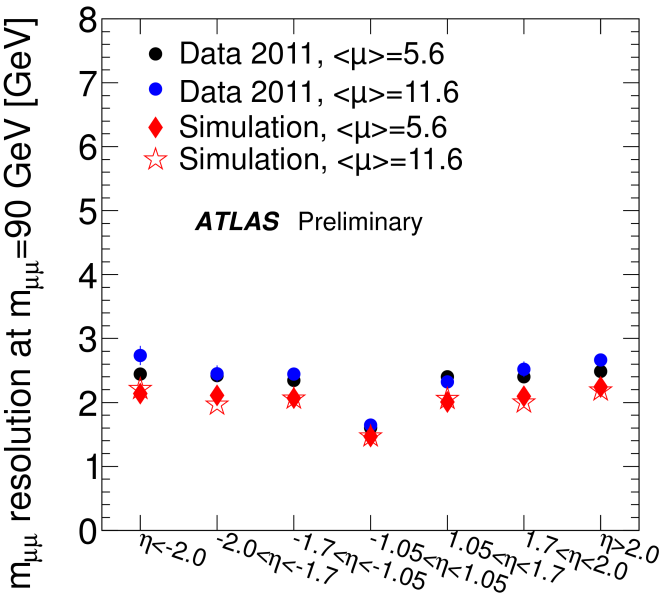

Figure 3.13: Di-muon mass resolution for $M_{\mu\mu} = 90$ GeV for muons with $p_T > 20$ GeV as a function of η [77].

3.2.7 The ATLAS Trigger

The ATLAS trigger has three levels; Level 1 (L1), Level 2 (L2) and the Event Filter (EF). Together L2 and EF are often referred to as the High Level Trigger (HLT). These three stages are illustrated in figure 3.14. At nominal running, the LHC will provide a bunch crossing rate of 40 MHz (it was 20 MHz in 2011). The three trigger levels are designed to reduce the output rate of ATLAS from about 40 MHz to about 200 Hz. Each level refines the decision of the previous level, by taking advantage of the better resolution available to each level and including a larger volume of the detector in the decision. Level 1 is hardware based using dedicated electronics to make the trigger decision. The HLT however is software based, with the trigger decision taking place on a processor farm adjacent to the detector.

Level 1 searches for high p_T electrons, muons, photons, jets and taus decaying to hadrons, it also considers total and missing transverse energy. L1 bases its decision on a subset of the detectors using a reduced granularity, reducing the data rate to ~ 75 kHz. If the Level 1 trigger accepts the event, then it defines a region of interest (RoI) around the objects that were triggered on. The Level 2 trigger is then seeded with the RoIs defined by Level 1.

The Level 2 trigger uses the full detector information within the RoI to make its decision. The Level 2 trigger reduces the data rate to about 3.5 kHz, taking an average processing time of 40 ms. For the muon triggers, Level 2 allows further rejection by sharpening and sometimes raising the p_T threshold used by Level 1. To do this information from both the muon chambers and the inner detector are used. Level 2 also allows the activity around the muon candidate in the calorimeters to be considered.

Events accepted by the Level 2 trigger are passed onto the Event Filter which uses offline algorithms adapted to the online environment to perform a complete event reconstruction, allowing further refinement of the trigger decisions to be made. The Event Filter takes about 4 seconds to make its decision, reducing the data rate to 200 Hz. The 200 Hz is the total data rate out of ATLAS and is divided up among many different triggers, each designed to select different physics objects. This selection of triggers is called the trigger menu and changes with the different beam conditions of the LHC. The analysis presented in this thesis uses the `EF_2mu10_loose` trigger, this is a di-muon trigger requiring 2 muons both with $p_T \geq 10$ GeV at the event filter. This trigger is originally seeded by the Level 1 `L1_2MU0` trigger, which requires 2 muons with no p_T requirement, this decision is made by the front-end electronics looking for two station coincidences of muon tracks in different RPG and TGC layers as described in section 3.2.4.2. Events that pass the L1 trigger are then passed on to the Level 2 `L2_2mu10_loose` trigger, which includes ID tracking information, before being refined further by the `EF_2mu10_loose` event filter trigger.

3.3 The ATLAS Computing Model

The central feature of the ATLAS computing model is the `ATHENA` framework. `ATHENA` is a collection of C++ packages and used in every phase of the processing chain, which is outlined in figure 3.15. Once an event has been selected by the trigger it is readout by the

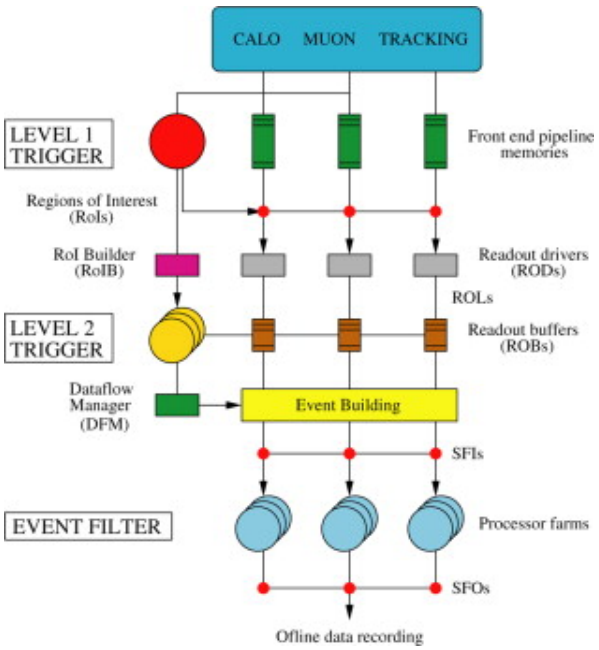

Figure 3.14: The ATLAS trigger levels [81].

Data Acquisition System (DAQ) as the byte stream which contains the signals from the individual sub-detector electronics. The Converters then turn this stream of bytes into a more useful RAW format which identifies detector elements that have received a hit or energy deposit along with the details of, for example, the amount of energy deposited. In order to carry out a physics analysis, physics objects such as electrons, muons or jets are more useful than simply a list of detector elements that are above threshold. To create these, reconstruction algorithms run over the RAW data, which is used together with conditions and geometry databases to fit tracks to the hits in the tracking detectors, and create clusters in the calorimeters, this first phase of reconstruction is known as detector reconstruction. Next the clusters and tracks are used together to identify the physics object that caused them, an electron, a muon, or a jet for example, this phase is known as combined reconstruction. Once these objects are created they can be used for physics analysis. The output of the reconstruction is written to two main output formats Analysis Object Data (AOD) which contain the reconstructed physics objects or Event Summary Data (ESD) which also contain enough information to re-run parts of the reconstruction such as track refitting or jet calibration. A third output format is also widely used which is the Derived Physics Data (D3PD), this is a completely flat `ROOT` [82] ntuple, which contain a subset of the physics objects in the AOD. There are many D3PDs for each of the AODs, which are produced centrally by the physics analysis groups in ATLAS with different subsets of these objects. The appeal of D3PDs is that they can be read by standalone user analysis code rather than requiring the use of the `ATHENA` framework, which is powerful but comparatively difficult to use.

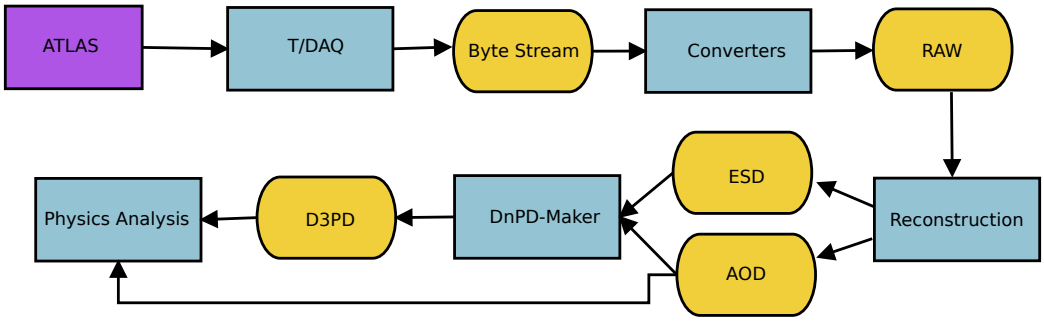

Figure 3.15: The ATLAS data processing chain. The blue rectangles denote a process and the orange ovals denote a data format.

3.4 ATLAS Monte Carlo

Monte Carlo simulation for ATLAS is available for a number of different Monte Carlo generators. This analysis uses Monte Carlo from the `Pythia` [83], `HERWIG` [84] and `MC@NLO` [47] generators. Monte Carlo events are generated with the required generator, typically either the whole generation is done within the `ATHENA` framework or 4-vectors are generated with standalone generator code and hadronised using another generator within the `ATHENA` framework (as is done with `MC@NLO`). Once the hard scatter has been generated (known as generator level Monte Carlo), the propagation of the produced particles through ATLAS and the detector's response needs to be simulated. The propagation of the particles is modelled using the `GEANT4` toolkit [85]. `GEANT4` is supplied with the configuration of the detector, including distortions and misalignments, it then simulates deposits in the detector which are recorded as "hits" containing position and time of the energy deposition. Next the simulated event undergoes digitisation, producing a Monte Carlo version of the RAW data format, mentioned in section 3.3, called a Raw Data Object (RDO) file. The main difference being that RDO files also contain truth information about the event, and connections between the hits and the generated particles. To make the events in the RDO as similar to RAW as possible the generator event not only has the hard scatter but also backgrounds from simulated minimum bias, beam gas, beam halo and cavern background events which are overlaid onto the signal simulation. The digitisation stage also adds detector noise to the events and each of the triggers are evaluated and their decisions recorded without removing events as would be done in data. The RDO files can then be passed to the reconstruction algorithms in the same way as the RAW files, and output files are then produced in the same way as for data as described in section 3.3. The final AOD, ESD or D3PD files can then be analysed in exactly the same way as for data, but with the additional advantage of containing the truth information. [86]

Chapter 4

Analysis and Selection

This chapter describes the data and Monte Carlo samples used in the analysis, the event selection used, and many of the corrections made to the Monte Carlo samples to enable them to be compared to the data, with additional corrections derived for this analysis presented in chapters 5 and 6. Control plots demonstrating the agreement between data and Monte Carlo can be seen in chapter 7.

4.1 Drell-Yan Final State

The final state considered in this analysis is $pp \to \mu^+\mu^- + X$, where X is any particles produced from initial state QCD radiation. As seen in section 4.4 the events are required to have at least two oppositely charged muons, but no further restriction is made on other physics objects in the event. For example, jets or missing transverse energy are not considered. The final differential mass cross section measurement is made in a mass range of $26 < M_{\mu\mu} < 66$ GeV using muons of opposite charge in a fiducial volume of

- $p_T^{\mu_1} > 15$ GeV
- $p_T^{\mu_2} > 12$ GeV
- $|\eta^{\mu_{1,2}}| < 2.4$

Where μ_1 and μ_2 are the leading and sub-leading muons respectively. As seen in section 8.1, the measured cross section is unfolded, taking into account QED final state radiation (FSR). This is referred to as unfolding to the Born level.

4.1.1 Background Processes

The main background processes to the Drell-Yan process are other process that can produce two or more muons that can be misidentified as originating from the Drell-Yan process.

The two largest backgrounds are from $\gamma^*/Z \to \tau^+\tau^-$ decays and multijet processes. As well as decaying to two oppositely charged muons, the γ^*/Z is equally likely to decay to two oppositely charged taus. These can then go onto decay to two oppositely muons via $\tau^+\tau^- \to \mu^+\nu_\mu\bar{\nu}_\tau\mu^-\bar{\nu}_\mu\nu_\tau$. As discussed in more detail in chapter 6, multijet events are also a

large contribution to the background. Muons can be produced in a jet and will typically be produced surrounded by the other decay products of the jet. Taking advantage of this allows the background to be reduced, but the large cross section of multijet processes means that a significant contribution to the total background is still made.

Contributing much less to the total background are muons produced in $t\bar{t}$ decays. These can decay leptonically such that $t\bar{t} \rightarrow W^+W^- \rightarrow b\bar{b} \rightarrow \mu^+\nu_\mu\mu^-\bar{\nu}_\mu$, producing two oppositely charged muons. Leptonic decays of di-boson processes ($WW/ZZ/WZ$) can also produce two or more muons that can be mistaken as the Drell-Yan process, for example as $W^-Z \rightarrow \mu^-\bar{\nu}_\mu\mu^+\mu^-$. The final background considered is from $W \rightarrow \mu\nu$ decays where only one muon is produced. This can mistaken as the Drell-Yan process when the muon produced is paired with a muon of the opposite charge produced in a jet.

Table 4.1 shows the contribution from all of the background processes to the selected data sample. All the backgrounds are estimated use Monte Carlo apart from the multijet background. This is estimated using a template fit method using both data and Monte Carlo, this is described in section 6.2. The percentage contributions shown for the different background processes are after the full selection defined in section 4.4 is made. All corrections to the Monte Carlo samples discussed in section 4.3 have been applied.

Background Process	Estimate	Percentage Contribution
$Z/\gamma^* \rightarrow \tau\tau$	Monte Carlo	3.7%
Multijet	Data enriched template fit	3.4%
$t\bar{t}$	Monte Carlo	0.6%
$WW/ZZ/WZ$	Monte Carlo	0.2%
$W \rightarrow \mu\nu$	Monte Carlo	0.1%

Table 4.1: Background processes to the Drell-Yan process.

It can clearly be seen from table 4.1 that the largest backgrounds come from $Z/\gamma^* \rightarrow \tau\tau$ and Multijet processes, but that even these are small, leading to a signal rich analysis.

An irreducible background to the Drell-Yan process is $\gamma\gamma \rightarrow \mu\mu$ processes, where the initial state photons are being radiated by quarks inside the proton, as described in section 2.2.4.3. As muon pairs produced by this process cannot be separated from those originating from $q\bar{q}$ collisions they are included in the final state. A correction is made to the theoretical predictions that the measured cross section is compared to as described in section 8.3.1.3.

4.2 Samples

4.2.1 Data Samples

The data used for this analysis was collected between 14$^{\text{th}}$ of April and 4$^{\text{th}}$ August in 2011 with a 50 ns bunch spacing at the LHC. The total integrated luminosity of the sample is 1.64 fb^{-1}, as defined by the Good Runs List discussed in section 4.4.

4.2.2 Monte Carlo Samples

A number of Monte Carlo samples are used in the analysis to estimate the amount of signal and background processes selected, this allows them to be used to optimise the cuts to improve the background rejection and signal efficiency. Tables 4.2 and 4.3 show the signal and background Monte Carlo samples respectively. Signal samples produced by `Pythia` are used to compare to the data and to estimate the detector response via the unfolding, as described in section 8.1. Background samples are produced with a number of different generators; `Pythia` and `HERWIG` are leading order generators which differ in their use of hadronisation models. `PythiaB` provides an interface to `Pythia` within `ATHENA`, adding the ability to produce specific decay chains for a process and to implement cuts either before or after hadronisation. This is particularly useful when generating rare charm and bottom events, where rather than fully generating huge numbers of events and rejecting the majority of them to have a sample containing only one decay chain or kinematic region. `MC@NLO` is a next to leading order generator, which only generates the four-vectors of the hard scatter, these then need to be given to another Monte Carlo generator to be hadronised.

Generator	Mass Range [GeV]	Lepton Filters	N_{events}	$\sigma_{tot} \cdot \varepsilon_{filter}$ [nb]
`Pythia`	$15 < M_{\mu\mu} < 60$	$2 \times p_T > 3; \lvert\eta\rvert < 2.7$	1M	$1.295 \cdot 0.395$
`Pythia`	$M_{\mu\mu} > 60$	-	10M	$0.856 \cdot 1.000$

Table 4.2: Signal, $Z/\gamma^* \to \mu\mu$, Monte Carlo samples.

Generator	Process	Lepton Filters	N_{events}	$\sigma_{tot} \cdot \varepsilon_{filter}$ [nb]
`PythiaB`	Multijet ($c\bar{c} + b\bar{b}$)	$2 \times p_T > 10; \lvert\eta\rvert < 2.5$	3M	$2.727 \cdot 1.000$
`Pythia`	$Z \to \tau\tau$ ($M_{\tau\tau} > 60$ GeV)	–	1M	$0.854 \cdot 1.000$
`Pythia`	$Z/\gamma^* \to \tau\tau$ ($10 < M_{\tau\tau} < 60$ GeV)	–	2M	$3.455 \cdot 1.000$
`Pythia`	$W \to \mu\nu$	–	7M	$8.938 \cdot 1.000$
`MC@NLO`	$t\bar{t}$	$1 \times p_T > 1$	13M	$0.167 \cdot 0.474$
`HERWIG`	WW	$1 \times p_T > 10; \lvert\eta\rvert < 2.8$	2.5M	$0.02956 \cdot 0.349$
`HERWIG`	ZZ	$1 \times p_T > 10; \lvert\eta\rvert < 2.8$	250k	$0.00460 \cdot 0.278$
`HERWIG`	WZ	$1 \times p_T > 10; \lvert\eta\rvert < 2.8$	1M	$0.01125 \cdot 0.192$

Table 4.3: Background Monte Carlo samples. The lepton filter on the $t\bar{t}$ sample applies to the lepton from the W in the decay. Although the multijet sample has filters applied, the cross section for the sample comes with the filter efficiency already applied, so no additional factor is needed.

Lepton filters are applied which cut on the generator level lepton p_T or $|\eta|$ so that computer CPU and storage is not wasted on creating and storing events that will be rejected by the analysis cuts. This greatly increases the number of usable events in a sample. These filters are listed in tables 4.2 and 4.3. The filter efficiency, ε, is defined as the fraction of events remaining after the lepton filter has been applied. This is used to correct the cross section obtained from the generator before the lepton filter is applied. It is this effective cross section, σ^{mc}_{eff}, that is then used as the cross section for the sample. The multijet sample also has cuts on the b quarks at the parton level requiring them to have $p_T > 15$ GeV and $|\eta| < 4.5$. While `PythiaB` has the ability to impose cuts on the stable particles at the end of the b-decay chain the multijet sample used in this analysis

has no cuts applied.

4.3 Monte Carlo Corrections

ATLAS Monte Carlo is generated as described in section 3.4. This is generated with the best knowledge and understanding of the physics and the detector at the time, however it is not suitable for comparison to the data until corrections have been applied. The corrections can be grouped together into two main categories either theoretical corrections (section 4.3.1 and chapter 6) or corrections due to mismodelling of the detector or beam conditions (section 4.3.2 and chapter 5). The corrections discussed in this section are supplied by analysis tools either created centrally, by others involved in the Drell-Yan analysis team, or are too standard and trivial to warrant their own chapter (as is the case with the luminosity normalisation). The following two chapters discuss in detail corrections calculated for this thesis.

4.3.1 Theoretical Corrections

There are two corrections made to the Monte Carlo which are theoretically driven and are needed to have an appropriate normalisation of the Monte Carlo to allow it to be compared to the data.

4.3.1.1 k–Factors

Few of the Monte Carlo samples listed in tables 4.2 and 4.3 are used with the cross section as predicted by the generators directly. Instead, they get scaled to a higher order cross section, the scale factors in this case are called k–factors. The di-boson samples and the Z resonance samples have k–factors applied to them to scale the LO cross section up to that of NNLO. The NNLO cross sections were calculated by `MCFM` [87] for the di-boson samples and `FEWZ` [88] for the Z resonance samples. The k–factors are given by

$$k_f = \frac{\sigma_{NNLO}}{\sigma_{LO}}, \tag{4.1}$$

where σ_{LO} and σ_{NNLO} are the LO and NNLO cross sections respectively for each sample. The top quark sample also has a k–factor applied to it which scales it from NLO to NNLO using cross sections calculated in `HATHOR` [89] and cross-checked with the numerical cross section calculator `Top++` [90, 91]. All of the k–factors used in the analysis are listed in table 4.4. It can clearly been seen that the k–factors can have a large effect, with some samples having up to 60% corrections to the LO cross section. With the k–factors applied an uncertainty on the electroweak and $\bar{t}t$ cross sections of 5% is used [92]. The k-factors partially account for missing higher orders in the perturbative cross section expansion, but kinematic effects are not included as in a full higher order calculation because distributions such as the lepton p_T are not considered. As such, single k–factors applied to the cross section only change the number of predicted events in the sample, the shapes of the distributions do not change. This is not the case for the k–factors used for the low mass signal sample which has NNLO k–factors [93] applied to it that are dependant on the mass

and rapidity of the γ^*. These $k-$factors were calculated using VRAP [94], which calculates the cross sections at LO and NNLO analytically. The ratio of these cross sections are then provided as the $k-$factor to apply to the Monte Carlo, these $k-$factors are shown in figure 4.1 as a function of the invariant mass and rapidity of the Z/γ^*.

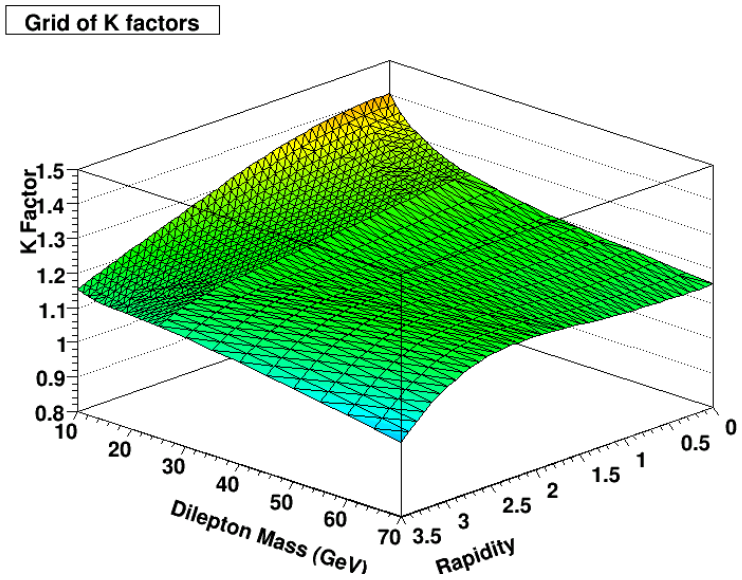

Figure 4.1: NNLO $k-$factors [93] for the low mass signal Monte Carlo sample as a function of invariant mass and rapidity calculated with VRAP.

Sample	$k-$Factor	Order	Source	σ^{mc}_{eff} $[nb]$
Signal ($15 < M_{\mu\mu} < 60$ GeV)	see figure 4.1	NNLO	VRAP	$0.498 \cdot k_f$
Signal ($M_{\mu\mu} > 60$ GeV)	1.155	NNLO	FEWZ	0.989
Multijet ($c\bar{c} + b\bar{b}$)	-	-	-	2.727
$Z \to \tau\tau$ ($M_{\tau\tau} > 60$ GeV)	1.158	NNLO	FEWZ	0.989
$Z/\gamma^* \to \tau\tau$ ($10 < M_{\tau\tau} < 60$ GeV)	-	-	-	3.455
$W \to \mu\nu$	-	-	-	8.938
$t\bar{t}$	1.146	NNLO	HATHOR	90.565×10^{-3}
WW	1.520	NNLO	MCFM	17.460×10^{-3}
ZZ	1.292	NNLO	MCFM	1.261×10^{-3}
WZ	1.593	NNLO	MCFM	5.543×10^{-3}

Table 4.4: Table showing the $k-$factors for each sample. The effective cross section, σ^{mc}_{eff}, for each sample is also listed, this is given by the generator cross section multiplied by any filter efficiencies and $k-$factors.

4.3.1.2 Luminosity Normalisation

The integrated luminosity of the Monte Carlo samples ($\mathcal{L}^{mc}$) must be normalised to that of the data ($\mathcal{L}^{data}$). Table 4.4 lists the Monte Carlo samples used and the effective cross sections of the samples. Typically with Monte Carlo generation as many events as possible are generated to give a reduced statistical uncertainty. The luminosity correction is an

event weight given by

$$w_{\mathcal{L}} = \frac{\mathcal{L}^{data}}{\mathcal{L}^{mc}} \tag{4.2}$$

$$= \mathcal{L}^{data} \cdot \frac{\sigma_{eff}^{mc}}{N^{mc}}, \tag{4.3}$$

where σ_{eff}^{mc} is the effective cross section of the Monte Carlo sample as listed in table 4.4 and N^{mc} is the number of generated events before any selection has been made.

4.3.2 Mismodelling

Detector effects concerned with the mismodelling of the detector efficiency are largely corrected for using scale factors, s_f, which are defined as

$$s_f = \frac{\varepsilon_{data}}{\varepsilon_{mc}}, \tag{4.4}$$

where ε_{data} is the efficiency in the data and ε_{mc} is the efficiency modelled in the Monte Carlo. Scale factors are determined with uncertainties which allow the central values to be used in the selection with the uncertainties propagated through to the measured differential cross section. Scale factors are determined for all efficiencies relevant to the analysis.

4.3.2.1 Muon Reconstruction Efficiency

The reconstruction efficiencies of the muons in the Monte Carlo are corrected to that of the data with scale factors calculated using a tag-and-probe method at the Z resonance [79,95]. As discussed in section 3.2.6, these are determined by reconstructing one of the $Z \to \mu\mu$ decay muons in both the inner detector and the muon spectrometer. The other is identified in just one of the systems so that the reconstruction efficiency in the other can be probed. The efficiency corrections to the Monte Carlo are provided as a scale factor dependant on the η and p_T of each muon using a centrally produced package[1]. To obtain the weight to be applied to the event the scale factors for the two muons in the event are multiplied together. The tool also provides systematic and statistical errors for the scale factors. Figure 4.2 shows the scale factors as a function of muon p_T for the barrel ($|\eta| < 1.05$) and end-caps ($|\eta| \geq 1.05$). As can be seen for both, the scale factors are very close to 1, demonstrating the efficiencies were well modelled in the Monte Carlo at production. Figure 4.2 also demonstrates that for this analysis there is no p_T dependence on the scale factors.

4.3.2.2 Trigger Efficiency

The trigger efficiency for the single muon trigger `EF_mu10_loose` for `muid` muons with $p_T > 12$ GeV was estimated using a tag and probe method at the Z resonance by the ATLAS low mass Drell-Yan group [1]. Efficiencies and scale factors were calculated as a function of the muon p_T and η, separately for positively and negatively charged muons.

[1] `MuonEfficiencyCorrections-01-01-00`

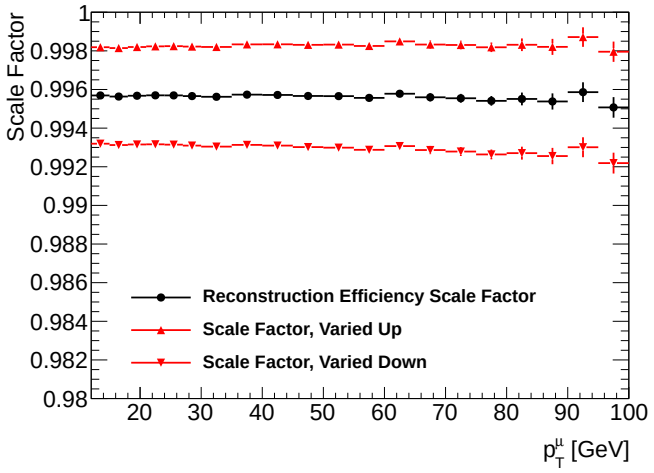

(a) Barrel

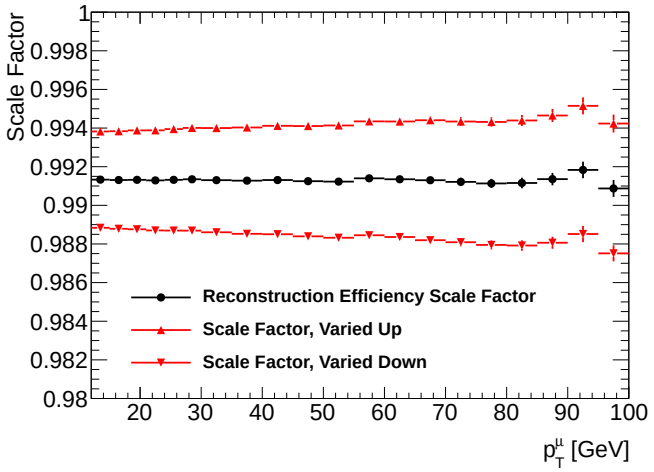

(b) End-caps

Figure 4.2: Muon reconstruction scale factors showing the shifts due to the combined statistical and systematic errors.

Figure 4.3 shows an example of the trigger efficiency for Monte Carlo and data with the corresponding scale factor. This is as a function of p_T for muons in the end-cap with $+1.2 < \eta < +1.4$. The importance of separating the charge of the muons can be seen in the figure. It can be seen from figure 4.3 that the efficiency at this η is high, typically over 90%, and relatively flat as a function of muon p_T. The data used in this analysis was taken during seven data taking periods (labelled D-J). The total trigger efficiency was measured in the barrel and endcap for each of these data taking periods. These can be seen in table 4.5.

Both a statistical and systematic uncertainty is associated with the trigger efficiency scale factors. Systematic uncertainties for the scale factors are estimated by varying the tag and probe selection used in the efficiency study.

In the low mass Drell-Yan analysis, the scale factors were retrieved for each of the two muons in the event and then multiplied to give a weight for the event. This gives the scale factor to correct to the efficiency of the di-muon `EF_2mu10_loose` trigger. Figure 4.4 shows the average scale factor from the individual muon as a function of muon p_T for selected

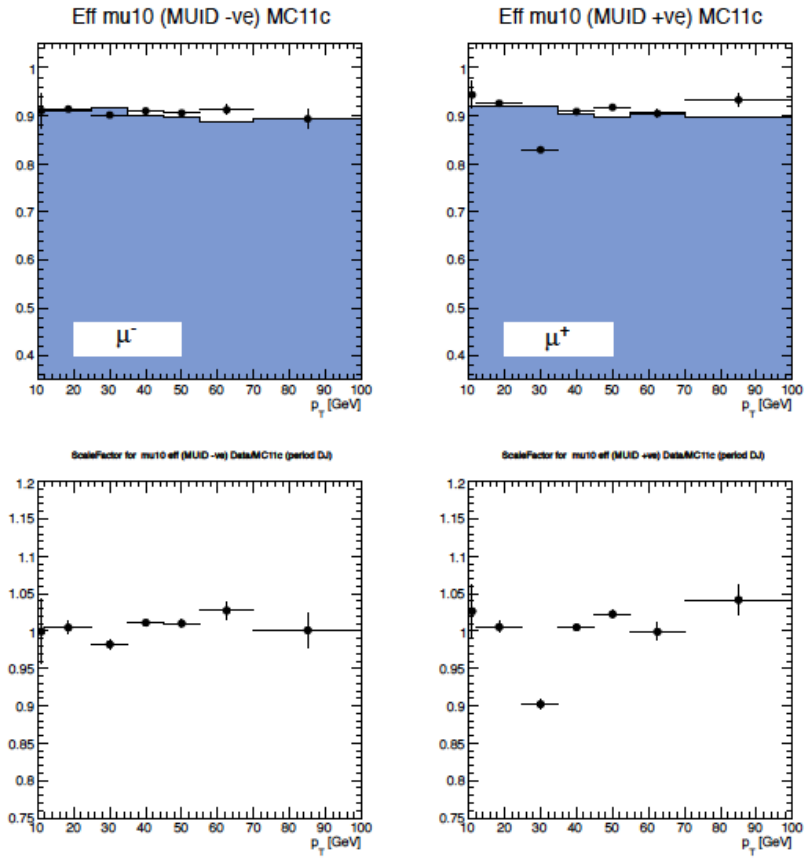

Figure 4.3: Example of the trigger efficiency (top) and scale factors (bottom) as a function of p_T for $+1.2 < \eta < +1.4$ for positive (right) and negative (positive) muons. Only statistical errors are shown [1].

Period	Barrel	End-cap
D	72.4 ± 0.2	89.9 ± 0.1
E	71.6 ± 0.4	90.0 ± 0.3
F	70.9 ± 0.2	91.2 ± 0.1
G	71.0 ± 0.1	91.4 ± 0.1
H	76.0 ± 0.2	92.0 ± 0.1
I	76.0 ± 0.1	92.1 ± 0.1
J	76.4 ± 0.2	91.6 ± 0.1
Monte Carlo	73.2 ± 0.0	90.7 ± 0.0

Table 4.5: Trigger efficiency for $p_T > 12$ GeV muons for Monte Carlo and each data period considered in 2011 [1].

muons. The barrel and end-caps as shown separately. Again the good modelling of the trigger in the Monte Carlo is shown by the average scale factors being close to 1. The uncertainties on the average scale factors shown in figure 4.4 are the RMS spread of the scale factors. It can be seen that the average scale factor is fairly constants in p_T within the uncertainties.

Figure 4.5 again shows the average scale factors from the individual muon as a function of muon p_T. But here the shifts to the scale factors from the statistical uncertainty and the total uncertainty (the systematic and statistical uncertainty in quadrature) are shown.

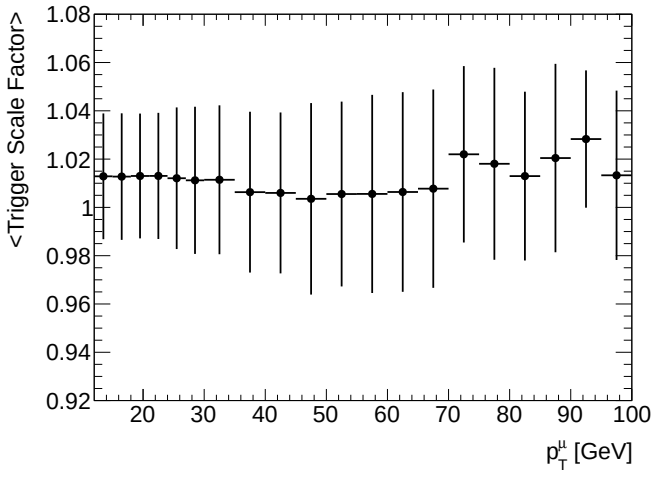

(a) Barrel

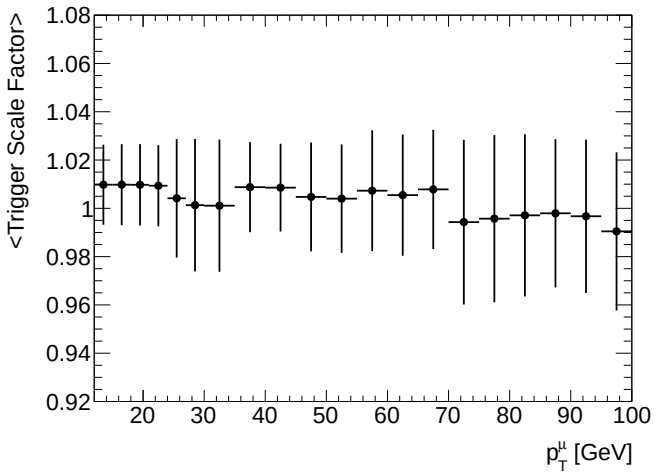

(b) End-caps

Figure 4.4: Average muon trigger efficiency scale factors for the `EF_mu10_loose` *trigger as a function of muon p_T for selected Drell-Yan events. Muons in the barrel and end-caps are shown in figures (a) and (b) respectively. The uncertainties show the RMS spread of the scale factors in each bin.*

It can clearly be seen that statistical uncertainty is the dominate uncertainty on the scale factors. This uncertainty from the trigger scale factors becomes the largest uncertainty on the measured cross section in the majority of mass bins.

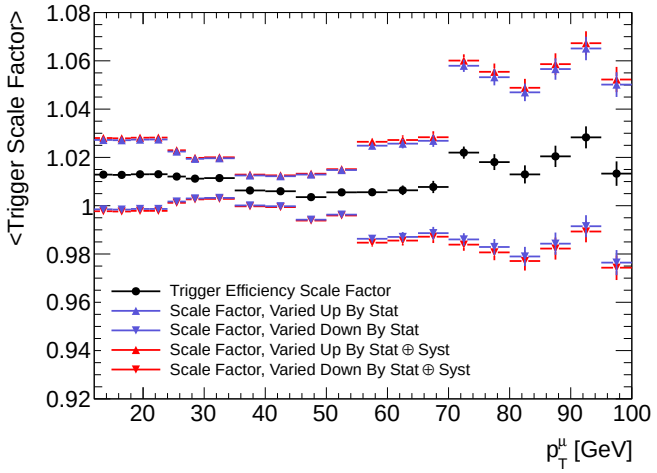

(a) Barrel

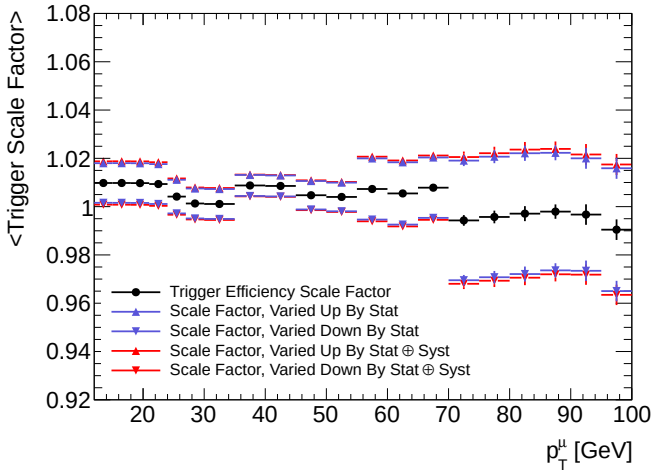

(b) End-caps

Figure 4.5: Average muon trigger efficiency scale factors for the `EF_mu10_loose` *trigger as a function of muon p_T for selected Drell-Yan events. Muons in the barrel and end-caps are shown in figures (a) and (b) respectively. The effect of shifting the scale factors up and down by the statistical and total uncertainty on the scale factor are shown.*

4.3.2.3 Muon Isolation Efficiency

Scale factors were also used to correct the Monte Carlo isolation efficiency to that of the data. These scale factors, defined as in equation 4.4 are calculated for `muid` muons for this analysis. Details are given in chapter 5, where the efficiency in data and Monte Carlo is calculated using a tag-and-probe method using Z resonance decays.

4.3.2.4 Muon Momentum Resolution and Scale Corrections

The momentum of the muons is corrected to better model the resolution seen in the detector. Again, these corrections are provided from a centrally produced package[2] and are calculated using a tag-and-probe method at the Z resonance [76]. The scale corrections correct for shifts in the reconstructed M_Z value, whereas the resolution corrections randomly shift the momenta of the muons to increase the width of the Z resonance. Rather than applying a scale factor to weight the whole event, muon momentum corrections smear the p_T of the muons, the 4-vector of the muon is then recalculated with this new p_T value. As well as the smearing a shift is applied to better describe the muon momentum scale. Figure 4.6 shows the effect of the muon momentum corrections to the analysis.

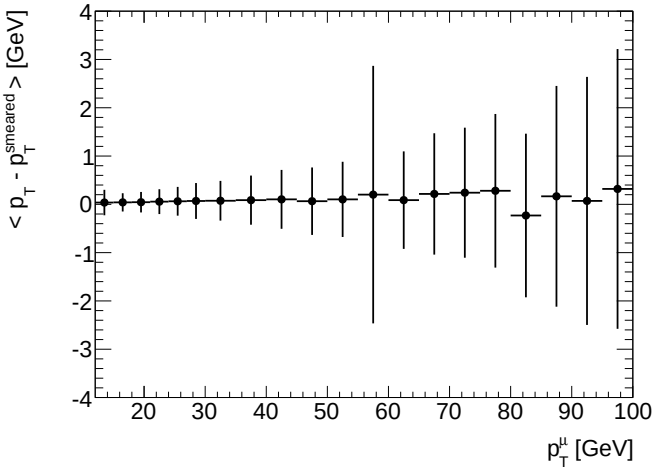

Figure 4.6: Plot showing the average difference in muon p_T due to the smearing as a function of muon p_T. The shift from 0 shows the effect of applying the muon momentum scale shift. The error bars represent the RMS in each bin.

4.3.2.5 Pile-up Reweighting

The affect of pile-up also needs to be considered. ATLAS Monte Carlo is generated with a minimum bias sample overlaid onto the hard scatter, as described in section 3.4. A sample is split up into four periods each of which reflect beam conditions from different parts of the 2011 data taking. Different detector conditions are also reflected in the different Monte Carlo periods. The pile-up reweighting tool[3], reweights the distribution of the average number of interactions per bunch crossing, $\langle\mu\rangle$, in the Monte Carlo to that of the data. It does this separately for each of the Monte Carlo periods, returning an event weight

[2] `MuonMomentumCorrections-00-05-00`
[3] `PileupReweighting-00-02-01`

based both on the simulated value of $\langle\mu\rangle$ and on the Monte Carlo period the event was generated in. Figure 4.7 shows the affect of the pile-up reweighting on the number of primary vertices in the event.

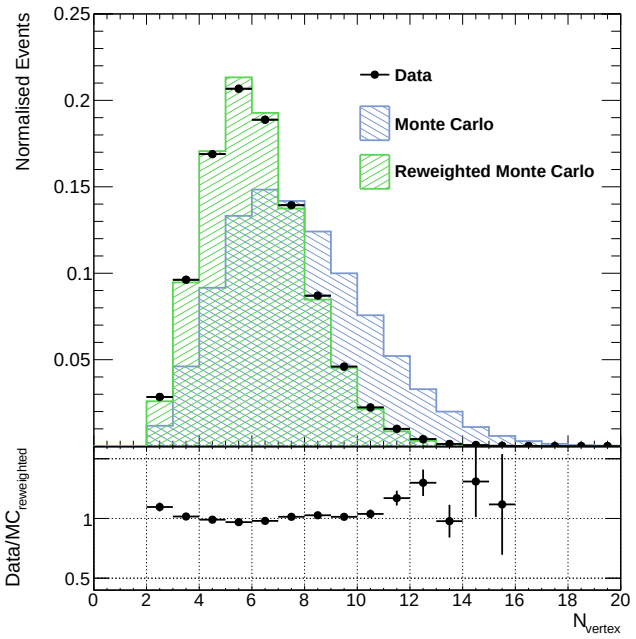

Figure 4.7: Effect of reweighting the $\langle\mu\rangle$ distribution of the Monte Carlo showing the distribution of the number of primary vertices before and after reweighting.

4.4 Event Selection

The aim of the event selection is to select Drell-Yan events while rejecting as much background as possible. The effect of applying each cut in order can been seen in the cutflow tables in chapter 7. Events are selected with the following requirements:

- Good Runs List (GRL)
- `EF_2mu10_loose` trigger
- Reject LAr Errors
- At least 2 muons in the event with opposite charge
- A primary vertex with ≥ 3 tracks
- Muon $|\eta| < 2.4$
- Leading muon $p_T > 15$ GeV
- Sub-leading muon $p_T > 12$ GeV
- Track quality cuts
- Muon isolation $\sum p_T^{\Delta R=0.4}/p_T^{\mu} < 0.18$
- 26 GeV $< M_{\mu\mu} <$ 66 GeV

The Good Runs List (GRL) is a list of luminosity blocks in the data that have sufficient quality to be used in a physics analysis. The GRL used in this analysis contains events suitable for Z and $W^{\pm}$ like analyses. A luminosity block is a time interval in which the integrated luminosity is calculated. Luminosity blocks are of the order of one minute long, but vary due to the instantaneous luminosity of the beam falling during a run [96]. Different GRLs are made for different physics analysis groups as they reflect the operation of the different sub-detectors in ATLAS, and not all analyses would be affected by a problem in only one sub-detector. The cut requiring a good luminosity block only affects the data. This analysis uses the GRL[4] created for the ATLAS Standard Model group.

The Trigger requirement that the `EF_2mu10_loose` trigger has fired is a powerful discriminating cut that quickly removes unsuitable events. The trigger is discussed in more detail in section 3.2.7.

Rejection of LAr Errors allows events where the liquid argon calorimeters have noise bursts during data taking to be rejected. As these noise bursts are very short the events are removed individually rather than by the GRL. Removal of the whole luminosity block would be unnecessary and remove data that is otherwise suitable for analysis. Again this cut only effects the data selection as noise bursts are not modelled in the Monte Carlo samples. Once the GRL and trigger selection has been made, the rejection of LAr errors reduces the data sample by 0.4%.

Number of Muons is required to be at least two, where the muons are combined muons from the `muid` collection. From these two or more muons the two with the highest p_T are selected as the Drell-Yan candidate muons. These candidates are then required to have opposite electric charge, as expected in a Drell-Yan event. Only these muons have further cuts applied to them. The number of muons after the full selection has been applied is shown in figure 4.8. As would be expected the vast majority of events have only two muons.

Vertex Requirements that there is at least three tracks associated to the vertex ensures that the vertex is well reconstructed. In addition to a cut on the number of tracks to the vertex it is ensured that the two Drell-Yan candidate muons in the event are two of the tracks associated with the vertex. Tracks associated to the vertex are compared to the ID track of each of the muons. If both the muons are matched the event is accepted. Figure 4.9 shows the distribution of the number of primary vertices after the full selection cuts have been applied. It can be seen that the modelling of the distribution for $N_{vertex} > 10$, mostly likely due to the effect of pileup.

[4] `data11_7TeV.periodAllYear_DetStatus-v36-pro10_CoolRunQuery-00-04-08_WZjets_allchannels.xml`

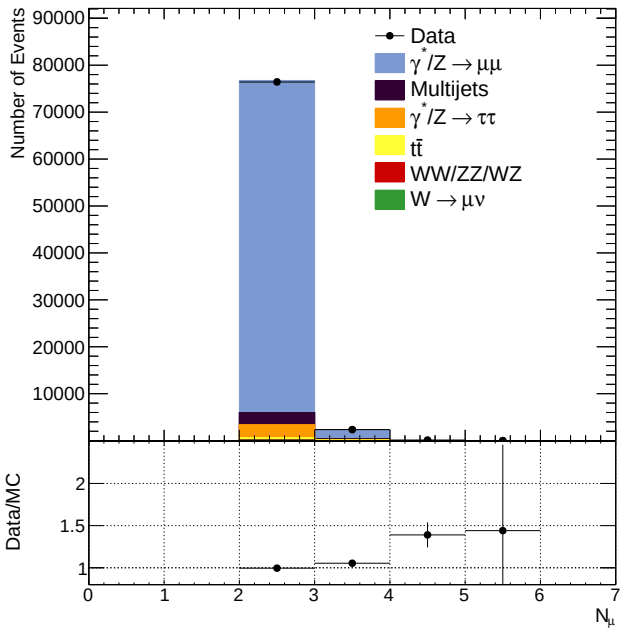

Figure 4.8: Number of combined `muid` *muons, after all selections are made.*

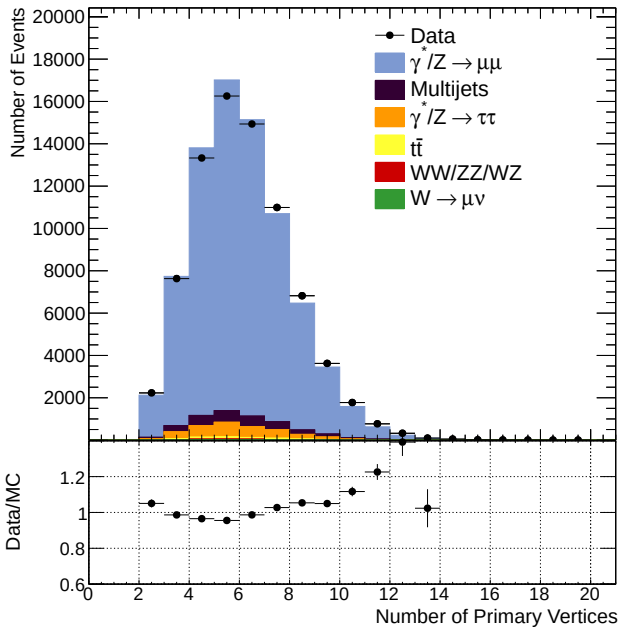

Figure 4.9: Number of primary vertices, after all selections are made.

Fiducial Volume Cuts are the cuts on the muon p_T and η. The η cut ensures that the muons are well within the acceptance of the inner detector which extends out to $|\eta| < 2.5$. The p_T cuts applied to the muons need to be above the turn on curve of the trigger, in the plateau of the trigger efficiency, so that the trigger efficiency can be relied on. As the trigger requires two muons with $p_T > 10$ GeV, the selection requirement of $p_T > 12$ GeV and $p_T > 15$ GeV are suitable for this. The cuts are asymmetric in order to avoid the region of phase space where $M_{\gamma^*} \approx 2p_T^{\mu}$ where perturbative QCD calculations are unstable and produce unphysical predictions at leading order. The muon p_T and η distributions can be seen in chapter 7.

Track Quality Cuts are recommended cuts presented by the Muon Combined Performance (MCP) group in ATLAS and are an updated version of the selection outlined in [79]. These reflect the number of hits a muon would be expected to have in the inner detector, they also take into account that the detector on occasions suffers from inefficiencies due to certain sensors not being operational. The recommended cuts are:

- Number of b-layer hits > 0, unless no b-layer hit is expected
- Number of pixel hits plus the number of crossed dead pixel sensors > 1
- Number of SCT hits plus the number of crossed dead SCT sensors > 5
- Number of pixel holes and number of SCT holes < 3
- A successful extension into the TRT where expected

Figure 4.10 shows the distribution of the number of hits and crossed dead sensors for the pixel and SCT detectors before the track quality cuts are made. All other event selections have been applied. As discussed in chapter 3 the pixel detector has three layers in the barrel and each end-cap. The pixel detector is designed to give three precision measurements, but muons traversing both the barrel and the end-cap (being deflected by the magnetic field) can cross more than six layers in the pixel detector due to the overlapping arrangement of modules to provide a hermetic coverage. The SCT is designed to give eight precision measurements. The SCT has four double sided layers in the barrel and nine double sided layers in each end-cap. As well as muons traversing both the barrel and end-cap of the SCT, again, the overlapping arrangement of the SCT modules would also allow additional hits within a single region. The distributions in figure 4.10 demonstrates these features. The figure also demonstrates the poor modelling of the Monte Carlo in the less populated parts of the distributions.

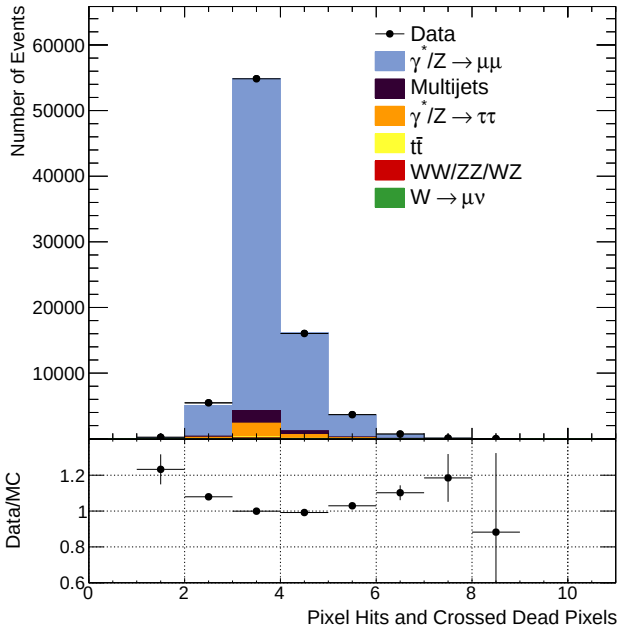

(a) Pixel

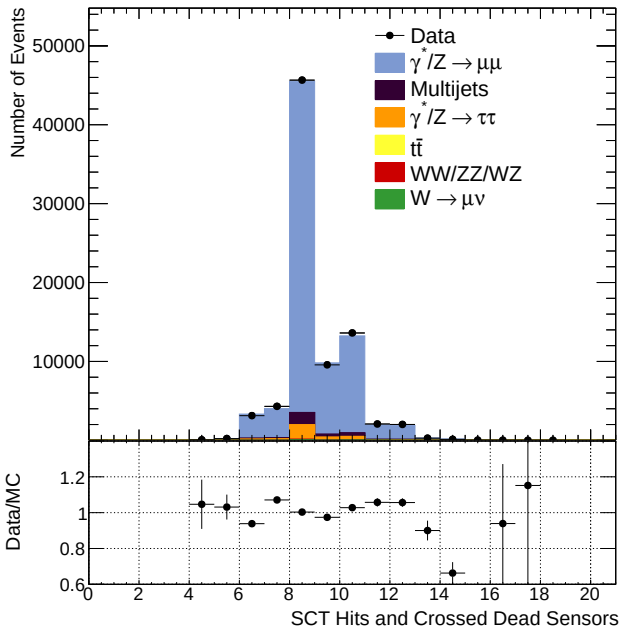

(b) SCT

Figure 4.10: (a) Number of pixel hits and crossed dead pixels and the (b) Number of SCT hits and crossed sensors. Both are shown for the leading muon before the track quality cuts are applied, all other cuts have been applied.

Muon Isolation is a powerful requirement to reject background multijet events. Muons produced via the Drell-Yan process will have isolated muons, whereas muons produced as part of a jet will not, for example muons from semi-leptonic b and c meson decays will be produced with nearby hadronic activity. This manifests itself as increased deposits of energy in a cone of ΔR around the muon in the calorimeters, or an increase in the amount of summed p_T from tracks around the muon in the inner detector. Four quantities are used to quantify the degree of isolation,

$$\texttt{PtConeX} = \sum p_T^{\Delta R}, \tag{4.5}$$

$$\texttt{PtRatioX} = \sum p_T^{\Delta R}/p_T^{\mu}, \tag{4.6}$$

$$\texttt{EtConeX} = \sum E_T^{\Delta R}, \tag{4.7}$$

$$\texttt{EtRatioX} = \sum E_T^{\Delta R}/p_T^{\mu}, \tag{4.8}$$

where `X` are the different cone sizes, `20,30,40`, for $\Delta R = 0.2, 0.3, 0.4$ respectively. `PtConeX` is the sum of the p_T of all the tracks in a cone of ΔR associated to the same vertex as the muon, this is used without the inclusion of the p_T of the original muon in the sum. `PtRatioX` is the `PtConeX` variable divided by the p_T of the muon. The `EtConeX` and `EtRatioX` variables are constructed in a similar way, but consider the sum of the E_T in the calorimeter around the muon. Only the track based isolation has been examined as a way to impose isolation on the muons as it is effected less by pile up than the calorimetric isolation variables. To settle on an isolation cut the effect of the cut on the multijet background rejection and the signal efficiency is considered which is estimated using Monte Carlo. When the two Drell-Yan muons fall in each others cones then the p_T of the other muon is removed from the sum. Figure 4.11 shows these two quantities plotted against each other for different cuts on `PtConeX` and `PtRatioX`. The optimal cut on the isolation was determined to be `PtRatio40` < 0.18. This gives good background rejection of 96.4% while maintaining a high signal efficiency of 95.7%.

This is demonstrated in figure 4.12 which shows the `PtRatio40` distribution before the isolation requirements are made. It can be seen that the majority of the signal lies below the `PtRatio40` < 0.18 cut, while the majority of the multijet background lies above it. In this figure the multijet background is estimated with the template fit method described in chapter 6.

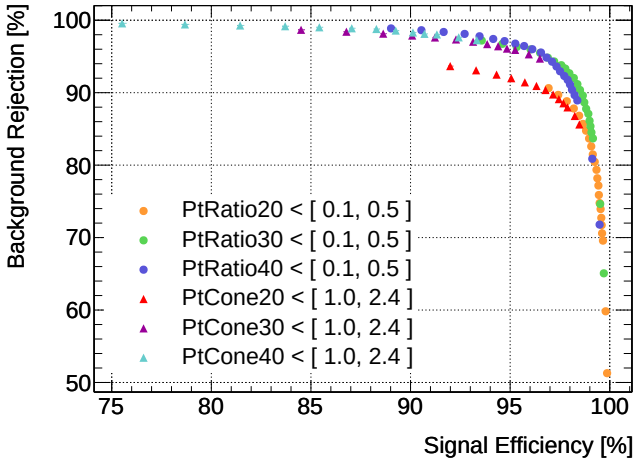

(a)

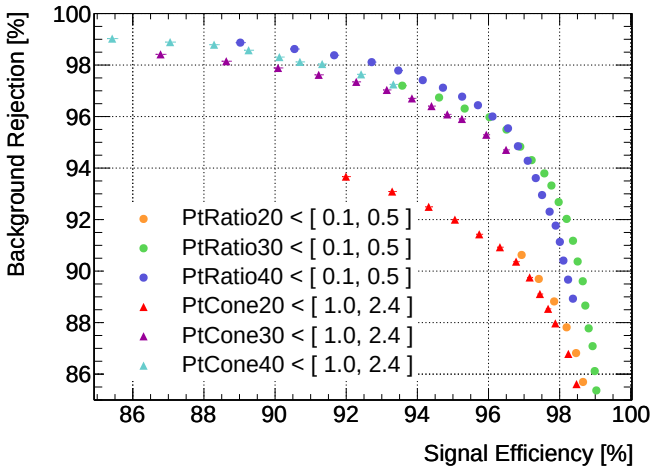

(b)

Figure 4.11: (a) Variation of multijet rejection versus signal efficiency for $\Delta R = 0.2, 0.3, 0.4$ *with* `PtCone` *and* `PtRatio`*, for a selection of cut values. (b) close-up of region where the optimal cut lies.*

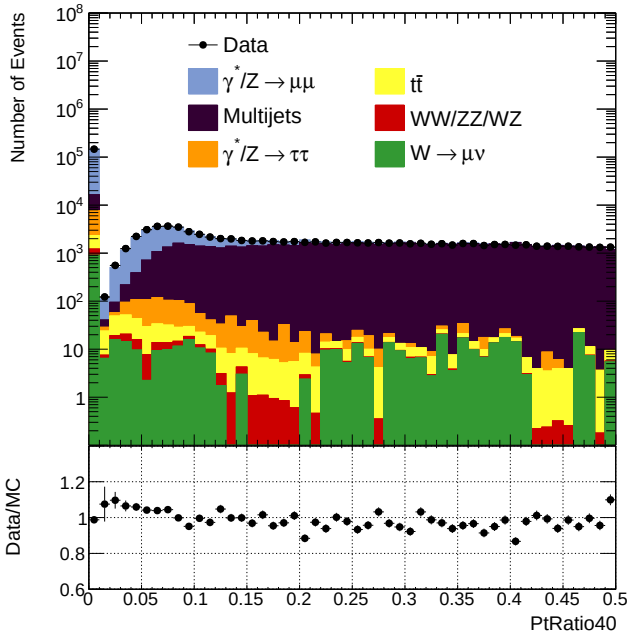

Figure 4.12: The `PtRatio40` *spectrum for both muons. The full event selection has been made apart from the isolation cut of* `PtRatio40` < 0.18. *The multijet background is estimated using the template fit method.*

The Invariant Mass Range was chosen to be 26 GeV < $M_{\mu\mu}$ < 66 GeV. The upper limit is in the region where the weak component of the cross section becomes more dominant than the electromagnetic part, as seen in figure 2.8. It is also used by the ATLAS 2010 inclusive Z cross section measurement [92] as the minimum mass cut, allowing a smooth transition between two ATLAS measurements. The lower mass cut is motivated by keeping the statistics high in each bin of the $M_{\mu\mu}$ spectrum. Due to the muon p_T cuts, statistics quickly decrease for $M_{\mu\mu} < 26$ GeV. High statistics are important in the low $M_{\mu\mu}$ region where the multijet background is at its largest and confidence must be had that it is controlled correctly. Figure 4.13 shows the di-muon mass spectrum with all analysis cuts applied apart from the $26 < M_{\mu\mu} < 66$ GeV mass cut. The effect of the muon p_T cuts can clearly be seen for $M_{\mu\mu} < 30$ GeV and the Z boson resonance at $M_{\mu\mu} > 66$ GeV

4.4.1 Event Yield

A stable selection criteria should produce a constant yield across the data taking period. This particularly demonstrates that the selection is not effected by pile-up which became more prevalent as the year progressed. The event yield is defined as,

$$y = \frac{N}{\mathcal{L}}, \tag{4.9}$$

where N is the number of data events selected using the criteria described in section 4.4 and $\mathcal{L}$ is the integrated luminosity. Figure 4.14 shows the yield as a function of run number, n_R. ATLAS assigns a run number every time the detector is in a stable data taking condition. Run numbers are assigned regardless of the LHC beam conditions, as such the large gaps between run numbers seen in figure 4.14 are largely due to ATLAS runs where there were no stable beams. The average yield is obtained by fitting a flat line to the yield as a function of run number, as shown in figure 4.14. A yield of 47.37 ± 0.20 nb^{-1} is obtained, with a χ^2 per degree of freedom, ndf, for the fit of 1.1.

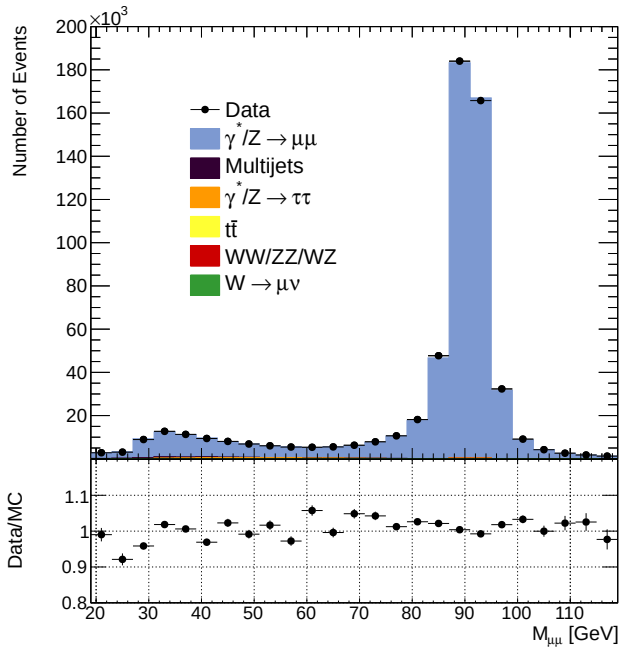

(a) Di-muon mass distribution with a linear scale

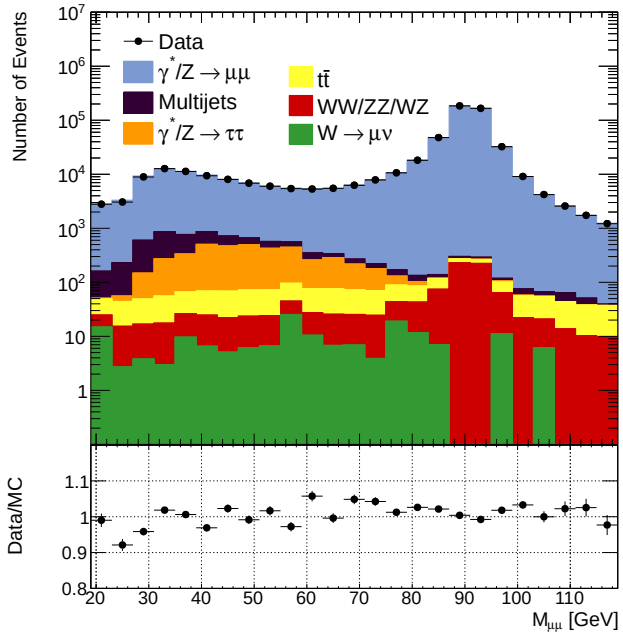

(b) Di-muon mass distribution with a log scale

Figure 4.13: Di-muon mass distribution with. All selection cuts apart from the mass cuts of $26 < M_{\mu\mu} < 66$ *GeV are applied.*

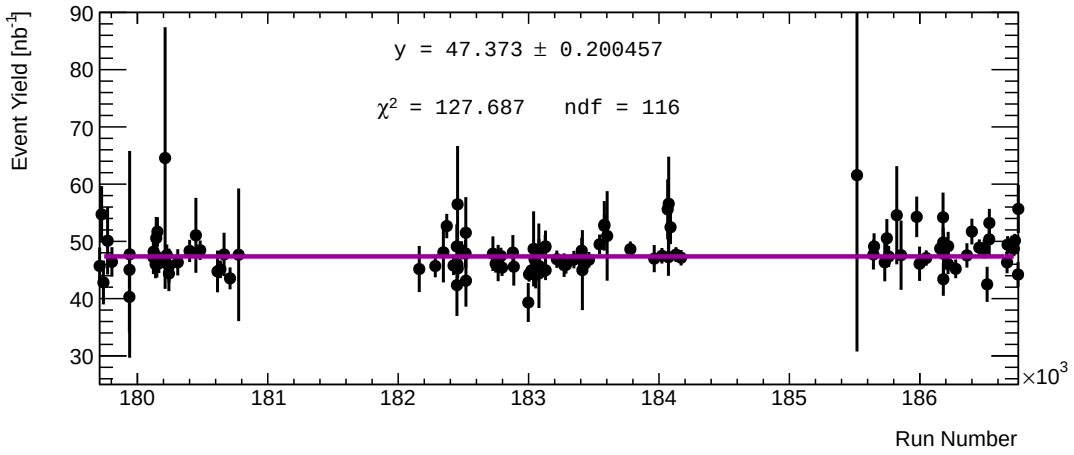

Figure 4.14: Event yield as a function of run number.

Chapter 5

Muon Isolation Efficiency

As described in chapter 4 the selected events are required to have two isolated muons with `PtRatio40` ≥ 0.18. The `PtRatio40` variable is the sum of the p_T of tracks from the same vertex in a cone of $\Delta R = 0.4$ expressed as a fraction of the p_T of the muon itself. As the muons produced by the Drell-Yan process and the processes that form the electroweak backgrounds are the sole product of the decay (or produced with undetectable neutrinos) they are not surrounded by other tracks in the inner detector. In contrast, the muons produced in multijet processes are produced with a large number of surrounding tracks. This was seen from the isolation spectrum in figure 4.12. As such, a cut upon `PtRatio40` is a powerful cut for reducing the multijet background.

The isolation efficiency is measured in data and Monte Carlo as a function muon transverse momentum, p_T^μ. This allows scale factors valid down to $p_T^\mu = 12$ GeV to be calculated for `muid` muons. To do this a tag and probe method has been used using $Z \to \mu\mu$ resonant decays which is an ideal region in which to assess the muon isolation efficiency. There is an abundance of isolated muons coming from the decay of the Z which dominates over any background processes in the mass range of 66 GeV $< M_{\mu\mu} <$ 116 GeV. As described in section 4.3.2 scale factors are the ratio of the efficiency measured in the data and the Monte Carlo, so both need to be evaluated.

5.1 Z Selection

The Z event selection is based on that used by the 2010 ATLAS inclusive Z analysis [92], with the following requirements:

- Good Runs List
- `EF_mu18` OR `EF_mu18_MG` trigger
- 2 `muid` muons
- ≥ 1 Primary vertex with ≥ 3 tracks
- $z_{vtx} < 200$ mm
- Muon $p_T > 12$ GeV

- Muon $|\eta| < 2.4$
- Oppositely charged muons
- Track Quality Cuts
- 66 GeV $< M_{\mu\mu} <$ 116 GeV.

This selection was made on the data and Monte Carlo samples for the signal and background samples for multijet, $Z/\gamma^* \to \tau\tau$ and $W \to \mu\nu$ processes. Many of the cuts are similar to or the same as the cuts in the low mass Drell-Yan selection. The z_{vtx} variable is the z position of the primary vertex with respect to the nominal interaction point. The `EF_mu18` trigger is a single muon trigger requiring that the event has a muon with a $p_T > 18$ GeV, the `EF_mu18_MG` trigger is similar but using the `MuGirl` algorithm. A logical OR of the two triggers is used in order to maximise efficiency.

The total number of selected events for the data and each of the Monte Carlo samples is given in table 5.1 where it can clearly be seen that only a small amount of background is selected with respect to signal events. For this study the multijet background is estimated by normalising the Monte Carlo sample to the data in the non-isolated region (for events where both muons have `PtRatio40` ≥ 0.18). The normalisation factor was found to be 0.766 ± 0.013. More sophisticated techniques are discussed in chapter 6, but as the amount of multijet background in the Z peak mass range is very small, this simpler, if less accurate, method was deemed sufficient.

Sample	Events
Data	624492
$\gamma^*/Z \to \mu\mu$	627714
Multijets	519
$\gamma^*/Z \to \tau\tau$	437
$W \to \mu\nu$	105

Table 5.1: Number of events selected using the Z peak selection.

Figures 5.1 to 5.4 shows control plots of the selected events. The distributions are shown both on a linear scale, and on a log scale so that the background contributions can be seen. Figure 5.1 shows the muon η distribution and demonstrates good agreement between the data and the Monte Carlo, it can be seen that the background contributions are relatively flat as a function of muon η. Figure 5.2 shows the muon p_T which demonstrates less good agreement. The "S" shape seen in the ratio plot is due to a shift in the muon p_T spectrum in the Monte Carlo with respect to the data. The reason for this shift is not currently known but is probably due in part to the modelling of the boson p_T in the Monte Carlo. It is in any case small enough that it is not expected to have an effect on the calculated isolation efficiencies. As would be expected the backgrounds are more prominent a low p_T.

Figure 5.3 shows the invariant di-muon mass distribution. This shows a good agreement between the data and Monte Carlo. The background contribution can be seen to reduce slightly with increasing mass. Figure 5.4 shows the di-muon rapidity distribution. Agreement between the data and the Monte Carlo is seen to be good at central rapidities,

but the modelling is less good at the edges of the distribution. The asymmetry in the background distribution is most likely due to the low statistics of the Monte Carlo.

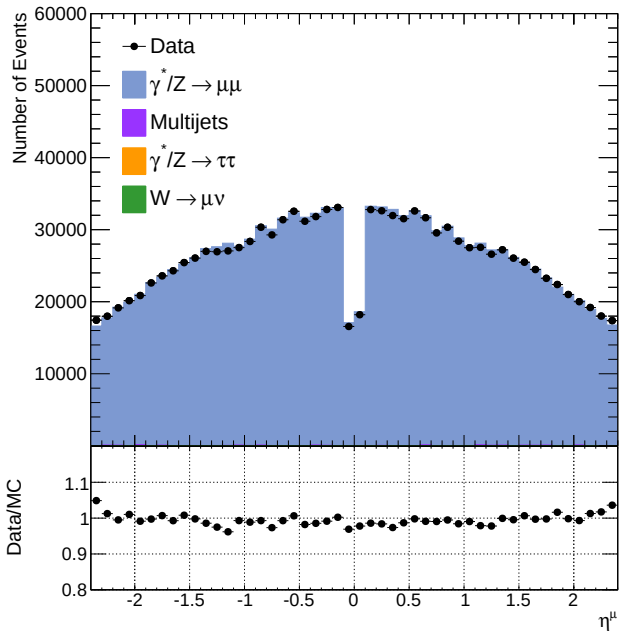

(a)

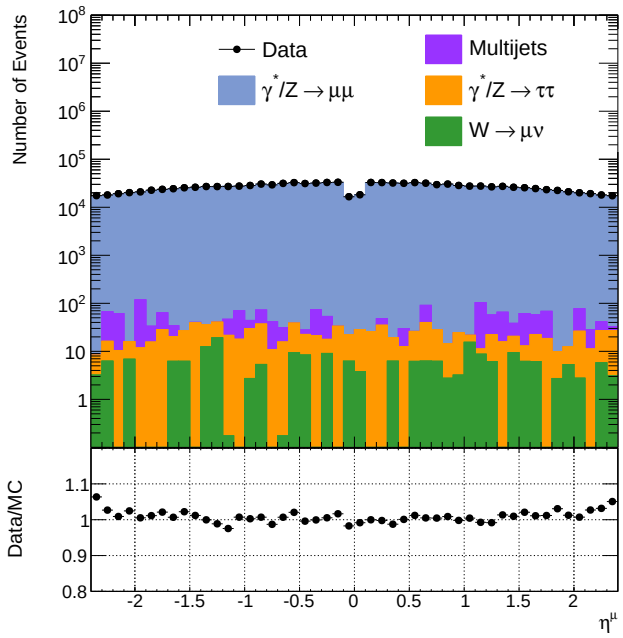

(b)

Figure 5.1: Muon η distribution for the Z selection. Shown on a linear (a) and log (b) scale.

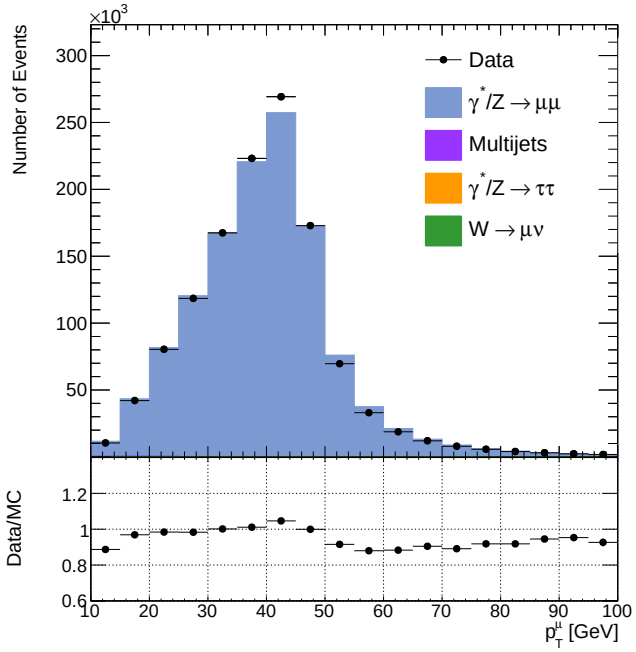

(a)

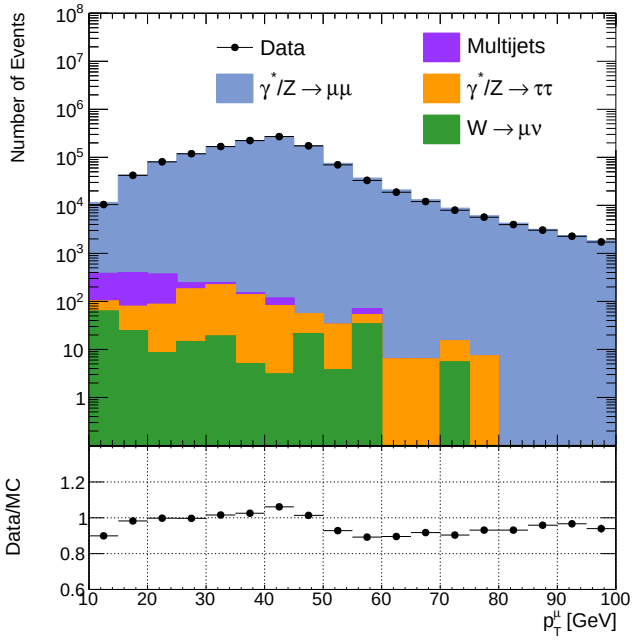

(b)

Figure 5.2: Muon p_T distribution for the Z selection. Shown on a linear (a) and log (b) scale.

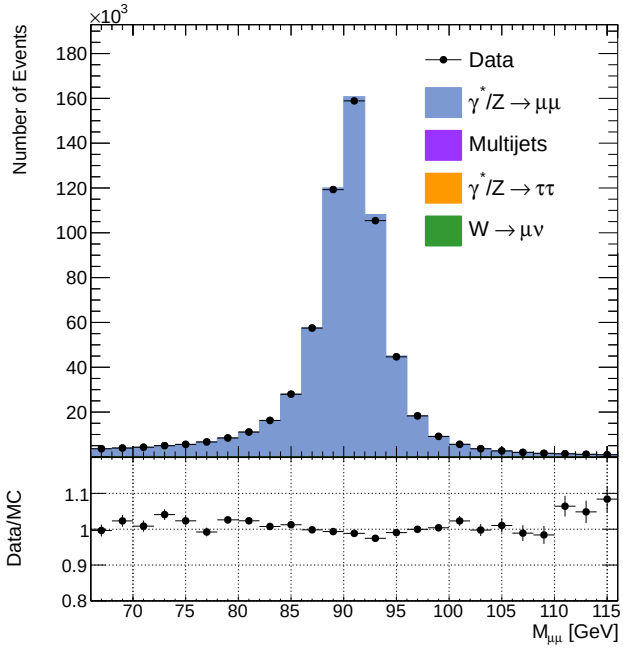

(a)

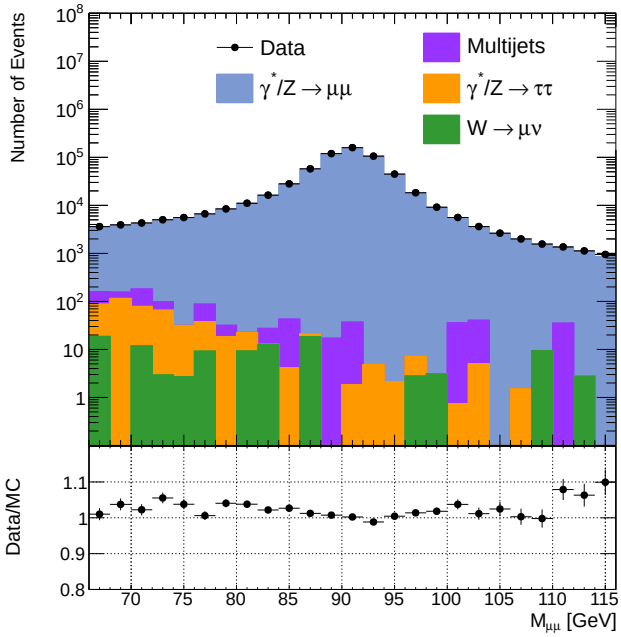

(b)

Figure 5.3: Di-muon invariant mass distribution for the Z selection. Shown on a linear (a) and log (b) scale.

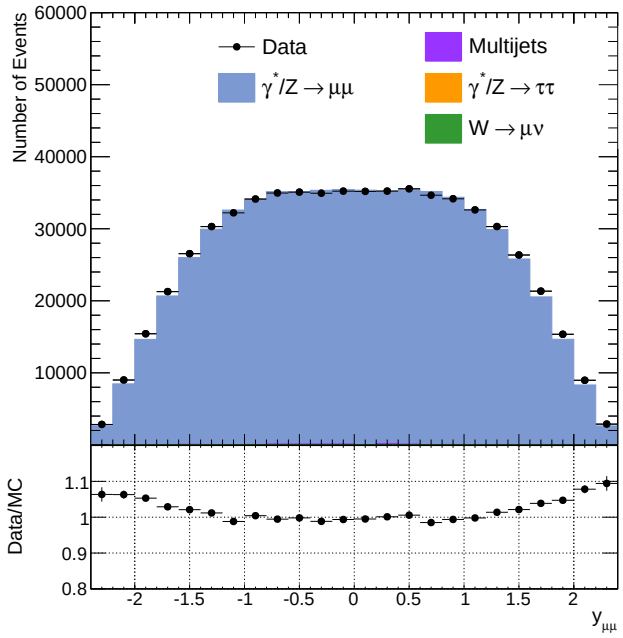

(a)

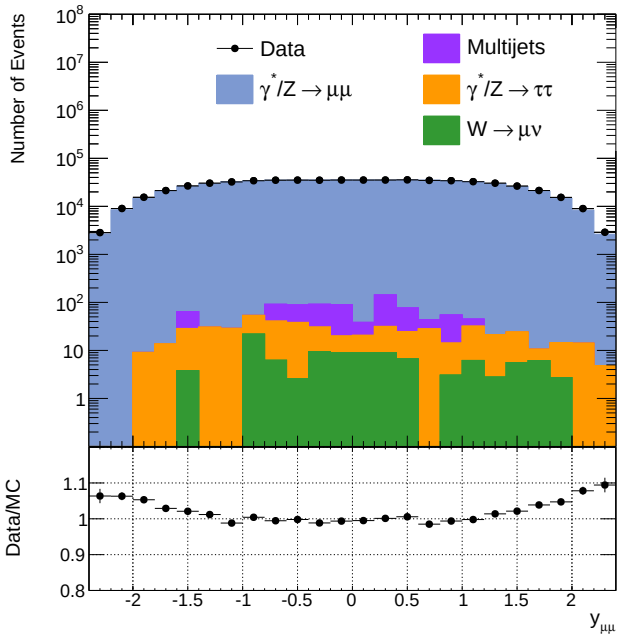

(b)

Figure 5.4: Di-muon rapidity distribution for the Z selection. Shown on a linear (a) and log (b) scale.

5.2 Tag and Probe Method

The tag and probe method exploits the kinematic correlations between the two muons produced by the Z boson. The idea is to select one muon with a tight criteria (the tag), and take advantage of the correlations to measure the efficiency of interest with the second muon (the probe). In the case of the isolation efficiency, if both muons are from the Z decay they should have similar levels of isolation. By requiring a tag muon which is isolated (`PtRatio40` < 0.18 in our case) the probe associated with it should be too. Further cuts are applied to select the tag and probe to ensure a very pure Z sample, the cuts are again based on those used to calculate the isolation efficiency for the 2010 Z analysis [92]. It should be noted that no isolation requirement was made to the sample before the tag selection. As all probe muons should be isolated, the isolation efficiency is simply the fraction of probe muons that pass the isolation cut.

5.2.1 Tag Requirements

Once the Z selection has been made, both of the muons are tested to see if they qualify as a tag muon. A muon is considered a tag if it passes the following additional selection:

- $p_T^{\mu} > 20$ GeV
- $|z_0| < 10$ mm
- `PtRatio40` < 0.18

As the events are required to fire the `EF_mu18` or `EF_mu18_MG` triggers a cut of $p_T > 20$ GeV is used which is suitably above the turn on curve of the triggers. The cut on the longitudinal impact parameter, z_0, is a loose cut to help ensure the tag muon is from the zeroth primary vertex.

5.2.2 Probe Requirements

If an event contains a tagged muon, the other muon in the event is tested with the probe requirements, which are defined as:

- $p_T^{\mu} > 12$ GeV
- $|z_0| < 10$ mm
- $|\Delta\phi(tag, probe)| > 2$
- $|\Delta z_0(tag, probe)| < 3$ mm
- $|\Delta d_0(tag, probe)| < 3$ mm
- $|M_Z^{PDG} - M(tag, probe)| < 10$ GeV

The p_T cut is the lower of the two asymmetric cuts in the low mass Drell-Yan selection, as the isolation efficiency scale factors need to be applied to the full p_T spectrum. Again, the cut on z_0, is a loose cut to help ensure the probe muon is from the zeroth primary vertex.

The difference in the longitudinal and transverse, d_0, impact parameters between the tag and the probe, is a tighter cut helping to ensure that both the muons are from the zeroth primary vertex. The $\Delta\phi$ cut ensures that the tag and probe muons are not co-linear, as it is uncommon for two muons to be produced co-linearly in Z decays unless balanced by large initial state QCD radiation. Co-linear muons would potentially also need to undergo overlap removal to remove each muon from the sum of p_T in the $\Delta R = 0.4$ cone of the other muon. As the aim of the tag and probe selection is to select a very pure sample of muons from Z decays without too much concern for selection efficiency, both of these situations are avoided with the $\Delta\phi$ cut. This is also the reason for the tight cut on the invariant mass of the tag and probe pair to be less than 10 GeV from the PDG value of $M_Z^{PDG} = 91.1876$ GeV [2].

It is possible that both of the muons in an event are tagged, in which case both are tested with the probe selection using the other muon in the event as the tag. Once a sample of probes is acquired, the background probes are subtracted from the data sample. Reference to data from here on is to data that has had the background Monte Carlo samples subtracted.

5.3 Isolation Efficiency

Once a selection of probe muons has been made, the isolation efficiency can be calculated by testing if they pass the isolation cut from the low mass Drell-Yan analysis selection of `PtRatio40` < 0.18. The isolation efficiency is given by:

$$\varepsilon_{iso} = \frac{N_{\text{isolated probes}}}{N_{\text{probes}}}. \tag{5.1}$$

This was evaluated in bins of η and p_T of the probe muons for both the data and the signal Monte Carlo.

5.3.1 Evaluation of Uncertainties

5.3.1.1 Statistical Uncertainties

As the numerator in equation 5.1 is a sub-set of the denominator, binomial errors are used to calculate the statistical uncertainty on the isolation efficiency. These are given by,

$$\delta(\varepsilon_{iso})^{stat} = \sqrt{\frac{\varepsilon_{iso} \cdot (1 - \varepsilon_{iso})}{(N_{\text{probes}})}}, \tag{5.2}$$

and are calculated in each bin of probe muon η and p_T.

5.3.1.2 Systematic Uncertainties

The systematic uncertainties quantify the dependence of the efficiency on the choice of tag and probe cuts. Changing the value of the cuts changes how much background is selected in the sample. More background leads to lower efficiencies. Ideally the sample would only contain prompt muons from a Z decay. The variation of the cuts are all designed to give

an uncertainty due to the background contamination of the sample. The uncertainties are evaluated by varying a number of the tag and probe cuts one at a time, using the shifts detailed below:

- p_T^{tag} : ±10%
- $|M_Z^{PDG} - M(tag, probe)|$:
  - $|M_Z^{PDG} - M(tag, probe)| < 7$ GeV
  - $|M_Z^{PDG} - M(tag, probe)| < 15$ GeV
- Multijet Normalisation Factor: ±30%
- Tag Isolation:
  - `PtRatio20` < 0.1
  - `PtRatio20` < 0.2

The choice of variation was driven by those made in the published inclusive Z measurement. The 10% variation on the p_T cut on the tag muon was used in that analysis, and chosen here for consistency. The difference in the invariant mass from the PDG value is varied somewhat arbitrarily, but varied asymmetrically, since the background will approximately scale linearly with the $|M_Z^{PDG} - M(tag, probe)|$ window size, whereas the signal will scale more slowly. The multijet normalisation factor is varied by the uncertainty on the multijet Monte Carlo method described in section 6.1. The tag muon isolation was not varied by a percentage of the nominal `PtRatio40` < 0.18 value to avoid biasing the study. Instead, two different cuts were used. The Z inclusive measurement used `PtRatio20` < 0.1 as the nominal isolation cut, so this was used as one variation. The Z analysis uses variation of 10% to estimate the uncertainty from the isolation cut on the tag. It was felt that in such a low background environment as the Z resonance region, a variation of 10% would not change the amount of background sufficiently. As such, a second variation of `PtRatio20` < 0.2 was chosen.

The isolation efficiency is evaluated for each of the variations and the uncertainty from each systematic source is obtained by taking,

$$\delta^{syst} = \frac{\varepsilon_{up} - \varepsilon_{down}}{2}, \tag{5.3}$$

where ε_{up} and ε_{down} are the upward and downward shifted efficiencies. These uncertainties can be seen in figure 5.5 and figure 5.6 as a function of muon $|\eta|$ and p_T respectively. The uncertainties from each for each source are added together in quadrature to obtain the total systematic uncertainty.

It can be seen in the Monte Carlo plots in figures 5.5 and 5.6, that the variation of these cuts also produces a change in the efficiency measured in the signal Monte Carlo. This is due to kinematic effects, and these should also be reflected in the efficiencies from data. Once the scale factor is calculated the kinematic effects should cancel in the ratio of the two efficiencies. What should be left is variations due to the background or mis-modelling in the isolation distribution of the Monte Carlo.

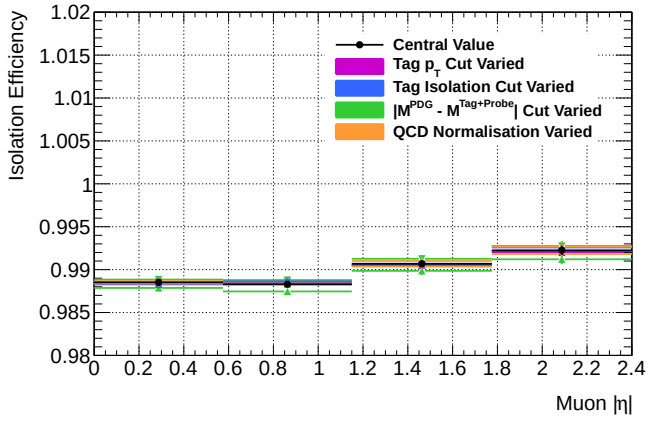

(a) Data

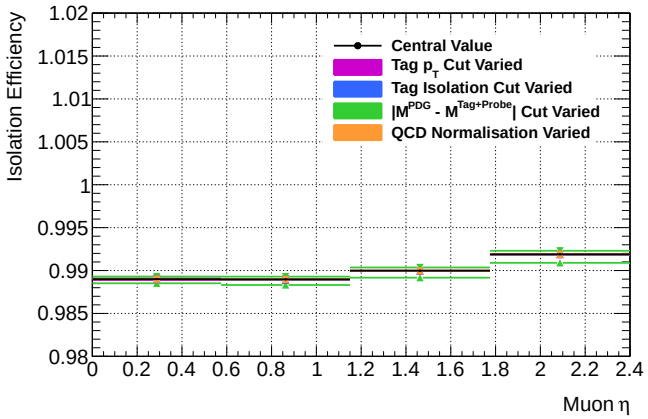

(b) Monte Carlo

Figure 5.5: Isolation efficiency for (a) data (background subtracted) and (b) Monte Carlo as a function of $|\eta|$.

5.4 Scale Factors

As described in section 4.3.2, the scale factor is defined as

$$s_f^{iso} = \frac{\varepsilon_{iso}^{mc}}{\varepsilon_{iso}^{data}}, \tag{5.4}$$

where ε_{iso}^{mc} and ε_{iso}^{data} are the isolation efficiencies for the Monte Carlo and data respectively. This is calculated for each η and p_T bin, the results of which are shown in figure 5.7. Figure 5.7(a) shows the scale factors as a function of $|\eta|$ with two bins in the barrel and two in the end-caps. Figure 5.7(b) shows the scale factors as a function of p_T. Both plots show the statistical, systematic and total uncertainty of the scale factors. As the scale factors are relatively constant and close to unity as a function of $|\eta|$, it was decided to only implement the scale factors in the analysis as a function of p_T as two dimensional scale factors would lead to larger statistical uncertainties. From figure 5.7(b) it can be seen that both the statistical and systematic uncertainties on the scale factor become large at low p_T, but for $p_T > 20$ GeV the uncertainty is $< 0.2\%$ in total. The large uncertainty at low p_T is one of the limiting factors for the measurement of the cross section in the lowest mass bins.

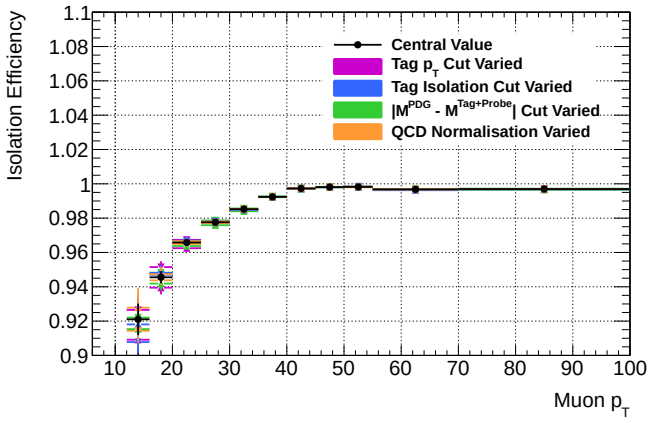

(a) Data

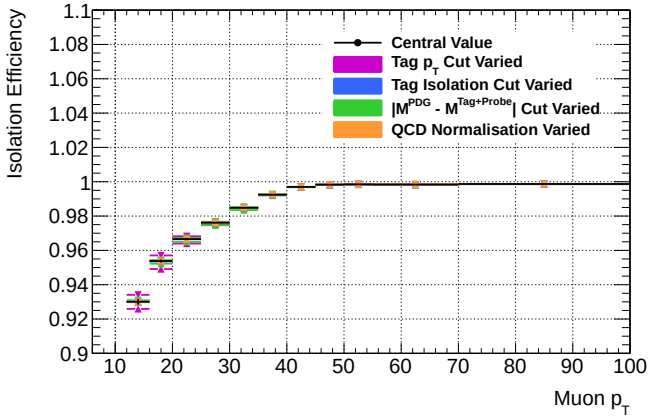

(b) Monte Carlo

Figure 5.6: Isolation efficiency for (a) data (background subtracted) and (b) Monte Carlo as a function of p_T^{probe}.

The scale factors are applied in the analysis by obtaining the scale factor for each of the Drell-Yan candidate muons and multiplying the scale factors together to get an event weight which is multiplied with the other weights discussed in section 4.3 to obtain the total weight for the event.

5.5 Validation of Method

In order to validate the study described above, the isolation efficiency and scale factors were calculated using the 2010 Z analysis isolation cut of `PtRatio20` < 0.1. In table 5.2 the total efficiencies and scale factors are considered rather than considering them as a function of the probe muon $|\eta|$ or p_T. The 2010 Z peak analysis used the `staco` reconstruction algorithm whereas this analysis uses the `muid`, so exact agreement is not expected, but neither would a large disagreement be expected as the two algorithms are very competitive. Another difference is clearly that this analysis uses 2011 data rather than 2010. Despite this it can seen that the efficiencies are close between the two analyses although a slightly lower efficiency is obtained here, most likely due to the increase in pileup during the

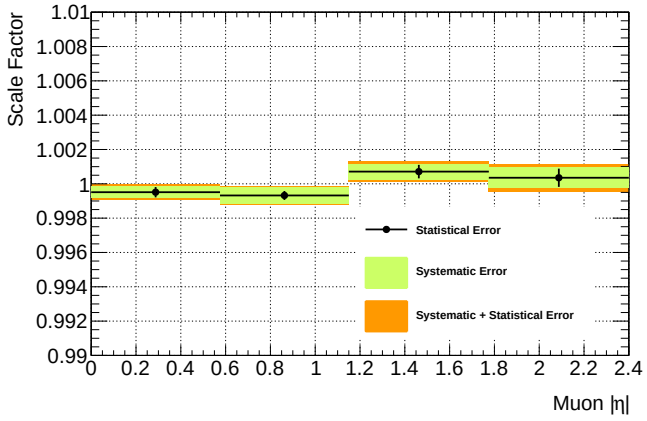

(a)

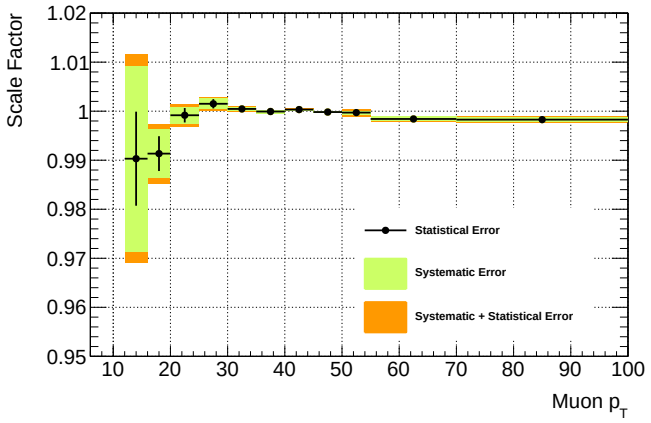

(b)

Figure 5.7: Isolation efficiency scale factors in bins of (a) muon $|\eta|$, and (b) muon p_T, with statistical and systematic errors shown.

2011 data taking. The scale factor for both analyses is the same. While this test is far from conclusive due to the differences mentioned, it adds confidence that the method was implemented correctly.

	2010 Analysis	Cross-Check
Data Efficiency	0.9947 ± 0.0006	0.9933 ± 0.0008
MC Efficiency	0.9952 ± 0.0000	0.9938 ± 0.0007
Scale Factor	0.9995 ± 0.0006	0.9995 ± 0.0002

Table 5.2: Comparison of isolation efficiencies and scale factors between the those listed in the support note for the 2010 inclusive Z analysis [92] for `staco` *muons and the those calculated using the method described in this chapter for* `muid` *muons using the Z analysis isolation cut of* `PtRatio20` < 0.1.

Chapter 6

Multijet Background Studies

The requirement that the muons are isolated removes a large fraction of potential multijet background events. However, multijet processes have large cross sections and therefore still remain a large background, particularly at lower muon p_T and di-muon invariant mass. Muons are produced in multijet processes via the decay of mesons produced in the jet. These mesons can be classed as either light or heavy flavoured depending on the constituent quarks. The mesons can decay semileptonically where one of the quarks decays via a charged current weak decay to produce a charged lepton and neutrino. It is this charged lepton that can be misidentified as coming from the Drell-Yan interaction. Only energetic charged leptons produced from meson decays will be selected by the Drell-Yan selection. However, the other decay products are produced collinearly with the charge lepton, allowing the cut on the isolation variable to be used to reject these events. Cascade decays can occur as illustrated in figure 6.1 where the quark changes flavour to a lighter quark due to the emission of the W boson, this can then go on to decay to yet lighter quarks. As such, although the $b\bar{b}$ and $c\bar{c}$ Monte Carlo used is described as heavy flavoured, it will also contain light flavoured mesons, such as pions and kaons, due to these cascade decays. The background is described as multijet as the charged current decays of the constituent quarks in the meson can also produce a quark-antiquark pair causing an additional jet. The isolation variable `PtRatio40` discussed in chapter 5 is the sum of

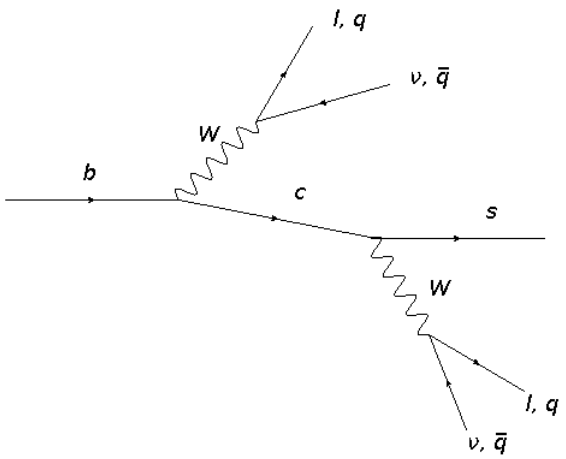

Figure 6.1: A cascade decay.

the p_T of tracks in a cone of ΔR = 0.4 around the muon expressed as a fraction of the

muon p_T. The sum of p_T which includes the products from the meson decay, also includes tracks from pileup and the underlying event. Multijet processes are inherently hard to model in Monte Carlo and as such data is used to either correct the normalisation or shape of the heavy flavour multijet Monte Carlo. Alternatively, data-driven methods can be used to estimate the multijet background mainly using data with no multijet Monte Carlo involvement. Three methods are considered in this chapter, each of which is more data driven than the previous.

6.1 Monte Carlo Method

The Monte Carlo method is the simplest estimate of the multijet background. It works on the premise that the Monte Carlo sufficiently estimates the shape of the multijet distributions but that the normalisation of these distributions is incorrect. To rectify this, the multijet Monte Carlo is normalised to the data in a "non-isolated" control region. The non-isolated region is selected by applying the full event selection outlined in section 4.4 but with the isolation cut inverted, so that both muons are required to have `PtRatio40` > 0.18. The normalisation factor, $\mathcal{N}_{\mathrm{MC}}$, is obtained by rearranging,

$$\frac{N_{data} - N_{SigMC} - N_{EWMC}}{\mathcal{N}_{\mathrm{MC}} \cdot N^{OS}_{b,cMC}} = 1, \tag{6.1}$$

where N_{data}, N_{SigMC}, N_{EWMC} and $N^{OS}_{b,cMC}$ are the number of data, signal, electroweak and multijet events respectively in the non-isolated region. For ease of discussion the electroweak background refers to all the backgrounds apart for the multijet, but including the $t\bar{t}$ background. The normalisation factor is found to be $\mathcal{N}_{\mathrm{MC}} = 0.502 \pm 0.003$.

Figure 6.2 shows the invariant mass spectrum in the non-isolated region after the multijet sample has been scaled by $\mathcal{N}_{\mathrm{MC}}$. It can be seen that the level of agreement across the mass spectrum varies but that at its largest it is about 30%, as such an uncertainty of 30% is assigned to this method.

Figure 6.3(b) shows the `PtRatio40` distribution for both of the muons without any isolation cut applied. There is good agreement between data and Monte Carlo at lower values of `PtRatio40` but this becomes increasingly worse for less isolated muons. It should be noted however that only events from the first two bins contribute to the signal region, where the large signal and electroweak contributions are clearly visible.

The disagreement seen between the normalised heavy flavoured Monte Carlo and the data is most likely due to the fact the Monte Carlo doesn't fully include the light flavoured contributions (only those produced from cascade decays) and there is potential for mismodelling of the pileup energy or underlying event energy flow.

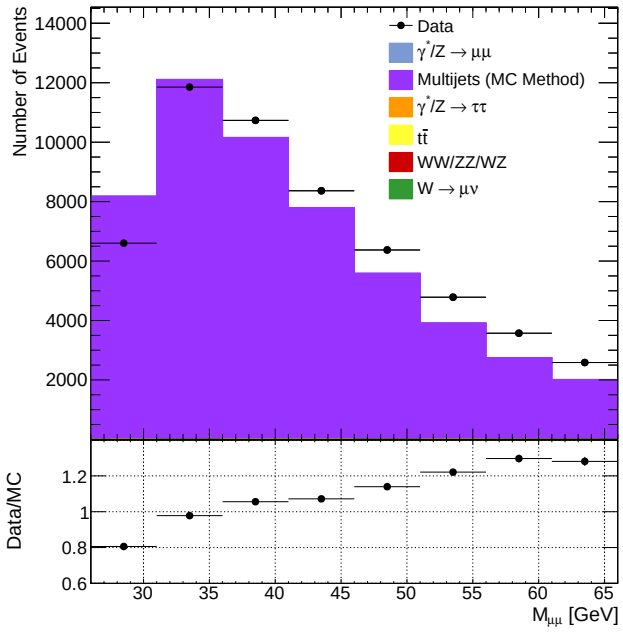

Figure 6.2: Invariant mass distribution in the non-isolated region using the Monte Carlo method multijet estimation.

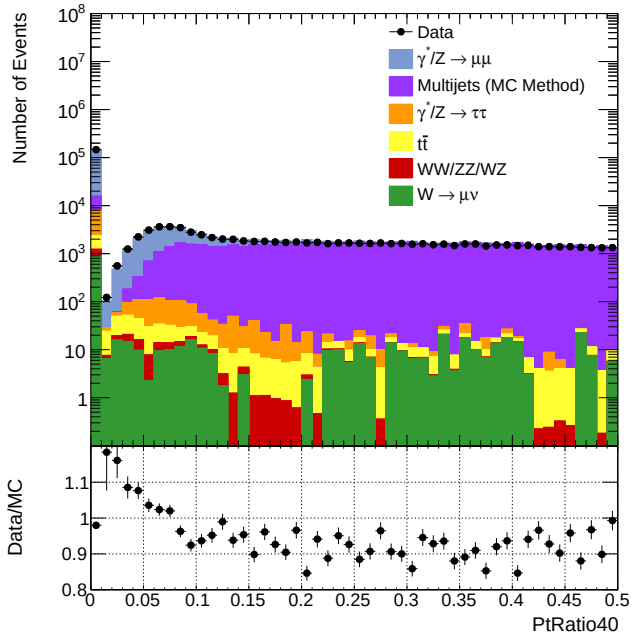

(a)

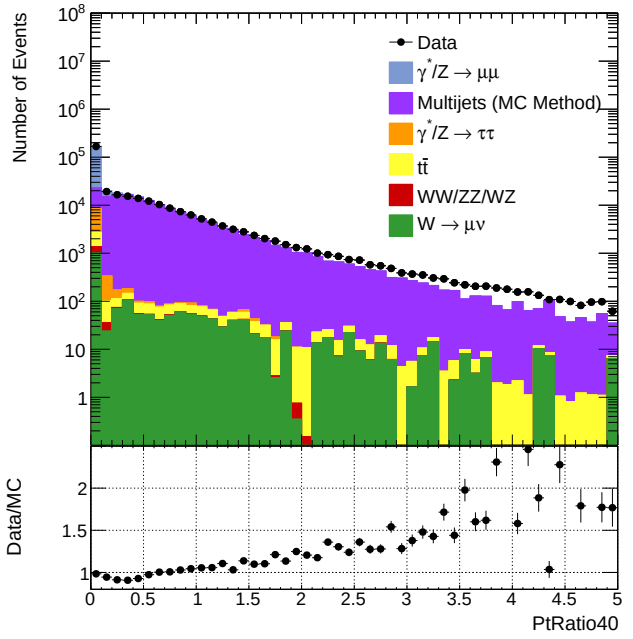

(b)

Figure 6.3: Isolation spectra using Monte Carlo method multijet estimation. The full analysis selection has been applied apart from the isolation requirement of `PtRatio40` < 0.18. *Figure (a) shows the more isolated end of the distribution where the signal can be found. Figure (b) shows the same distribution over a wider range.*

6.2 Template Fit Method

A more sophisticated estimate of the multijet background comes in the form of the Template Fit method. This method relies on accurately improving the modelling of the muon isolation spectrum using a two component data enhanced template fit. As with the Monte Carlo method both the number of multijet events is estimated and an uncertainty assigned to the estimate based on the agreement between data and the multijet estimate in the non-isolated region.

The multijet Monte Carlo consists of heavy flavoured b and c jets, but at low invariant mass and low muon p_T, a contribution from light flavoured jets from u, d and s quarks might also be expected. In order to include these into the multijet background estimate, data events where the two muons have the same electric charge are used as a proxy for the opposite sign events coming from light flavoured multijet processes. This is done as light flavoured jets will produce muons and antimuons with no preference, so same sign events can be used in place of the opposite sign events that are indistinguishable from the signal in data.

In the template fit method a sample of same sign (SS) data events is used to correct the shape of the Monte Carlo estimate. This is done as the Monte Carlo alone was seen in section 6.1 not to describe the data well. Using a multijet rich selection, these two samples are used as templates in the fit. The fit determines the normalisation factors needed to be applied to each of the templates so that together they describe the data.

To do this the `TFractionFitter` class in `ROOT` is used, which calculates normalisation factors to be applied to two template distributions needed to give the best agreement to a third control distribution by minimising the negative log likelihood of a fit [97]. The normalisation factors are the only free parameters of the fit, which considers the agreement in each bin, but returns a single normalisation factor for the whole template distribution.

The outline of the template fit method is given below, followed by a detailed explanation of each step:

1. Select a multijet rich sample
2. Create control distribution and two templates
3. Perform Template Fit
4. Find template normalisation factors
5. Obtain estimate of multijet background in the signal region
6. Assign uncertainty to estimated multijet background

1. Select a multijet rich sample

An unbiased sample that is rich is multijet events is needed. The full analysis selection is made as described in chapter 4, apart from the isolation requirement. Instead, a harsh anti-isolation cut requiring `PtRatio40` > 0.38 is made on one muon at random, while the `PtRatio40` of the other muon is plotted. This allows the full `PtRatio40` spectrum to

be plotted for events that have been selected to be very unisolated. The muon that the harsh anti-isolation cut is applied to is chosen at random to remove any p_T bias that might have been introduced by only considering the leading or sub-leading muon. The cut of `PtRatio40` > 0.38 was chosen as it produces a multijet rich sample with less than 1% of signal Monte Carlo passing the cut. This was seen as a level of contamination small enough for the method to work without limiting the statistics of the templates.

2. Create control distribution and two templates

Templates of the `PtRatio40` spectrum are formed from a sample of same sign data events and a sample of opposite sign heavy flavoured Monte Carlo events (that has had the same sign events subtracted from them to avoid double counting). A sample of opposite sign data events is used to create the `PtRatio40` distribution to which the templates are fitted. These are summarised in table 6.1 and can be seen plotted in figure 6.4(a)

Use	Sample	Events
Control Distribution	Data OS	50540
Template 1	Multijet Monte Carlo OS-SS	67675
Template 2	Data SS	22639

Table 6.1: The control distribution and the two templates that are fitted to it. All three distributions have had a harsh anti-isolation cut of `PtRatio40` < 0.38 *applied to the other muon in the event.*

3. Perform Template Fit

The histograms of all three distributions are passed to the `TFractionFitter` code which returns two relative normalisation factors, s_1 and s_2. As the fit is carried out using the three distributions once they are normalised to unity, s_1 and s_2 are the free parameters of the fit. These represent the amount the templates for the multijet Monte Carlo and the same sign data respectively need to be scaled so that together they describe the data distribution of opposite sign events. The scales are found to be $s_1 = 0.517 \pm 0.015$ and $s_2 = 0.483 \pm 0.015$.

4. Find template normalisation factors

As s_1 and s_2 only describe the relative normalisation of the two templates (it can be seen that $s_1 + s_2 = 1$) they cannot be used to scale the input templates. In order to scale the original templates correctly the original normalisation needs to be reinstated, this produces the normalisation factors f_1 and f_2 which are defined as,

$$f_1 = s_1 \cdot \frac{N^{OS-SS}_{QCD,MC}}{N^{OS}_{Data}}, \tag{6.2}$$

$$f_2 = s_2 \cdot \frac{N^{SS}_{Data}}{N^{OS}_{Data}}, \tag{6.3}$$

where $N^{OS-SS}_{QCD,MC}$, N^{SS}_{Data} and N^{OS}_{Data} are the unnormalised number of multijet Monte Carlo events (with same sign events subtracted), same sign and opposite sign data events respectively as listed in table 6.1. The factors are found to be $f_1 = 0.386 \pm 0.020$ and $f_2 = 1.077 \pm 0.007$. Once these normalisation factors are applied to the original multijet templates a good agreement is seen with the opposite sign data distribution, as shown in figure 6.4(b). The small disagreement in the first two bins is due to the signal contamination of the multijet sample. This could be subtracted off from the opposite sign data distribution before the fit is made, but this would introduce an additional reliance on the modelling of the Monte Carlo. A cross-check was made where this was done and it was found not to effect the final estimate within errors.

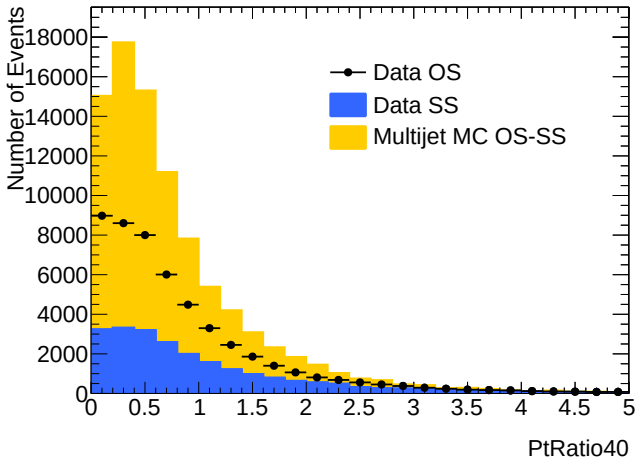

(a) Before normalisation

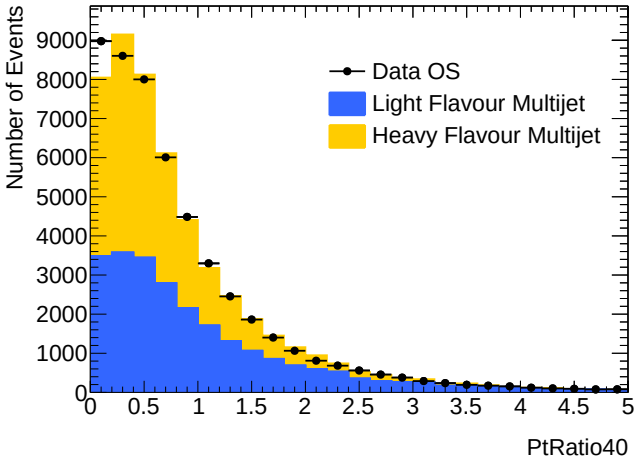

(b) After normalisation

Figure 6.4: The two templates used in the template fit method compared to opposite sign data events, before and after normalisation with factors obtained from the `TFractionFitter` *code as described in the text.*

5. Obtain estimate of multijet background in the signal region

The aim of the method to is find normalisation factors that can be applied for the standard analysis selection. While f_1 and f_2 give good agreement for a very harsh anti-isolated selection, it needs to be ensured that the normalisation is appropriate in the phase space in which the analysis is made. In order to do this, an additional normalisation factor $\mathcal{N}_{template}$ is applied to the multijet OS-SS Monte Carlo distributions. To do this the non-isolated region as used by the Monte Carlo method was examined. This requires both muons to have `PtRatio40` > 0.18. The factor $\mathcal{N}_{template}$ given by the rearrangement of,

$$\frac{N_{data} - N_{SigMC} - N_{EWMC}}{[\mathcal{N}_{template} \cdot f_1 \cdot (N^{OS}_{b,cMC} - N^{SS}_{b,cMC})] + [f_2 \cdot N^{SS}_{data}]} = 1, \tag{6.4}$$

where the variables are as defined previously. The correction to the normalisation is found to be small (close to unity), with $\mathcal{N}_{template} = 0.940 \pm 0.051$.

Figure 6.5 shows the isolation spectrum for both muons. The full analysis selection has been applied apart from the isolation requirement. The light and heavy flavoured multijet is shown separately. Both have the appropriate normalisation factors, summarised in table 6.2, applied. It can be seen that the isolation spectrum is now described well by the signal and background distributions. The improvement compared to the Monte Carlo method shown in figure 6.3 is clear. Figure 6.6 shows the di-muon invariant mass distribution with the full analysis selection, including the isolation requirements. It can been seen that the light flavoured multijet background is a small but non-negligible component of the multijet background, making up 35.9% of it.

Normalisation Factor	Template 1	Template 2
Relative normalisation	$s_1 = 0.517 \pm 0.015$	$s_2 = 0.483 \pm 0.015$
Template normalisation	$f_1 = 0.386 \pm 0.020$	$f_2 = 1.077 \pm 0.007$
Phase-space normalisation	$\mathcal{N}_{template} = 0.940 \pm 0.051$	-

Table 6.2: Normalisation factors obtained from the Template Fit estimation method. The relative normalisation factors are the output of the `TFractionFitter` *code. The template normalisation factors are the factors that are actually applied to the two templates to give good agreement with the control distribution. These are also applied to the OS-SS multijet Monte Carlo and the SS data events selected by the Drell-Yan analysis selection. The phase-space normalisation factor ensures the correct normalisation in the analysis phase-space.*

6. Assign uncertainty to estimated multijet background

In order to assign an uncertainty to this method, the agreement between the data and the Monte Carlo in the non-isolated region is once again considered. As can be seen in figure 6.7 the largest disagreement between data and Monte Carlo is now about 20%, which is therefore used as the systematic uncertainty on the background estimate from this method.

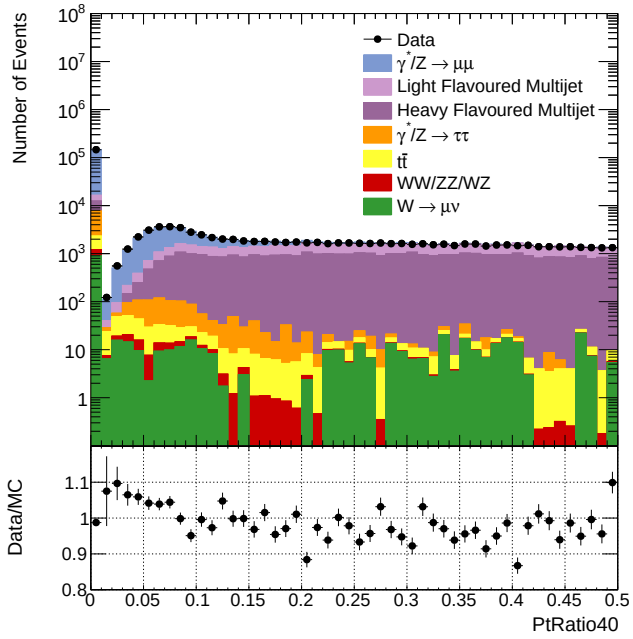

(a)

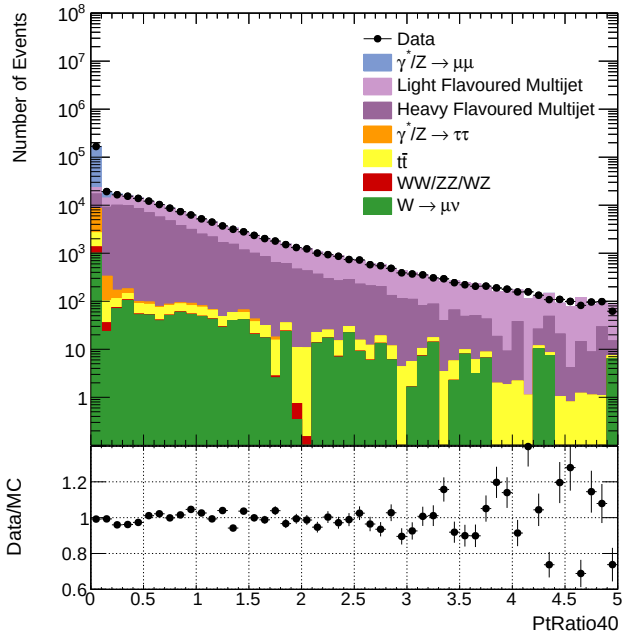

(b)

Figure 6.5: Isolation spectra using template fit method multijet estimation. The full analysis selection has been applied apart from the isolation cut of `PtRatio40` < 0.18. *Figure (a) shows the more isolated end of the distribution where the signal can be found. Figure (b) shows the same distribution over a wider range.*

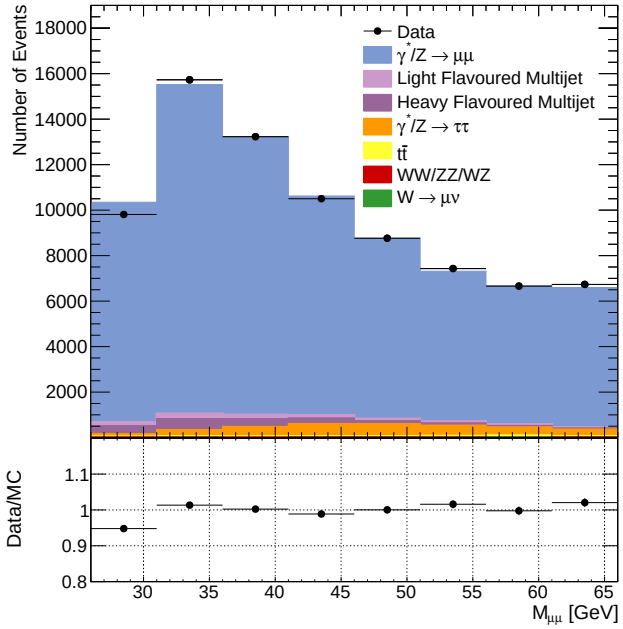

Figure 6.6: Isolated invariant mass distribution using the template fit method multijet estimation.

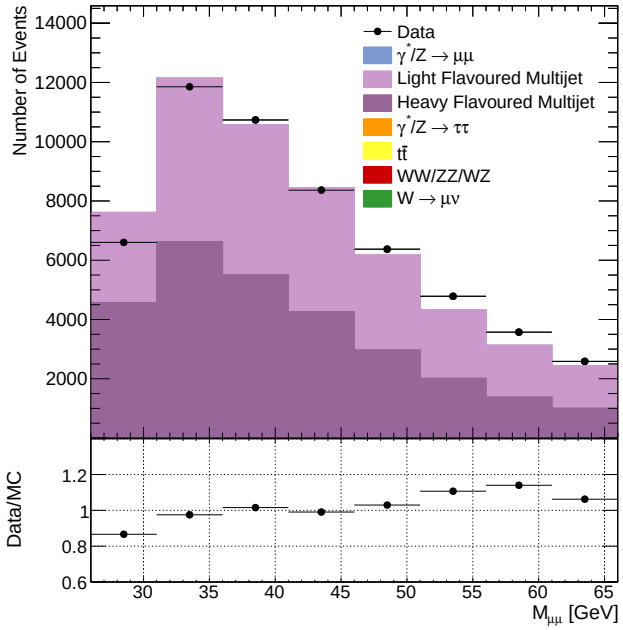

Figure 6.7: Non-isolated invariant mass distribution using the template fit method multijet estimation. It can be seen in the ratio plot that maximum disagreement is about 20%. This is taken as the uncertainty on the template fit estimate.

6.3 ABCD Methods

The move from a completely Monte Carlo based multijet background estimate to a partially data driven one, in the form of the Template Fit method, showed a marked improvement of the description of key distributions. The ABCD method, would allow the estimate to be far more data driven, and as such is investigated in order to either improve upon or verify the result from the Template Fit method.

The ABCD method relies on two uncorrelated multijet background discriminating variables to estimate the contribution of the multijet background in the signal region. In the plane of the two variables, two cuts divide the sample into a signal region (A) and three background rich regions (B, C, D). As the variables are uncorrelated the relationship of

$$\frac{N_A}{N_C} = \frac{N_B}{N_D}, \tag{6.5}$$

should hold. Where N_A, N_B, N_C and N_D are the number of multijet events in quadrants A, B, C and D respectively. In this way, the data measured in the other three quadrants can be used to estimate the amount of multijet background in the signal quadrant. Ideally with only minimal reliance on Monte Carlo (the electroweak and signal events need to be subtracted from the data in B, C and D). Due to this, the variables chosen and the cuts made should be ones that are not only uncorrelated, but offer strong discrimination between the signal and multijet background.

Three variations of the ABCD method are investigated, these are discussed below. The first two are quickly ruled out as useful variable combinations. The third, as will be discussed, is used only as a cross-check of the Template Fit method, as it proves to still be too reliant on the modelling of the Monte Carlo.

6.3.1 ABCD Method I

The first ABCD method considered looks at isolated and non-isolated events for both di-muon events and electron-muon events. The quadrants are defined as shown in figure 6.8(a). It would be expected that a jet would produce equal numbers of electrons and muons, from semi-leptonic decays. This means there should be a similar number of events with an electron and a muon as with two muons. The selection used to select the $e\mu$ events is:

- Good Runs List
- `EF_2mu10_loose` OR `EF_e10_medium_mu6` Trigger
- Reject LAr Errors
- $N_{vertex} > 1$ with $N_{tracks} > 2$
- $N_{electrons} > 0$ (with electron `author` 1 OR 3)
- $N_{muons} > 0$ (combined muons)

- $|\eta_{e,\mu}| < 2.4$ and reject electrons in $1.37 < |\eta_e| < 1.52$
- $p_T^{l_1} > 15$ GeV
- $p_T^{l_2} > 12$ GeV
- Muon Track Quality Cuts
- Electron is `medium++`
- 26 GeV $< M_{ll} <$ 66 GeV

Many of the cuts that are applied are the same as for the standard di-muon analysis. Electrons are rejected in the $1.37 < |\eta| < 1.52$ transition region between the barrel and end-cap electromagnetic calorimeters. Only electrons with an `author` value of 1 OR 3 are used. These are electrons that are reconstructed by either the `standard` reconstruction algorithm or by the `standard` and `softe` reconstruction algorithm. The `standard` algorithm reconstructs electrons seeded in the EM calorimeter and then matched to tracks. The `softe` algorithm is seeded by low p_T tracks and then extrapolated to deposits in the EM calorimeter. Electrons are also required to pass the `medium++` selection, which are a set of official ATLAS requirements that consider shower shapes and number of hits in the inner detector [98]. Events are considered isolated if both leptons pass the `PtRatio40` < 0.18

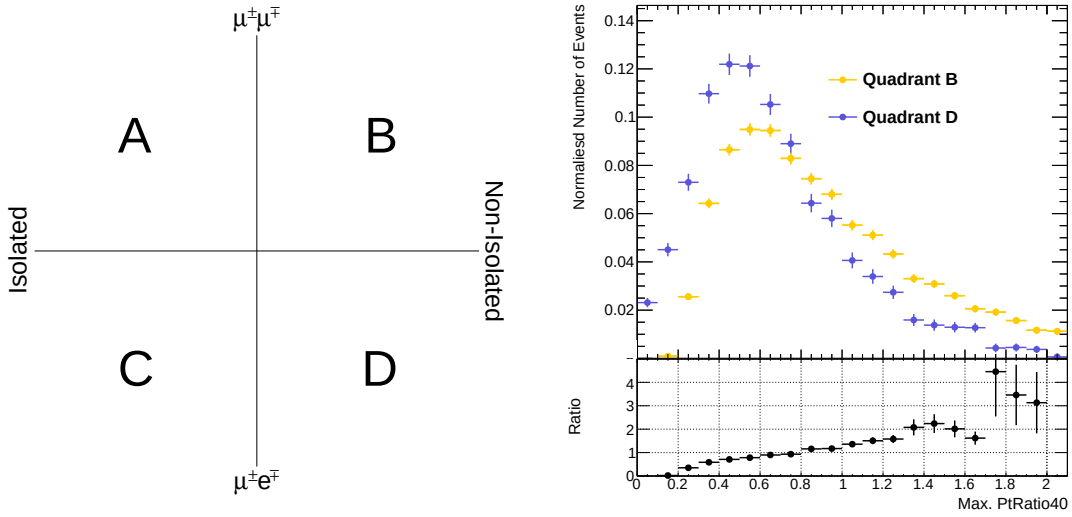

(a) (b)

Figure 6.8: Figure (a) shows the definition of the quadrants for the ABCD method I. Figure (b) shows the isolation spectra in the non-isolated quadrants B and D, here the `PtRatio40` *of the least isolated of the two muons is plotted.*

isolation requirement. The first test if this is a viable method is to check that the isolation spectra in the two non-isolated quadrants have similar shapes. It can be seen in figure 6.8(b), however, that the spectra have very poor agreement, as such this method is ruled out. The poor agreement is believed to be due to the use of track based isolation for the electrons. As with muons, the isolation can either be defined by summing the p_T

of the tracks or calorimeter clusters in a cone around the lepton. As electrons undergo much more bremstrahlung than muons, track based isolation is less suitable as it will not consider bremstrahlung photons as being associated with the electron. However, as long as the photons remain collinear to the electron they will form deposits into the same calorimeter clusters as the electron, so information will not be lost. It is possible to use calorimetric isolation for the muons so that a useful comparison could be made, but this would involve changing the main selection, which is undesirable as the current cut was chosen to be optimal and calorimetric isolation for muons is not as resilient to pile-up as track based isolation.

6.3.2 ABCD Method II

A second variation of the ABCD method uses muon isolation as one discriminating variable and the charge of the muon pair as the other. This divides the plane into same sign and opposite sign events. For this method the standard di-muon selection was used, but with inversion of the charge requirement on the muons to form the quadrants outlined in figure 6.9(a). Again the isolation spectra in the two non-isolated quadrants are examined, as shown in figure 6.9(b). The spectra show very poor agreement, so again the method is rejected. The disagreement seen in figure 6.9 is suspected to be due to the same sign

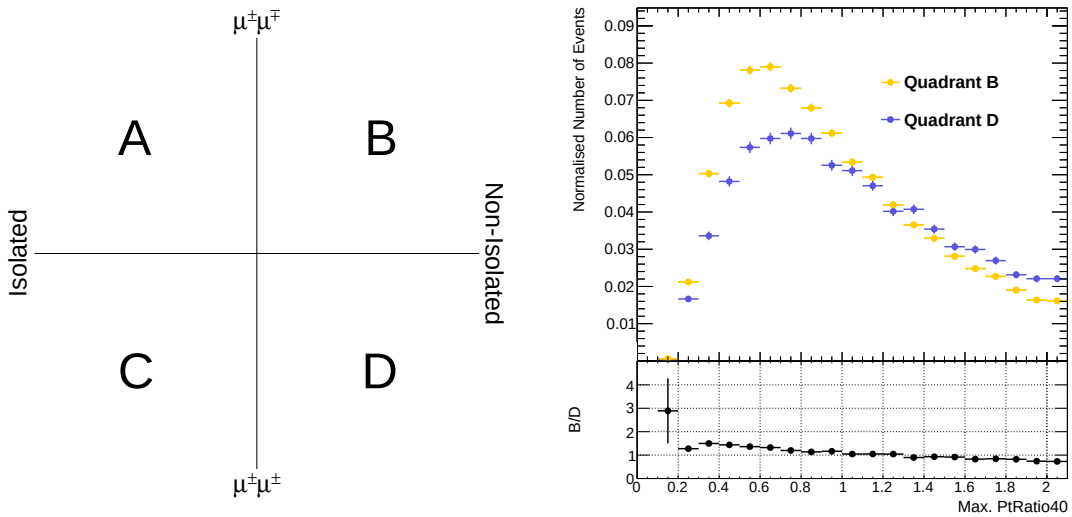

(a) (b)

Figure 6.9: Figure (a) shows the definition of the quadrants for the ABCD method II. Figure (b) shows the isolation spectra in the non-isolated quadrants B and D, here the `PtRatio40` *of the least isolated of the two muons is plotted.*

muon pairs being sampled from further down the decay chain shown in figure 6.1. This was not investigated further, as it is clear the disagreement is large, demonstrating the unsuitability of the choice of ABCD variables.

6.3.3 ABCD Method III

The final approach using the ABCD method involves adding an additional cut to the standard selection. As shown in figure 6.11(a), as well as the isolation cut, the d_0 significance, s_{d_0}, is considered. This is defined as

$$s_{d_0} = \frac{d_0}{\delta_{d_0}}, \tag{6.6}$$

where δ_{d_0} is the error on the measurement of the d_0 impact parameter. Figure 6.10 shows the $|s_{d_0}|$ distribution in the signal region, where the multijet background is represented by the Monte Carlo method described in section 6.1. It can be seen that the signal is predominantly at low $|s_{d_0}|$, while the multijet background extends to larger $|s_{d_0}|$.

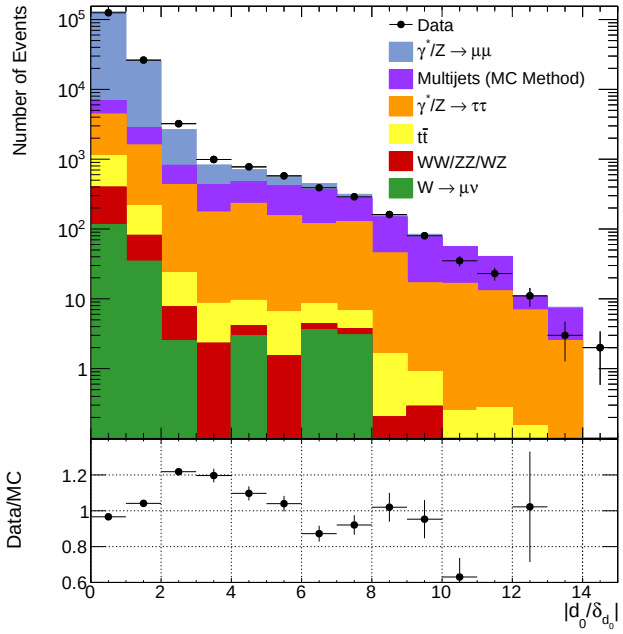

Figure 6.10: Control plot showing the data and Monte Carlo agreement of the s_{d_0} distribution in the signal region.

Quadrants A and B require that both muons have $s_{d_0} < 3.0$, while quadrants C and D require at least one of the muons has $s_{d_0} \geq 3.0$. Considering the two non-isolated regions in figure 6.11(b) good agreement, within 10%, can be seen between the two distributions. Further verification of the suitability of this ABCD method is to check that the `PtRatio40` and s_{d_0} variables are truly uncorrelated. Using a sample of harsh anti-isolated events using the same selection used to obtain the templates for the template fit method in section 6.2 requiring one muon to have `PtRatio40` > 0.38. The correlation is shown in figure 6.12(a) for data and 6.12(b) for the multijet Monte Carlo. The correlation is expressed by the correlation coefficient, ρ, which is defined as:

$$\rho_{xy} = \frac{V_{xy}}{\delta_x \delta_y}, \tag{6.7}$$

where x and y are the two variables whose correlation is being considered, δ_x and δ_y are

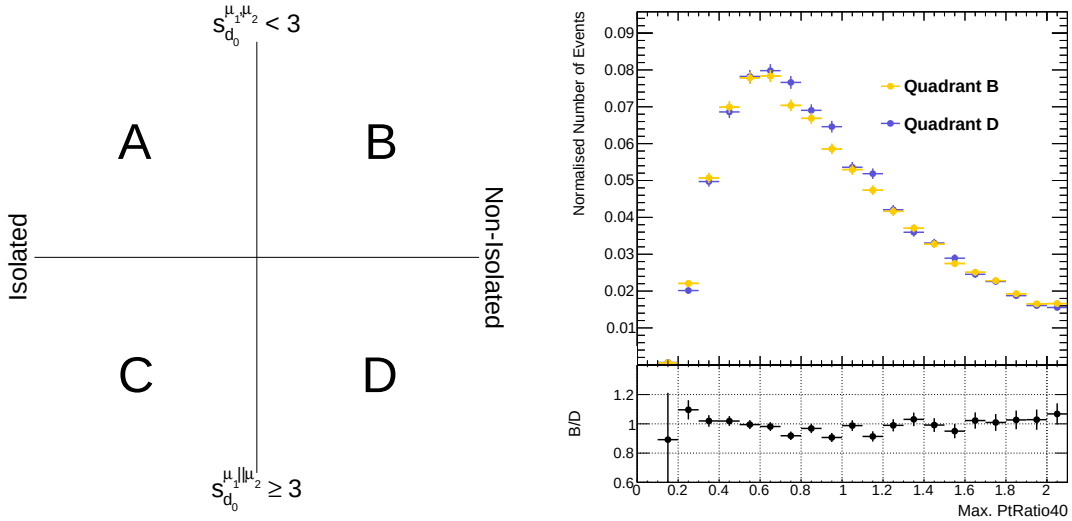

(a) (b)

Figure 6.11: Figure (a) shows the definition of the quadrants for the ABCD method III. Figure (b) shows the isolation spectra in the non-isolated quadrants B and D, here the `PtRatio40` *of the least isolated of the two muons is plotted.*

the uncertainties on x and y, and V_{xy} is the covariance matrix. The correlation coefficient lies in the range $-1 \leq \rho_{xy} \leq +1$. Values close to 0 represent uncorrelated variables, -1 have negative correlation, and $+1$ have positive correlation [99]. When examined for the data and the multijet Monte Carlo in figure 6.12 correlations coefficients of 0.007 and 0.017 are found for data and the multijet Monte Carlo respectively. This demonstrates a very small degree of correlation.

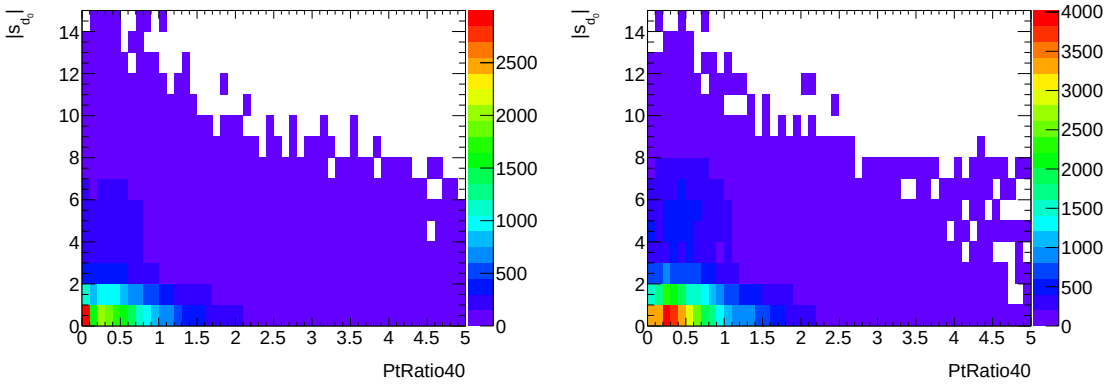

(a) Data (b) Multijet Monte Carlo

Figure 6.12: Correlation plots showing `PtRatio40` *and s_{d_0} variables for the free muon in harsh anti-isolated sample. (a) Data ($\rho = 0.007$). (b) multijet Monte Carlo ($\rho = 0.017$).*

The di-muon invariant mass distribution in each quadrant is shown in figure 6.13. The multijet background Monte Carlo is shown here for comparison, but is not involved in the estimate of the multijet background in quadrant A. The number of multijet events in

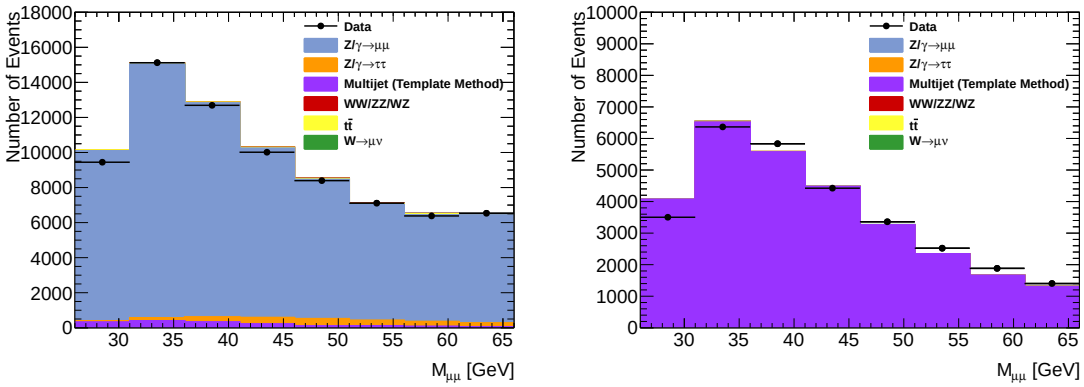

(a) Quadrant A

(b) Quadrant B

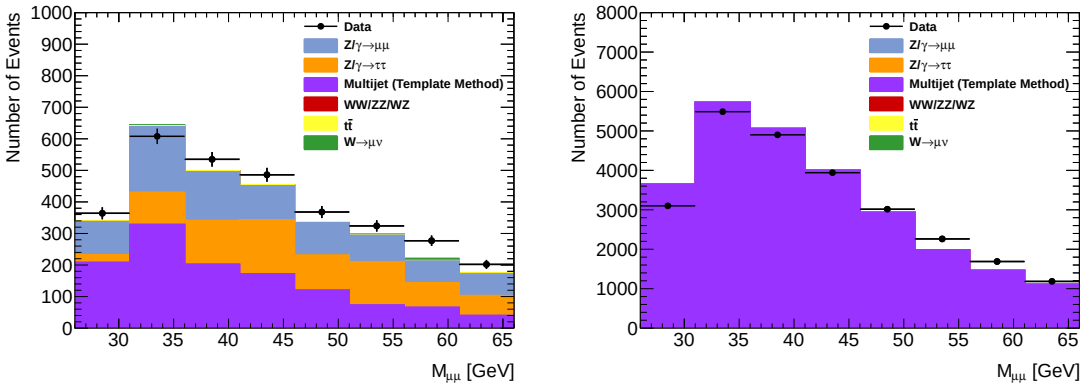

(c) Quadrant C

(d) Quadrant D

Figure 6.13: Di-muon invariant mass distributions in quadrants A-D, showing data and Monte Carlo agreement. As stated in the text the multijet Monte Carlo is shown here for comparison, but is not involved in the estimate at any point. Quadrant A is shown to help illustrate the relative amount of multijet back background to be estimated.

quadrant A, $N^A_{multijet}$, in each mass bin is estimated from the other three quadrants using the relation,

$$N^A_{multijet} = (N^C_{data} - N^C_{ew} - N^C_{sig})\frac{(N^B_{data} - N^B_{ew} - N^B_{sig})}{(N^D_{data} - N^D_{ew} - N^D_{sig})}, \tag{6.8}$$

where N_{data}, N_{ew} and N_{sig} are the number of data, electroweak Monte Carlo, and signal Monte Carlo events in each region respectively. As can be seen in figure 6.13 subtracting the Monte Carlo distributions from the data in quadrants B and D is a small subtraction, but in quadrant C the subtraction is much larger. This has two effects, the number of events in quadrant C, which are already small are reduced further and a dependence is introduced on the modelling of the Monte Carlo that the ABCD method was used to avoid. The error bars in figure 6.14(a), which shows the normalised data distributions after the Monte Carlo samples have been subtracted, clearly show the discrepancy in sample size for the three regions. Figure 6.14(b) shows the ratio of events in quadrants B and D after the signal and electroweak Monte Carlo has been subtracted. The ratio labelled "bin-by-bin" is the simple ratio of mass distributions in quadrants B and D, whereas the "integral" ratio uses the ratio of the total number of events in quadrants B and D.

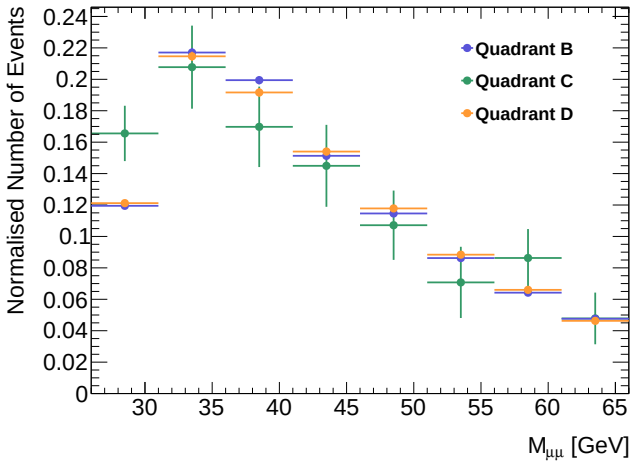

(a)

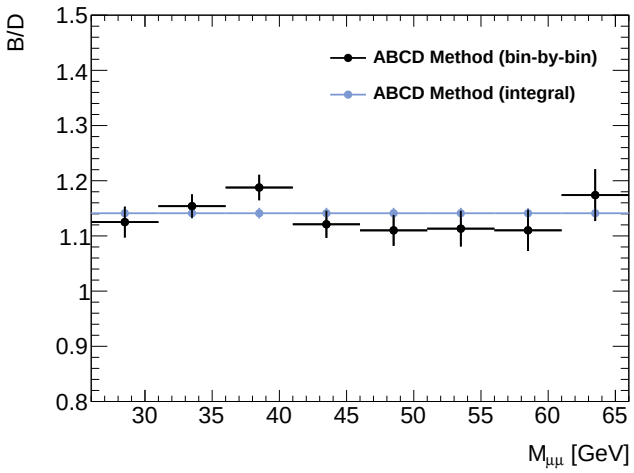

(b)

Figure 6.14: (a) Normalised di-muon invariant mass distributions in quadrants B-D for the data with the Monte Carlo signal and electroweak backgrounds subtracted. (b) The ratio of quadrants B and D for the data with the Monte Carlo signal and electroweak backgrounds subtracted.

The dependence of the multijet estimate on the choice of d_0 significance cut is examined in figure 6.15. It can be seen that although the effect of the cut is significant in quadrants B and D, the change in the estimate of the multijet background in quadrant A is small, with the results all being consistent with each other within uncertainties.

Continuing with the cut of $s_{d_0} < 3$ for quadrants A and B and $s_{d_0} \geq 3$ for quadrants C and D. The estimated number of multijet events in quadrant A is shown again in figure 6.16, where it is compared to results from the template method. The template fit is repeated here with the s_{d_0} cut included so a direct comparison can be made. Two variations of the ABCD method are shown, the difference being which of the distributions in figure 6.14(b) is used as the ratio shown in equation 6.8. For the "integral" method all the shape information comes from quadrant C, as can be seen, this only has a small effect on the shape of the distribution estimated for quadrant A. The majority of the bins are consistent with the 20% uncertainty assigned to the template fit method. It is expected

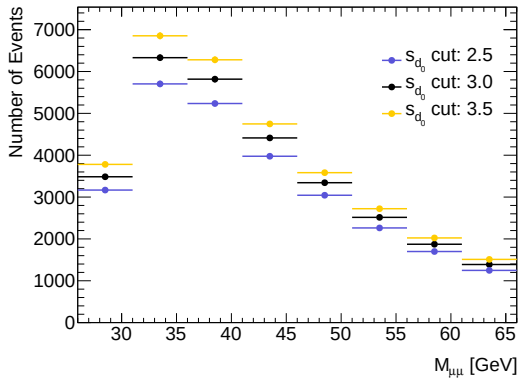

(a) Quadrant B

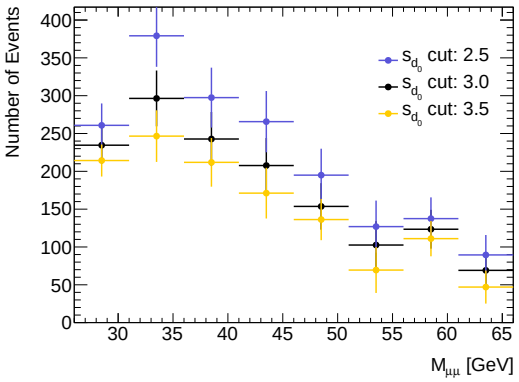

(b) Quadrant C

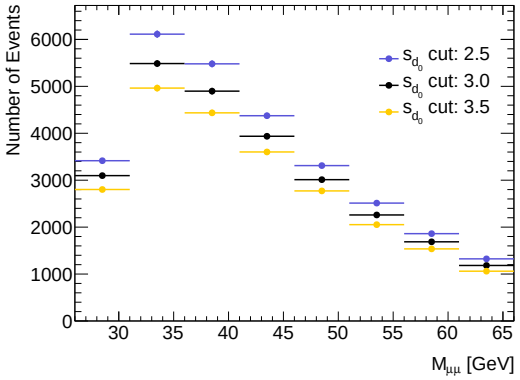

(c) Quadrant D

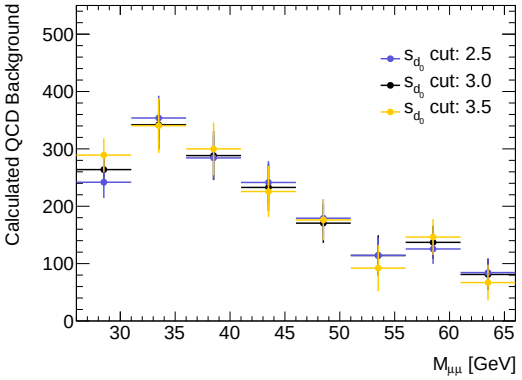

(d) Quadrant A Estimate

Figure 6.15: Distributions showing the effect of varying the s_{d_0} cut in quadrants B-D for the data with the Monte Carlo signal and electroweak backgrounds subtracted in (a) - (c). The effect of the variation on the estimate of multijet background in quadrant A is shown in (d).

that the disagreement of the remaining bins is due to the reliance on the modelling in the Monte Carlo coming from quadrant C, as it was seen in figure 6.10 that the d_0 significance distribution is not well described.

As the ABCD method agrees within two standard deviations with the template fit method even for the bins with the worst agreement it is considered to validate the template fit method. An ideal agreement would be more desirable, but as the choice of variables requires a heavier than desired reliance on the modelling in the Monte Carlo of the s_{d_0} distribution the agreement is sufficient as a cross-check of the template fit method, which will be used as the multijet background estimate with the associated 20% uncertainty, as described previously.

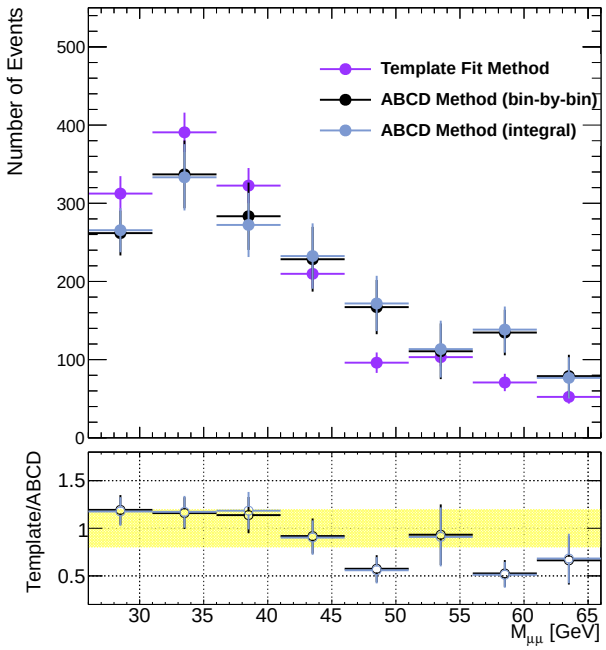

Figure 6.16: The estimated multijet background in quadrant A, as compared to that calculated with the template fit method which was repeated as described in section 6.2, but with the inclusion of the d_0 significance cut.

Chapter 7

Comparison of Data and Monte Carlo

Once all the corrections have been made to the Monte Carlo samples the level of agreement between the data and the Monte Carlo needs to be examined. This gives confidence that the selection properly controls the backgrounds. It also gives confidence that bin-by-bin unfolding will be appropriate as the acceptances will be well described. The control plots shown in this chapter demonstrate good data and Monte Carlo agreement and the small amount of background selected by the analysis. The number of events selected in data and each of the Monte Carlo samples can be seen in the cutflow tables shown in tables 7.1 and 7.2.

7.1 Control Plots

Figures 7.1, 7.2 and 7.3 show the control plots for the leading (muon1) and sub-leading (muon2) muons. Figure 7.4 shows control plots for the di-muon pairs. All the figures demonstrate the data and Monte Carlo agreement after the full selection has been made. All Monte Carlo weights discussed in the previous chapters have been applied. The plots show the Monte Carlo samples stacked on top of each other and compared to the black data points. The ratio plots below the distributions show the ratio of the data and all the Monte Carlo samples added together, the uncertainty on the ratio shows the statistical error from the data.

Figures 7.1 and 7.2 show the ϕ and η distributions for the leading and sub-leading muons. Both demonstrate good agreement of the Monte Carlo to the data, with some variations but no more than 10%. The shapes of the distributions are governed by the position of the detector supports and the gap at $\eta = 0$ for cabling. The p_T distribution of the muons is shown in figure 7.3, again the data are well described by the Monte Carlo although statistics are poor in the tail of the distributions. Figures showing the muon distributions plotted with both muons on the same plot can be seen in appendix A.

The four-vectors of the two selected muons are added together to give the four-vector of the Z/γ^*, referred to as the di-muon pair. Figure 7.4(a) shows that the p_T of the di-muon pair is not well described by the Monte Carlo, the effect of reweighting this

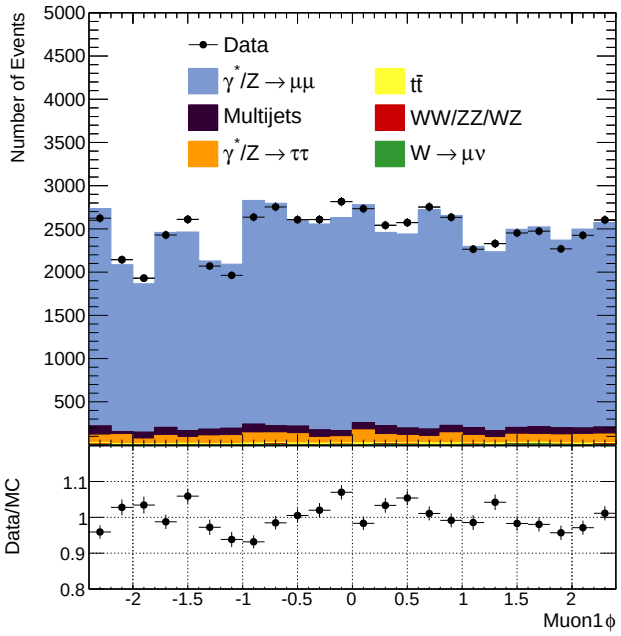

(a) Leading Muon ϕ Distribution

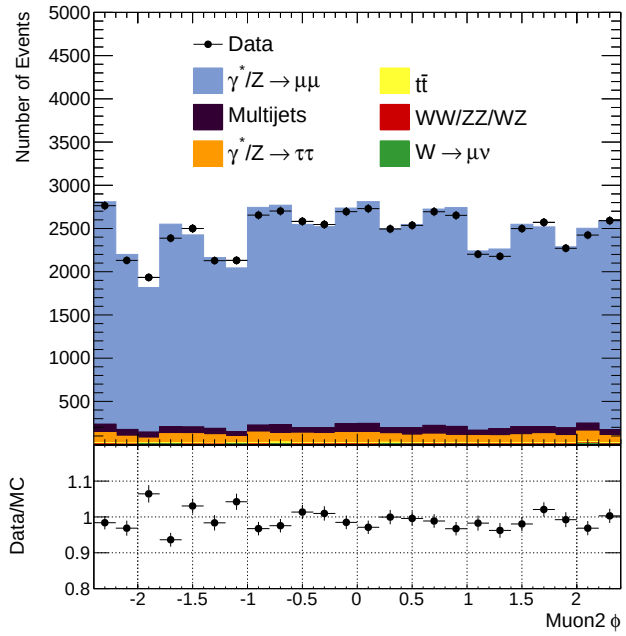

(b) Sub-leading Muon ϕ Distribution

Figure 7.1: Muon ϕ control plots.

distribution to another boson p_T model is examined in section 8.2.9 and is included as a systematic uncertainty on the measured cross section. Figure 7.4(b) shows the modulus of the rapidity of the di-muon pair which has acceptable agreement between the data and the Monte Carlo. Figure 7.5 shows the invariant mass distribution of the di-muon pair, again showing good agreement between the data and Monte Carlo. The distribution is shown in the 5 GeV wide binning in which the differential cross section is measured.

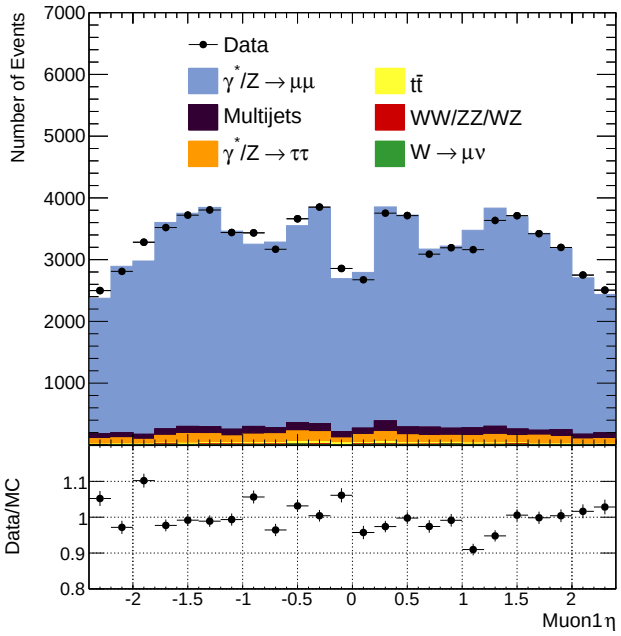

(a) Leading Muon η Distribution

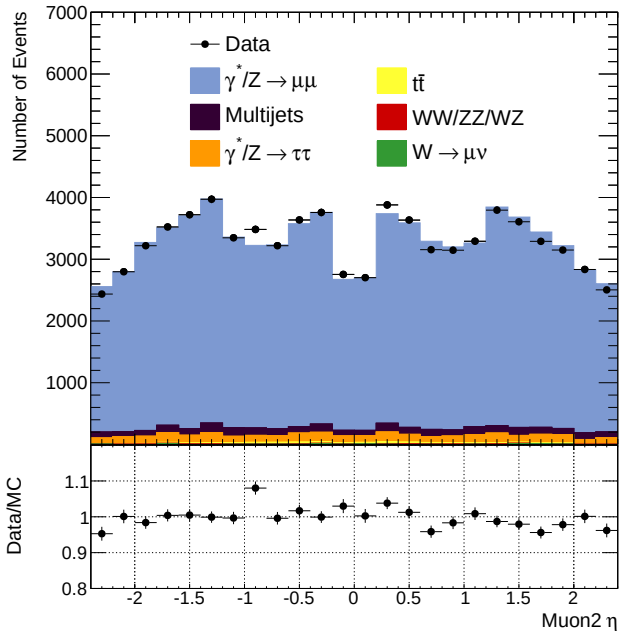

(b) Sub-leading Muon η Distribution

Figure 7.2: Muon η control plots.

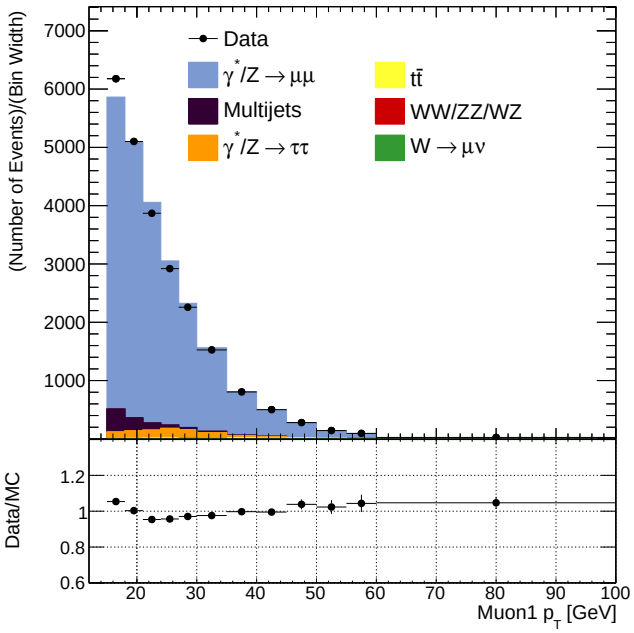

(a) Leading Muon p_T Distribution

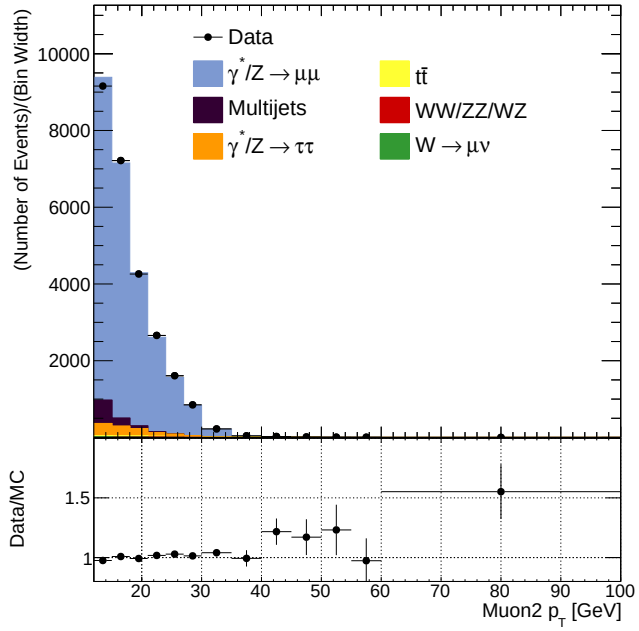

(b) Sub-leading Muon p_T Distribution

Figure 7.3: Muon p_T control plots.

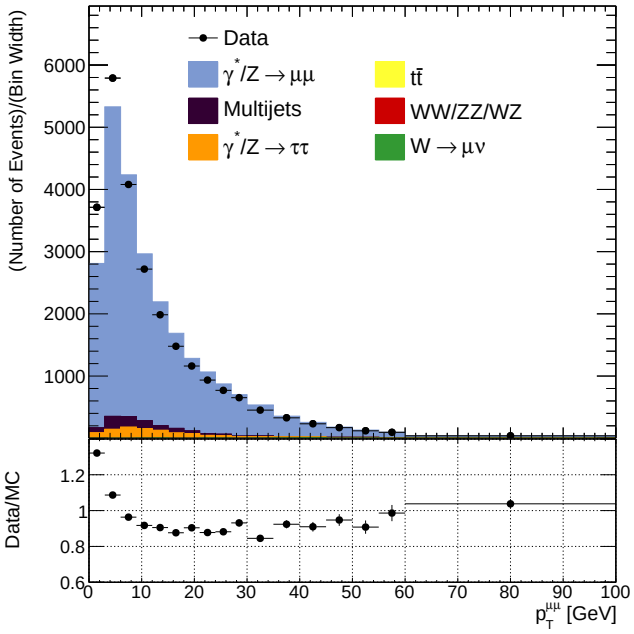

(a) $p_T^{\mu\mu}$ Distribution

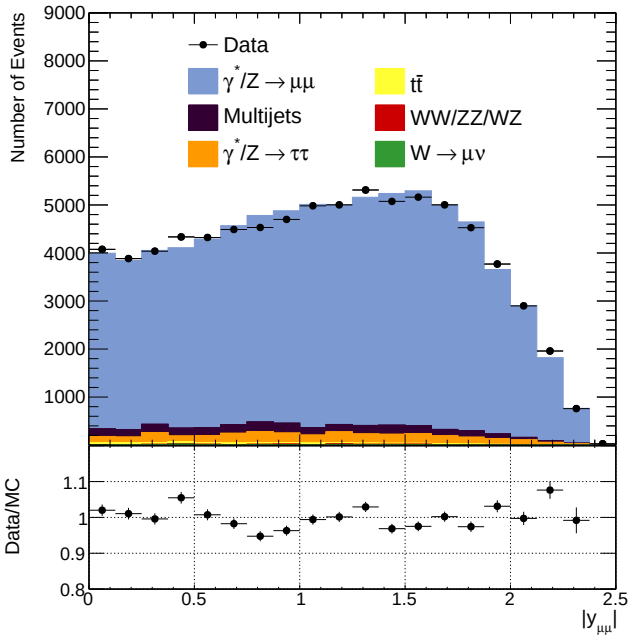

(b) $|y_{\mu\mu}|$ Distribution

Figure 7.4: Di-muon $p_T^{\mu\mu}$ and $|y_{\mu\mu}|$ control plots.

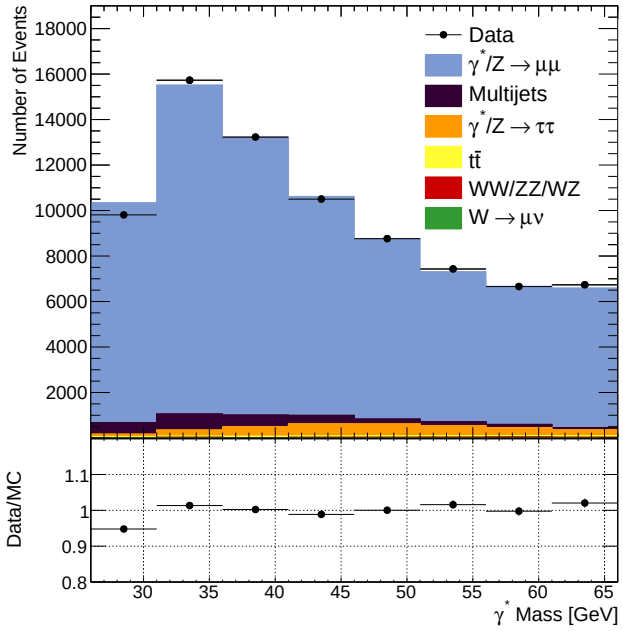

Figure 7.5: $M_{\mu\mu}$ Distribution.

7.2 Cutflow Tables

The effect of each cut is shown in the cutflow tables 7.1 and 7.2 where each of the cuts is applied in turn. As well as the cuts described in section 4.4 an additional loose cut on the muon p_T and η was included in order to increase the speed of the analysis code. For these cuts both the muons are required to have $p_T > 6$ GeV and $|\eta| < 2.5$. The p_T cut was chosen to allow the scale factor packages to be used effectively as they are only valid for muons with $p_T > 6$ GeV. Therefore after this cut the scale factors are applied, although $k-$factors, luminosity normalisation and pile-up reweighting are applied throughout. It is the introduction of the scale factors that is the cause of the increase of events seen between the N_{vertex} cut and the loose p_T and η cuts for the signal Monte Carlo sample. The multijet background estimation described in chapter 6 cannot be applied until after the charge of the muons has been considered and is therefore not applied until this cut, with the number of events listed before that being treated the same as the other background Monte Carlo samples. It should be noted that the small percentage of signal events passing the trigger is due to the fact that the sample goes down to $p_T^{\mu} > 3$ GeV. Thus the `EF_2mu10_loose` trigger will remove a relatively large fraction of events. Similarly the small percentage of signal events passing the invariant mass cut is due to the lower mass sample being produced for masses $M_{Z/\gamma^*} > 15$ GeV and the larger mass sample being produced with no explicit upper mass cut. Due to this the ratio of the final and first numbers in the signal row of table 7.1 does not give the signal efficiency.

Sample	GRL	Trigger	LAr Errors	N_{Muon}	N_{Vertex}	Muon p_T and η Loose	Same Vertex	Track Quality	Muon p_T and η	Opposite Charge	Isolation	$M_{\mu\mu}$
Data	1.76×10^8	3.32×10^6	3.31×10^6	2.67×10^6	2.67×10^6	2.59×10^6	1.69×10^6	1.62×10^6	865397	819235	642384	78847
$Z/\gamma^* \to \mu\mu$	2.45×10^6	694161	694161	689026	685543	710264	706580	603359	590657	590551	574343	72703
$Z/\gamma^* \to \tau\tau$	7.27×10^6	6477	6477	6289	6267	6253	5352	5112	3558	3519	3310	2919
Multijet	4.46×10^6	2.32×10^6	2.32×10^6	2.26×10^6	2.26×10^6	2.25×10^6	1.01×10^6	972967	303707	129915	8218	2715
$t\bar{t}$	174186	7571	7571	7485	7482	5818	3686	3544	3033	2375	1454	446
$WW/ZZ/WZ$	39686	1427	1427	1405	1402	1400	1358	1297	1220	1174	1090	168
$W \to \mu\nu$	1.46×10^7	12130	12130	5428	5419	5271	4116	3810	2338	1847	215	80

Table 7.1: A cut flow table showing the number of events passing each cut. The dashed vertical lines indicate the point in the cut flow where weights were applied to the Monte Carlo, as described in the text.

Sample	GRL	Trigger	LAr Errors	N_{Muon}	N_{Vertex}	Muon p_T and η Loose	Same Vertex	Track Quality	Muon p_T and η	Opposite Charge	Isolation	$M_{\mu\mu}$
Data	100.0%	1.9%	99.6%	80.7%	99.8%	97.1%	65.4%	95.6%	53.4%	94.7%	78.4%	12.3%
$Z/\gamma^* \to \mu\mu$	100.0%	28.3%	100.0%	99.3%	99.5%	103.6%	99.5%	85.4%	97.9%	100.0%	97.3%	12.7%
$Z/\gamma^* \to \tau\tau$	100.0%	0.1%	100.0%	97.1%	99.7%	99.8%	85.6%	95.5%	69.6%	98.9%	94.1%	88.2%
Multijet	100.0%	52.1%	100.0%	97.3%	99.9%	99.6%	44.9%	96.2%	31.2%	42.8%	6.3%	33.0%
$t\bar{t}$	100.0%	4.3%	100.0%	98.9%	100.0%	77.7%	63.4%	96.1%	85.6%	78.3%	61.2%	30.7%
$WW/ZZ/WZ$	100.0%	3.6%	100.0%	98.5%	99.7%	99.9%	97.0%	95.5%	94.1%	96.2%	92.9%	15.4%
$W \to \mu\nu$	100.0%	0.1%	100.0%	44.7%	99.8%	97.3%	78.1%	92.6%	61.4%	79.0%	11.6%	37.1%

Table 7.2: A cut flow table showing the percentage of events passing each cut with respect to the previous cut. The dashed vertical lines indicate the point in the cut flow where weights were applied to the Monte Carlo, as described in the text.

Chapter 8

Low Mass Drell-Yan Differential Cross Sections

The fiducial differential cross section as a function of the di-muon invariant mass has been measured in the kinematic region defined by the muon selection p_T and $|\eta|$ cuts and is also extrapolated to the total phase space.

In this chapter the calculation of the cross sections and the uncertainties considered are discussed. The fiducial differential cross section measurement is compared to NLO and NNLO theoretical predictions.

The differential mass cross section is defined for each bin, i, as

$$\left(\frac{d\sigma}{dM_{\mu\mu}}\right)_i = \frac{N_i - B_i}{\mathcal{L} C_{\gamma^* i} (\Delta M)_i}, \tag{8.1}$$

where N_i and B_i are the number of selected data and Monte Carlo background events respectively, $\mathcal{L}$ is the integrated luminosity of the data (1.64 pb^{-1}), $C_{\gamma^* i}$ is the unfolding factor discussed in section 8.1 and $(\Delta M)_i$ is the width of the histogram bins (5 GeV).

8.1 Unfolding

The detector has a finite resolution which can cause distortions to physical distributions. Corrections to the Monte Carlo discussed in section 4.3 only adjust the efficiencies and resolution of the Monte Carlo to that of the data. The full effect of these distortions on the cross section is taken into consideration by unfolding the `Pythia` signal Monte Carlo samples after all corrections have been applied.

These distortions are estimated using the Monte Carlo both at the generator level and after reconstruction has be applied, which takes into account the detector effects. The detector effects can cause events to be reconstructed in a different bin to where they were generated. Events can also not be reconstructed at all, or be reconstructed where there was no event generated (due to detector noise). These three effects are described by the response matrix, R_{ij}, which connects the events generated in one bin to those

reconstructed in others. The matrix is defined [99] as

$$R_{ij} = \frac{P(\text{observed in bin } i \text{ and true value in bin } j)}{P(\text{true value in bin } j)}, \tag{8.2}$$

$$= P(\text{observed in bin } i \mid \text{true value in bin } j), \tag{8.3}$$

which describes the truth distribution in bins of j, and the reconstructed distribution in bins of i. If the effects of resolution are negligible the response matrix (if $N_i = N_j$) is diagonal, $R_{ij} = \delta_{ij}\varepsilon_j$, where ε_j is the average detection efficiency over bin j.

The inverse of the response matrix can be applied to the measured cross section to unfold the result. However, if the migrations between bins are small enough and the mass bins (in our case) are large enough compared to the mass resolution of the detector then the diagonal elements alone can be used. This significantly simplifies the unfolding procedure and is known as bin-by-bin unfolding. The unfolding factor for each invariant mass bin, i, is given by

$$C_{\gamma^* i} = \frac{N_i^{reco}}{N_i^{gen}}, \tag{8.4}$$

where N_i^{gen} is the number of events generated in that bin and N_i^{reco} is the number of events reconstructed in that bin. This factor accounts both for efficiency and for migration of events between bins. The numerator has all Monte Carlo corrections applied and is simply taken from the Monte Carlo signal distribution as seen in the di-muon invariant mass control plot in figure 7.5. It is through the numerator that the scale factor corrections to the signal Monte Carlo are propagated to measured cross section. The denominator is obtained from the generator level events in the signal Monte Carlo samples. Born level (muons before they emit a FSR photon) generator Monte Carlo events are used. This allows the C_{γ^*} factor to also account for FSR. Cuts to select events in the fiducial volume are applied at generator level, selecting the two muons with the highest p_T, such that,

- $p_T^{\mu_1} > 15$ GeV
- $p_T^{\mu_2} > 12$ GeV
- $|\eta^{\mu_{1,2}}| < 2.4$
- 26 GeV $< M_{\mu\mu} <$ 66 GeV
- Opposite sign

Appropriate Monte Carlo corrections are also applied to the generator distribution, here the NLO k-factors, luminosity normalisation and pile-up reweighting corrections are made. The C_{γ^*} distribution can be seen in figure 8.1(a), the statistical errors on this ratio, plotted in figure 8.1(b), are calculated using binomial uncertainties. This is an approximate treatment of the errors. Although the numerator is not a true sub-selection of the denominator it is highly correlated to a sub-selection of it. The small uncertainty in the final invariant mass bin of figure 8.1 is due to it being populated by the Monte Carlo sample

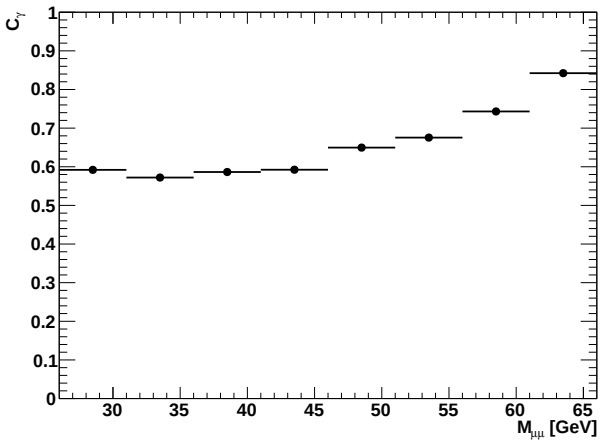

(a)

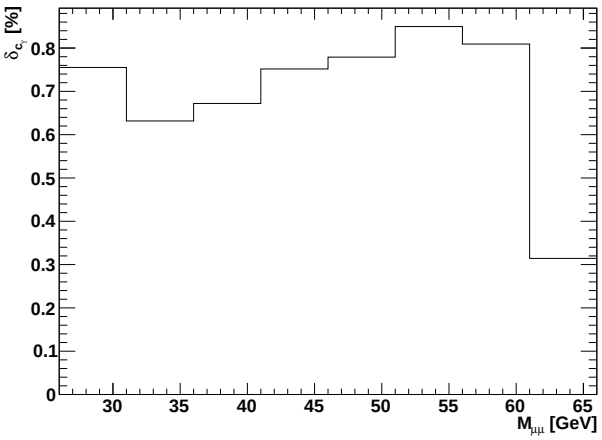

(b)

Figure 8.1: Figures showing (a) the bin-by-bin unfolding factor C_{γ^*} and (b) the statistical uncertainty on the unfolding factor.

generated in a mass range of $M_{\gamma^*/Z} > 60$ GeV, this sample has much higher statistics than the low mass sample, leading to a smaller uncertainty.

Bin-by-bin unfolding does not fully take into account migration of events between bins due to the effect of detector resolution. However, this effect is expected to be small as the purity of the bins is high. The purity has been calculated by the ATLAS low mass Drell-Yan group [1] and is defined as

$$Purity = \frac{N(\text{generated and reconstructed in bin } i)}{N(\text{reconstructed in bin } i)}. \tag{8.5}$$

The purity, as shown by figure 8.2(a), is greater than 80% for all bins, increasing up to ~ 92% in the lowest mass bin. Figure 8.2(b) shows the average mass difference between the reconstructed and truth level events. The $y-$axis error bars show the RMS of the mass difference for each bin, this is a measure of the mass resolution for the selected muons. It can clearly be seen that the RMS spread of the mass difference is much smaller than the width of the mass bins. This further demonstrates the suitability of the bin-by-bin

unfolding method.

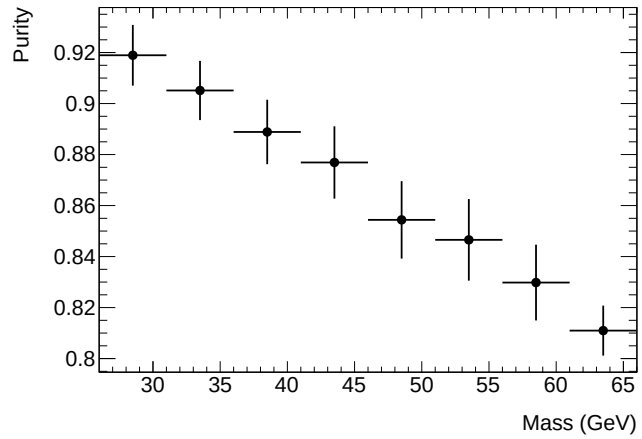

(a)

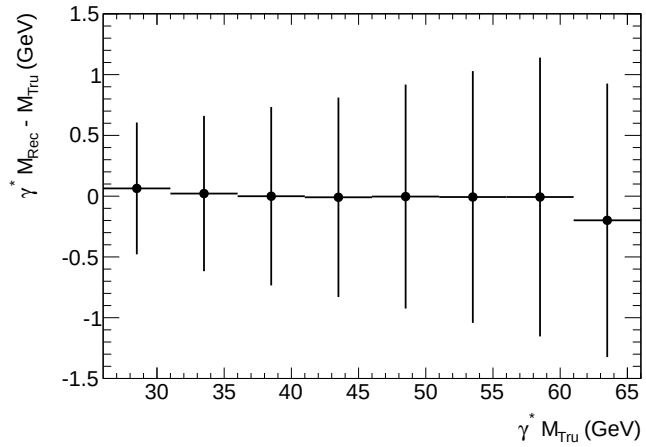

(b)

Figure 8.2: Figures showing (a) purity as a function of mass and (b) mass resolution as a function of mass [1].

Bin-by-bin unfolding can introduce a bias, this is the difference between the unfolded cross section and the true cross section in nature. This can be expressed for each bin, i, as

$$b_i = \left(\frac{N_i^{gen}}{N_i^{reco}} - \frac{N_i^{gen'}}{N_i^{reco'}} \right) N_i^{reco'} \tag{8.6}$$

$$= \left(\frac{1}{C_{\gamma^* i}} - \frac{1}{C'_{\gamma^* i}} \right) N_i^{reco'} \tag{8.7}$$

where, N_i^{gen} and N_i^{reco} are the number of generated and reconstructed events as in equation 8.4. The primed variables, $N_i^{gen'}$, $N_i^{reco'}$, and $C'_{\gamma^* i}$ are the values of N_i^{gen},N_i^{reco}, and $C_{\gamma^* i}$ if perfectly represented nature. These are in principle unknown, as this is the reason for making the measurement. The more accurately $C_{\gamma^* i}$ describes $C'_{\gamma^* i}$ the smaller the bias. The value of N_i^{gen} can differ from $N_i^{gen'}$ due to the mis-modelling of the mass spectrum being wrong either through mis-modelling or due to processes in nature not being

represented. The value of N_i^{reco} can also wrong for the same reasons, as well as due to mis-modelling of the detector response or of physical variables used in the event selection. The use of bins wider than any smearing that occurs means that while N_i^{gen} and N_i^{reco} can be mis-modelled the ratio, $C_{\gamma^* i}$, will be approximately correct [100]. The effect of the bias is to pull the unfolded cross section towards that of the generator used to calculate the C_{γ^*} factors. The effect of this could be estimated by using different Monte Carlo generators to calculate C_{γ^*}, or by reweighting the existing Monte Carlo samples.

Although the effect of the bias was not estimated for this measurement, the unfolding method was cross-checked with an iterative Bayesian unfolding technique [101] which was found to give consistent results [1]. The iterative Bayesian unfolding technique, uses the Bayes approach, using an iterative procedure to overcome the lack of a knowledge of a prior distribution. It has been shown that the method does not bias the result [101]. The approach is however much more involved, and it was felt that as the bin-by-bin unfolding could be justified it was better to use the simpler option, using the Bayesian unfolding as a cross check. The ratio of the unfolding factors from these two methods can be seen in figure 8.3. The uncertainties on the ratio come from the bin-by-bin unfolding alone, demonstrating that the uncertainty from the finite Monte Carlo statistics alone covers any difference between the two unfolding methods.

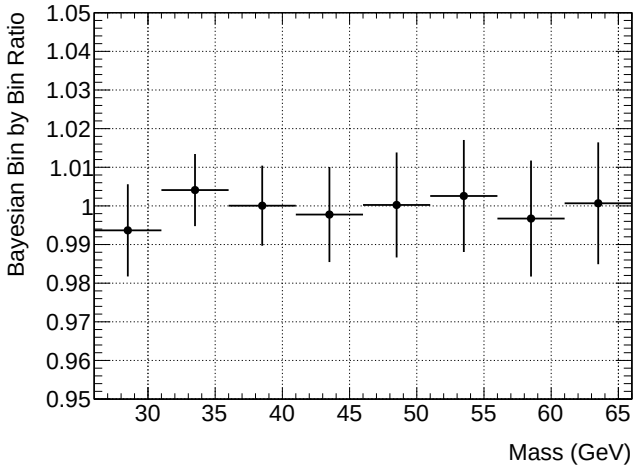

Figure 8.3: Figure showing the ratio of the unfolding factor as calculated by the bin-by-bin and Bayesian methods. The uncertainties are from the bin-by-bin unfolding [1].

8.2 Uncertainties on the Cross Section

Uncertainties on the cross section measurement are considered for a number of sources. Systematic uncertainties are obtained by calculating the fiducial differential mass cross section using the standard Monte Carlo corrections as discussed in section 4.3, then varying the corrections by the uncertainties associated with them. The difference between the central value and the cross section value coming from the shifted uncertainty is given as the cross section uncertainty. Figure 8.4 shows the percentage uncertainty on the fiducial differential cross section from each of the sources considered, these are discussed in the following section. The values for each source of systematic uncertainty is given in table 8.1.

The total systematic uncertainty is obtained by adding the uncertainty from each source in quadrature. This is also listed for each mass bin in table 8.2, along with the statistical uncertainty for each bin.

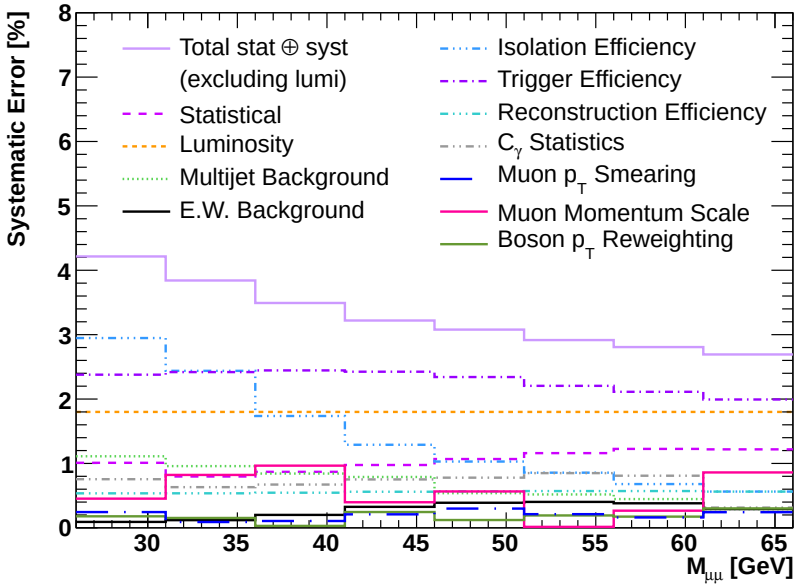

Figure 8.4: Percentage uncertainties on the cross section from a number of sources. The luminosity error of 1.8% *is not included in the total error.*

8.2.1 Data Statistical Precision

The fractional uncertainty for each invariant mass bin, i, is calculated as

$$\delta_i^{stat} = \sqrt{N_i}, \tag{8.8}$$

where, as with equation 8.1, N_i is the number of data events in each bin. This gives an uncertainty on the measured cross section that varies between 0.8% and 1.2%.

8.2.2 Efficiency Scale Factors

The scale factors applied to the Monte Carlo to correct the reconstruction, isolation and trigger efficiencies all have uncertainties associated with them, as seen in section 4.3.2. The cross section is calculated using the scale factor shifted up and down by its uncertainty. As the amount of background is very small, these scale factor shifts mainly enter the cross section through the $C_{\gamma*}$ factor. The cross section uncertainty from each scale factor, δ, is then taken as the largest shift away from the central value, such that

$$\delta = \max\left(\sigma_0 - \sigma_+, \sigma_0 - \sigma_-\right), \tag{8.9}$$

where σ_0 is the central cross section and σ_+ and σ_- are the cross sections calculated with the scale factor under consideration shifted up and down respectively. The isolation and reconstruction efficiency correction scale factors have uncertainties coming from both sta-

tistical and systematic sources. To get the total shifts from these, the uncertainty on the cross section from each source was calculated and added in quadrature. The trigger efficiency scale factor uncertainties have already had the statistical and systematic errors added in quadrature, so only a single pair of shifted cross sections are calculated. It can clearly be seen in figure 8.4 that the largest contribution to the systematic uncertainty in the majority of mass bins comes from trigger efficiency scale factor uncertainty, δ^{trig}, varying from 2.4% down to 2.0% with increasing mass. The isolation efficiency scale factor uncertainty, δ^{iso}, which varies from 3.0% down to 0.6% with increasing mass is the dominant source of uncertainty in the first mass bin. The uncertainty from the reconstruction efficiency scale factors, δ^{reco}, is both smaller and more constant, giving a 0.5% uncertainty in all invariant mass bins.

8.2.3 Muon p_T Smearing

The cross section uncertainty from smearing the Monte Carlo muon p_T is obtained by separately shifting the smearing to the muon spectrometer (MS) and inner detector (ID) parts of the muon track by their respective uncertainties. The cross section is calculated for each smearing and an uncertainty for that smearing type determined as the smearing that causes the maximum shift away from the central cross section [76]. The uncertainty from the MS and ID smearing are then added in quadrature, such that

$$\delta^{p_T\ \text{smear}} = \max(\sigma_0 - \sigma_+^{ms}, \sigma_0 - \sigma_-^{ms}) \oplus \max(\sigma_0 - \sigma_+^{id}, \sigma_0 - \sigma_-^{id}). \tag{8.10}$$

This produces small uncertainties on the measured cross section between 0.1% and 0.3%.

8.2.4 Muon Momentum Scaling

The uncertainty on the momentum scale correction was obtained by calculating the differential cross section with the scale correction turned off and taking the difference with the central cross section [76]. This contributes a cross section uncertainty, $\delta^{p_T\ \text{scale}}$, varying between 0.0% and 1.0%.

8.2.5 Luminosity

The official ATLAS luminosity uncertainty for the 2011 dataset is given as 1.8% [96]. As is convention this uncertainty is not included in the total cross section uncertainty.

8.2.6 Monte Carlo Statistics

The statistical uncertainty on the cross section is solely from data. Statistical uncertainty from the Monte Carlo, δ^{MC}, is treated as a systematic error, the uncertainty from the C_{γ^*} factor shown in figure 8.1(b) is used for this purpose, producing cross section uncertainties between 0.3% and 0.9%.

8.2.7 Electroweak Backgrounds

The uncertainty from the production cross sections of the electroweak backgrounds are also considered. These are the backgrounds from $WW/WZ/ZZ$ diboson, $\tau\tau$, $t\bar{t}$ and $W \to \mu\nu$ events. The total number of selected electroweak events is varied up and down by the 5% production cross section uncertainty, as was done in [92]. The uncertainties on the calculated Drell-Yan cross section, $\delta^{e.w.}$, is obtained with equation 8.9, giving an uncertainty on the measured cross section that varies between 0.1% and 0.4%.

8.2.8 Multijet Estimation

The multijet background contribution is varied by the 20% uncertainty calculated in chapter 6, the uncertainty on the cross section, $\delta^{m.j.}$, is then calculated with equation 8.9, which gives a cross section uncertainty varying between 0.3% and 1.1% with decreasing invariant mass.

8.2.9 Di-Muon p_T Reweighting

The 2011 ATLAS tuned `Pythia6` signal Monte Carlo samples do not model the Z/γ^* p_T distribution well. This was evident in figure 7.4(a) where the poor agreement between data and Monte Carlo could be seen. The effect of reweighting the di-muon p_T distribution of the signal Monte Carlo samples to a sample generated with `POWHEG` and hadronised with `Pythia8` was examined using the official `BosonPtReweightingTool`[1]. The difference between the unweighted and reweighted cross section was considered as an additional systematic uncertainty, δ^{reweight}, due to the modelling of the Monte Carlo. Figures 8.5(a), 8.5(b) and 8.5(c) show the di-muon p_T, the di-muon invariant mass and the muon p_T spectra after p_T reweighting has been applied.

The reweighting improves the agreement between the data and the Monte Carlo for the di-muon p_T and invariant mass spectra. However agreement between the data and the Monte Carlo in the muon p_T spectra is much worse, particularly at higher muon p_T. The effect of the p_T reweighting on the measured differential fiducial cross section was also examined. The uncertainty on the differential cross section is found to be between 0.0% and 0.3%.

[1] From the `egammaAnalysisUtils-00-03-59` package.

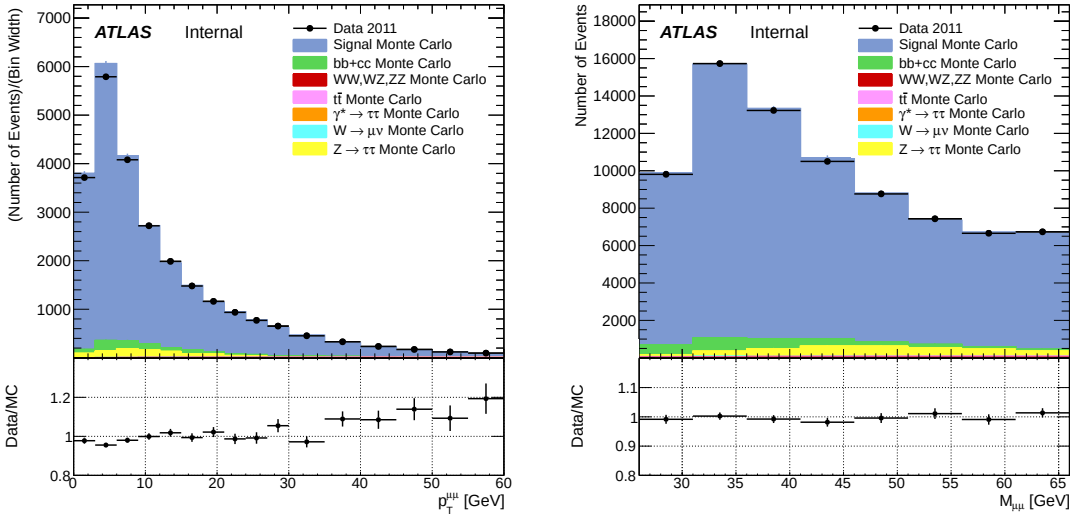

(a) (b)

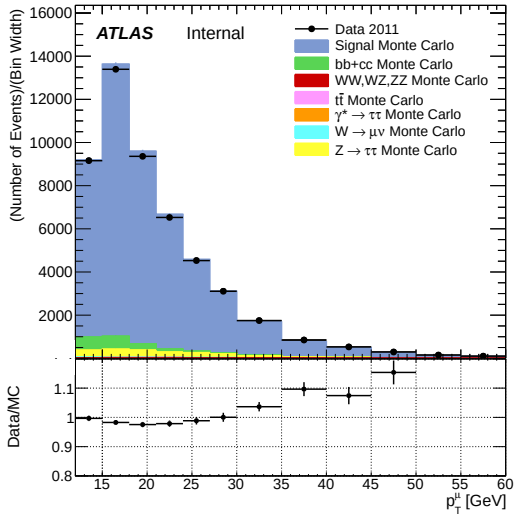

(c)

Figure 8.5: Control plots after the p_T reweighting has been applied to the signal Monte Carlo samples. Figures (a) and (b) show the di-muon p_T and invariant mass. Figure (c) shows the p_T of the muons.

8.2.10 Correlation of Uncertainties

Bin-to-bin correlations of the uncertainties have been considered, if a change to the source of the uncertainty causes the values of the cross section to change in all bins then the uncertainty is considered correlated. Table 8.1 shows the systematic uncertainties obtained; $\delta^{\text{reco}}_{\text{cor}}$ and $\delta^{\text{iso}}_{\text{cor}}$ are the uncertainties on the cross section from varying the reconstruction and isolation scale factors by the systematic uncertainty associated with them. The $\delta^{\text{reco}}_{\text{unc}}$ and $\delta^{\text{iso}}_{\text{unc}}$ uncertainties are obtained from varying the scale factors by the statistical uncertainty associated with them. The uncertainty from the trigger efficiency scale factors is considered uncorrelated as the uncertainty on the scale factor is dominated by the statistical uncertainty. This information is important when combining this analysis with the

electron channel as discussed in chapter 9.

	Correlated						Uncorrelated				
$M_{\mu\mu}$	$\delta^{\text{reco}}_{\text{cor}}$	$\delta^{\text{iso}}_{\text{cor}}$	$\delta^{\text{m.j.}}$	$\delta^{\text{e.w.}}$	$\delta^{p_T \text{ scale}}$	δ^{reweight}	$\delta^{\text{reco}}_{\text{unc}}$	δ^{trig}	$\delta^{\text{iso}}_{\text{unc}}$	δ^{smear}	δ^{MC}
[GeV]	[%]	[%]	[%]	[%]	[%]	[%]	[%]	[%]	[%]	[%]	[%]
26 – 31	0.5	2.6	-1.1	-0.1	-0.5	-0.2	0.2	2.4	1.4	0.2	0.8
31 – 36	0.5	2.1	-1.0	-0.1	-0.8	0.2	0.2	2.4	1.2	0.1	0.6
36 – 41	0.5	1.5	-0.8	-0.2	-1.0	0.0	0.2	2.4	0.9	0.1	0.7
41 – 46	0.5	1.1	-0.8	-0.3	-0.4	-0.3	0.2	2.4	0.7	0.2	0.8
46 – 51	0.5	0.9	-0.5	-0.4	-0.6	-0.1	0.2	2.3	0.5	0.3	0.8
51 – 56	0.5	0.7	-0.5	-0.4	-0.0	-0.2	0.2	2.2	0.5	0.2	0.9
56 – 61	0.5	0.6	-0.4	-0.4	-0.3	-0.2	0.2	2.1	0.4	0.2	0.8
61 – 66	0.5	0.5	-0.3	-0.3	0.9	-0.3	0.2	2.0	0.3	0.2	0.3

*Table 8.1: Bin-by-bin breakdown of the systematic uncertainties. The luminosity uncertainty (*1.8%*) is not included.*

The signs assigned to the correlated uncertainties are assigned consistently by the electron and muon channels. This is important for the combination of the two measurements in PDF fits. The $\delta^{\text{m.j.}}$ and $\delta^{\text{e.w.}}$ uncertainties are negative as an increase in the cross section of these backgrounds would cause the calculated Drell-Yan cross section to decrease. The $\delta^{\text{reco}}_{\text{cor}}$ and $\delta^{\text{iso}}_{\text{cor}}$ which are calculated via the scale factors are positive, as an increase in the efficiency of the Monte Carlo would cause a decrease in the scale factor which in turn would lead to an increase in the calculated Drell-Yan cross section. The $\delta^{p_T \text{ scale}}$ has the sign assigned according to whether turning the p_T scaling off causes the calculated Drell-Yan cross section to increase or decrease. A similar approach is taken to assigning a sign to δ^{reweight}, where the effect of turning the reweighting on is considered.

All of the systematic uncertainties are considered either fully correlated or fully uncorrelated. This approach was taken as reasonable approximation. As mentioned above the uncorrelated systematic uncertainties are taken as uncorrelated as they arise from mostly statistical fluctuations either in data, or Monte Carlo or in the scale factor estimates. All other systematic uncertainties are considered to be 100% correlated bin-to-bin. This assumes for example, that the multijet and electroweak background estimates only differs from the true background in normalisation. Whereas the reconstruction, isolation and muon p_T scale uncertainties are defined to be coherent shifts of the efficiency (or scale) and must be taken to be 100% correlated.

8.3 Fiducial Differential Cross Section

The fiducial differential cross section was calculated as described in equation 8.1. The born fiducial cross section is the main measurement of this analysis. Although it is only measured in a restricted phase space defined by the fiducial cuts on the muons, all of the uncertainty on the result is due to experimental errors. This is in contrast to the extrapolated cross section discussed in section 8.4 which has large theoretical uncertainties associated with it. It is therefore the fiducial cross section that is best compared to theory, and it is the fiducial cross section that can be used in PDF fits. The cross section and

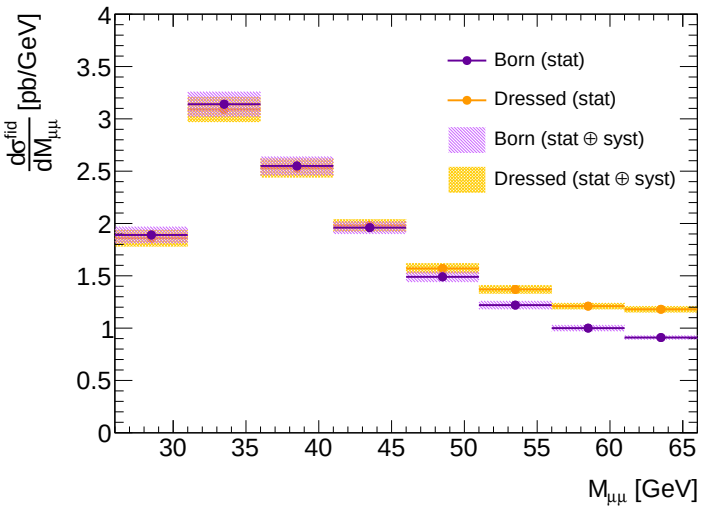

Figure 8.6: Fiducial differential cross section measured at the born and dressed levels.

statistical and systematic uncertainty for each invariant mass bin is shown in table 8.2. The total uncertainty shown is the systematic and statistical uncertainties added in quadrature. The measurement is dominated by the systematic uncertainties which vary between 4.1% and 2.4% in increasing mass.

In addition to the born fiducial cross section, the dressed fiducial cross section has also been measured. Here, corrections [1] calculated from generator level Monte Carlo are applied to the born level cross section to consider FSR photons in a cone of $\Delta R = 0.1$ around each muon, the four-vectors of which are then added to that of the muon. The dressed cross section is of less interest for theory comparisons, but can be useful for Monte Carlo tuning.

$M_{\mu\mu}$ [GeV]	N	B	C_{γ^*}	δ^{stat} [%]	δ^{syst} [%]	δ^{total} [%]	$\frac{d\sigma}{dM_{\mu\mu}}$ [pb/GeV]	$\frac{d\sigma^{dressed}}{dM_{\mu\mu}}$ [pb/GeV]
26-31	9809	675	0.59	1.0	4.1	4.2	1.89 ± 0.08	1.86 ± 0.08
31-36	15729	1053	0.57	0.8	3.8	3.8	3.14 ± 0.12	3.09 ± 0.12
36-41	13226	1005	0.59	0.9	3.4	3.5	2.55 ± 0.09	2.53 ± 0.09
41-46	10501	995	0.59	1.0	3.1	3.2	1.96 ± 0.06	1.98 ± 0.06
46-51	8762	831	0.65	1.1	2.9	3.1	1.49 ± 0.05	1.57 ± 0.05
51-56	7430	715	0.68	1.2	2.7	2.9	1.22 ± 0.04	1.37 ± 0.04
56-61	6657	597	0.74	1.2	2.5	2.8	1.00 ± 0.03	1.21 ± 0.03
61-66	6733	457	0.84	1.2	2.4	2.7	0.91 ± 0.02	1.18 ± 0.03

Table 8.2: Bin-by-bin breakdown of the nominal muon channel differential cross section measurement, at born, $\frac{d\sigma}{dM_{\mu\mu}}$, and dressed, $\frac{d\sigma^{dressed}}{dM_{\mu\mu}}$, level as described in the text. Where N, B, and C_{γ^*} are defined as for equation 8.1. The statistical, δ^{stat}, systematic, δ^{syst}, and total, δ^{total}, uncertainties on the cross section are shown. The luminosity uncertainty (1.8%) is not included.

Figure 8.6 shows both the born and dressed fiducial differential cross sections. It is clear that the dressed corrections have a larger effect at higher mass, this is due to the migration of events which radiate photons, moving towards lower reconstructed masses away from the Z resonance.

8.3.1 Comparison to Theory

The born fiducial differential cross section obtained is compared to three theoretical predictions. All three sets of predicted cross sections and uncertainties, shown in table 8.3, were calculated by the ATLAS low mass Drell-Yan group [1]. Two of these sets are produced using FEWZ, one at NLO in α_s, and one at NNLO in α_s. The third comparison is made with POWHEG which is a NLO Monte Carlo generator that also includes leading-log parton showers (LLPS) matched to the NLO result. The table shows the uncertainties from scale and PDF variations.

	POWHEG			NLO FEWZ			NNLO FEWZ		
M_{ll} [GeV]	$\frac{d\sigma}{dM_{ll}}$ [pb/GeV]	δ^{pdf} [%]	δ^{scale} [%]	$\frac{d\sigma}{dM_{ll}}$ [pb/GeV]	δ^{pdf} [%]	δ^{scale} [%]	$\frac{d\sigma}{dM_{ll}}$ [pb/GeV]	δ^{pdf} [%]	δ^{scale} [%]
26 – 31	1.80	2.5	$^{+7.3}_{-11.4}$	2.22	2.7	$^{+4.9}_{-7.9}$	1.93	$^{+3.5}_{-2.6}$	5.7
31 – 36	3.12	2.4	$^{+5.3}_{-10.0}$	3.49	2.7	$^{+4.7}_{-6.3}$	2.99	$^{+3.2}_{-2.5}$	4.5
36 – 41	2.64	2.3	$^{+4.6}_{-8.8}$	2.68	2.6	$^{+4.1}_{-5.0}$	2.52	$^{+3.1}_{-2.4}$	2.3
41 – 46	2.03	2.2	$^{+3.5}_{-7.5}$	1.99	2.6	$^{+3.6}_{-4.2}$	1.94	$^{+3.1}_{-2.3}$	2.1
46 – 51	1.54	1.9	$^{+3.7}_{-6.1}$	1.51	2.5	$^{+3.2}_{-3.5}$	1.47	$^{+3.0}_{-2.2}$	1.7
51 – 56	1.19	2.4	$^{+4.5}_{-5.1}$	1.17	2.4	$^{+2.8}_{-2.9}$	1.15	$^{+2.9}_{-2.2}$	1.3
56 – 61	1.00	2.4	$^{+2.3}_{-4.7}$	0.96	2.4	$^{+2.6}_{-2.6}$	0.96	$^{+2.9}_{-2.1}$	1.3
61 – 66	0.90	2.1	$^{+2.0}_{-4.5}$	0.87	2.3	$^{+2.3}_{-2.3}$	0.86	$^{+2.8}_{-2.1}$	1.2

Table 8.3: Theoretical predictions at NLO, NLO+LLPS and NNLO including the NLO EW and photon induced corrections described in table 8.4. The scale uncertainty, δ^{scale}, is defined as the envelope of variations for $0.5 \leq \mu_R, \mu_F \leq 2$ with the constraint that $0.5 \leq \mu_R/\mu_F \leq 2$ for POWHEG. For FEWZ the scale uncertainty is defined by the variation $0.5 \leq \mu_R = \mu_F \leq 2$. The PDF uncertainty is defined in section 8.3.1.2 [1]

8.3.1.1 Scale Variations

The uncertainties from the renormalisation, μ_R, and factorisation, μ_F, scales were estimated for all three theoretical predictions. Due to the extensive computing requirements of FEWZ the FEWZ and POWHEG samples have different definitions of the scale uncertainty. For POWHEG the uncertainty is defined by the envelope of $0.5 \leq \mu_R, \mu_F \leq 2$ with the constraint that $0.5 \leq \mu_R/\mu_F \leq 2$, whereas for the FEWZ predictions it is defined as $0.5 \leq \mu_R = \mu_F \leq 2$. As the two scales can be varied independently in POWHEG it would be expected to have larger scale uncertainties than the FEWZ prediction and this is shown in table 8.3. It can also be seen that these scale uncertainties for POWHEG are generally much larger than the PDF uncertainty. This can also be seen to a lesser extent for the NLO FEWZ predictions at lower masses. This is understood as being due to the fact that the region $M_{\mu\mu} \sim 2p_T^{\mu}$ cannot be populated fully. The move to NNLO FEWZ significantly reduces this theoretical uncertainty.

8.3.1.2 PDF Variations

All three theoretical predictions were produced using the appropriate MSTW2008 PDF set, the 68% CL uncertainty was calculated for each of these using the eigenvector error sets discussed in chapter 2. The uncertainty on the fiducial cross section, δ^{pdf}, for each bin, i, is defined [18] for the symmetric uncertainties as

$$\delta_i^{pdf} = \frac{1}{2}\sqrt{\sum_{k=1}^{n}\left[\sigma_i(S_k^+) - \sigma_i(S_k^-)\right]^2}, \tag{8.11}$$

where $\sigma_i(S_k^+)$ and $\sigma_i(S_k^-)$ are the cross sections calculated with the positive, S_k^+, or negative S_k^- PDF error from the k^{th} eigenvector pair. The asymmetric uncertainties are calculated as in equations 2.56 and 2.57.

8.3.1.3 Electroweak and Photon Induced Corrections

All three theoretical predictions have NLO in α electroweak corrections, Δ^{HOEW}, applied that consider initial and final state radiation and the interference between the two, calculated in `FEWZ` using the G_μ electroweak scheme (a parameterisation scheme which parameterises the electroweak theory in terms of G_μ, α and M_Z [102]). These corrections to the cross section vary between 1.10% and 4.09% with increasing mass. An uncertainty, δ^{scheme} is associated with these corrections, quantifying the difference between using the G_μ and the on-mass-shell electroweak schemes [2].

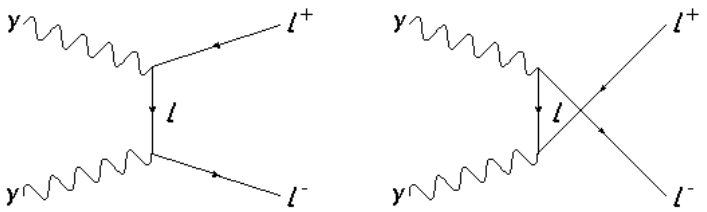

(a) (b)

Figure 8.7: Photon-photon processes producing a di-lepton pair.

All three predictions also have photon induced corrections, Δ^{PI}, applied, these corrections consider photon-photon interactions within the proton that produce a muon-antimuon pair as shown in figure 8.7. These are calculated using the LO MRST2004QED PDF set [36] which includes the photon distribution in the PDF, an uncertainty, δ^{PI}, of about 36% is applied to this which was calculated with equation 8.11. This correction increases the theoretical predictions by up to 2.2% in the higher mass bins.

Both sets of corrections can seen in table 8.4, the electroweak corrections are multiplicative and the photon induced corrections are additive.

8.3.2 Conclusion

Figure 8.8 shows the comparison of the measured fiducial differential cross section with the NLO predictions. It can be seen that `POWHEG` with its additional LLPS describes the data more accurately in the lower invariant mass bins than the NLO `FEWZ` prediction.

$M_{\mu\mu}$ [GeV]	Δ^{HOEW} [%]	Δ^{PI} [pb/GeV]	δ^{PI}[%]	δ^{scheme} [%]
26 – 31	1.10	0.005	36.0	4.6
31 – 36	3.10	0.051	35.9	1.5
36 – 41	3.92	0.053	35.7	0.8
41 – 46	4.25	0.045	35.6	0.5
46 – 51	4.46	0.036	35.6	0.4
51 – 56	4.43	0.029	35.7	0.4
56 – 61	4.47	0.023	35.8	0.3
61 – 66	4.09	0.019	35.9	0.4

Table 8.4: Higher order EW corrections; Δ^{HOEW}, the missing electroweak contribution, Δ^{PI}, the Photon Induced correction, δ^{PI}, the uncertainty in the photon induced piece, and δ^{scheme}, the uncertainty due to the non-convergence of calculations derived with different electroweak scheme. [1]

Figure 8.9 shows the comparison of the data to the NNLO `FEWZ` prediction. It can be seen that this also describes the data well. As such it is clear that a move beyond NLO is needed to describe the data. This statement can be made stronger by combining the results with the electron channel as dicussed in chapter 9.

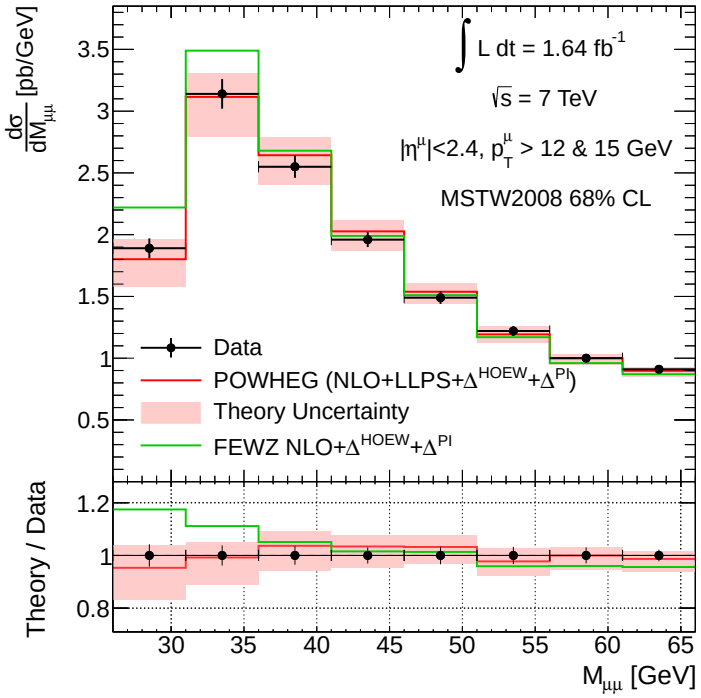

Figure 8.8: Measured differential cross section compared to NLO theoretical predictions.

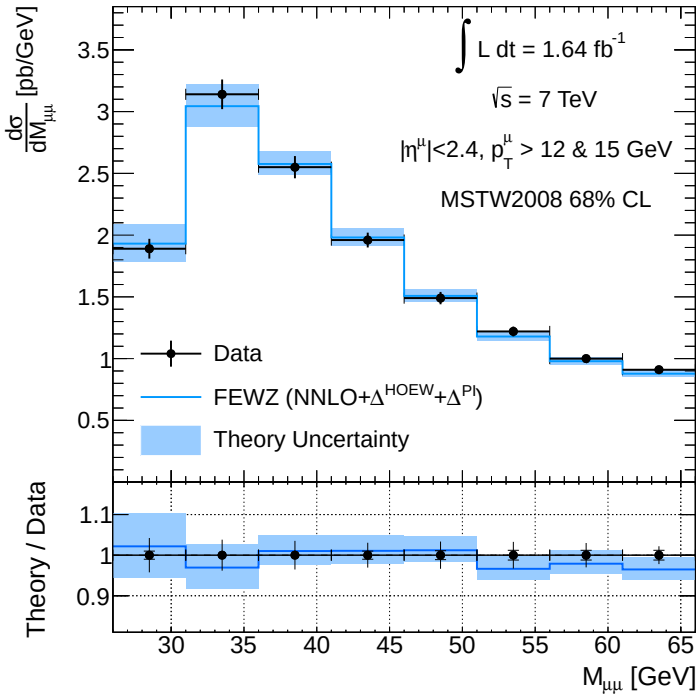

Figure 8.9: Measured differential cross section compared to NNLO theoretical predictions.

8.4 Extrapolated Differential Cross Section

The differential fiducial cross section is constrained by the ATLAS detector with the detector geometry imposing the $|\eta|$ range and trigger menu imposing the p_T cuts. Extrapolation to the full 4π and muon $p_T > 0$ phase space removes these constraints but is heavily reliant on Monte Carlo. The extrapolated cross section is presented to allow comparison with calculations that don't apply lepton cuts. The extrapolation to the total phase space is done with the acceptance factor, $\mathcal{A}$, which can be defined for each bin, i, as

$$\mathcal{A}_i = \frac{\sigma_i^{\text{fid}}}{\sigma_i^{\text{tot}}}, \tag{8.12}$$

where σ_i^{fid}, is the fiducial cross section, after the born level truth selection has been applied, and σ_i^{tot} is the cross section in the full phase space. These acceptances factors were determined by the ATLAS low mass Drell-Yan group using NNLO `FEWZ` with the MSTW2008nnlo PDF set. The acceptance factor for each bin is shown in table 8.5 along with the PDF and scale uncertainties, which are calculated as described in section 8.3.1.

The acceptance factors are applied to each bin, i, of the fiducial cross sections such that

$$\left(\frac{d\sigma^{\text{tot}}}{M_{\mu\mu}}\right)_i = \left(\frac{d\sigma^{\text{fid}}}{M_{\mu\mu}}\right)_i \cdot \frac{1}{\mathcal{A}_i}, \tag{8.13}$$

where $\left(\frac{d\sigma^{\text{tot}}}{M_{\mu\mu}}\right)_i$ and $\left(\frac{d\sigma^{\text{fid}}}{M_{\mu\mu}}\right)_i$ are the total cross section and fiducial cross section respectively in each mass bin. The corrections to the full phase space are large, varying between a

$M_{\mu\mu}$ [GeV]	$\mathcal{A}$	$\delta_{\mathcal{A}}^{\text{scale}}$ [%]	$\delta_{\mathcal{A}}^{\text{pdf}+\alpha_s}$ [%]
26 – 31	0.069	$^{-4.3}_{+4.7}$	$^{-2.0}_{+1.4}$
31 – 36	0.194	$^{-3.3}_{+3.7}$	$^{-1.6}_{+1.1}$
36 – 41	0.270	$^{-1.1}_{+1.6}$	$^{-1.4}_{+0.9}$
41 – 46	0.321	$^{-1.1}_{+1.5}$	$^{-1.2}_{+0.8}$
46 – 51	0.356	$^{-0.8}_{+1.2}$	$^{-1.0}_{+0.7}$
51 – 56	0.381	$^{-0.4}_{+0.8}$	$^{-1.0}_{+0.6}$
56 – 61	0.406	$^{-0.6}_{+0.9}$	$^{-0.9}_{+0.6}$
61 – 66	0.427	$^{-0.5}_{+0.8}$	$^{-0.8}_{+0.5}$

Table 8.5: The acceptance $\mathcal{A}$ and associated systematic uncertainties from scale variations and PDF+α_s uncertainties. The MSTW2008nnlo PDFs are used and the calculation is performed using NNLO `FEWZ`.

factor of 2.34 and 14.49 with decreasing invariant mass. The extrapolated differential cross section can be seen in figure 8.10. It can clearly be seen that the uncertainties at lower invariant mass have greatly increased compared to the fiducial cross section, these are dominated by the scale uncertainty on the acceptance factor. This is again due to the inability of the theoretical prediction to describe the $M_{\mu\mu} \sim 2p_T^{\mu}$ region due to the use of a fixed order calculation and highlights an area for theoretical improvement.

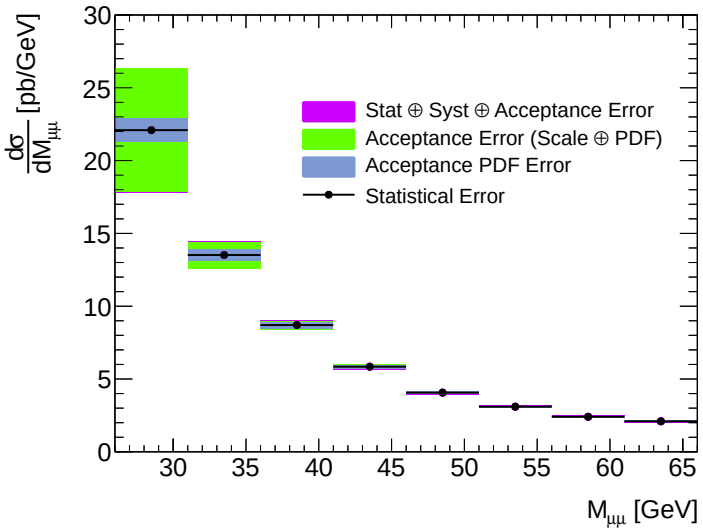

Figure 8.10: Extrapolated differential cross section.

8.5 Comparison to Other Experimental Results

The conclusions of this analysis are consistent with low mass Drell-Yan measurements made by the CMS [103] and LHCb [104] collaborations.

The CMS measurement was made using 36 pb^{-1} of 2010 collision data. The differential mass cross section was measured in an invariant mass range of $15 < M_{ll} < 600$ GeV. Both

the muon and electron channels are used and normalised to the cross section measured at the Z resonance ($60 < M_{ll} < 120$ GeV). The differential cross section over the full mass range is shown in figure 8.11.

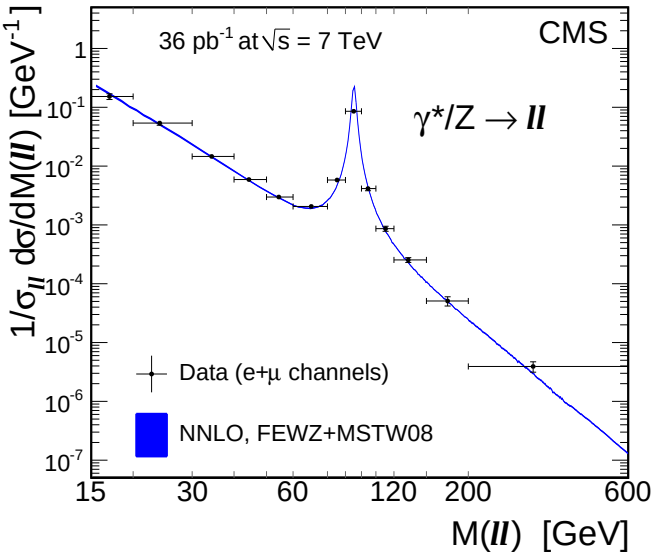

Figure 8.11: The CMS differential mass cross section normalised the the Z resonance region [103]. The vertical error bars indicate the experimental (statistical and systematic) uncertainties summed in quadrature with the theory uncertainties. Horizontal error bars indicate the bin width, with the position of each point being determined using bin centered corrections [105]. The uncertainty on the NNLO FEWZ prediction is indicated by the width of the curve.

For the muon channel, a kinematic region is defined where the triggered muon (a single muon trigger is used) is required to have $p_T^{trig} > 16$ GeV and $|\eta^{trig}| < 2.1$, with the other muon required to have $p_T > 7$ GeV and $|\eta| < 2.4$. The measurement also applies a restriction on the opening angle between the two muons, requiring that it differ from π by more than 5 mrad. This selects events where the dilepton system has been boosted, selecting higher order events where a gluon has been radiated from one of the colliding quarks, As such the measurement also concludes that NNLO theoretical predictions are needed to describe the cross section distribution for $M_{ll} < 30$ GeV. The normalisation to the Z resonance region allows the measurement to be independent of the luminosity uncertainty and to reduce many of the systematic uncertainties. The uncertainties on the fiducial ratio, (at the Born level) vary between 4.5% and 8.7% in the mass range $20 < M_{ll} < 60$ GeV which largely corresponds to the mass range considered in this thesis.

The LHCb result uses the muon channel in the acceptance of $2.0 < \eta < 4.5$ to measure the differential mass cross section in a mass range of $5 < M_{\mu\mu} < 120$ GeV as shown in figure 8.12. The cross section is also measured as a function of the rapidity of the muon pair in two mass regions.

Again, the measurement uses 2010 data, with a dataset of 37 pb^{-1}. Kinematic cuts require that both the muons have a momentum greater than 10 GeV and $p_T > 3$ GeV (or

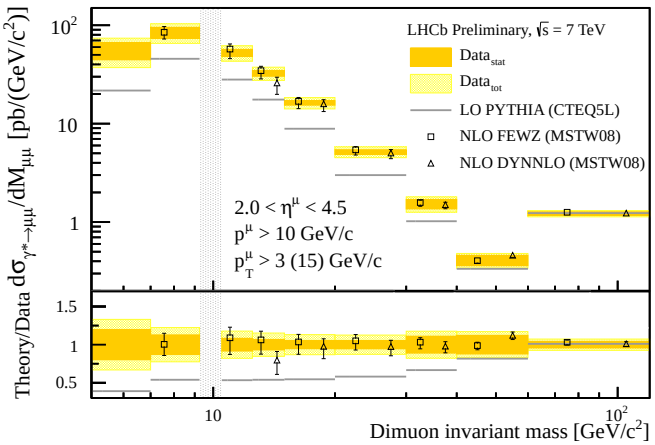

Figure 8.12: The LHCb differential mass cross section [104]. A comparison to Pythia, NLO FEWZ, and NLO DYNNLO is made. The points for the theoretical predictions are offset for clarity. The shaded vertical band indicates the Υ mass region which was excluded from the measurement. The two bins with $M_{\mu\mu} > 40$ GeV require $p_T^{\mu} > 15$ GeV. The good agreement with the NLO predictions can clearly be seen in the ratio plot.

$p_T > 15$ GeV for $M_{\mu\mu} > 40$ GeV). The differential mass cross section achieves uncertainties between 12.13% and 16.41% in the mass range of $20 < M_{\mu\mu} < 60$ GeV. The result is compared to NLO theoretical predictions from `FEWZ` and `DYNNLO` where good agreement is seen across the full mass range (apart from the lowest, $5 < M_{\mu\mu} < 7.5$ GeV, mass bin where no theoretical prediction can be obtained from `FEWZ` or `DYNNLO`). The LHCb analysis achieves a good agreement with an NLO calculation, whereas the analysis presented here and the one by CMS need an NNLO calculation to describe the data because of the choice of kinematic cuts. As discussed, the need to move beyond an NLO calculation is due to the region of phase space $M_{ll} \sim 2p_T^l$ not being properly populated. As the LHCb measurement has a selection with $M_{\mu\mu} \sim p_T^{\mu}$ this problem is avoided.

Chapter 9

Combination and QCD Fits

The work presented in this thesis forms part of a paper that is, at the time of writing, undergoing internal ATLAS approval [1]. The analysis presented in the paper consists of three analysis strands. Firstly, the nominal muon channel, the majority of which is presented in this thesis. A corresponding, nominal electron channel measurement is also measured in the same fiducial region. The final strand is referred to as the extended muon channel. The extended channel [106] is measured in a fiducial region of $p_T^{\mu_{1,2}} > 9,6$ GeV, $|\eta^{\mu_{1,2}}| < 2.4$ in a invariant mass range of $12 < M_{\mu\mu} < 66$ GeV. It uses 36 pb^{-1} of data collected in 2010, taking advantage of the small amount of pileup and the lower trigger thresholds from that year. A short summary of the results from the three strands is given here in order to place the measurement presented in this thesis in more context.

9.1 Combination of Nominal Muon and Electron Channels

The two nominal channels are combined using a method [107, 108] developed for the HERA experiments, it has also been used in a number of other ATLAS Standard Model measurements, such as [92, 109]. An average value for the fiducial cross section, m^i, is determined in each mass bin, by minimising the χ^2, which is defined as

$$\chi^2 = \sum_{k,i} \frac{\left[m^i - \left(\mu_k^i + \sum_j \gamma_{j,k}^i m^i b_j\right)\right]^2}{\left(\delta_{stat,k}^i\right)^2 \mu_k^i \left(m^i - \sum_j \gamma_{j,k}^i m^i b_j\right) + \left(\delta_{unc,k}^i m^i\right)^2} + \sum_j b_j^2, \tag{9.1}$$

where i, j and k run over bins, correlated systematic error sources and channels respectively. The measured cross section of bin i in channel k is given by μ_k^i. The relative correlated systematic, relative statistical and relative uncorrelated systematic uncertainties are given by $\gamma_{j,k}^i$ $\delta_{stat,k}^i$ and $\delta_{unc,k}^i$ respectively. The correlated systematic sources, j, are allowed to shift by b_j which is expressed as a fraction of the standard deviation. These shifts incur a χ^2 penalty of b_j^2, meaning deviations of m^i from μ_k^i are minimised. Figure 9.1 shows the nominal electron and muon channels and the combined differential cross section, which is in good agreement with a total $\chi^2/N_{DF} = 5.4/8$. No systematic error sources caused a shift of more than one standard deviation. The values for the combined cross sections, along with the associated uncertainties are given in table 9.1. It can be seen in figure 9.1 that the uncertainties on the muon channel are smaller than the elec-

tron channel. This means that the muon channel results will be given more weight in the combination.

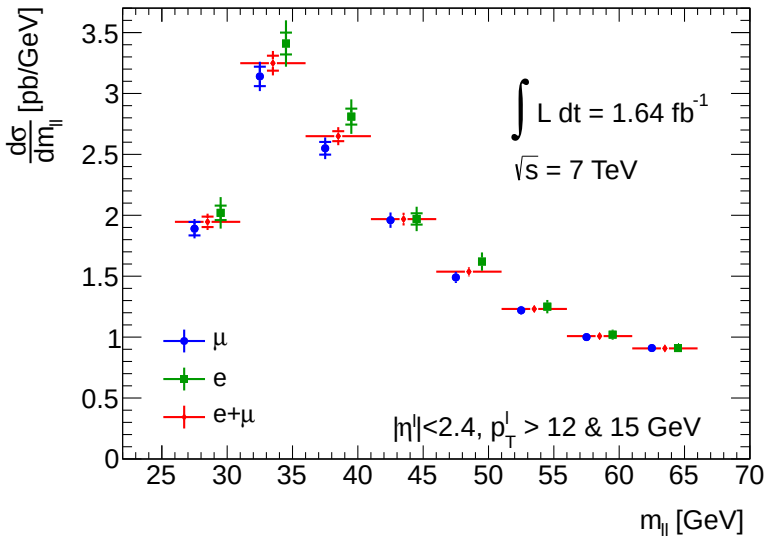

Figure 9.1: Fiducial differential cross section plot showing the nominal electron and muon channels along with the combined cross section [1].

The measured fiducial differential cross section for the combined analysis and the extended analysis are shown in figures 9.2 and 9.3, all plots compare data to theoretical predictions which have had NLO electroweak and photon induced corrections applied. The theoretical comparisons for the nominal analysis were discussed in section 8.3.1. Tables detailing the values and corrections for the extended muon analysis are given in appendix B.

It can be seen that all three theoretical predictions are largely in good agreement with the data at higher masses, but in the low mass bins, particularly in the extended analysis, the NLO `FEWZ` prediction doesn't describe the data well. As with the nominal muon channel alone, as discussed in section 8.3, the addition of the LLPS with the `POWHEG` prediction does a much better job of describing the data. Unlike with the nominal muon channel alone, however it can be seen that the move to full NNLO shows an even greater improvement in describing the data. This can be seen more quantitatively in table 9.2 which shows the χ^2 value comparing the data to each of the three theory predictions, where the χ^2 definition [110] takes into account the correlated systematic uncertainties. This the same χ^2 function shown in equation 9.7 where it is used in a PDF fit to the data. It is discussed further in appendix C.

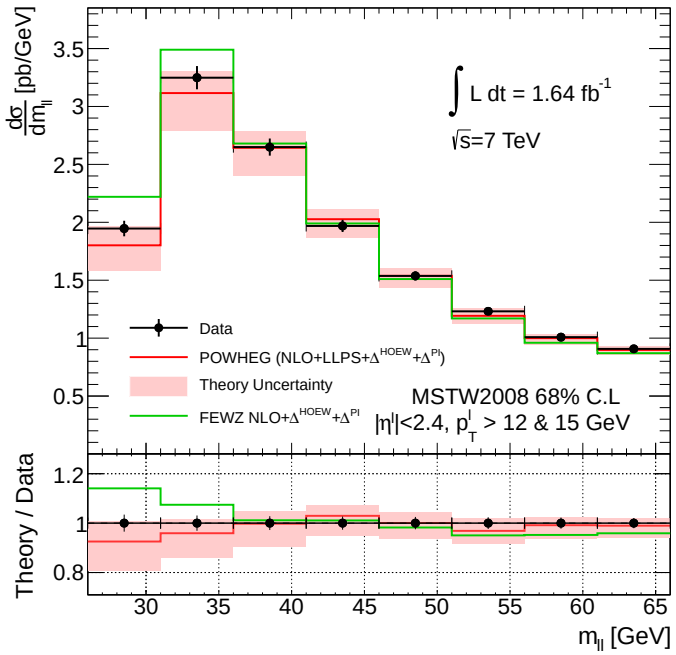

(a) Nominal Analysis

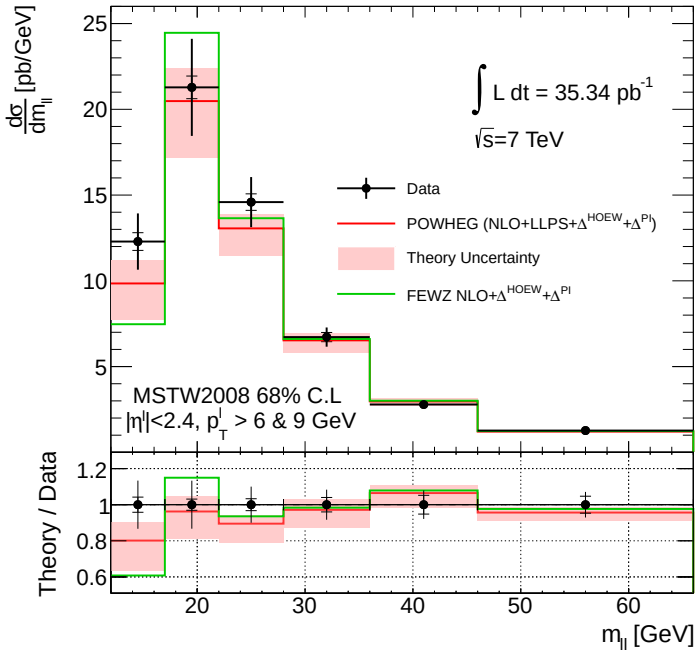

(b) Extended Analysis

Figure 9.2: Fiducial differential cross section at the born level for the combined electron and muon nominal analyses in (a) and the 2010 extended muon analysis in (b). Both plots compare data to theoretical predictions from NLO `FEWZ` *and NLO+LLPS* `POWHEG`*, both of which have NLO electroweak and photon induced corrections applied [1].*

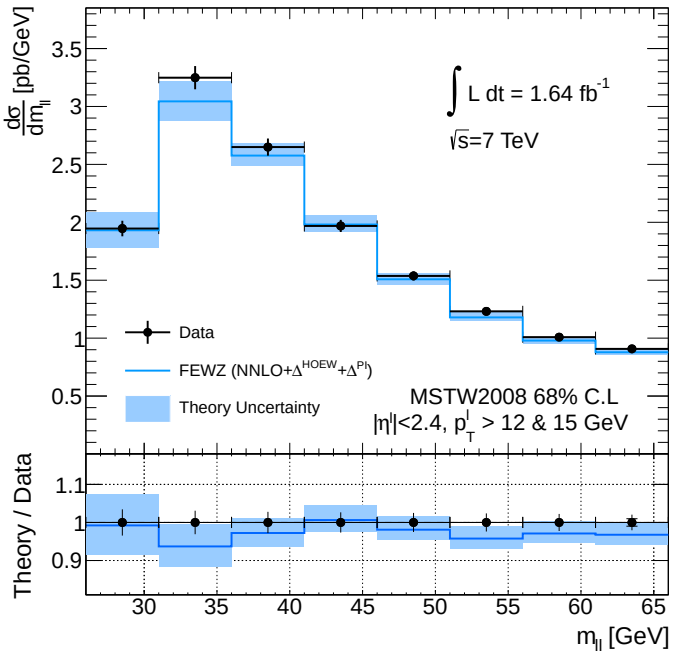

(a) Nominal Analysis

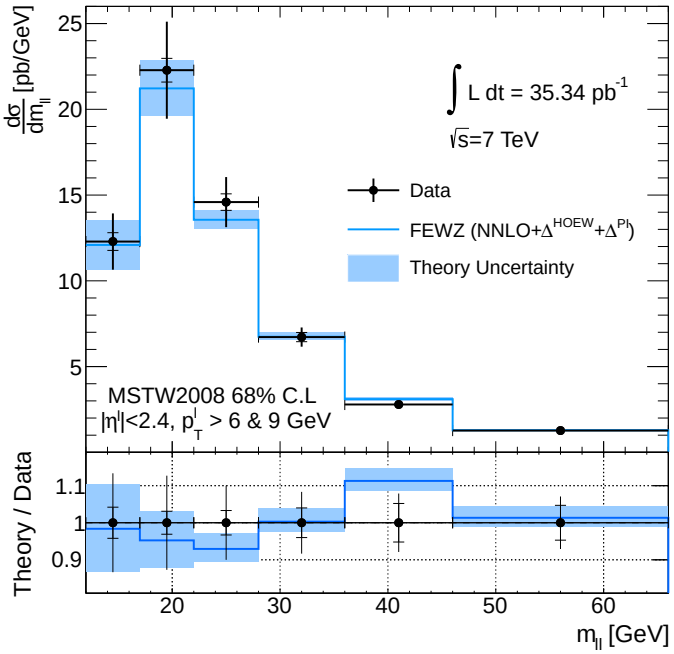

(b) Extended Analysis

Figure 9.3: Fiducial differential cross section at the born level for the combined electron and muon nominal analyses in (a) and the 2010 extended muon analysis in (b). Both plots compare data to theoretical predictions from NNLO `FEWZ` *which has NLO electroweak and photon induced corrections applied [1].*

m_{ll}	$\frac{d\sigma}{dm_{ll}}$	δ^{stat}	δ_1^{cor}	δ_2^{cor}	δ_3^{cor}	δ_4^{cor}	δ_5^{cor}	δ_6^{cor}	δ_7^{cor}	δ_8^{cor}	δ_9^{cor}	δ_{10}^{cor}	δ_{11}^{cor}	δ_{12}^{cor}	δ^{cor}	δ^{unc}	δ^{tot}
[GeV]	[pb/GeV]	[%]	[%]	[%]	[%]	[%]	[%]	[%]	[%]	[%]	[%]	[%]	[%]	[%]	[%]	[%]	[%]
26 - 31	1.95	0.8	0.9	0.4	0.6	0.2	-0.8	0.5	0.5	-1.4	-0.0	-0.6	-0.2	0.5	2.2	2.5	3.4
31 - 36	3.25	0.6	0.8	0.4	0.6	0.1	-0.6	0.4	0.3	-1.2	-0.3	-0.4	-0.3	0.3	1.9	2.4	3.1
36 - 41	2.65	0.7	0.7	0.3	0.5	0.0	-0.4	0.4	0.4	-0.9	-0.4	-0.2	-0.3	0.2	1.5	2.2	2.8
41 - 46	1.97	0.8	0.6	0.3	0.5	0.0	-0.2	0.4	0.4	-0.6	-0.2	-0.4	-0.1	0.1	1.3	2.2	2.7
46 - 51	1.54	0.9	0.5	0.4	0.5	-0.1	-0.1	0.3	0.3	-0.4	-0.2	-0.1	-0.3	0.1	1.0	2.1	2.5
51 - 56	1.23	1.0	0.5	0.4	0.5	-0.1	0.0	0.2	0.3	-0.3	-0.0	-0.4	-0.1	-0.0	1.0	2.0	2.4
56 - 61	1.01	1.0	0.4	0.3	0.4	-0.1	0.0	0.2	0.3	-0.2	-0.0	-0.2	-0.2	-0.0	0.9	1.8	2.2
61 - 66	0.91	1.0	0.3	0.3	0.4	-0.1	0.1	0.1	0.1	-0.1	0.7	-0.1	-0.2	-0.1	1.0	1.5	2.1

Table 9.1: The combined born level fiducial differential cross section $\frac{d\sigma}{dm_{ll}}$, with breakdown of individual correlated sources δ_i^{cor}, total correlated δ^{cor}, uncorrelated δ^{unc}, and total δ^{total} uncertainties. The luminosity uncertainty (1.8%) is not included. The labels 1-12 indicate the correlated uncertainties on the combined cross section and are a linear combination of the correlated uncertainties in the nominal electron and muon channels [1].

9.2 Comparison of Nominal and Extended Analyses

The nominal and extended analyses have not been combined due to the difference in binning. However the differential cross sections extrapolated to the full phase-space. The nominal channel uses the same NNLO acceptance factors shown in table 8.5. The acceptance factors of the extended channel are shown in appendix B. The two extrapolated cross sections are compared in figure 9.4 where the good agreement between them can be seen by eye.

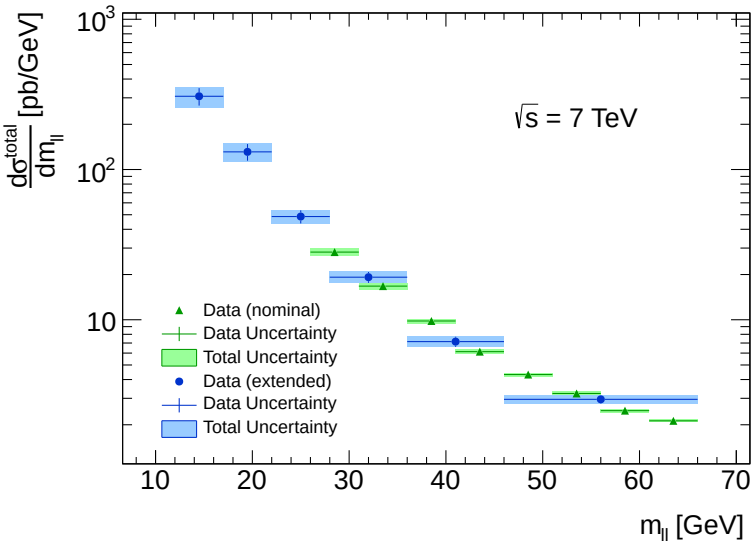

Figure 9.4: Comparison of the nominal and extended measurements extrapolated differential cross sections [1].

9.3 QCD Fits

The theoretical predictions discussed so far use a fixed PDF. In order to investigate further the improvement in the theoretical description when moving to NNLO, a QCD analysis of the data is performed. It is also interesting to see the impact of the Drell-Yan measurement on a PDF fit, as an improvement of the PDFs (when used in conjunction with Z resonance measurements) was the main motivation for the measurement.

The PDFs are fitted to deep inelastic scattering data from HERA [111] and the nominal and extended Drell-Yan analyses. The QCD fit is performed using the `HERAFitter` framework [111, 112] at NLO and at NNLO using NNLO k-factors from `FEWZ`. The PDFs are parameterised using functional forms as used in [113]. Terms are added in the polynomial term of the PDFs only when required by the data, as described in [111]. The most

appropriate functional forms are found to be:

$$xu_v(x) = A_{u_v}x^{B_{u_v}}(1-x)^{C_{u_v}}(1+E_{u_v}x^2) \quad (9.2)$$

$$xd_v(x) = A_{d_v}x^{B_{d_v}}(1-x)^{C_{s_v}} \quad (9.3)$$

$$x\bar{U}(x) = A_{\bar{U}}x^{B_{\bar{U}}}(1-x)^{C_{\bar{U}}} \quad (9.4)$$

$$x\bar{D}(x) = A_{\bar{D}}x^{B_{\bar{D}}}(1-x)^{C_{\bar{D}}} \quad (9.5)$$

$$xg(x) = A_g x^{B_g}(1-x)^{C_g} - A'_g x^{B'_g}(1-x)^{C'_g}\,. \quad (9.6)$$

The normalisation parameters of the valence quarks, A_{u_v} and B_{u_v} are fixed using the quark-counting sum rules. While the momentum sum rule is used to fix the normalisation parameter for the gluon density, A_g. Both of these rules were explained in chapter 2. An extra term for the valence density (E_{u_v}) is added, as it significantly improves the quality of the fit both for the NLO and NNLO fits. The strange sea density is taken as the fraction of the d sea density, $x\bar{s} = r_s\bar{d}$, with r_s fixed to 1 as suggested in a recent ATLAS measurement of the strange quark density [113]. The $x\bar{u}$ and $x\bar{d}$ sea quark densities are required to be equal for $x \to 1$, this condition imposes additional constraints on the $x\bar{U} = x\bar{u}$ and $x\bar{D} = x\bar{d} + x\bar{s}$ B-coefficients (they are set equal), and normalization parameters. The gluon density uses a form used in MSTW analyses, with $C'_g = 25$. The value of the C'_g parameter ensures that the additional term only contributes at low x. With all these constraints applied, both the NLO and NNLO fits have 13 free parameters to describe the parton densities.

As discussed in chapter 2, PDF fits are carried out by minimising a χ^2 function. In the QCD fit by the ATLAS Drell-Yan analysis team presented here, the χ^2 function used by the HERAPDF group is used. This allows both the bin-to-bin correlated and uncorrelated uncertainties to be taken into account. The function takes the form of

$$\chi^2 = \sum_i \frac{\left[\mu_i - m_i\left(1-\sum_j \gamma_j^i b_j\right)\right]^2}{\delta^2_{i,\mathrm{unc}} m_i^2 + \delta^2_{i,\mathrm{stat}}\mu_i m_i\left(1-\sum_j \gamma_j^i b_j\right)} + \sum_j b_j^2 + \sum_i \ln\frac{\delta^2_{i,\mathrm{unc}} m_i^2 + \delta^2_{i,\mathrm{stat}}\mu_i m_i}{\delta^2_{i,\mathrm{unc}}\mu_i^2 + \delta^2_{i,\mathrm{stat}}\mu_i^2}, \quad (9.7)$$

where m_i is the theoretical prediction and μ_i is the measured cross section at point i, (Q^2, x, s) with the relative statistical and uncorrelated systematic uncertainty $\delta_{i,\mathrm{stat}}$, $\delta_{i,\mathrm{unc}}$, respectively. γ_j^i denotes the relative correlated systematic uncertainties and b_j their shifts with a penalty term $\sum_j b_j^2$ added. In order to protect from a bias introduced by statistical fluctuations, the expected rather than the observed number of events are used, with the corresponding errors scaled accordingly. This scaling of errors introduces a ln term, coming from the likelihood transition to χ^2. Neglecting the ln term gives very similar results and does not alter any of the conclusions. This is the same definition of the χ^2 function used to describe the agreement between the data and theoretical predictions presented in table 9.2 and is discussed in more detail in appendix C.

The NLO and NNLO QCD fits using only HERA data yield acceptable fits. When the Drell-Yan measurements are added the NLO fit also has an acceptable overall χ^2 of 479.66 for 551 degrees of freedom, but the fit for the Drell-Yan data is poor as seen in table 9.2. Variations of the predictions by the scale uncertainty do not significantly improve the

description. However, the QCD analysis performed at NNLO gives an acceptable total fit with a χ^2 value of 613.91 for 551 measurements, while also achieving a good fit from the Drell-Yan data as seen in table 9.2. The QCD analysis further emphasises the need to move to NNLO theoretical predictions in order to describe the data.

Prediction	χ^2 (8 pnts) Nominal	χ^2 (6 pnts) Extended
`POWHEG` NLO+LLPS	8.81	21.80
`FEWZ` NLO	22.97	133.79
`FEWZ` NNLO	9.86	6.43
QCD Fit NLO	18.97	113.02
QCD Fit NNLO	4.20	6.97

Table 9.2: χ^2 values of the ATLAS nominal and extended DY cross section measurements for predictions from `FEWZ` *at NLO and NNLO and* `POWHEG` *using MSTW2008 PDFs accounting properly for the correlated systematic uncertainties. The QCD fit values are the partial χ^2 in the QCD fit in which the nominal and extended measurements are fitted with the HERA-I data [1].*

The uncertainties obtained from the PDF fits were evaluated using the Hessian method (see chapter 2) with a tolerance criteria of $\Delta\chi^2 = 1$. Although only experimental uncertainties are shown in the plots below, a number of fit uncertainties were also examined. The effect of model uncertainties was considered by varying theoretical inputs such as the mass of the b and c quarks, or the initial scale at which the PDFs are parameterised. Parametrisation uncertainties are also included. These are evaluated by adding additional terms into the functional forms shown in equations 9.2-9.6 and the impact on the central PDF value examined. Finally, theoretical uncertainties are evaluated by varying the factorisation and renormalisation scales.

Figure 9.5 shows the valance quark densities obtained from the NNLO fit. A comparison is made to the reference fit to the HERA data alone. Figure 9.5 shows the same for the sea quark densities. The effect of the inclusion of the low mass Drell-Yan data can be seen more clearly in figure 9.7 where the relative uncertainties are plotted. The uncertainties on the valance quark uncertainties shown in figure 9.7(a) clearly show an improvement in xu_v uncertainties at $0.001 \lesssim x \lesssim 0.01$. While improvement in xd_v uncertainties is seen at $0.03 \lesssim x \lesssim 0.4$. For the sea quark distributions shown in figure 9.7(b), the impact is much smaller. Both the $x\bar{u}$ and $x\bar{d}$ densities see a small improvement both at lower x as well as at larger x. The greater improvement in the valance quark densities is due to the HERA data constraining these densities less well than the sea quark densities in the x range of this measurement. This was discussed in section 2.3.4. Although the improvements seen here are small, when used in a fit together with the Z resonance measurement the low mass Drell-Yan measurements will allow ATLAS data to disentangle the u-type and d-type quark densities as discussed in chapter 2.

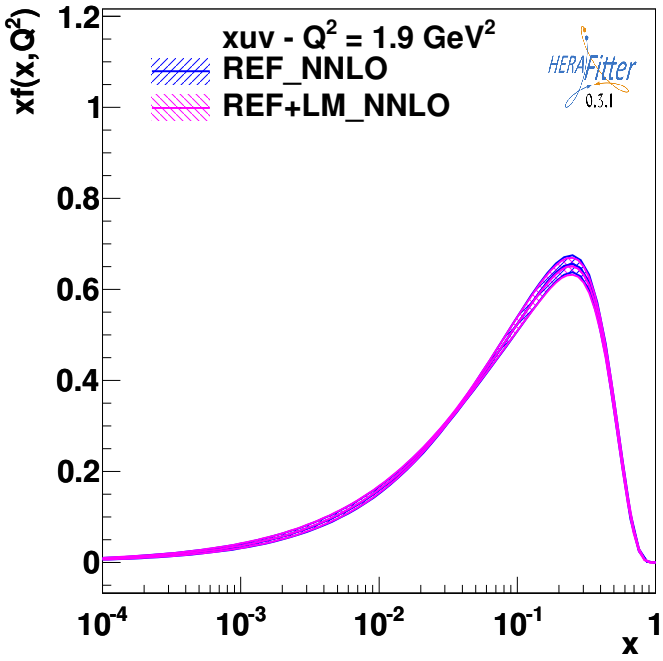

(a) xu_v valance distribution

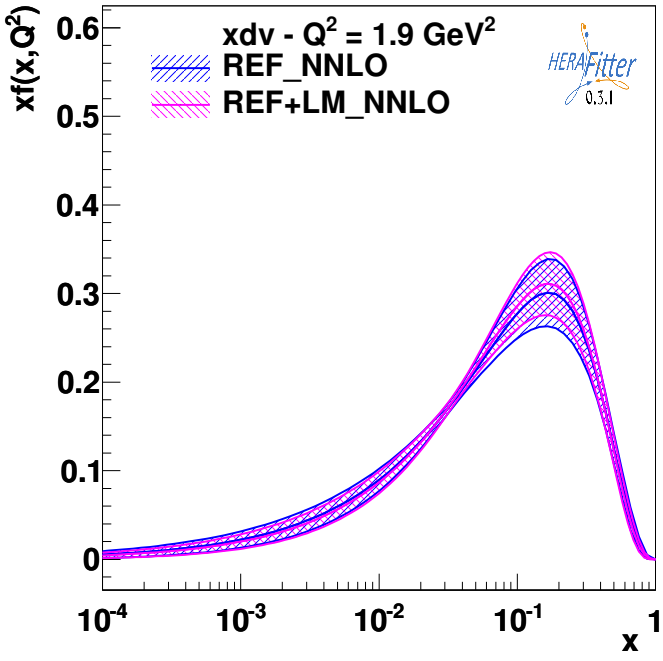

(b) xd_v valance distribution

Figure 9.5: Valance quark densities as a function of x for $Q^2 = 1.9$ GeV. The outer light shaded area indicates a fit to the HERA data only. The inner dark shaded band shows a fit to the HERA and ATLAS data. Only experimental uncertainties are shown [1].

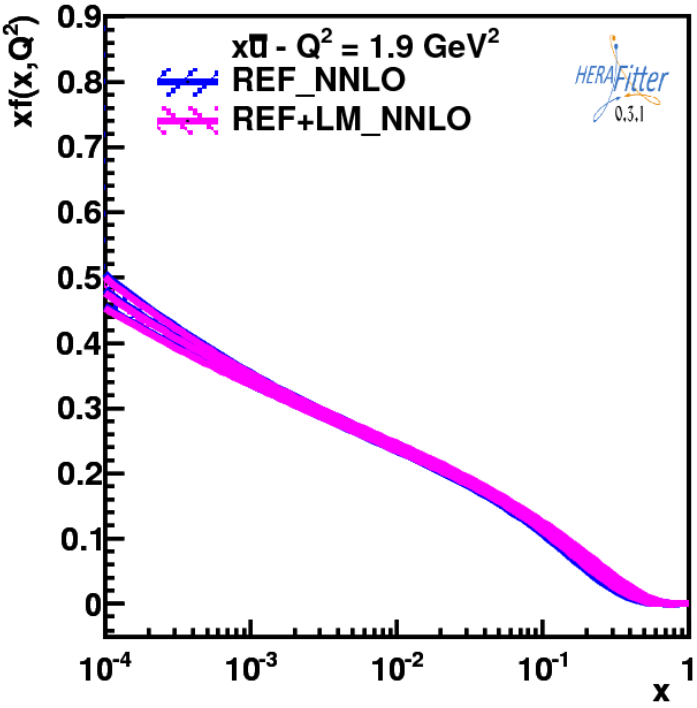

(a) $x\bar{u}$ distribution

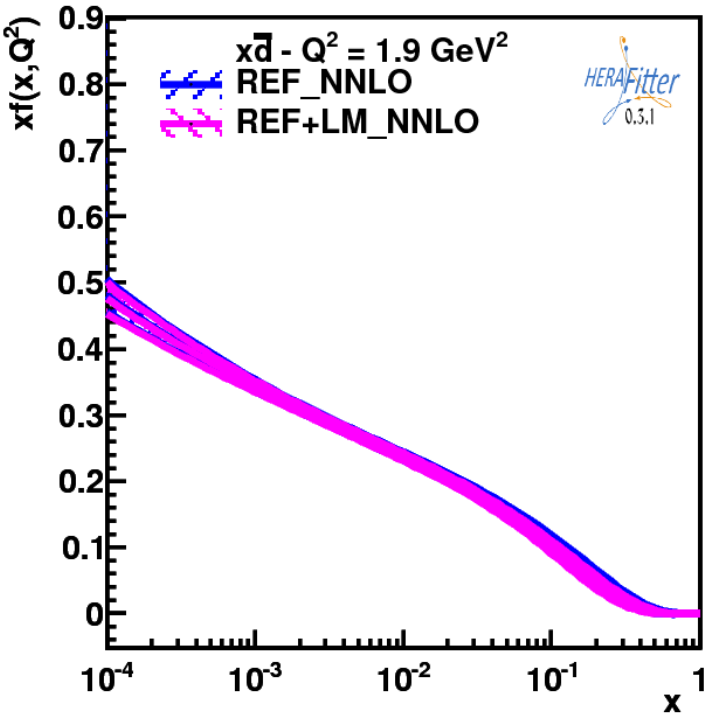

(b) $x\bar{d}$ distribution

Figure 9.6: Sea quark densities as a function of x for $Q^2 = 1.9$ GeV. The outer light shaded area indicates a fit to the HERA data only. The inner dark shaded band shows a fit to the HERA and ATLAS data. Only experimental uncertainties are shown [1].

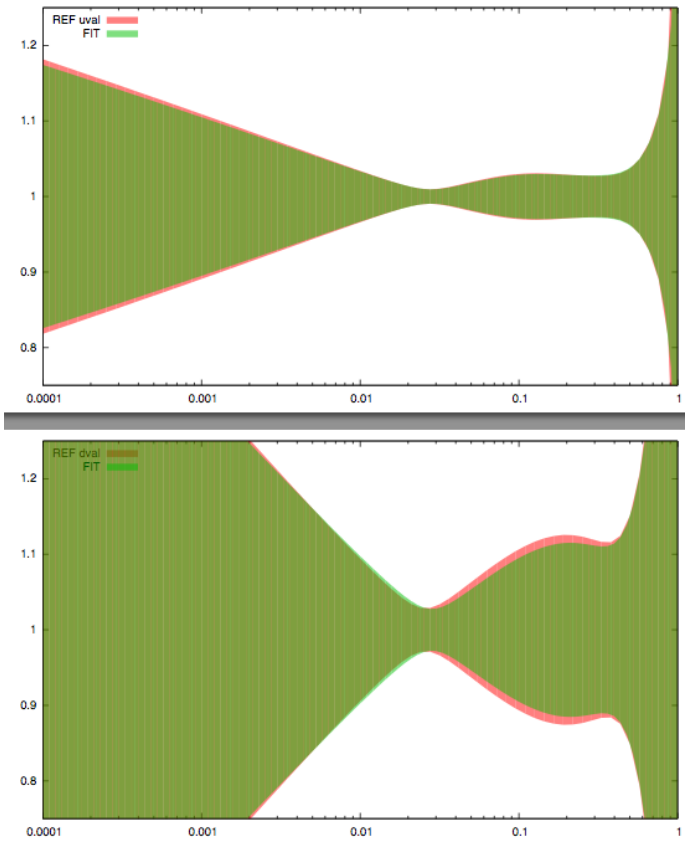

(a) u_v (top) and d_v (bottom)

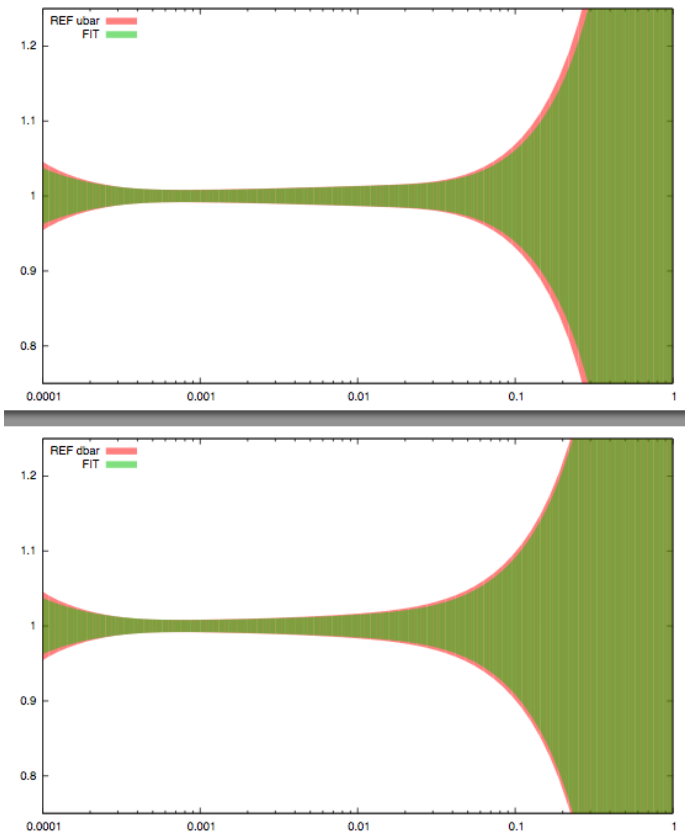

(b) $\bar{u}$ (top) and $\bar{d}$ (bottom)

Figure 9.7: Relative uncertainties for valence and sea quark densities as a function of x for $Q^2 = 1.9$ GeV. The outer pink shaded area is from a fit only to HERA data. The inner green band shows the fit to HERA and the ATLAS low mass Drell-Yan data. Only experimental uncertainties are shown [1].

Chapter 10

Conclusions

The analysis presented in this thesis measures the differential mass cross section of the Drell-Yan process in a mass range of $26 < M_{\mu\mu} < 66$ GeV. The backgrounds have been shown to be well understood and good agreement is seen between the data and Monte Carlo in the control plots. The differential cross section itself is compared to three different theoretical predictions and demonstrates that pure NLO calculations are unable to accurately describe the data at low invariant mass.

The relevant theoretical topics are covered in chapter 2 where the PDFs are briefly explained, describing how they are determined from fits to experimental results. The potential impact of a low mass Drell-Yan measurement is also explained. The design of the ATLAS experiment is described in chapter 3 where particular emphasis is given to the sub-detectors responsible for making a measurement of low p_T muons.

Chapter 4 describes the data sample and choice of Monte Carlo samples and corrections, along with a discussion of the selection cuts for the analysis. It is shown that they select a constant yield across the data taking period.

Chapter 5 covers the determination of the scale factors to correct the isolation efficiency in the Monte Carlo to match that of the data. A tag and probe method using a sample of $Z \to \mu^+\mu^-$ resonance events allowed scale factors as a function of muon p_T to be obtained. Systematic uncertainties on these scale factors were estimated from varying the sample selection cuts. Over the majority of the p_T spectrum the total uncertainty (statistical and systematic) was less than 0.2%, but becomes much larger in the two lowest bins of the p_T spectrum. This leads to the isolation uncertainty being the largest uncertainty on the fiducial differential cross section in the $26 < M_{\mu\mu} < 31$ GeV invariant mass bin with a 3.0% uncertainty.

Chapter 6 considers an estimate of the background from multijet events. This is potentially a large background, particularly at lower invariant mass which needs to be controlled and estimated well. Three methods of estimating the multijet contribution are considered. The first using a Monte Carlo sample of heavy flavoured ($c\bar{c}$ and $b\bar{b}$) decays that has been normalised to the non-isolated region. This approach allows the isolation spectra of the muons to be described well by the Monte Carlo for the more isolated muons, but is it clear from considering the non-isolated mass spectrum that the shape of the data is not reproduced well by the Monte Carlo, leading to a 30% uncertainty being assigned to this method. A second approach that uses templates from data and Monte Carlo to

describe the multijet background is considered. This uses same sign di-muon data events as a proxy for the light flavoured opposite sign contribution to the multijet background. This, along with a template for the heavy flavoured contribution from Monte Carlo are included in a template fit, which determines the normalisation factors needed for the two templates to best describe the data. This method gives an excellent description of the entire isolation spectrum for the muons and gives a much better description of the non-isolated mass spectrum. An uncertainty of 20% is assigned to the estimate due to the non-isolated mass spectrum not being perfectly described. A third method that is far more data driven is also considered, which couldn't be fully used due to low statistics and poor modelling of the d_0 significance in the Monte Carlo, but which did allow a cross check of the template fit method to be made.

Once an estimate of the multijet background has been made and all the necessary corrections to the Monte Carlo samples determined, a comparison of the data and the Monte Carlo can be made. This is done after all the analysis cuts are applied. This is shown in chapter 7, where control plots demonstrate good agreement of the data and Monte Carlo. This gives confidence that the backgrounds are properly controlled and that a bin-by-bin unfolding technique for the cross section is appropriate.

Chapter 8 discusses the determination of the differential mass cross section. The unfolding of the cross section to correct for detector resolution is described and the different sources of uncertainty on the cross section are discussed. The total uncertainty decreases from 4.2% in the lowest mass bin to 2.7% in the highest mass bin. The dominant systematic uncertainty comes from the trigger efficiency scale factors. Apart from in the first mass bin where the uncertainty from the isolation efficiency scale factor is dominant. The fiducial differential cross section is compared to theoretical predictions from `POWHEG` and NLO and NNLO `FEWZ`. It is demonstrated that the NLO `FEWZ` prediction does not predict the cross section well, and the parton showers included in the `POWHEG` prediction or the full move to NNLO in pQCD is needed. This is due to the p_T cuts on the muons combining with the invariant mass cut on the muon pair to restrict the phase space in such a way that the NLO corrections are not sufficient. The issue with the need to move beyond NLO to describe the measurement, while of interest is in many ways a technical issue of the calculations in the phase space studied. The fact that once NNLO is used the data is described well demonstrates the accuracy of Standard Model predictions. This is seen both in the comparison of the cross section with the NNLO theoretical predictions, and by the Monte Carlo comparisons seen in chapter 7 (where NNLO k-factors are applied). Chapter 8 also shows the cross section extrapolated to the full phase space, giving a result that has large theoretical uncertainties which are dominated by the scale uncertainties. The conclusions of this analysis are consistent with low mass Drell-Yan measurements made by the CMS and LHCb collaborations.

Chapter 9 puts the analysis described in the previous chapters in the context of the ATLAS low mass Drell-Yan analysis [1]. The muon analysis described is combined with an electron channel measurement. The results from a muon analysis that uses 2010 data to measure the differential mass cross section at lower invariant mass and muon p_T are also shown. Together they further demonstrates the need to move beyond pure NLO

calculations. Also discussed in chapter 9 is the QCD fit carried out by the ATLAS low mass Drell-Yan team. The fit using the ATLAS low mass Drell-Yan data and the HERA-I data demonstrates further the need to move to NNLO in pQCD to describe the data. Also shown is the impact that the measurement has had on the PDFs in relation to the HERA-I data alone. This is shown at the initial parameterisation scale of $Q^2 = 1.9$ GeV. The relative uncertainty on u valence density is seen to improve in a range of $0.001 \lesssim x \lesssim 0.01$. An even greater improvement is seen in the relative uncertainty of d valence density in the $0.03 \lesssim x \lesssim 0.4$ range, with the sea quark densities uncertainties also seeing some improvement. All four densities shown also seen a small change in the central value. Although the improvements seen are small, when used together with the ATLAS Z resonance measurements the low mass Drell-Yan measurement will allow the u-type and d-type quark densities to be disentangled by ATLAS data.

An obvious improvement to this measurement would be to reduce impact of the trigger scale factor uncertainties. An attempt to do this by propagating the uncorrelated component through to the measured cross section using toy Monte Carlo will be included in the published ATLAS paper [1]. A reduction in the muon channel uncertainty will allow it to be given even more weight in the combination with the electron channel. It will also lead to smaller combined uncertainties which will lead to greater impact when included into a PDF fit with the HERA-I data. The next largest uncertainty in most bins of the measured differential cross section is from the isolation efficiency scale factors. The systematic uncertainty on these could be improved, as it possible that it currently over estimates the uncertainties. The variation of the cuts chosen to investigate the systematics could be better optimised. An issue with the current method of simply varying cuts is that it will give a systematic uncertainty even for a perfectly pure $Z \to \mu^+\mu^-$ sample. As such a better approach to obtaining the systematic uncertainty could be investigated.

To further improve the impact of the measurement presented in this thesis a number of extensions could be made. Most obviously a measurement at lower invariant mass and muon p_T would allow the phase space to be increased. Consideration of cuts of $M_{\mu\mu} \sim 2p_T^{\mu}$ producing problems with the theoretical calculations would also be taken into account as, although this is purely a theoretical problem, it does mean that the measurement presented here will not be able to be included in NLO PDF fits. As discussed in section 2.2.4 the change in Q^2 of the PDFs is very well described theoretically by DGLAP evolution, but x dependence of the PDFs is determined by the fits to data. To contribute to constraining the x dependence of the PDFs a measurement of the Drell-Yan differential rapidity cross section would be useful. Using the full 2011 ATLAS dataset a measurement of the double differential cross section in $M_{\mu\mu}$ and $y_{\mu\mu}$ would most likely be possible with sufficient statistical precision and would compliment the measurement made by LHCb. Finally, a measurement of the Drell-Yan process at $\sqrt{s} = 14$ TeV would allow a factor of two improvement in the x reach. This would be a challenging measurement requiring a dedicated suite of triggers and good background rejection in the high pileup environment.

Bibliography

[1] **ATLAS** Collaboration, *Measurement of the Low-Mass Drell-Yan Differential Cross Section at $\sqrt{s} = 7$ TeV using the ATLAS Detector*, arXiv:1404.1212.

[2] **Particle Data Group** Collaboration, J. B. *et al.*, *2012 Review of Particle Physics*, *Phys. Rev. D* **86** (2012), no. 010001. http://pdg.lbl.gov.

[3] R. Eisberg and R. Resnick, *Quantum Physics of Atoms, Molecules, Solids, Nuclei, and Particles*. Wiley, Second ed., 1985.

[4] *Proceedings of the School for Experimental High Energy Physics Students*, Tech. Rep. RAL-TR-2010-010, RAL, September, 2009. http://www.stfc.ac.uk/PPD/hepsummerschool/23413.aspx.

[5] F. Englert and R. Brout, *Broken Symmetry and the Mass of Gauge Vector Mesons*, *Phys. Rev. Lett.* **13** (1964) 321–323.

[6] P. W. Higgs, *Broken Symmetries, Massless Particles and Gauge Fields*, *Phys. Lett.* **12** (1964) 132–133.

[7] G. Guralnik, C. Hagen, and T. Kibble, *Global Conservation Laws and Massless Particles*, *Phys. Rev. Lett.* **13** (1964) 585–587.

[8] P. W. Higgs, *Spontaneous Symmetry Breakdown without Massless Bosons*, *Phys. Rev.* **145** (1966) 1156–1163.

[9] T. Kibble, *Symmetry Breaking in Non-Abelian Gauge Theories*, *Phys. Rev.* **155** (1967) 1554–1561.

[10] **ATLAS** Collaboration, *Observation of a New Particle in the Search for the Standard Model Higgs Boson with the ATLAS Detector at the LHC*, *Physics Letters B* **716** (2012), no. 1 1 – 29. http://www.sciencedirect.com/science/article/pii/S037026931200857X.

[11] **CMS** Collaboration, *Observation of a New Boson at a Mass of 125 GeV with the CMS Experiment at the LHC*, *Physics Letters B* **716** (2012), no. 1 30 – 61. http://www.sciencedirect.com/science/article/pii/S0370269312008581.

[12] **ATLAS** Collaboration, "Study of the Spin of the New Boson with up to 25 fb^{-1} of ATLAS Data." ATLAS-CONF-2013-040. http://cds.cern.ch/record/1542341, April, 2013.

[13] **CMS** Collaboration, *Study of the Mass and Spin-Parity of the Higgs Boson Candidate via its Decays to Z Boson Pairs*, *Phys. Rev. Lett.* **110** (2013) 081803, [arXiv:1212.6639].

[14] C. Quigg, *Unanswered Questions in the Electroweak Theory*, *Ann. Rev. Nucl. Part. Sci.* **59** (2009) 505–555, [arXiv:0905.3187].

[15] D. H. Perkins, *Introduction to High Energy Physics*. Cambridge University Press, Fourth ed., 2000.

[16] J. C. Collins and D. E. Soper, *The Theorems of Perturbative QCD*, *Annual Review of Nuclear and Particle Science* **37** (1987), no. 1 383–409. http://www.annualreviews.org/doi/abs/10.1146/annurev.ns.37.120187.002123.

[17] V. D. Barger and R. J. N. Philips, *Collider Physics*. Addison-Weasley Publishing Company, Inc., Updated ed., 1996.

[18] A. Martin, W. Stirling, R. Thorne, and G. Watt, *Parton Distributions for the LHC*, *Eur. Phys. J.* **C63** (2009) 189–285, [arXiv:0901.0002].

[19] H.-L. Lai, M. Guzzi, J. Huston, Z. Li, P. M. Nadolsky, et al., *New Parton Distributions for Collider Physics*, *Phys. Rev.* **D82** (2010) 074024, [arXiv:1007.2241].

[20] **NNPDF** Collaboration, R. D. Ball et al., *Unbiased Global Determination of Parton Distributions and their Uncertainties at NNLO and at LO*, *Nucl.Phys.* **B855** (2012) 153–221, [arXiv:1107.2652].

[21] I. Abt et al., *The H1 Detector at HERA*, *Nuclear Instruments and Methods in Physics Research Section A: Accelerators, Spectrometers, Detectors and Associated Equipment* **386** (1997), no. 2-3 310–347. http://www.sciencedirect.com/science/article/pii/S0168900296008935.

[22] Y. L. Dokshitzer, *Calculation of Structure Functions of Deep-Inelastic Scattering and e^+e^- Annihilation by Perturbation Theory in Quantum Chromodynamics*, *JETP* **46** (1977) 641. http://www.jetp.ac.ru/cgi-bin/e/index/e/46/4/p641?a=list (English Translation).

Y. L. Dokshitzer *Zh. Eksp. Teor. Fiz.* **73** (1977) 1216. (Russian Original).

[23] V. N. Gribov and L. N. Lipatov *Sov. J. Nucl. Phys.* **15** 675. (English Translation).

V. N. Gribov and L. N. Lipatov *Yad. Fiz.* **15** 1218. (Russian Original).

[24] V. N. Gribov and L. N. Lipatov *Sov. J. Nucl. Phys.* **15** 438. (English Translation).

V. N. Gribov and L. N. Lipatov *Yad. Fiz.* **15** 781. (Russian Original).

[25] G. Altarelli and G. Parisi, *Asymptotic Freedom in Parton Language*, *Nuclear Physics B* **126** (1977), no. 2 298 – 318. http://www.sciencedirect.com/science/article/pii/0550321377903844.

[26] E. Perez and E. Rizvi, *The Quark and Gluon Structure of the Proton*, *Rep. Prog. Phys.* **76** (2013) 046201, [arXiv:1208.1178].

[27] J. Pumplin, D. Stump, R. Brock, D. Casey, J. Huston, et al., *Uncertainties of Predictions from Parton Distribution Functions. 2. The Hessian Method*, *Phys. Rev.* **D65** (2001) 014013, [hep-ph/0101032].

[28] J. Pumplin, D. Stump, and W. Tung, *Multivariate Fitting and the Error Matrix in Global Analysis of Data*, *Phys. Rev.* **D65** (2001) 014011, [hep-ph/0008191].

[29] J. Pumplin, D. Stump, J. Huston, H. Lai, P. M. Nadolsky, et al., *New Generation of Parton Distributions with Uncertainties from Global QCD Analysis*, *JHEP* **0207** (2002) 012, [hep-ph/0201195].

[30] **ATLAS** Collaboration, J. Goddard, *Measurement of Inclusive W and Z Production in ATLAS*, June, 2013. LHCP2013 Conference Proceedings http://cds.cern.ch/record/1558740.

[31] M. Botje, *Error Estimates on Parton Density Distributions*, *J. Phys.* **G28** (2002) 779–790, [hep-ph/0110123].

[32] S. Alekhin, S. Alioli, R. D. Ball, V. Bertone, J. Blumlein, et al., *The PDF4LHC Working Group Interim Report*, arXiv:1101.0536.

[33] S. Forte, *Parton Distributions at the Dawn of the LHC*, *Acta Phys. Polon.* **B41** (2010) 2859–2920, [arXiv:1011.5247].

[34] J. Pumplin, *Data Set Diagonalization in a Global Fit*, *Phys. Rev.* **D80** (2009) 034002, [arXiv:0904.2425].

[35] J. Pumplin, *Experimental Consistency in Parton Distribution Fitting*, *Phys. Rev.* **D81** (2010) 074010, [arXiv:0909.0268].

[36] A. Martin, R. Roberts, W. Stirling, and R. Thorne, *Parton Distributions Incorporating QED Contributions*, *Eur. Phys. J.* **C39** (2005) 155–161, [hep-ph/0411040].

[37] S. Carrazza, *Towards the Determination of the Photon Parton Distribution Function Constrained by LHC Data*, arXiv:1307.1131.

[38] S. Carrazza, *Towards an Unbiased Determination of Parton Distributions with QED Corrections*, arXiv:1305.4179.

[39] M. Roth and S. Weinzierl, *QED Corrections to the Evolution of Parton Distributions*, *Phys. Lett.* **B590** (2004) 190–198, [hep-ph/0403200].

[40] **ATLAS** Collaboration, *Measurement of the High-Mass Drell–Yan Differential Cross-Section in pp Collisions at $\sqrt{s}$=7 TeV with the ATLAS Detector*, arXiv:1305.4192.

[41] S. D. Drell and T.-M. Yan, *Massive Lepton-Pair Production in Hadron-Hadron Collisions at High Energies*, *Phys. Rev. Lett.* **25** (August, 1970) 316–320. http://link.aps.org/doi/10.1103/PhysRevLett.25.316.

S. D. Drell and T.-M. Yan, *Erratum to: "Massive Lepton-Pair Production in Hadron-Hadron Collisions at High Energies": [Phys. Rev. Lett. 25 (1970) 316]*, *Phys. Rev. Lett.* **25** (September, 1970) 902–902. http://link.aps.org/doi/10.1103/PhysRevLett.25.902.2.

[42] R. P. Feynman, *Very High-Energy Collisions of Hadrons*, *Phys. Rev. Lett.* **23** (Dec, 1969) 1415–1417. http://link.aps.org/doi/10.1103/PhysRevLett.23.1415.

[43] J. M. Campbell, J. Huston, and W. Stirling, *Hard Interactions of Quarks and Gluons: A Primer for LHC Physics*, *Rept. Prog. Phys.* **70** (2007) 89, [hep-ph/0611148].

[44] R. K. Ellis, W. J. Stirling, and B. R. Webber, *QCD and Collider Physics*. Cambridge University Press, 1996. Related site: http://www.hep.phy.cam.ac.uk/theory/webber/QCDupdates.html.

[45] R. Hickling. PhD Student at Queen Mary, University of London, Private Communication.

[46] S. Alioli, P. Nason, C. Oleari, and E. Re, *NLO Vector-Boson Production Matched with Shower in POWHEG*, *JHEP* **0807** (2008) 060, [arXiv:0805.4802].

[47] S. Frixione and B. R. Webber, *Matching NLO QCD Computations and Parton Shower Simulations*, *JHEP* **06** (2002) 029, [hep-ph/0204244].

[48] R. Frederix, M. Mandal, P. Mathews, V. Ravindran, and S. Seth, *Drell-Yan, ZZ, W+W- production in SM and ADD Model to NLO+PS Accuracy at the LHC*, *Eur. Phys. J.* **C74** (2014) 2745, [arXiv:1307.7013].

[49] S. Catani and M. Grazzini, *An NNLO Subtraction Formalism in Hadron Collisions and its Application to Higgs Boson Production at the LHC*, *Phys. Rev. Lett.* **98** (2007) 222002, [hep-ph/0703012].

[50] S. Catani et al., *Vector Boson Production at Hadron Colliders: A Fully Exclusive QCD Calculation at NNLO*, *Phys. Rev. Lett.* **103** (2009) 082001, [arXiv:0903.2120].

[51] R. Hamberg, W. van Neerven, and T. Matsuura, *A Complete Calculation of the Order α_s^2 Correction to the Drell-Yan K Factor*, *Nucl. Phys.* **B359** (1991) 343–405.

[52] G. Watt, *Parton Distribution Function Dependence of Benchmark Standard Model Total Cross Sections at the 7 TeV LHC*, *JHEP* **1109** (2011) 069, [arXiv:1106.5788].

[53] L. Evans and P. Bryant, *LHC Machine*, *Journal of Instrumentation* **3** (August, 2008) S08001. http://stacks.iop.org/1748-0221/3/i=08/a=S08001.

[54] **ATLAS** Collaboration, *The ATLAS Experiment at the CERN Large Hadron Collider*, *Journal of Instrumentation* **3** (August, 2008) S08003. http://stacks.iop.org/1748-0221/3/i=08/a=S08003.

[55] **CMS** Collaboration, *The CMS Experiment at the CERN LHC*, *Journal of Instrumentation* **3** (August, 2008) S08004. http://stacks.iop.org/1748-0221/3/i=08/a=S08004.

[56] **ALICE** Collaboration, *The ALICE Experiment at the CERN LHC*, *Journal of Instrumentation* **3** (August, 2008) S08002. http://stacks.iop.org/1748-0221/3/i=08/a=S08002.

[57] **LHCb** Collaboration, *The LHCb Detector at the LHC*, *Journal of Instrumentation* **3** (August, 2008) S08005. http://stacks.iop.org/1748-0221/3/i=08/a=S08005.

[58] F. Marcastel, *CERN's Accelerator Complex*, October, 2013. http://cds.cern.ch/record/1621583.

[59] **ATLAS** Collaboration, "Public Luminosity Results." [Cited: January 2013], http://twiki.cern.ch/twiki/bin/view/AtlasPublic/LuminosityPublicResults .

[60] **ATLAS** Collaboration, J. Pequenao and P. Schaffner, "A Computer Generated Image Representing How ATLAS Detects Particles." http://cds.cern.ch/record/1505342, January, 2013.

[61] **ATLAS** Collaboration, J. Pequenao, "Computer Generated Image of the Whole ATLAS Detector." http://cds.cern.ch/record/1095924, March, 2008.

[62] **ATLAS** Collaboration, "The ATLAS Coordinate System." [Online] [Cited: October 2012], http://atlas.fis.utfsm.cl/atlas/hlt/ATLAS_coord.gif.

[63] **ATLAS** Collaboration, *ATLAS Detector and Physics Performance Technical Design Report: Volume One*, . CERN/LHCC 99-15.

[64] **ATLAS** Collaboration, J. Pequenao, "Computer Generated Image of the ATLAS Inner Detector." http://cds.cern.ch/record/1095926, March, 2008.

[65] Helmuth Spieler, *Semiconductor Detector Systems*. Oxford University Press, 2005.

[66] **ATLAS** Collaboration, *The ATLAS Transition Radiation Tracker (TRT) Proportional Drift Tube: Design and Performance*, *Journal of Instrumentation* **3** (February, 2008) P02013. http://stacks.iop.org/1748-0221/3/i=02/a=P02013.

[67] B. Dolgoshein, *Transition Radiation Detectors*, *Nuclear Instruments and Methods in Physics Research Section A: Accelerators, Spectrometers, Detectors and Associated Equipment* **326** (1993), no. 3 434 – 469. http://www.sciencedirect.com/science/article/pii/016890029390846A.

[68] **ATLAS** Collaboration, *Particle Identification Performance of the ATLAS Transition Radiation Tracker*, Tech. Rep. ATLAS-CONF-2011-128, CERN, Geneva, September, 2011. http://cds.cern.ch/record/1383793.

[69] R. K. Bock and A. Vasilescu, *The Particle Detector BriefBook*. Springer, 14 ed., 1998. http://physics.web.cern.ch/Physics/ParticleDetector/BriefBook/.

[70] **ATLAS** Collaboration, J. Pequenao, "Computer Generated Image of the ATLAS Calorimeter." http://cds.cern.ch/record/1095927, March, 2008.

[71] B. R. Martin and G. Shaw, *Particle Physics*. Wiley, Third ed., 2008.

[72] C. W. Fabjan and F. Gianotti, *Calorimetry for Particle Physics*, *Rev. Mod. Phys.* **75** (Oct, 2003) 1243–1286. http://link.aps.org/doi/10.1103/RevModPhys.75.1243.

[73] **ATLAS** Collaboration, J. Pequenao, "Computer Generated Image of the ATLAS Muons Subsystem." http://cds.cern.ch/record/1095929, March, 2008.

[74] **ATLAS** Collaboration, "Cross-section of the Barrel of the ATLAS Muon Spectrometer." NIKHEF ATLAS Wiki [Online] [Cited: August 2013] http://www.nikhef.nl/pub/experiments/atlaswiki/index.php/Chapter_II.

[75] **ATLAS** Collaboration, B. Resende, *Muon Identification Algorithms in ATLAS*, September, 2009. Europhysics Conference on High Energy Physics Proceedings http://cds.cern.ch/record/1209632/.

[76] **ATLAS** Collaboration, "Muon Momentum Resolution in First Pass Reconstruction of pp Collision Data Recorded by ATLAS in 2010." ATLAS-CONF-2011-046. http://cds.cern.ch/record/1338575/, March, 2011.

[77] **ATLAS** Collaboration, "Pile-up Dependence of the ATLAS Muon Performance." ATL-COM-PHYS-2011-1640 http://cds.cern.ch/record/1403080, December, 2011.

[78] **ATLAS** Collaboration, *Measurement of Muon Momentum Resolution of the ATLAS Detector*, vol. 28 of *European Physical Journal Web of Conferences*, p. 12039, 2012. arXiv:1201.4704.

[79] **ATLAS** Collaboration, "Muon Reconstruction Efficiency in Reprocessed 2010 LHC Proton-Proton Collision Data Recorded with the ATLAS Detector." ATLAS-CONF-2011-063. http://cds.cern.ch/record/1345743/, April, 2011.

[80] **ATLAS** Collaboration, "ATLAS Muon Performance Public Plots." [Online: February 2014] http://twiki.cern.ch/twiki/bin/view/AtlasPublic/MuonPerformancePublicPlots.

[81] **ATLAS** Collaboration, *Architecture of the ATLAS High Level Trigger Event Selection Software*, *Nuclear Instruments and Methods in Physics Research Section A: Accelerators, Spectrometers, Detectors and Associated Equipment* **518** (2004), no. 1-2 537 – 541. http://www.sciencedirect.com/science/article/pii/S0168900203029462.

[82] R. Brun and F. Rademakers, *ROOT - An Object Oriented Data Analysis Framework*, *Nuclear Instruments and Methods in Physics Research Section A: Accelerators, Spectrometers, Detectors and Associated Equipment* **389** (1997), no. 1-2 81 – 86. http://www.sciencedirect.com/science/article/pii/S016890029700048X.

[83] T. Sjöstrand, S. Mrenna, and P. Skands, *PYTHIA 6.4 Physics and Manual*, *Journal of High Energy Physics* **2006** (2006), no. 05 026. http://stacks.iop.org/1126-6708/2006/i=05/a=026.

[84] G. Corcella et al., *HERWIG 6.5: an event generator for Hadron Emission Reactions With Interfering Gluons (including supersymmetric processes)*, *JHEP* **01** (2001) 010, [hep-ph/0011363].

[85] **GEANT4** Collaboration, S. Agostinelli et al., *GEANT4: A Simulation Toolkit*, *Nucl. Instrum. Meth.* **A506** (2003) 250–303.

[86] *The ATLAS Simulation Infrastructure*, *European Physical Journal C* **70** (2010) 823–874, [arXiv:1005.4568].

[87] J. M. Campbell and R. K. Ellis, *MCFM for the Tevatron and the LHC*, arXiv:1007.3492.

[88] C. Anastasiou, L. J. Dixon, K. Melnikov, and F. Petriello, *High Precision QCD at Hadron Colliders: Electroweak Gauge Boson Rapidity Distributions at NNLO*, *Phys.Rev.* **D69** (2004) 094008, [hep-ph/0312266].

[89] M. Aliev, H. Lacker *et al.*, – *HATHOR – HAdronic Top and Heavy quarks crOss section calculatoR*, arXiv:1007.1327.

[90] M. Cacciari *et al.*, *Top-Pair Production at Hadron Colliders with Next-to-Next-to-Leading Logarithmic Soft-Gluon Resummation*, arXiv:1111.5869.

[91] M. Czakon and A. Mitov, *Top++: A Program for the Calculation of the Top-Pair Cross-Section at Hadron Colliders*, arXiv:1112.5675.

[92] **ATLAS** Collaboration, *Measurement of the Inclusive $W^{\pm}$ and Z/gamma Cross Sections in the Electron and Muon Decay Channels in pp Collisions at $\sqrt{s} = 7$ TeV with the ATLAS Detector*, *Phys. Rev.* **D85** (2012) 072004, [arXiv:1109.5141].

[93] R. Hickling, "Drell-Yan k-Factors." http://pprc.qmul.ac.uk/~hickling/kfactors.html.

[94] L. Dixon, *A Program for Computing Rapidity Distributions for Production of Lepton-Pairs via Virtual Photons, W or Z Bosons at Hadron Colliders at NNLO in QCD*, July, 2010. [Online] [Cited: July 2010], http://www.slac.stanford.edu/~lance/Vrap/.

[95] **ATLAS** Collaboration, *Determination of the Muon Reconstruction Efficiency in ATLAS at the Z Resonance in Proton-Proton Collisons at* $\sqrt{s} = 7$ *TeV*, . http://cds.cern.ch/record/1330715.

[96] **ATLAS** Collaboration, *Improved Luminosity Determination in pp Collisions at* $\sqrt{s} = 7$ *TeV using the ATLAS Detector at the LHC*, *Eur.Phys.J.* **C73** (2013) 2518, [arXiv:1302.4393].

[97] R. Barlow and C. Beeston, *Fitting using Finite Monte Carlo Samples*, *Computer Physics Communications* **77** (1993) 219–228.

[98] **ATLAS** Collaboration, *Electron Performance Measurements with the ATLAS Detector using the 2010 LHC Proton-Proton Collision Data*, *The European Physical Journal C* **72** (2012), no. 3 1–46.

[99] Glen Cowan, *Statistical Data Analysis*. Oxford University Press, 1998.

[100] **ATLAS** Collaboration, *Unfolding in ATLAS*, arXiv:1104.2962.

[101] G. D'Agostini, *A Multidimensional Unfolding Method Based on Bayes' Theorem*, *Nucl. Instrum. Meth.* **A362** (1995) 487–498. http://www.sciencedirect.com/science/article/pii/016890029500274X.

[102] S. Dittmaier and M. Huber, *Radiative Corrections to the Neutral-Current Drell-Yan Process in the Standard Model and its Minimal Supersymmetric Extension*, *JHEP* **1001** (2010) 060, [arXiv:0911.2329].

[103] **CMS** Collaboration, *Measurement of the Drell-Yan Cross Section in pp Collisions at* $\sqrt{s} = 7$ *TeV*, *JHEP* **1110** (2011) 007, [arXiv:1108.0566].

[104] **LHCb** Collaboration, *Inclusive Low Mass Drell-Yan Production in the Forward Region at* $\sqrt{s} = 7$ *TeV*, . DIS2012 Proceedings, http://cds.cern.ch/record/1434424/.

[105] G. Lafferty and T. Wyatt, *Where to Stick Your Data Points: The Treatment of Measurements within Wide Bins*, *Nuclear Instruments and Methods in Physics Research Section A: Accelerators, Spectrometers, Detectors and Associated Equipment* **355** (1995), no. 2 â€“- 3 541 – 547.

[106] E. Piccaro, *Measurement of the Low Mass Drell-Yan Cross Section in the Di-Muon Channel in Proton-Proton Collisions at* $\sqrt{s} = 7$ *TeV with the ATLAS Detector.* PhD thesis, Queen Mary, University of London, London, 2012. http://ph.qmul.ac.uk/sites/default/files/EPiccaro_thesis.pdf.

[107] A. Glazov, *Averaging of DIS Cross Section Data*, *AIP Conf. Proc.* **792** (2005) 237–240.

[108] **H1** Collaboration, F. Aaron et al., *Measurement of the Inclusive ep Scattering Cross Section at Low* Q^2 *and x at HERA*, *Eur. Phys. J.* **C63** (2009) 625–678, [arXiv:0904.0929].

[109] **ATLAS** Collaboration, *Measurement of Angular Correlations in Drell-Yan Lepton Pairs to probe Z/γ^* Boson Transverse Momentum at $\sqrt{s} = 7$ TeV with the ATLAS Detector*, *Phys. Lett.* **B720** (2013) 32–51, [arXiv:1211.6899].

[110] **H1 and ZEUS** Collaboration, V. Radescu, *HERA Precision Measurements and Impact for LHC Predictions*, arXiv:1107.4193.

[111] **H1 and ZEUS** Collaboration, F. Aaron et al., *Combined Measurement and QCD Analysis of the Inclusive e+- p Scattering Cross Sections at HERA*, *JHEP* **1001** (2010) 109, [arXiv:0911.0884].

[112] **H1** Collaboration, F. Aaron et al., *A Precision Measurement of the Inclusive ep Scattering Cross Section at HERA*, *Eur. Phys. J.* **C64** (2009) 561–587, [arXiv:0904.3513].

[113] **ATLAS** Collaboration, *Determination of the Strange Quark Density of the Proton from ATLAS Measurements of the $W \to l\nu$ and $Z \to ll$ Cross Sections*, *Phys. Rev. Lett.* **109** (2012) 012001, [arXiv:1203.4051].

[114] **HERAFitter** Collaboration, *HERAFitter - PDF Fitting Package*, 0.3.1 ed., April, 2013. Manual https://wiki-zeuthen.desy.de/HERAFitter/HERAFitter/DownloadPage.

[115] "Minuit." [Online: Feburary 2014] http://seal.web.cern.ch/seal/snapshot/work-packages/mathlibs/minuit/.

Appendices

Appendix A

Muon Distributions

This appendix contains muon control plots in which both the leading and sub-leading muons have been plotted together. These plots show better agreement between the data and the Monte Carlo than was seen in chapter 7, particularly in the tail of the p_T distribution.

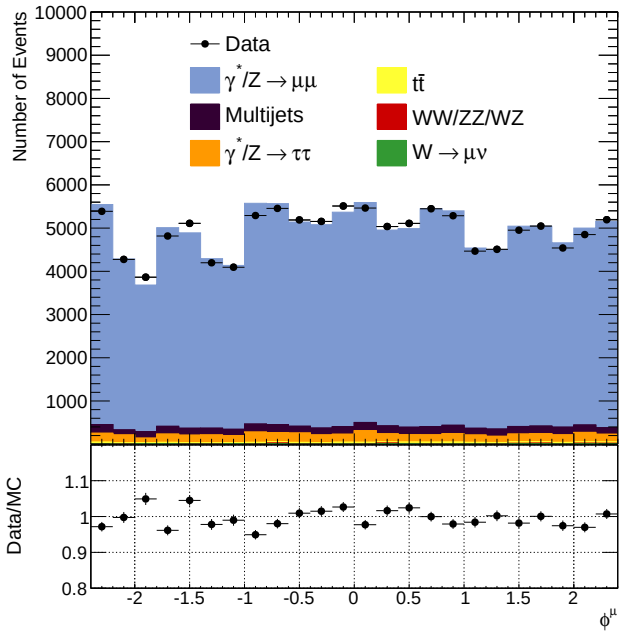

Figure A.1: Leading and sub-leading muon ϕ control plot.

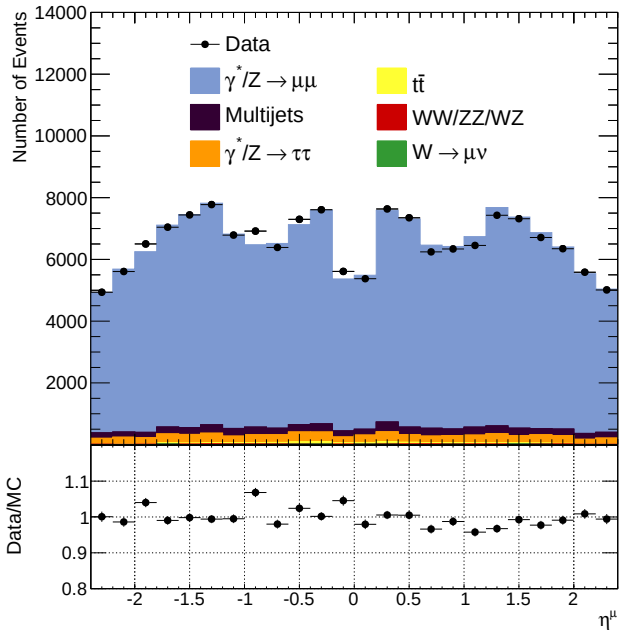

Figure A.2: Leading and sub-leading muon η control plot.

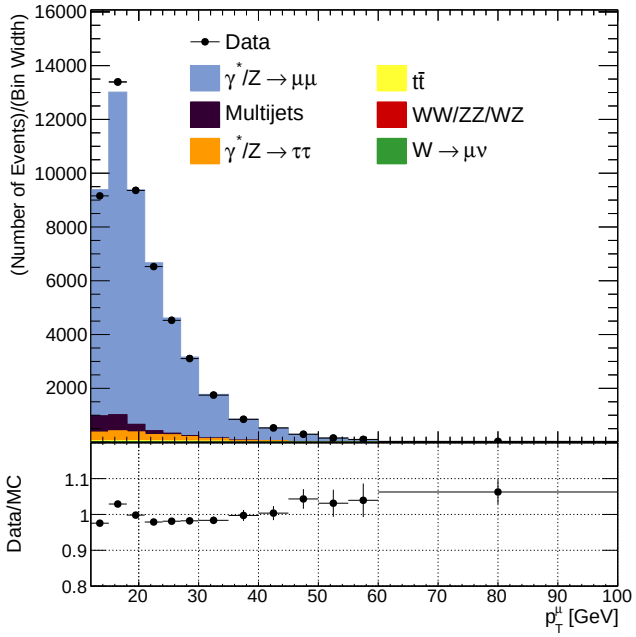

Figure A.3: Leading and sub-leading muon p_T control plot.

Appendix B

Extended Analysis Cross Sections

Tables for the extended muon analysis [106] discussed in chapter 9 are given here for completeness. A description of each table is given in the captions. Discussion of the variables presented can be found in chapters 8 and 9 where they are described for the nominal electron and muon channels.

$M_{\mu\mu}$	$\frac{d\sigma}{dM_{\mu\mu}}$	δ^{stat}	δ^{syst}	δ^{total}	$\mathcal{D}$	$\mathcal{A}$	$\delta_{\mathcal{A}}^{\text{scale}}$	$\delta_{\mathcal{A}}^{\text{pdf+}\alpha_s}$	$\delta_{\mathcal{A}}^{\text{total}}$
[GeV]	[pb/GeV]	[%]	[%]	[%]			[%]	[%]	[%]
12 – 17	12.29	4.2	12.6	13.3	1.00	0.04	$^{-7.9}_{+7.5}$	$^{-4.1}_{+2.7}$	$^{-16.0}_{+15.5}$
17 – 22	22.28	3.1	12.3	12.7	0.98	0.17	$^{-4.7}_{+4.1}$	$^{-3.0}_{+2.0}$	$^{-13.9}_{+13.5}$
22 – 28	14.59	3.3	9.5	10.0	0.98	0.30	$^{-1.1}_{+0.7}$	$^{-2.3}_{+1.6}$	$^{-10.3}_{+10.2}$
28 – 36	6.72	4.0	7.4	8.4	0.99	0.35	$^{-0.6}_{+0.02}$	$^{-1.8}_{+1.2}$	$^{-8.5}_{+8.4}$
46 – 66	1.27	4.7	5.2	7.0	1.16	0.43	$^{-0.9}_{+0.5}$	$^{-1.0}_{+0.6}$	$^{-6.6}_{+6.4}$

Table B.1: The extended muon channel Born level fiducial differential cross section $\frac{d\sigma}{dM_{ll}}$, with breakdown of statistical δ^{stat}, systematic δ^{syst}, and total δ^{total} uncertainties. Also shown is the correction factor used to derive the dressed cross section ($\mathcal{D}$), and the extrapolation factor ($\mathcal{A}$) used to derive the cross section for the full phase space, along with the uncertainties associated to variations in scale $\delta_{\mathcal{A}}^{scale}$, and PDF uncertainty $\delta_{\mathcal{A}}^{pdf}$. The total uncertainty on an extrapolated cross section is shown as $\delta_{\mathcal{A}}^{total}$. The luminosity uncertainty (3.5%) is not included.

	Correlated					Uncorrelated	
$M_{\mu\mu}$	δ^{reco}	δ^{trig}	δ^{iso}	δ^{qcd}	$\delta^{p_T \text{ scale}}$	δ^{res}	δ^{MC}
[GeV]	[%]	[%]	[%]	[%]	[%]	[%]	[%]
12 – 17	2.5	4.0	6.6	-3.0	-0.2	0.5	0.6
17 – 22	1.4	3.7	6.6	-2.8	+0.1	0.3	0.3
22 – 28	0.9	3.6	5.5	-1.8	+0.0	0.1	0.4
28 – 36	0.7	3.6	4.5	-1.6	-0.1	0.2	0.4
36 – 46	0.7	3.6	3.3	-1.3	-0.1	0.1	0.5
46 – 66	0.6	3.6	1.9	-0.7	-0.0	0.1	0.5

Table B.2: Bin-by-bin breakdown of the systematic uncertainties for the extended muon channel cross section measurement. The luminosity uncertainty (3.5%) is not included.

$M_{\mu\mu}$ [GeV]	POWHEG $\frac{d\sigma}{dM_{\mu\mu}}$ [pb/GeV]	POWHEG δ^{pdf} [%]	POWHEG δ^{scale} [%]	NLO FEWZ $\frac{d\sigma}{dM_{\mu\mu}}$ [pb/GeV]	NLO FEWZ δ^{pdf} [%]	NLO FEWZ δ^{scale} [%]	NNLO FEWZ $\frac{d\sigma}{dM_{\mu\mu}}$ [pb/GeV]	NNLO FEWZ δ^{pdf} [%]	NNLO FEWZ δ^{scale} [%]
12 – 17	9.55	1.1	$^{+11.9}_{-20.0}$	7.47	2.7	$^{+10.7}_{-15.8}$	12.09	$^{+3.7}_{-3.0}$	10.0
17 – 22	20.85	1.0	$^{+8.0}_{-15.2}$	24.46	3.0	$^{+10.1}_{-13.3}$	21.03	$^{+3.7}_{-2.8}$	6.1
22 – 28	13.63	0.6	$^{+5.3}_{-11.5}$	13.65	2.9	$^{+6.2}_{-8.6}$	13.32	$^{+3.4}_{-2.6}$	2.3
28 – 36	6.88	0.7	$^{+6.1}_{-10.0}$	6.61	2.7	$^{+5.0}_{-6.5}$	6.59	$^{+3.3}_{-2.5}$	1.3
36 – 46	3.17	0.6	$^{+3.9}_{-7.6}$	3.01	2.6	$^{+4.0}_{-4.4}$	3.02	$^{+3.1}_{-2.3}$	1.2
46 – 66	1.31	0.6	$^{+2.9}_{-5.1}$	1.24	2.4	$^{+2.8}_{-3.0}$	1.25	$^{+2.9}_{-2.1}$	1.3

Table B.3: Theoretical predictions at NLO, NLO+LLPS, and NNLO including higher order electroweak corrections, for the extended analysis. The scale uncertainty is defined as the envelope of variations for $0.5 \leq \mu_R, \mu_F \leq 2$ *for* POWHEG*. For* FEWZ *the scale uncertainty is defined by the variation* $0.5 \leq \mu_R = \mu_F \leq 2$*.*

M_{ll} [GeV]	Δ^{HOEW} [%]	Δ^{PI} [pb/GeV]	δ^{PI} [%]	δ^{scheme} [%]
12 – 17	0.37	0.0	36	5.4
17 – 22	1.58	0.19	36.7	3.2
22 – 28	3.04	0.24	36.2	0.9
28 – 36	3.77	0.15	35.8	0.5
36 – 46	4.38	0.085	35.6	0.3
46 – 66	4.64	0.037	35.6	0.2

Table B.4: Higher order EW corrections in the extended binning; Δ^{HOEW}*, the missing electroweak contribution,* Δ^{PI}*, the Photon Induced correction,* δ^{PI}*, the uncertainty in the photon induced piece, and* δ^{scheme}*, the uncertainty due to the non-convergence of calculations derived with different electroweak schema.*

Appendix C

Definitions of the χ^2 Function

Throughout this thesis, a number of χ^2 definitions have been given. In relation to PDF fitting (equations 2.53 and 9.7) and used in the combination results (equation 9.1). A χ^2 value is also used to quantify the agreement (or lack thereof) between the measured results and theoretical predictions (equation 9.7 again).

All three of these definitions are more complicated than what could be thought of as the standard χ^2 definition. This is due to the inclusion of systematic uncertainties. This appendix explains the relation between the three definitions given in this thesis and the more well known definition.

C.1 The χ^2 Function

The χ^2 function for a number of data points, i, is commonly defined [114] as,

$$\chi^2(\vec{t}) = \sum_i \frac{[d_i - t_i(\vec{p})]^2}{\sigma^2_{stat,i}}, \tag{C.1}$$

where d_i are the data points, $t_i(\vec{p})$ the theoretical prediction (with parameters $\vec{p}$) and $\sigma_{stat,i}$ the statistical uncertainty on the data. When comparing data and theory, all the variables are kept constant, and the value of χ^2 simply evaluated. When a fit is being performed, the value of t_i is a free parameter in the fit, allowing some, or all of its $\vec{p}$ theoretical parameters to vary. The best fit is found for the values of $t_i(\vec{p})$ that give the minimum of the χ^2 function. Minimisation of the χ^2 function is often done iteratively using `minuit` [115].

C.2 Including Systematic Uncertainties

To include systematic uncertainties that are uncorrelated between the points (σ_{uncor}) into the χ^2 definition, they are simply added in quadrature with the statistical uncertainties. This leads to,

$$\chi^2(\vec{t}) = \sum_i \frac{[d_i - t_i(\vec{p})]^2}{\sigma^2_{stat,i} + \sigma^2_{uncor,i}}. \tag{C.2}$$

To include systematic uncertainties that are correlated between points (σ_{corr}), the numerator is adapted to include the correlated systematic uncertainty into $t_i(\vec{p})$. Such that $t_i(\vec{p}) \rightarrow t_i'(\vec{p}) = t_i(\vec{p}) + \sum_j b_j \sigma_{corr,i,j}$ [114]. Where the sum is over the sources of correlated systematic uncertainty (j). The value b_j is introduced as a nuisance parameter. The nuisance parameter can be thought of as due to the calibration of the experiment, leading to a set of 'measurements' of $b_j = 0 \pm 1$ [31]. The values of the σ_{corr} are given by $\sigma_{corr,i} = \gamma_{ij} t_i(\vec{p})$ where γ_{ij} are relative correlated uncertainties. Substituting into equation C.2 gives,

$$\chi^2(\vec{t},\vec{b}) = \sum_i \frac{\left[d_i - t_i(\vec{p})(1+\sum_j b_j \gamma_{ij})\right]^2}{\sigma^2_{stat,i} + \sigma^2_{uncor,i}}. \tag{C.3}$$

However, as the nuisance parameter b_j has now been added to the definition of the χ^2 an extra term is required to constrain the fitted values of b_j. This leads to,

$$\chi^2(\vec{t},\vec{b}) = \sum_i \frac{\left[d_i - t_i(\vec{p})(1+\sum_j b_j \gamma_{ij})\right]^2}{\sigma^2_{stat,i} + \sigma^2_{uncor,i}} + \sum_j b_j^2. \tag{C.4}$$

This is the definition of the χ^2 function given in equation 2.53. Here, when used in a fit both $\vec{t}$ and $\vec{b}$ are free parameters. When used to compare data and theoretical predictions only $\vec{b}$ is free, and the χ^2 value quoted to describe the agreement is χ^2_{min}.

C.3 Relation to the Covariance Matrix Method

In the case of off diagonal uncertainties, the χ^2 function is

$$\chi^2(\vec{t},\vec{b}) = \sum_{ik} \left(d_i - t_i(\vec{p})(1+\sum_j b_j\gamma_{ij})\right) V^{-1}_{ik} \left(d_k - t_k(\vec{p})(1+\sum_j b_j\gamma_{kj})\right) + \sum_j b^2. \tag{C.5}$$

where the the correlation matrix V_{ik} represents the statistical and uncorrelated systematic uncertainties,

$$V_{ik} = (V_{stat})_{ik} + (V_{uncor})_{ik}, \tag{C.6}$$

with

$$(V_{stat})_{ik} = \rho \sigma_{stat,i} \sigma_{stat,k} \tag{C.7}$$

$$(V_{uncor})_{ik} = \delta_{ik} \sigma_{uncor,i} \sigma_{uncor,k}, \tag{C.8}$$

where, ρ is the statistical correlations between bins and δ_{ik} is a Kronecker delta. Any dependence of the statistical uncertainty on b_j is ignored. Equation C.5 allows for two methods to determine the minimum without needing to include the nuisance parameters into the `minuit` minimisation. The first method uses a minimisation of χ^2 vs. b_j to define

a covariance matrix for the systematic uncertainties,

$$(V_{corr})_{ik} = \sum_j \sigma_{corr,ij}\sigma_{corr,kj}. \tag{C.9}$$

This allows the total covariance matrix to be given by

$$V_{tot} = V_{stat} + V_{corr} + V_{uncor} \tag{C.10}$$

and the χ^2 takes the function of

$$\chi^2 = \sum_{i,k}(d_i - t_i)(V_{tot}^{-1})_{ik}(d_k - t_k). \tag{C.11}$$

The second method determines the optimal shifts of the nuisance parameters in each iteration. Shifts given by minimising equation C.5 leads to a system of linear equations,

$$\sum_j \sum_{ik} V_{ik}^{-1}\sigma_{ij}\sigma_{kj} \cdot b_j = \sum_{ik} V_{ik}^{-1}\sigma_{il}(d_k - t_k), \tag{C.12}$$

where $1 \leq l \leq N_{syst}$, the total number of correlated systematic uncertainties.

Although the definition of the χ^2 function given in equation C.11 appears more elegant than the nuisance parameter approach, it involves the inversion of what can be a very large matrix. The χ^2 definition using a nuisance parameter avoids this and also has the advantage that when used in fit it can be used in the determination of fit uncertainties as discussed in chapter 2.

C.4 Avoiding Statistical Fluctuations

The χ^2 definition given in equation C.4 uses statistical and uncorrelated systematic uncertainties that are absolute. However, if the systematic uncertainties depend on the central value of the measurement, the χ^2 function has to be modified further to allow for this scaling as defined in [108]. The relative uncertainty values are given by $\delta_{stat,i} = \sigma_{stat,i}/d_i$ and $\delta_{uncor,i} = \sigma_{uncor,i}/d_i$ (the systematic uncertainty was already being used in its relative form as it is applied to the theoretical value). This gives,

$$\chi^2(\vec{t},\vec{b}) = \sum_i \frac{\left[d_i - t_i(\vec{p})(1 + \sum_j b_j\gamma_{ij})\right]^2}{(\delta_{stat,i}d_i)^2 + (\delta_{uncor,i}d_i)^2} + \sum_j b_j^2. \tag{C.13}$$

In order to avoid any bias from statistical fluctuations, the uncertainties can all be applied as a function of the expected rather than the measured result. This can be done by simply substituting the relevant d_i variables with t_i. A more complex scaling can be used which depends on the shifts in b_j for each iteration of the minimisation. This also leads to the covariance matrix being modified in each iteration as explained in [114]. This is included into the χ^2 function by scaling the uncertainties appropriately. This is taken into account by a $\delta_{i,stat}^2 d_i(t_i - \sum_j \gamma_{ij}t_i b_j)$ term [111]. This more complex scaling also introduces a ln term to the χ^2 function which corresponds to a non-constant value

in the covariance matrix [114]. This is to correct for any bias introduced by updating the covariance matrix during the minimisation iterations. Once these modifications are made the final χ^2 definition is found,

$$\chi^2(\vec{t},\vec{b}) = \sum_i \frac{\left[d_i - t_i(\vec{p})(1+\sum_j b_j\gamma_{ij})\right]^2}{\delta^2_{i,stat} d_i(t_i(\vec{p}) - \sum_j \gamma_i j t_i(\vec{p}) b_j) + (\delta_{uncor,i} d_i)^2} + \sum_j b_j^2 + 2\ln\frac{\sigma_i(t_i(\vec{p}))}{\sigma_i(d_i)}. \quad \text{(C.14)}$$

This gives the form of the χ^2 function used in equation 9.7 to perform the QCD fits to the ATLAS and HERA data, as well as to produce the χ^2 values for the comparisons to theory. The ln term is found to not change the values of χ^2 obtained by much, and when used in a combination, is found to have no influence. This leads to the term being excluded from the χ^2 given in equation 9.1.